Abstract

Preliminary results in the search for the electron electric dipole moment in PbO*

Paul Hamilton

2010

The discovery of an electric dipole moment (EDM) of a fundamental particle would provide evidence for physics beyond the Standard Model. Many popular extensions to the Standard Model, such as supersymmetry, predict electron electric dipole moments (eEDMs) within a few orders of magnitude of the current experimental limit. The PbO* experiment uses several unique characteristics of the diatomic molecule lead oxide, that make it a particularly sensitive probe for detecting an eEDM. The valence electrons in PbO experience an effective intramolecular electric field of $> 10^{10}$ V cm^{-1} which greatly enhances the energy shift due to an eEDM. Because PbO is chemically stable, unlike many other molecules used in EDM searches, it can be used in a high temperature vapor cell. The large densities in the vapor cell give the PbO* experiment a high statistical sensitivity. In this thesis we will discuss improvements to both the apparatus and the experimental methods that have increased the statistical sensitivity to the point that a competitive limit on the eEDM may be feasible in the near future. Although the eEDM sensitivity was not high enough to place a new eEDM limit, a preliminary measurement was made that placed stringent limits on possible systematic effects. Finally we conclude with a proposed second generation of the experiment based on a microwave absorption measurement. A preliminary analysis suggests the second generation experiment could have sensitivity a few orders of magnitude higher than the current experiment. In the course of investigating this new method, we found several applications in the current experiment. In particular microwave absorption measurements of the PbO vapor pressure and the population transfer of PbO during laser excitation helped to explain the lower sensitivity of the experiment in the past.

Preliminary results in the search for the electron electric dipole moment in PbO*

A Dissertation

Presented to the Faculty of the Graduate School

of

Yale University

in Candidacy for the Degree of

Doctor of Philosophy

by

Paul Hamilton

Dissertation Director: Professor David DeMille

December 2010

To my family, present and future

Acknowledgments

This thesis would not have been possible without the help and support of my co-workers, friends, and family.

First and foremost I would like to thank my advisor, David DeMille, for his support throughout my graduate school career. His sheer enthusiasm for his research brought me into AMO physics; a field which I would never have expected to enter before graduate school, but which I now love. I have learned a tremendous amount through his explanations which are invariably tailored perfectly to the level of one's understanding. His interests in exploring both the big questions in physics and the smallest details of experimental methods are inspiring. Lastly, his patience with his students (in teaching; in letting us explore, i.e. make mistakes, independently; in dealing with issues outside the lab; in never putting the focus on getting results at the expense of understanding; etc.) is truly a virtue.

Next, I would like to thank the fellow members of the DeMille group for a fantastic graduate school experience. It has been wonderful working with a group of people who have been so supportive of each other, relaxed, and engaged in their research. In particular I would like to thank Yong Jiang, from whom I learned much of the physics and experimental details of the PbO experiment, and Sarah Bickman, who put up with and answered an endless number of questions from me as a young graduate student. Sid Cahn has always been more than willing to lend his time and expertise to any problem. I could not have kept the experiment running the last couple years without Hunter Smith's eager help with both the mundane tasks and some of the crazier experimental ideas. The enthusiasm of Nate Gilfoy and Jeremy Sage initially brought me into the group and they taught me much about AMO along with more practical concerns such as taking the time to enjoy the little victories in the lab.

I would also like to thank the members of my committee. Dan McKinsey's enthusiasm for

initiating conversations across subfields has kept my focus in physics from becoming too narrow. I have learned much from Steve Lamoreaux's questions and explanations during seminars on an incredible variety of subjects, both theoretical and experimental. Witold Skiba does an amazing job of explaining high energy particle theory in a way that an experimentalist can both understand and appreciate. Jack Sandweiss's breadth of knowledge and enthusiasm for all of physics has been inspiring and I have appreciated both his interest in my research and his personal support.

I would like to thank my family for their support. From an early age my parents instilled in me a passion for reading and learning. My dad's interest in trying to understand the universe led me to the field of physics. My mom's untiring efforts in making sure I was always challenged and able to follow my interests were instrumental in my education. Their support, particularly throughout the writing of this thesis, has been above and beyond and I could not have done without it.

Lastly, I would like to thank my wife for her unending support in following my dreams. Her unshakable confidence in me has kept me on the path I am today. I will never be able to repay her for her many personal sacrifices, which she has made and continues to make without the slightest hesitation. I am blessed to have such a strong partner who has continually pushed me to follow a career that I love.

Contents

1 Introduction **1**

1.1 Motivation 1

1.2 EDM measurement overview 5

1.2.1 Experimental sensitivity 9

1.2.2 Survey of electron EDM experiments 9

1.3 Overview of the PbO experiment 11

1.3.1 Quantum beats 13

1.3.2 Experimental reversals in PbO 14

1.4 Introduction to EDM systematics 15

1.4.1 Motional and transverse magnetic fields 16

1.4.2 Leakage currents 17

1.4.3 Geometric phases 17

2 Outline of the thesis **19**

3 Molecular calculations **20**

3.1 Molecular structure 20

3.2 Quick introduction to electronic structure 23

3.3 States with no internal angular momentum 24

3.3.1 Stark and Zeeman effects 25

3.4 Hund's case (c) states with internal angular momentum 26

3.4.1 Electric dipole operator 27

3.4.2 Magnetic dipole operator 28

3.5 The $a(1)[^3\Sigma^+]$ state of PbO . . . 29
3.5.1 Stark effect . . . 31
3.5.2 EDM shift . . . 33
3.5.3 Zeeman effect . . . 34
3.5.4 The EDM measurement states . . . 35
3.5.5 Ω-doubling . . . 37
3.5.6 Electric field dependence of g factors . . . 40

4 Electron EDM enhancement in atoms and molecules 43
4.1 Schiff's theorem . . . 44
4.1.1 Shielding of the electric field . . . 44
4.1.2 Evasion of Schiff's Theorem . . . 45
4.2 Back of the envelope estimate of the effective electric field . . . 47
4.3 Introduction to EDM enhancement factor calculations . . . 48
4.3.1 Enhancement in atoms . . . 48
4.3.2 Enhancement in molecules . . . 50
4.3.3 Molecules do NOT have permanent EDMs . . . 51
4.4 Overview of *ab initio* methods . . . 52
4.5 Enhancement in PbO . . . 55
4.5.1 Electronic structure of PbO . . . 55
4.5.2 Semi-empirical calculation . . . 59
4.5.3 *Ab initio* calculations . . . 65

5 Apparatus 67
5.1 Overview of apparatus . . . 68
5.2 Electrical connections . . . 78
5.3 Leakage currents . . . 78
5.3.1 In-cell leakage currents . . . 78
5.3.2 Benchtop leakage current tests . . . 81
5.4 Degaussing system . . . 83
5.5 Polarization-sensitive detection . . . 83
5.5.1 Polarization in light pipes . . . 84

5.5.2 Sources of birefringence . . . 87
5.5.3 Observations with wire grid polarizers . . . 89
5.6 Oven and heat shielding . . . 89
5.7 Spectral filters . . . 95
5.8 Christiansen filters . . . 103
5.9 Microwave system . . . 108
5.10 Dye laser system . . . 114
5.10.1 Laser line width problem . . . 114
5.10.2 Laser excitation efficiency problem . . . 117
5.11 Seeded dye laser . . . 120
5.11.1 High power infrared laser . . . 121
5.11.2 Optical waveguide frequency doubler . . . 124
5.11.3 CW seeded dye amplifier . . . 126
5.11.4 Fabry Perot . . . 127
5.11.5 Results with the new laser system . . . 129
5.11.6 The YAG laser . . . 132

6 EDM measurement methods and results 134
6.1 Fluorescence detection of quantum beats . . . 134
6.2 Data fitting . . . 137
6.3 EDM state preparation . . . 139
6.3.1 Microwave state preparation . . . 139
6.3.2 Microwave erasure . . . 144
6.3.3 Two frequency fitting . . . 147
6.4 Reversals and rejection of systematics . . . 148
6.5 EDM data and results . . . 152

7 Microwave absorption 155
7.1 Basic principle . . . 155
7.2 Signal to Noise . . . 157
7.2.1 Definitions . . . 158
7.2.2 Square Law Detector . . . 158

7.2.3 Homodyne detection . . . 168
7.3 Microwave absorption EDM measurement . . . 170
7.3.1 Expected absorption fraction . . . 170
7.3.2 Optimal absorption beam power . . . 171
7.3.3 Signal-to-noise ratio using the current apparatus . . . 172
7.3.4 EDM sensitivity with present apparatus . . . 173
7.3.5 Second generation absorption cell . . . 173
7.4 Excited state absorption . . . 176
7.5 Ground state absorption . . . 180
7.5.1 Stark modulation . . . 180
7.5.2 Ground state dipole moment . . . 182
7.5.3 Vapor pressure . . . 183
7.6 Pulsed dye laser excitation efficiency . . . 186

8 Conclusions and Future Directions **189**

A Mixing in a two level system **191**

B Comparison of cross section calculations **192**
B.1 Budker, Kimball, and Demille [86] . . . 192
B.2 Sakurai [131] . . . 193
B.3 Townes and Schawlow [69] . . . 194

C Optical alignment hints **195**
C.1 Tapered amplifier . . . 195
C.2 Polarization maintaining single mode fiber . . . 196
C.3 PPLN . . . 196
C.4 Four pass seeded dye amplifier . . . 197

D Data fitting **199**
D.1 Uncertainty in the beat frequency fit . . . 199
D.2 Extracting “scrambled” data . . . 203
D.2.1 Equivalence to g-2 ratio method . . . 205

Bibliography **206**

List of Figures

1.1 History of eEDM searches 2
1.2 Violation of P and T invariance 3
1.3 One-loop EDM diagram 5
1.4 Theoretical predictions of the eEDM 6
1.5 Ramsey spectroscopy 7
1.6 PbO cartoon 12
1.7 Quantum beats 13
1.8 Comagnetometer in action 15

3.1 Molecular structure 21
3.2 Hund's case (a) 24
3.3 Hund's case (c) 25
3.4 Stark effect in $^1\Sigma$ state. 26
3.5 The $a(1)$ rotational levels 30
3.6 Field-free J=1 state 31
3.7 The $a(1)$, $J = 1$ state in an electric field 33
3.8 Polarization of $a(1)$ levels 34
3.9 The $a(1)$, $J = 1$ state in a magnetic field 35
3.10 The EDM measurement states. 36
3.11 Difference between g factors 42

4.1 Parity eigenstates 52
4.2 PbO molecular orbital diagrams 58

5.1 Vapor cell . . . 68
5.2 Oven . . . 70
5.3 Au/AuPd thermocouple calibration . . . 71
5.4 Insulation and terminal blocks . . . 72
5.5 The vacuum chamber . . . 73
5.6 Magnetic shields and vacuum . . . 74
5.7 Schematic of the optical system . . . 76
5.8 Experiment timing schematic . . . 77
5.9 Ceramic insulated twisted wire pairs . . . 79
5.10 In-cell leakage currents . . . 80
5.11 Three electrode leakage current measurement . . . 81
5.12 Sapphire resistance in air. . . . 82
5.13 Reflection of polarized light. . . . 84
5.14 Geometry for light pipe polarization calculation . . . 85
5.15 Benchtop test of polarization after a light pipe . . . 86
5.16 Polarization scrambling in a light pipe . . . 87
5.17 Effect of wire grid polarizer . . . 88
5.18 Heat shields . . . 91
5.19 Mock oven for heat shield testing . . . 92
5.20 Tests of metal foil heat shields. . . . 93
5.21 Thermal insulation . . . 94
5.22 Ceramic insulation versus metal foil heat shield . . . 95
5.23 Effective wavelength and probability density for interference filters. . . . 96
5.24 Modeled transmission of an Omega interference filter . . . 97
5.25 Signal and blackbody sizes through interference filters 1 . . . 98
5.26 Transmission of IF at varying angles of incidence . . . 99
5.27 Signal and blackbody sizes through interference filters 2 . . . 101
5.28 Measured and modeled EDM sensitivity for various filter combinations . . . 102
5.29 Scattering via refraction in a sphere . . . 103
5.30 Random angular walk. . . . 105
5.31 Theoretical transmission for Christiansen filter test . . . 106

5.32 Transmission of a Christiansen filter for PbO 107
5.33 Microwave system schematic 1 109
5.34 Microwave system schematic 2 110
5.35 Timing diagram of the microwave system 111
5.36 Fluorescence and quantum beat spectrum 115
5.37 Dye laser spectrum from quantum beat spectroscopy 116
5.38 Saturation of quantum beats 119
5.39 Green seeded dye laser system. 122
5.40 Periodic poled lithium niobate waveguide chip 125
5.41 Four pass seeded dye amplifier 126
5.42 Fabry Perot 127
5.43 Fabry Perot image 128
5.44 Frequency spectrum of seeded dye laser 129
5.45 Quantum beat spectra with seeded dye laser 130
5.46 Higher power four pass amplifier frequency spectrum 131
5.47 Fabry Perot image of YAG pulse 132

6.1 Pulsed dye laser excitation to the a(1) state 135
6.2 Decay paths leading to quantum beats 136
6.3 Fit of quantum beat data 137
6.4 RF EDM state preparation 139
6.5 Microwave Raman EDM state preparation 140
6.6 Population transfer by a frequency chirped microwave pulse 142
6.7 Microwave erasure 145
6.8 Microwave erasure evidence 145
6.9 Problems with microwave erasure 146
6.10 Accuracy of two frequency fitting 148
6.11 Order of reversals during EDM data taking 152
6.12 Histogram of the $\mathcal{E}$-odd, N-odd combination 153
6.13 EDM results from 2008 data run 154

7.1 Spontaneous optical decay versus microwave absorption 156

7.2 Square law detector PSDs 163
7.3 Microwave absorption cell 174
7.4 Microwave pump-probe scheme 175
7.5 Microwave absorption proof of principle 177
7.6 Microwave absorption setup 177
7.7 Calibration of Agilent R422C diode detector 178
7.8 Time domain microwave absorption signal 179
7.9 Microwave absorption lineshape 179
7.10 Stark modulation. 180
7.11 Stark modulation signal. 181
7.12 Saturation of microwave absorption 182
7.13 Stark modulation at several field strengths 183
7.14 PbO partial vapor pressure 185
7.15 Partial and total vapor pressure for PbO polymers above solid PbO 185
7.16 Vapor pressure versus cell body and stem temperatures 186
7.17 Excitation efficiency measurement 188

List of Tables

1.1 Electron EDM searches. A good figure-of-merit (FOM) in determining EDM sensitivity is $\mathcal{E}_{eff}\tau\sqrt{\dot{N}_{eff}}$, where $\mathcal{E}_{eff}$ is the effective electric field, τ is the measurement coherence time, and $\dot{N}_{eff}$ is the effective counting rate. 9

3.1 Atomic and molecular spectroscopic notation 23

3.2 Hund's case (c) matrix elements for rank-1 tensor 28

3.3 $a(1)$ eigenstates in an electric field 32

4.1 *Ab initio* methods 53

4.2 PbO configurations and term values 58

4.3 PbO states 59

4.4 PbO $\sigma^2\pi^3\pi^*$ state expansions 62

4.5 PbO $\sigma\pi^4\pi^*$ state expansions 63

4.6 Effective fields in PbO $a(1)$ state 66

6.1 Beat frequency combinations and systematic effects 151

7.1 Signal-to-noise improvements from absorption cell 176

Chapter 1

Introduction

Searches for an electric dipole moment (EDM) of a particle have now been carried out for nearly 60 years with null results. The field started in 1950 when Ramsey and Purcell first pointed out, in a short note [1], that even though an EDM would violate the invariance of physics under parity,

> ...existence of an electric dipole moment of a nucleus or of an elementary particle...becomes a purely experimental matter.

Since the 1950s, the limit on the electron EDM[1] has been improved by over 14 orders of magnitude to $d_e < 1.6 \times 10^{-27}\, e\,\text{cm}$ [3] (see Fig. 1.1). To put this in perspective, if an electron[2] was expanded to the size of the earth, this limit corresponds to a shift in the charge distribution of less than 40 nm. From the perspective of the first experimentalists in the field, one might be inclined to politely suggest that the experimental question of the existence of EDMs has been resolved. However, as we will discuss below, motivations for EDM searches are stronger today than ever before.

1.1 Motivation

The present day motivation for EDM searches is to discover (or constrain) new sources of CP violation beyond the Standard Model (SM). CP violation is a difference in the laws of physics under two transformations: charge conjugation (C), or, roughly speaking, swapping of particles for antiparticles, and parity (P), or spatial inversion. An EDM is evidence of CP violation because

[1] There is a similar history for the neutron EDM. See, e.g. [2].
[2] Here we consider an electron to have a classical radius, $r_e = e^2/m_e c^2 \approx 3 \times 10^{-13}$ cm.

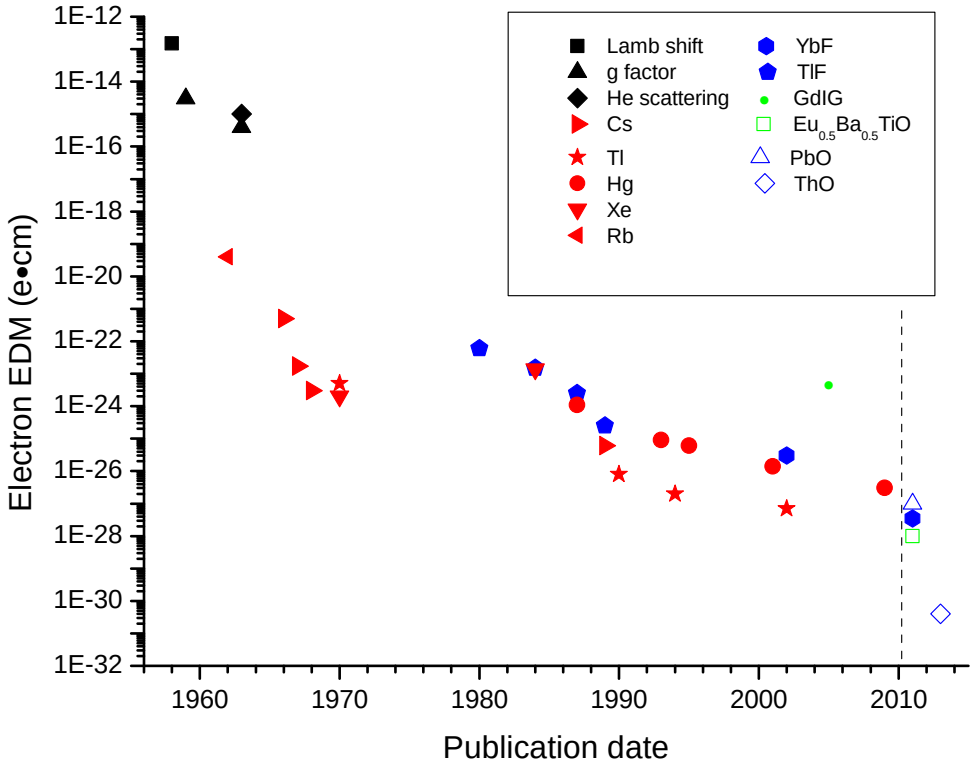

Figure 1.1: History of eEDM searches. Previous measurements: Lamb shift [4], g factor of e^- [5, 6], e^- scattering on He [7], rubidium [8], cesium [9–13], thallium [3, 14–16], xenon [17, 18], thallium fluoride [19–22], mercury [23–27], GdIG [28]. Projected limits for experiments in progress at Yale: PbO [29], ThO [30], $Eu_{0.5}Ti_{0.5}O_3$ [31]. Red, blue, and green symbols are atomic, molecular, and solid state experiments, respectively.

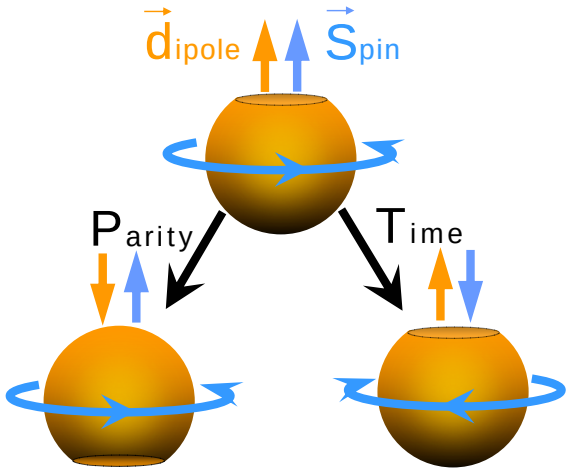

Figure 1.2: Violation of P and T invariance. A particle with an EDM is not invariant under either the parity or time reversal transformations. The charge distribution, here represented as a dented ball, is inverted under parity, changing the direction of the electric dipole moment, $\boldsymbol{d}$. Under time reversal the spin, $\boldsymbol{S}$, reverses direction while $\boldsymbol{d}$ is unaffected.

it is non-invariant under both time reversal (T) and parity (P) (see Fig. 1.2). The combined CPT symmetry, which holds for all Lorentz invariant field theories, implies that T violation is equivalent to CP violation.

CP violation is interesting for two main reasons. The first stems from the observation that the universe today consists almost entirely of matter, with virtually zero antimatter. The existence of the cosmic microwave background (CMB) suggests that shortly after the Big Bang there were nearly equal amounts of matter and antimatter. As the universe cooled, matter and antimatter annihilated producing the CMB photons we see today. The ratio of the number densities of the remaining baryons and CMB photons, denoted by η, is thus a good measure of the matter-antimatter asymmetry of the universe. Observations of the CMB combined with limits derived from the observed large scale structure of the universe give $\eta = 6.1(2) \times 10^{-10}$ [32]. While this number is extremely small the fact that it is not zero (and that there is a baryonic universe today!) is difficult to explain. In 1964, Sakharov [33] showed that in any theory that explains the asymmetry, three conditions must have been met in the early universe: violation of baryon number, C and CP violation, and thermal non-equilibrium. Estimates of η based on CP violation in the SM are generally over 10 orders of magnitude smaller [34, 35] than the observed value. Thus there must be

additional sources of CP violation. Note, it is entirely possible that the CP violation which explains the baryon asymmetry occurred at an extremely high energy scale (e.g. leptogenesis theories) and has no observable low energy effects.

However, this does lead us to our second motivation. Most theories beyond the SM introduce new sources of CP violation. In fact, without resorting to new symmetries, fine-tuning, or extremely high energy scales, it is generally difficult to devise a theory that has as little CP violation as the Standard Model.

In the SM, CP violation can occur in two places.[3] The Lagrangian for the strong force has one CP violating term, $\bar{\theta}$. The current experimental limit on the neutron EDM [36] constrains this term to be extremely small, $\bar{\theta} \leq 10^{-11}$. The second source of CP violation is a single phase in the Kobayashi-Maskawa (KM) quark mixing matrix [37]. Experimental observations constrain the KM phase to be on the order of one, i.e. it violates CP almost maximally. All observations, e.g. in the K [38] and B mesons [39, 40], are consistent with this single phase.[4] Symmetry in the structure of the KM matrix suppresses the effects of the CP violating phase in experiments. For the electron electric dipole moment (eEDM), four-loop terms lead to a Standard Model electron EDM prediction of $1 \times 10^{-40}\, e\,\text{cm}$ [2], 13 orders of magnitude below the current experimental limit of $1.6 \times 10^{-27}\, e\,\text{cm}$ [3].

However, many popular extensions to the SM, e.g. supersymmetry, naturally include CP violating phases that can give rise to EDMs even larger than current experimental limits. For the eEDM there is a simple, heuristic explanation for these values [42]. The eEDM arises from CP violating radiative corrections analogous to those that lead to the anomalous magnetic moment of the electron. Fig. 1.3 shows the one-loop diagram for the anomalous magnetic moment and a one-loop diagram, leading to an eEDM, that arises from a new CP violating interaction. A standard field theory calculation gives the one-loop contribution to the anomalous magnetic moment, $(g-2) = \frac{\alpha}{\pi}$. The EDM diagram is similar but has a coupling strength f instead of e, an extra CP-violating phase ϕ, and a propagator with mass m_X, which introduces a factor of $1/m_X^2$. Dimensional arguments suggest that

$$d_e = \sin\phi (f/e) \left(\frac{m_e}{m_X}\right)^2 (g-2). \tag{1.1}$$

[3] If massive neutrinos are considered part of the SM, there is an additional CP violating phase but it not thought to explain the baryon asymmetry or lead to observable EDMs.

[4] One recent experiment [41] reports a 3-σ deviation from the SM in neutral B mesons.

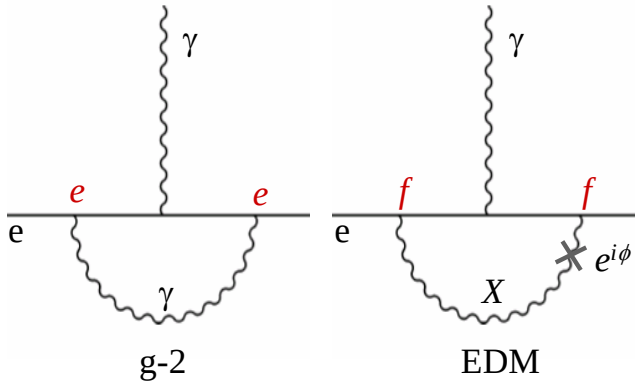

Figure 1.3: One-loop EDM diagram. Left: One-loop Feynman diagram for the anomalous magnetic moment. Right: One-loop diagram, leading to an eEDM, that arises from a hypothetical new CP violating interaction. The new interaction has a coupling f between the electron and a massive particle, X. The CP violating phase ϕ is schematically represented by the cross mark.

If we assume the couplings are comparable, the CP violating phase ϕ is on the order of 1, and use the value of the Bohr magneton, $\frac{e\hbar}{2m_e c} = 1.93 \times 10^{-11}\, e\,\text{cm}$, we find

$$d_e \approx \left(\frac{100\,\text{GeV}}{m_X}\right)^2 \times 1 \times 10^{-24}\, e\,\text{cm}. \tag{1.2}$$

Additional loops roughly give factors of $f^2/\pi \approx \alpha/\pi \approx 2 \times 10^{-3}$. Thus, even for a theory where the electron EDM appears only at the two-loop level, a propagator with mass $m_X = 100\,\text{GeV}$ gives $d_e = 2 \times 10^{-27}\, e\,\text{cm}$. Note, the 100 GeV mass scale is well-motivated theoretically. New particles are needed at this scale to stabilize the mass of the Higgs boson.

Fig. 1.4 shows the predictions for many popular SM extensions (see [43] and references therein for details). One can see that the current experimental limit has tightly constrained the most basic supersymmetry models. Lowering the experimental limit by a few orders of magnitude will tightly constrain many of these theories or perhaps lead to a discovery of the eEDM.

1.2 EDM measurement overview

Most EDM experiments use some form of the method of separated fields, also known as Ramsey spectroscopy[44]. This method, used in everything from atomic clocks to searches for the variation

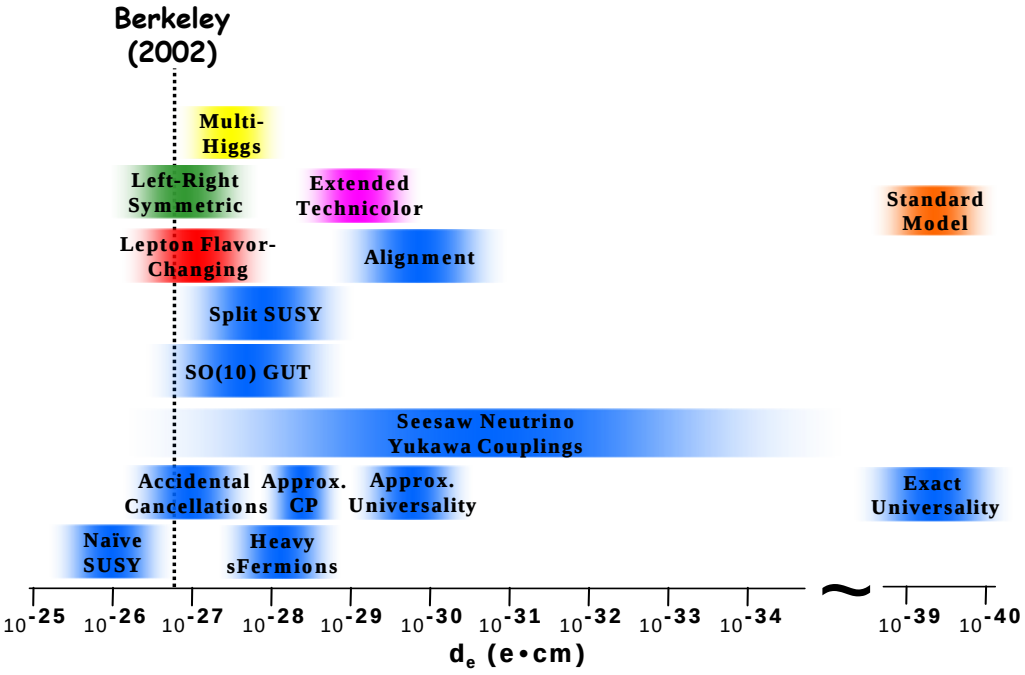

Figure 1.4: Theoretical predictions of the eEDM (see [43] and references therein for details). Colored regions indicate the range of predicted values for the electron EDM in various theories beyond the Standard Model. Blue indicates a supersymmetric (SUSY) model. The vertical line labeled "Berkeley (2002)" is the current experimental limit [3].

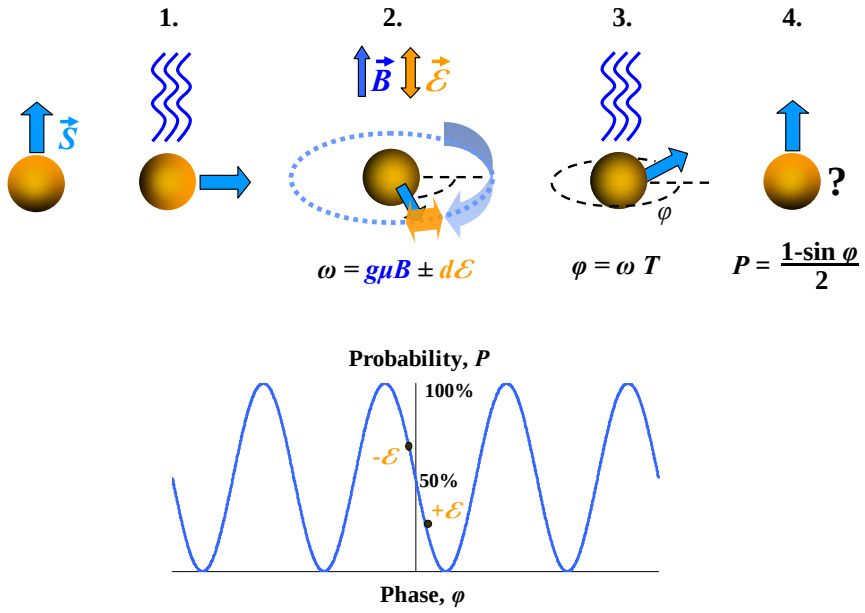

Figure 1.5: Ramsey spectroscopy for EDM experiments. 1. The spin of a particle is tipped, traditionally via an RF pulse, from vertical to horizontal, perpendicular to static electric and magnetic fields. 2. The spin magnetic moment undergoes Larmor precession. If the particle also has an EDM, the precession frequency is $\omega_\pm = g\mu B \pm dE$. 3. After a time T, a second RF pulse tips the spin towards vertical with a probability, $P = (1 - \sin\phi)/2$, dependent on the precession phase, $\phi = \omega_\pm T$. 4. Measuring the fraction of particles with vertical spin determines the phase. Measuring the change in phase when the electric field is reversed gives the energy shift due to the EDM. For $\phi \approx 2n\pi, \delta\phi \approx (\omega_+ - \omega_+)T = 2d\mathcal{E}T$.

of fundamental constants, is the workhorse of present day precision measurements. For an EDM experiment this method relies on the EDM pointing along the spin axis of a particle. Roughly speaking this must be the case, as any component of an EDM perpendicular to the spin will average to zero under rotation. More formally the same conclusion can be reached using the Wigner-Eckert theorem.

Ramsey spectroscopy consists of four steps (see Fig. 1.5). First, the spin of a particle is aligned perpendicular to static electric ($\mathcal{E}$) and magnetic fields (B), traditionally by using an RF magnetic field. Next, the spin magnetic moment, μ, undergoes Larmor precession. If the particle also has an EDM, d, the precession frequency changes slightly due to the torque from the electric field. The total precession frequency is $\omega_\pm = g\mu B \pm d\mathcal{E}$, where g is the magnetic g factor. After a time T, a

second RF pulse (or analogous method) transfers the particles to a readout state with probability $P = (1 - \sin\phi)/2$, which is dependent on the precession phase, $\phi = \omega_{\pm}T$. Lastly, the particles in the readout state are detected. For an ensemble the probability, P, is given by the fraction of particles detected in the readout state. Measuring the change in phase when the electric field is reversed gives the energy shift due to the EDM. For $\phi \approx 2n\pi, \delta\phi \approx (\omega_+ - \omega_-)T = 2d\mathcal{E}T$.

For neutral particles this method can be implemented straightforwardly. For example, in neutron EDM experiments neutrons are sent through a spin polarizer into a holding cell where electric and magnetic fields are applied. This is followed by spin sensitive detection (e.g. see [36, 45, 46]). Large electric fields are obviously desirable as bigger shifts in the precession frequency can be measured more precisely. For neutron EDM experiments the applied fields are usually limited only by dielectric breakdown and are typically $10 - 100\,\mathrm{kV\,cm^{-1}}$[47].

For charged particles applying an electric field poses a problem: not only is there a torque on the EDM, but there is the much stronger Coulomb force. Without a clever design this limits an experiment to the time it takes for the particle to hit the electrodes. There have been proposals to use storage rings for muon[48] and deuteron[49] EDM searches, but requirements on field stability and homogeneity are technically challenging. There is also a relatively new experiment proposing to use molecular ions in an electrostatic trap [50] with a co-rotating magnetic field.

For an electron EDM search one can avoid these difficulties by using a neutral atom or molecule. In fact, not only do neutral atoms and molecules help to confine the electrons, they can also enhance the effect of an electron EDM. The electrons interact with the internal electric field of the atom or molecule rather than the external electric field applied in the laboratory. As we will discuss in detail in Chapter 3, the internal electric fields of atoms and molecules can be enormous. For heavy nuclei, the average Coulomb field for an electron near the nucleus is proportional to Z^3 and can reach $\approx 10 - 100\mathrm{GV\,cm^{-1}}$! In atoms, which have a high degree of spherical symmetry, much of this enhancement is lost as one averages over the electric field direction. Molecules, on the other hand, can be completely polarized and EDM measurements can take full advantage of the enormous internal electric field [51].

Species	$\mathcal{E}_{eff}$ (V/cm)	τ (s)	$\dot{N}_{eff}(s^{-1})$	Relative FOM	Group
Tl	7×10^7	2.4×10^{-3}	10^9	1	Commins [3]
Cs	4.6×10^5	1.5×10^{-2}	10^{10}	0.1	Hunter [13]
Hg	2×10^2	100	10^7	0.01	Fortson [27]
PbO	2.5×10^{10}	5×10^{-5}	10^6	0.5	Demille [29, 52]
YbF	1.3×10^{10}	1×10^{-3}	5×10^4	0.5	Hinds [53]
PbF	2.9×10^{10}	1×10^{-3}?	?	?	Shafer-Ray [54, 55]
WC	5.4×10^{10}	1×10^{-3}	?	?	Leanhardt [56]
Molecular ion	$3 - 9 \times 10^{10}$	$0.2 - 1$	10	4-50	JILA [50]
Cs	1×10^7	1	10^8	20	Gould [57], Heinzen [58], Weiss [59]
ThO	10^{11}	2×10^{-3}	10^5	10	ACME [30]

Table 1.1: Electron EDM searches. A good figure-of-merit (FOM) in determining EDM sensitivity is $\mathcal{E}_{eff}\tau\sqrt{\dot{N}_{eff}}$, where $\mathcal{E}_{eff}$ is the effective electric field, τ is the measurement coherence time, and $\dot{N}_{eff}$ is the effective counting rate.

1.2.1 Experimental sensitivity

The effective electric field on an electron is only one of the key factors for determining the sensitivity of an EDM experiment. To achieve high precision, statistics are vitally important. Two factors are important in a spin-precession measurement. The first is the coherence time, τ, of the measurement. From the Heisenberg uncertainty principle, a single frequency measurement can achieve at best a sensitivity of $\delta\omega = 1/\delta\tau$ or $\delta f = 1/(2\pi\tau)$. Second, in an experiment not limited by technical noise, N measurements reduce the uncertainty by a factor of $\sqrt{N}$. Thus a good figure-of-merit (FOM) in determining EDM sensitivity is $\mathcal{E}_{eff}\tau\sqrt{\dot{N}}$, where $\dot{N}$ is the counting rate.

1.2.2 Survey of electron EDM experiments

An ideal EDM experiment would maximize the three factors in the sensitivity figure of merit: effective electric field, coherence time, and counting rate. In practice, most experiments can maximize one only at the expense of another. For example, the low density of beam experiments generally leads to long coherence times but low counting rates. The high density of vapor cells give large counting rates but limited coherence time. Atoms have smaller effective electric fields than molecules, but molecules give lower counting rates since their thermal population is spread amongst many more levels. In practice, none of these trade offs is absolute; clever experimental

techniques mean that each experiment must be considered on its own merits.

Table 1.1 shows a few past, present, and future electron EDM experiments. The top group of experiments have already been completed.

The Commins experiment [3], current holder of the best electron EDM limit, used the heavy atom thallium for a large effective electric field, relative to other atoms, and a high flux beam source.

The experiment by the Hunter group [13] used a room temperature cesium vapor cell with a paraffin coating that preserved the spin coherence through many wall collisions. The counting rate and coherence time were higher than the thallium experiment. However, a combination of the lower applied electric field and a lower Z atom led to an effective electric field a couple of orders of magnitude smaller.

The experiment by the Fortson group [23, 24, 26, 27] is somewhat of an anomaly since it was primarily designed to look for an EDM of the mercury nucleus. The experiment monitors the nuclear spin of mercury in a room temperature vapor cell with a paraffin coating giving coherence times of over 100 seconds. Over the decades the experiment has been running, the statistical sensitivity has improved to the point that it now gives a competitive limit on the electron EDM, despite the fact that the mercury atom has an enhancement factor of much less than one (i.e. the electron EDM effect is diminished).

The middle group of experiments, PbO and YbF, have matured to the point that EDM data has been taken.

The YbF experiment [53] utilizes the high effective electric field of a diatomic molecule and the relatively long coherence time of a beam experiment. Supersonic expansion of the molecular beam puts most of the molecules in the ground state, increasing the counting rate over typical thermal molecular beams. However, the counting rate remains orders of magnitude below a thermal atomic beam.

By comparison, in the PbO experiment we trade coherence time for a higher counting rate by using a high temperature vapor cell. In theory, the counting rate could be further increased by orders of magnitude with absorption detection, something not possible in a beam experiment. In addition, a feature of the electronic structure of PbO, called Ω-doubling, allows one to control the direction of the internal electric field of the molecule, which provides a significant advantage in eliminating systematic effects. This will be discussed in detail later in the thesis.

The last group of experiments are proposed EDM searches. The cesium experiments propose to

optically trap atoms, resulting in a long coherence time and high counting rate. A group at JILA [50] proposes to use molecular ions in a RF trap to combine the high effective electric fields of molecules with a long coherence time. The Shafer-Ray group [54] proposes to use PbF in a beam experiment similar in spirit to YbF but with lower sensitivity to systematic effects from magnetic fields. The Leanhardt group [56] plans to take advantage of the ground state Ω-doublet structure of WC in a cold beam experiment.

Finally, the ACME collaboration of DeMille, Doyle, and Gabrielse [30] plans to use ThO in a new high flux cold beam source. ThO has the highest known effective electric field of any molecule proposed for an EDM search and an Ω-doublet structure similar to PbO for systematic rejection. Note that the numbers shown in Table 1.1 for ThO are conservative estimates based mostly on measured quantities for the first generation of the experiment.

Not mentioned in this discussion are the solid state electron EDM searches. Because they use entirely different experimental methods it is difficult to give a common figure of merit for both types of experiments. The (Eu,Ba)TiO_3 experiment at Yale applies an electric field to a sample and looks for a small induced magnetization. If the electron has an EDM it tends to orient along the electric field which aligns the electron spins in the solid. The proposed sensitivity of this experiment is about one order of magnitude better than the Berkeley limit.

1.3 Overview of the PbO experiment

Because an electron EDM is aligned with the electron spin axis, EDM shifts can be seen only in molecular states with unpaired spins. In the past, molecular EDM experiments were considered solely with molecules which had unpaired spins in their ground state. These molecules, called free radicals, are chemically unstable and can only be used in molecular beams, where there are few collisions. The PbO experiment avoids this restriction by using an excited metastable state with unpaired spins for the EDM measurement. In the ground state, the spins are paired and thus PbO is chemically stable. As mentioned above, this allows the use of a high temperature vapor cell which typically give higher counting rates than molecular beams.

The EDM measurement process in the PbO experiment starts with the excitation of the molecules from the ground state to an energy level with angular momentum $J = 1$, in a metastable state. Next, the molecules are prepared in a superposition of the magnetic sublevels, $|\Psi\rangle = |J = 1, M = 1\rangle +$

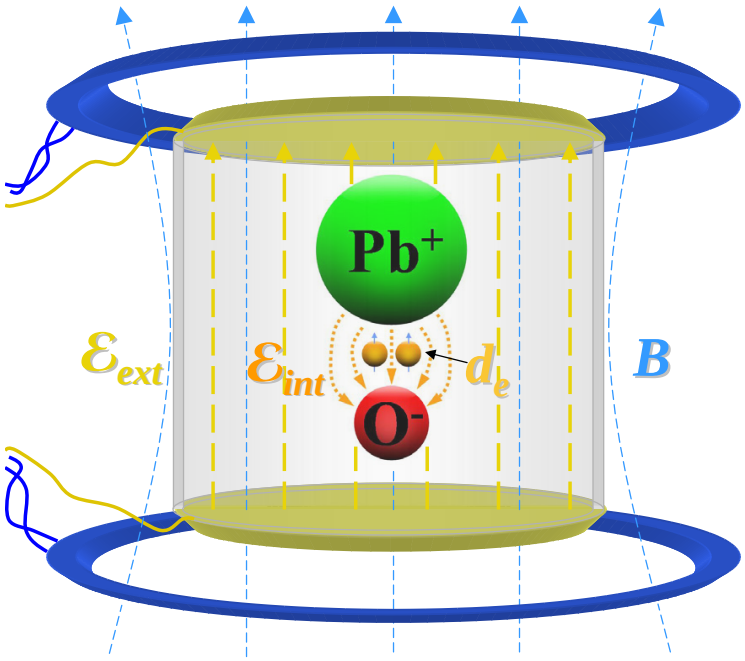

Figure 1.6: Cartoon version of the PbO experiment. Parallel electric, $\mathcal{E}_{ext}$, and magnetic, B, fields are applied to PbO molecules in a vapor cell. Valence electrons with parallel spins sit in the internal electric field, E_{int}, of the molecules. The EDM shift is determined by comparing energy splittings, $\Delta E = 2g\mu B + 2d_e\mathcal{E}_{int}$ between $|J = 1, M = \pm 1\rangle$ sublevels. Three different reversals E_{ext}, E_{int}, and B change the relative sign of the two terms in ΔE. Few systematic effects change in the same manner as the EDM term under these three reversals. The E_{int} reversal is particularly useful because it requires no changes to the external fields generated by the experimental apparatus.

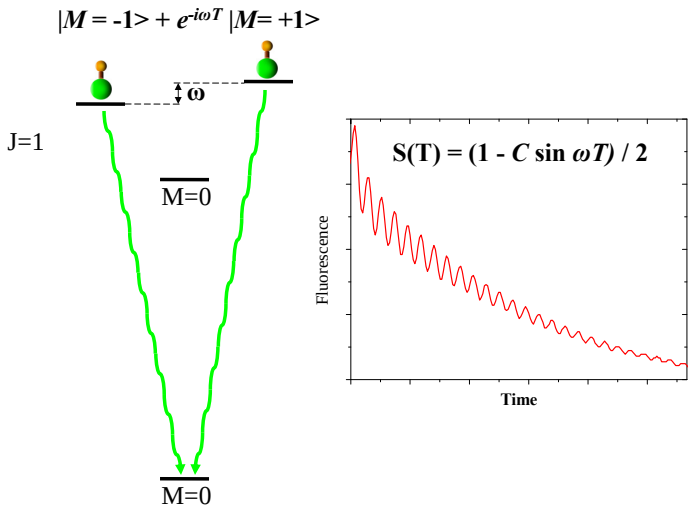

Figure 1.7: Quantum beats. If the $M = \pm 1$ sublevels of an excited state are split by energy ω, a superposition of states evolves according to $|\Psi(T)\rangle = |M = -1\rangle + e^{-i\omega T}|M = +1\rangle$. Because of the relative phase, the decay amplitudes to a common $M = 0$ level can interfere leading to a modulation of the form, $S(T) = (1 - C\sin\omega T)/2$, in the decay fluorescence called quantum beats. The contrast, C, accounts for decays to other sublevels in the ground state that do not exhibit interference.

$|J = 1, M = -1\rangle$, which is roughly the quantum mechanical analogue of a spin oriented in the $x - y$ plane. A magnetic field is applied in the z direction which causes a Zeeman shift of the sublevels $\delta E = g\mu MB$, which is analogous to the Larmor precession frequency in Ramsey spectroscopy. Electrodes in the vapor cell apply an electric field which causes a Stark shift common to both sublevels and polarizes the molecules (see Fig. 1.7). If the electron has an EDM, d_e, the internal electric field of the molecule causes an additional Stark shift giving $\delta E = g\mu MB + d_e M\mathcal{E}_{int}$.

A feature of the electronic structure of PbO, called Ω-doubling, allows us to choose the direction of the internal electric field of the molecules by selectively polarizing them with or against the external electric field. As we will discuss below, this novel ability is a powerful tool for rejecting systematics and has become a de facto requirement for new molecular EDM search proposals.

1.3.1 Quantum beats

From the Schrödinger equation, the relative phase between the states in the superposition evolves according to $|\Psi(T)\rangle = |J = 1, M = 1\rangle + e^{-i\omega_\pm T}|J = 1, M = -1\rangle$, where $\omega = 2g\mu B + 2d_e\mathcal{E}_{int}$ is the energy difference between the sublevels. If a molecule decays to a M=0 sublevel in the ground state the

decay amplitudes from the M=+1 and M=-1 levels can interfere due to this phase difference (see Fig. 1.7). In practice this interference shows up as an intensity modulation of the decay fluorescence with a time dependence of $(1 - C \sin \omega T)/2$, where the contrast, C, accounts for decays to other sublevels that do not exhibit interference. This modulation is referred to as quantum beats. Similar to Ramsey spectroscopy, the EDM shift is given by the difference of the quantum beat frequency for opposite directions of any of the fields (magnetic, external electric, or the the internal electric field).[5]

This method, called quantum beat spectroscopy, has several advantages over traditional Ramsey spectroscopy. First, because the quantum beat frequency is proportional to an energy difference it is not broadened by energy shifts common to both sublevels. For example, because the Doppler shift is common to both decay paths, the quantum beat frequency is not Doppler broadened to first order. Thus despite an 800 MHz Doppler width of the fluorescence transition, the beat frequency width is limited only by the lifetime of the metastable state to ≈ 4 kHz. Similarly the beat frequency is not affected by the few MHz broadening due to inhomogeneous electric fields in the vapor cell.

A second advantage of quantum beat spectroscopy is that each experimental data point is a frequency. In Ramsey spectroscopy the actual measured quantity is the number of particles in the readout state which corresponds to a height on the fringe curve (see Fig. 1.5). To infer a change in phase due to an EDM, one must use the total number of particles, which sets the height of the fringes, and the magnetic field, which sets the phase of the curves. Unknown fluctuations of either of these quantities leads to systematic errors or noise. In essence quantum beat spectroscopy generates the entire fringe curve in each shot.

1.3.2 Experimental reversals in PbO

The fact that the EDM shift can be determined from several unique combinations of quantum beat frequency measurements is useful for rejecting systematic effects. For example, the difference of the beat frequencies for opposite directions of the internal electric field gives, $\Delta\omega_{\mathcal{E}_{int}} = (2g\mu B + 2d_e\mathcal{E}_{int}) - (2g\mu B - 2d_e\mathcal{E}_{int}) = 4d_e\mathcal{E}_{int}$. Because this reversal is internal to the molecule and requires essentially no changes to the apparatus, it is particularly powerful at eliminating systematic effects. Through this difference, the states with opposite internal electric fields act as co-magnetometers by

[5]The two states with opposite internal electric field directions are defined by their polarization relative to the external field. Thus leaving the state unchanged and reversing the external electric field also reverses the internal electric field.

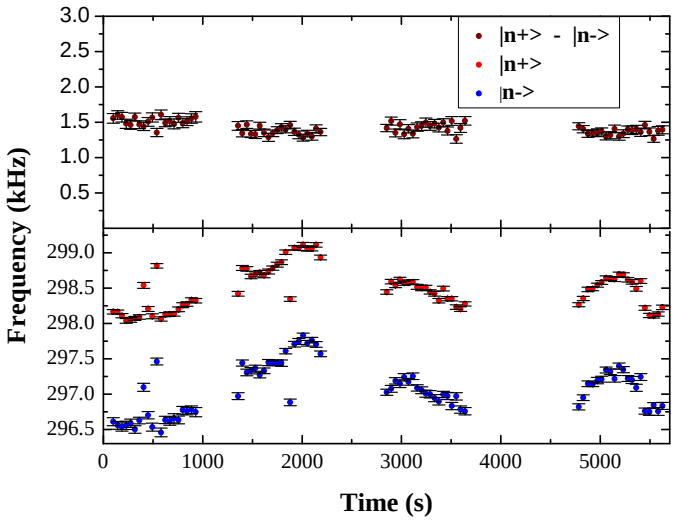

Figure 1.8: Comagnetometer in action. Bottom: Beat frequencies for two orientations of the molecule n_+ and n_- taken with only one layer of magnetic shielding. Top: Subtracting the beat frequencies cancels the drifting magnetic field. The discrete jumps seen in the bottom are most likely due to an elevator nearby the lab.

"measuring" and canceling magnetic field effects.

Fig. 1.8 shows data taken with only a single layer of magnetic shielding. Discrete jumps seen in the beat frequencies on the bottom are most likely due to changing magnetic fields from an elevator near the lab. Subtracting the frequencies for the two orientations of the molecule, labeled here as n_+ and n_-, cancels the drifting magnetic field.

Combinations of beat frequencies from reversals of the external electric field and magnetic field can be used similarly to measure or cancel various systematics. We will discuss this in more detail in Section 6.4. In fact, at this point there are no known systematics which survive all three reversals at the projected sensitivity of our experiment.

1.4 Introduction to EDM systematics

Energy shifts which change sign with the direction of the electric field and are proportional to the magnetic moment of a particle can mimic the effect of an EDM. The polarizibility of molecules and the ability to control the direction of the internal electric field with Ω-doubling can suppress these effects by orders of magnitude compared to atomic systems.

1.4.1 Motional and transverse magnetic fields

A particle moving with velocity, v, in an electric field, $\mathcal{E}$, will experience a transverse magnetic field in its rest frame, $B_m = v \times \mathcal{E}/c$. Because the motional field changes sign with the electric field its effect can be similar to an EDM. Motional fields were particularly problematic for atomic beam experiments which used large electric fields and high particle velocities. The use of counterprogating atomic beams in the thallium experiment reduced the first order effect, but a coupling between the motional fields and magnetic field gradients was ultimately the leading systematic error.

In molecular experiments the effect of transverse magnetic fields is highly suppressed. As alluded to above, the polarizibility of molecules leads to a large tensor Stark splitting, δE_{st}, between the $M = \pm 1$ and $M = 0$ sublevels. In a magnetic field, B, along the z axis a smaller transverse magnetic field, $\boldsymbol{B_\perp}$, gives a second order shift of[6]

$$\delta E_{B_\perp} = \frac{\left|\left\langle M = 0 \left| \, g\boldsymbol{\mu} \cdot \boldsymbol{B_\perp} \, \right| M = \pm 1 \right\rangle\right|^2}{2(\delta E_{st} \pm g\mu B)} = \frac{(g\mu B_\perp)^2}{2(\delta E_{st} \pm g\mu B)}. \tag{1.3}$$

This gives a shift in the quantum beat frequency of

$$\begin{aligned} \delta\omega &= \frac{(g\mu B_\perp)^2}{2}\left(\frac{1}{\delta E_{st} + g\mu B} - \frac{1}{\delta E_{st} - g\mu B}\right) \\ &\approx -g\mu B\left(\frac{g\mu B_\perp}{\delta E_{st}}\right)^2. \end{aligned} \tag{1.4}$$

The shift due to a transverse magnetic field in the absence of the tensor Stark effect is equal to the change in the usual Zeeman shift when $B \to B\cos\theta \approx B(1 - \theta^2/2)$, where $\theta \approx B_\perp/B$. The shift in the beat frequency is then $B_\perp^2/B$. Comparing with Eq. (1.4), the tensor Stark shift suppresses the shift due to a transverse field by $(g\mu B_\perp/\delta E_{st})^2$. For PbO, $g\mu \approx 1.3\,\mathrm{MHz\,G^{-1}}$ and $\delta E_{st} \approx 40\,\mathrm{MHz}$. For the usual magnetic field used in the experiment, $B = 100\,\mathrm{mG}$, and a perpendicular field, $B_\perp = 0.01B = 1\,\mathrm{mG}$, the suppression is $\approx 10^9$.

Returning to the motional fields, consider the worst case scenario for a molecule traveling perpendicular to the electric field. The perpendicular field is the sum of the motional field, $B_m = v\mathcal{E}/c$, and a field in the same direction, $B\sin\theta$, due to a small misalignment of angle θ in between

[6] Chapter 3 will discuss details on calculation of matrix elements for molecular states.

the electric and magnetic fields. The systematic shift has three terms

$$\begin{aligned}\delta\omega_{B_\perp} &= -g\mu B\left[\frac{g\mu(B\sin\theta + B_m)}{\delta E_{st}}\right]^2 \\ &= -g\mu B\frac{(g\mu)^2\left[(B\sin\theta)^2 + 2v\mathcal{E}B\sin\theta/c + (v\mathcal{E}/c)^2\right]}{(\delta E_{st})^2}.\end{aligned} \tag{1.5}$$

The first and third term are eliminated in differences between beat frequencies with the electric field reversed. Assuming a 1° misalignment of the magnetic field $B = 100\,\mathrm{mG}$; an electric field, $\mathcal{E} = 50\,\mathrm{V\,cm^{-1}}$, which leads to a Stark shift of $\approx 40\,\mathrm{MHz}$; and using the typical velocity of PbO at 700 °C, $v = 3\times10^4\,\mathrm{cm\,s^{-1}}$; the second term gives a shift, $\delta\omega_{B_\perp} = 100\,\mathrm{nHz}$, or a false EDM of $\approx 10^{-32}$ e·cm. In addition, reversal of the internal electric field of the molecule, which leaves this shift unchanged, provides further suppression.

1.4.2 Leakage currents

At high temperatures the resistance of insulators drops exponentially. In a vapor cell this leads to currents flowing between the electrodes. In the worst case, if the currents take a helical path around the vapor cell, they can produce a magnetic field along the z axis which reverses with electric field, mimicking an EDM. A typical leakage current of 10 μA produces a field of $B_{leak} \approx 2\,\mu\mathrm{G}$ at the center of our 8 cm diameter vapor cell. This corresponds to a beat frequency shift of $2g\mu B_{leak} \approx 4\,\mathrm{Hz}$ or a false EDM of 3×10^{-25} e·cm, which is significantly higher than our current sensitivity. However, as we will discuss in further detail in Section 6.4, the reversal of the internal electric field suppresses this effect by several orders of magnitude and can also be used to directly place a limit on B_{leak}.

1.4.3 Geometric phases

If the quantization axis of a particle changes over time, energy states can pick up an additional phase, called a geometric phase [60]. In the simplest case of a spin 1/2 particle the geometric phase is equal to the solid angle traced out by the quantization axis vector times the magnetic quantum number, m. Because of this dependence on m, the geometric phase acts as an effective magnetic field. A geometric phase due to a motional magnetic field, which is proportional to the electric field, is particularly problematic for EDM experiments.

For particles traveling through changing magnetic and electric fields it is not immediately obvi-

ous how to define the geometric solid angle, although calculational methods have been introduced for atomic beam experiments [61], traps [62], and neutron EDM experiments [63]. The internal angular momentum structure of polar molecules adds further complexity and makes geometric interpretations difficult. Amar Vutha, a former student on the PbO experiment now working on the ThO EDM experiment, has recently published a method [64] for calculating geometric phase shifts based on perturbative calculations of AC Stark and Zeeman shifts due to the changing fields.[7] In this paper, a J=1 state with no internal angular momentum (which neglects Ω-doubling as we have above) is considered in the limit of weak electrical polarization and Zeeman shifts much smaller than the tensor Stark shift. The geometric phase due to changing magnetic fields is strongly suppressed by the tensor Stark shift: $\phi_{geo,B} = (g\mu B_\perp/\delta E_{St})^2(\omega_\perp T)$, where $\omega_\perp$ is the rotational velocity of a the perpendicular field component due to the particles' motions for a time, T, through the fields. The inclusion of Ω-doubling and full electrical polarization yields a similar value.

For the PbO experiment $\omega_\perp$ is roughly the inverse of the time it takes a molecule to traverse the cell. At the optimal temperature of the vapor cell this time is approximately equal to the lifetime of the metastable state, $\tau = 40\,\mu s$, which gives a frequency $\omega_\perp \approx 25\,kHz$. Comparing with Eq. (1.5), if $B_\perp$ is a motional magnetic field this effect is smaller than the motional field systematic by the factor, $\omega_\perp/g\mu B < 0.1$. This effect is further suppressed by averaging over velocities in the vapor cell and reversing of the internal electric field [66].

[7] A recent paper by Meyer *et al.* [65] includes similar calculations.

Chapter 2

Outline of the thesis

Because the PbO experiment relies heavily on several features of its molecular structure, a quick introduction to molecular calculations is given in Chapter 3. In particular we focus on the details of the $a(1)$ electronic state used in the EDM measurement. In Chapter 4 we discuss the physics behind EDM enhancement in atoms and molecules and delve further into the theoretical calculations needed to determine the effective internal electric field of PbO. Chapter 5 gives a brief overview of the experimental apparatus and then focuses on improvements made during the course of this dissertation. Next, in Chapter 6, we discuss the detection techniques and state preparation methods used in the EDM measurement. The methods for systematic rejection are introduced. The results from an EDM data run are discussed. While the EDM limit placed is well over an order of magnitude larger than the current limit, tight constraints are placed on systematic effects. Chapter 7 then focuses on a proposed second generation of the PbO experiment based on a microwave absorption measurement. During the course of a proof-of-principle measurement, we found several uses for microwave absorption in our current apparatus. Lastly, Chapter 8 offers a few thoughts on the future of the PbO experiment.

Chapter 3

Molecular calculations

The extra degrees of freedom in molecules make them significantly more complicated than atoms. However, with proper approximations, many of these degrees can be considered independently. Even with these simplifications most molecular calculations still involve the couplings of several momenta. In this chapter we introduce the methods used for calculating energy levels of diatomic molecules and discuss some specific examples for PbO.

3.1 Molecular structure

To a good approximation the internal energy of a diatomic molecule is the sum of its electronic, vibrational, and rotational energies.

The largest energy scale is the electronic energy. Like atoms, transitions between electronic states in molecules typically involve optical radiation. In molecules electronic states are labeled with letters. X represents the ground state, while excited states are typically labeled roughly in order of energy by $A, B, C, \ldots$ or $a, b, c, \ldots$ with capital letters for states with the same multiplicity as the ground state and lowercase letters for other multiplicities. The order of labeling is sometimes historical and gives little information about the state. After the label one typically gives a designation, ${}^{2S+1}\Lambda_{\Omega}$, similar to the atomic notation of ${}^{2S+1}L_J$, describing the electronic state. We defer discussion of this notation to the next section.

After the electronic structure the next largest energy scale is the relatively evenly spaced ladder of vibrational energies (see Fig. 3.1). For each electronic state one can define a potential for the two

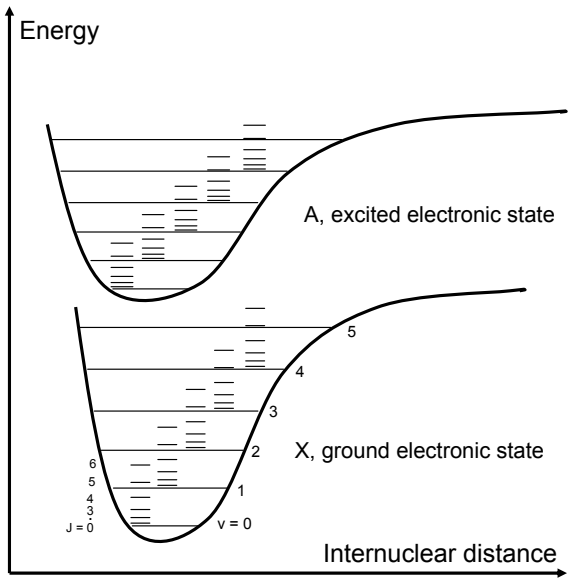

Figure 3.1: Molecular structure. Energy levels in molecules have three scales of structure. The largest scale is the electronic energy. Each electronic state is represented by an effective potential that depends on the internuclear distance. In each electronic state there is a ladder of vibrational levels, designated by the quantum number v, which are evenly spaced near the bottom of the potential well. For each vibration level there is a series of rotational levels, designated by the quantum number J. This figure is schematic only; energy spacings are not to scale and there are typically many more levels at all scales.

nuclei due to their Coulomb interactions with each other and the electrons. Near the bottom of the potential well (i.e. small vibrational quantum number) the electronic potential is nearly harmonic. Denoting the vibrational quantum number by v, the vibrational energies are given by (see Chapter 4, section 1 in [67])

$$G(v) = \omega_e \left(v + \tfrac{1}{2}\right) - \omega_e x_e \left(v + \tfrac{1}{2}\right)^2 + \omega_e y_e \left(v + \tfrac{1}{2}\right)^3 \tag{3.1}$$

where ω_e is the harmonic vibrational frequency and x_e, y_e are small corrections to account for anharmonicity. Vibrational transitions are usually in the far infrared.

The smallest energy scale common to all diatomic molecules is the rotational spectrum. Diatomic molecules can be approximated as rigid rotators with energies proportional to $J(J+1)$ where J is the rotational quantum number. With higher order corrections the rotation energies are

$$F = B_r J(J+1) - DJ^2(J+1)^2 + HJ^3(J+1)^3 \tag{3.2}$$

where B_r is called the rotational constant and D and H are higher order distortion corrections. Rotational transitions are typically in the microwave regime.

In actual diatomic molecules there is some coupling between vibrational and rotational energies. One method to account for this is the Dunham expansion:

$$F_{v,J} = \sum_{ij} Y_{ij} \left(v + \tfrac{1}{2}\right)^i J^j (J+1)^j \tag{3.3}$$

where $F_{v,J}$ is the energy of the rovibrational level. The most precise spectroscopic data for PbO (from Martin *et al.* [68]) does provide Dunham coefficients for the X and A states. In practice though it is often more accurate to use B_r, D, and H constants tabulated for each vibrational level (when available). These are provided in Martin *et al.* [68] for the levels in the X and a states most relevant to our experiment along with a term $G(v)$ defined to be the energy referred to the $(v = 0, J = 0)$ level of the X ground state. The energy, T, relative to the ground state is then

$$T = G(v) + B_r(v)J(J+1) - D(v)J^2(J+1)^2 + H(v)J^3(J+1)^3. \tag{3.4}$$

Table 3.1: Atomic and molecular spectroscopic notation

Atomic property			Molecular projection	
Symbol	Description	Values	Symbol	Values
S	Spin	$0, \frac{1}{2}, 1, \ldots$	Σ	$0, \frac{1}{2}, 1, \ldots$
L	Orbital angular momentum	$S, P, D, \ldots$	Λ	$\Sigma, \Pi, \Delta, \ldots$
J	Total electronic angular momentum	$0, \frac{1}{2}, 1, \ldots$	Ω	$0, \pm\frac{1}{2}, \pm 1, \ldots$

3.2 Quick introduction to electronic structure

The electronic structure of diatomic molecules is quite analogous to atomic structure. Instead of spherical symmetry, diatomic molecules possess only an axial symmetry around the internuclear axis. Electronic molecular states are typically specified by the notation $^{2S+1}\Lambda_\Omega$. S is the electronic spin. Ω and Λ are the projections along the internuclear axis[1] of the total electronic angular momentum J_e and the total electronic orbital angular momentum L, respectively (see Table 3.1). Because of axial symmetry only these projections, rather than L and J_e, can be good quantum numbers.

There are many different ways, called "Hund's cases", for the various momenta in molecules to couple with one another. Each case is associated with a certain basis set of "good" quantum numbers. In PbO we will be dealing mostly with Hund's case (a) for the ground state, X, and Hund's case (c) for the excited $a(1)$ state.

In Hund's case (a) L is coupled to the molecular axis by the strong internuclear electric field (see Fig. 3.2). As a consequence only its projection, Λ, is a good quantum number. S is not strongly affected by the internuclear electric field. However, more typically for low rotational levels, its coupling to Λ is stronger than its coupling to the rotational angular momentum, N. Hence, the projection on the internuclear axis, Σ, of S is also a good quantum number. The projections Λ and Σ add vectorially to give Ω.

Hund's case (c) often occurs in heavier molecules where spin-orbit interactions may couple L and S more strongly to each other than the internuclear axis (see Fig. 3.3). In this case only Ω is a good quantum number. These states are given notation such as $a(1)$, where a is the electronic state label, and the value in parentheses is Ω. Hund's case (a) states are specified by the $^{2S+1}\Lambda_\Omega$ notation

[1] The internuclear axis, denoted by $\hat{\boldsymbol{n}}$, is usually defined to be in the direction of the molecular electric dipole moment in the molecule fixed frame.

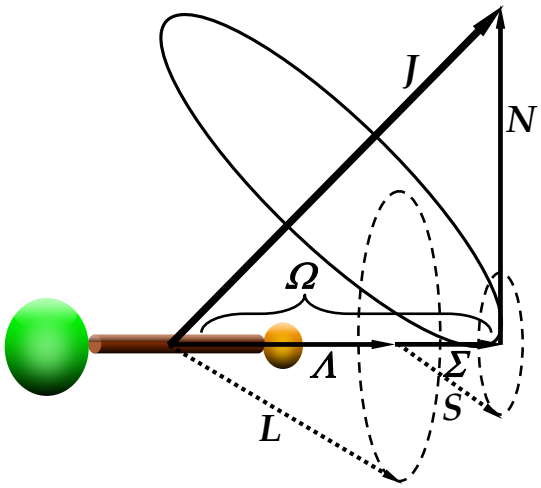

Figure 3.2: Hund's case (a). The orbital angular momentum, L, couples strongly to the internuclear axis. The spin angular momentum, S, is also quantized along the internuclear axis. Their respective projections, Λ and Σ, add to give Ω, the total projection of the electronic angular momentum. Ω and the rotational angular momentum N precess around the total angular momentum J.

mentioned above.

In both cases the projection of the electronic angular momentum, Ω, adds to the rotational angular momentum, N, to give the total angular momentum, J.

3.3 States with no internal angular momentum

Quantum mechanical calculations for molecular states with no internal angular momentum about the internuclear axis, such as $^1\Sigma$ states, are similar to those for atomic systems. For both, the angular wave functions are spherical harmonics. The methods below will be used for the ground state of PbO, $X(0^+)$, which is essentially a $^1\Sigma$ state.[2]

[2]See Section 4.5.1 for more details on the state composition.

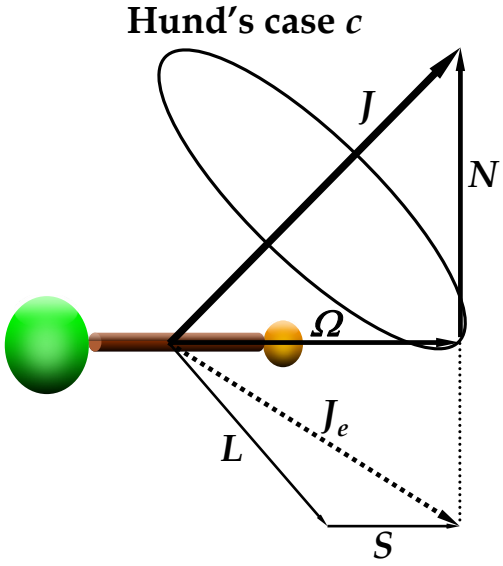

Figure 3.3: Hund's case (c). The orbital angular momentum, L, and the spin angular momentum, S, are strongly coupled. Only the projection on the internuclear axis, Ω, of the total electronic angular momentum, J_e, is defined. Ω and the rotational angular momentum, N, precess around the total angular momentum J.

3.3.1 Stark and Zeeman effects

Since the rotational levels of a $^1\Sigma$ state are non-degenerate there is no first order Stark effect. The second order Stark shift is

$$\Delta E_{St}^{(2)} = \sum_{J'm' \neq Jm} \frac{\left|\left\langle J', m' \right| -\boldsymbol{\mu} \cdot \boldsymbol{\mathcal{E}} \left| J, m \right\rangle\right|^2}{E_{J,m} - E_{J',m'}}, \tag{3.5}$$

where $\boldsymbol{\mu}$ is the electric dipole moment operator and $\boldsymbol{\mathcal{E}}$ is the laboratory electric field. Matrix elements with nearby rotational levels dominate since the energy difference in the denominator is typically orders of magnitude larger for vibrational or electronic transitions. Since $\boldsymbol{\mu}$ is a vector operator, there are only non-zero matrix elements for $J' = J \pm 1$. The matrix elements can be explicitly evaluated as integrals of the eigenstates (e.g., see Townes and Schawlow [69, Section 10-2]) which are spherical harmonics, $|J, m\rangle = Y_J^m(\theta, \phi)$. For an electric field, $\boldsymbol{\mathcal{E}} = \mathcal{E}\hat{z}$, we have (see Fig. 3.4),

$$\begin{aligned}\Delta E_{St}^{(2)} &= \frac{\left|\left\langle J-1, M \right| -\boldsymbol{\mu} \cdot \boldsymbol{\mathcal{E}} \left| J, M \right\rangle\right|^2}{2B_r J} - \frac{\left|\left\langle J+1, M \right| -\boldsymbol{\mu} \cdot \boldsymbol{\mathcal{E}} \left| J, M \right\rangle\right|^2}{2B_r (J+1)} \\ &= \frac{\mu^2 \mathcal{E}^2}{2B_r} \left\{ \frac{J^2 - M^2}{J(2J-1)(2J+1)} - \frac{(J+1)^2 - M^2}{(J+1)(2J+1)(2J+3)} \right\} = \frac{\mu^2 \mathcal{E}^2}{2B_r J(J+1)} \frac{J(J+1) - 3M^2}{(2J-1)(2J+3)}\end{aligned} \tag{3.6}$$

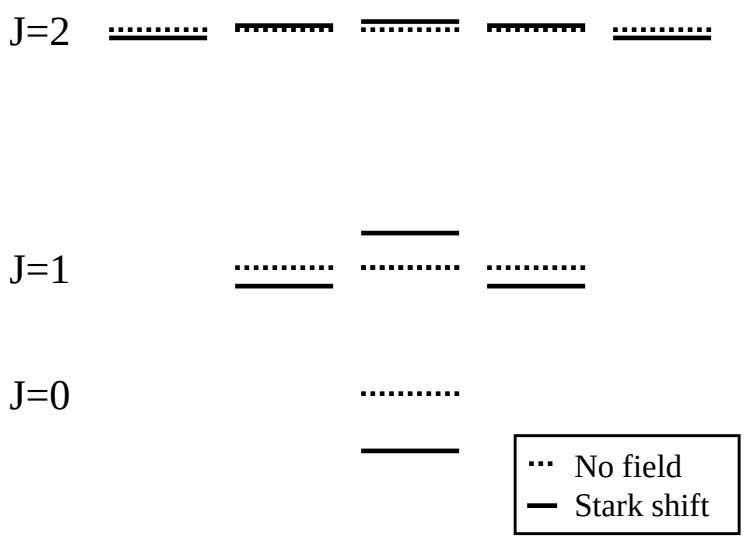

Figure 3.4: Stark effect for the first three rotational lines in a $^1\Sigma$ state. The Stark shifts shown are greatly exaggerated relative to the rotational splitting for typical laboratory electric fields.

except for J=0, which is a special case,

$$\Delta E^{(2)}_{St}\Big|_{J=0} = -\frac{\mu^2\mathcal{E}^2}{6B_r}. \tag{3.7}$$

We will use these results in 7.5 when we discuss a microwave absorption measurement in the $X(0^+)$ state using Stark modulation.

The Zeeman effect in a $^1\Sigma$ state is zero to first order since there are no unpaired electronic spins. In addition, for our experiment the isotope we typically use, $Pb^{208}O^{16}$, has no nuclear spins. There are higher order effects from molecular rotation and mixing of electronic states, but they can be neglected in our experiment.

3.4 Hund's case (c) states with internal angular momentum

For molecular states with internal angular momentum, calculations are a little more involved. Much of the difficulty lies in the fact that the internal angular momenta, i.e. Σ, Λ, Ω, are defined as projections on the internuclear axis which is rotating in the laboratory frame. Changing bases from the laboratory frame to molecule fixed frame simplifies the calculation of matrix elements. Landau

and Lifshitz [70, (110.6)] show that

$$\left\langle J', \Omega', m' \left| T^{(k)}_{q,lab} \right| J, \Omega, m \right\rangle = i^{J'J}(-1)^{\Omega - m} \sqrt{(2J'+1)(2J+1)} \sum_{q'} \begin{pmatrix} J' & k & J \\ -\Omega' & q' & \Omega \end{pmatrix} \begin{pmatrix} J' & k & J \\ -m' & q & m \end{pmatrix} \left\langle \Omega' \left| T^{(k)}_{q',mol} \right| \Omega \right\rangle, \quad (3.8)$$

where the matrix elements on the left and right hand sides are in the laboratory and molecular fixed frames respectively. $T^{(k)}_q$ is the qth component of a rank k spherical tensor. Equivalently one can use the Wigner-Eckert theorem

$$\left\langle J, m', \Omega' \left| T^{(k)}_{q,lab} \right| J, m, \Omega \right\rangle = (-1)^{J'-m'} \begin{pmatrix} J' & k & J \\ -m' & q & m \end{pmatrix} \left\langle J', \Omega' \left\| T^{(k)}_{lab} \right\| J, \Omega \right\rangle \quad (3.9)$$

and the relation (Brown and Carrington [71, Appendix 5.1])

$$\left\langle J', \Omega' \left\| T^{(k)}_{lab} \right\| J, \Omega \right\rangle = \sum_{q'} (-1)^{J'-\Omega'} \sqrt{(2J'+1)(2J+1)} \begin{pmatrix} J' & k & J \\ -\Omega' & q' & \Omega \end{pmatrix} \left\langle \Omega' \left| T^{(k)}_{q',mol} \right| \Omega \right\rangle. \quad (3.10)$$

For future reference let us calculate a few useful matrix elements. Consider the matrix element of a rank-1 spherical tensor for $\Delta\Omega = 0$,

$$\left\langle J', m', \Omega \left| T^{(1)}_{q,lab} \right| J, m, \Omega \right\rangle = (-1)^{2J'-m'-\Omega'} \sqrt{(2J'+1)(2J+1)} \begin{pmatrix} J' & 1 & J \\ -m' & q & m \end{pmatrix} \times \begin{pmatrix} J' & 1 & J \\ -\Omega & 0 & \Omega \end{pmatrix} \left\langle \Omega \left| T^{(1)}_{0,mol} \right| \Omega \right\rangle. \quad (3.11)$$

Table 3.2 summarizes the non-zero matrix elements of a rank 1 tensor for $|\Omega| \geq 1$.

3.4.1 Electric dipole operator

For matrix elements diagonal in Ω we need only the zeroth component of the electric dipole operator in the molecular frame. The z-axis of the molecular frame is by definition the internuclear axis,

Table 3.2: Hund's case (c) matrix elements for rank-1 tensor

J'	m'	Matrix element $\left\langle J', m', \Omega \middle\| T^{(1)}_{m'-m} \middle\| J, m, \Omega \right\rangle$
J	m	$\frac{m\Omega}{J(J+1)}$
$J+1$	m	$\frac{1}{J+1}\sqrt{\frac{[(J+1)^2-m^2]\,[(J+1)^2-\Omega^2]}{(2J+1)(2J+3)}}$
J	$m\pm1$	$\pm\frac{\Omega}{J(J+1)}\sqrt{\frac{J(J+1)-m(m\pm1)}{2}}$
$J+1$	$m\pm1$	$\frac{1}{J+1}\sqrt{\frac{(J+1\pm m)(J+2\pm m)\,[(J+1)^2-\Omega^2]}{2(2J+1)(2J+3)}}$

$\hat{\boldsymbol{Z}} = \hat{\boldsymbol{n}}$. Therefore $\boldsymbol{\mu_{e,0}} = \mu_e \hat{\boldsymbol{n}}$ and the molecular frame matrix element is trivially

$$\left\langle \Omega \middle| -\boldsymbol{\mu_{e,0}} \middle| \Omega \right\rangle = \langle \Omega \middle| -\mu_e \hat{\boldsymbol{n}} \middle| \Omega \rangle = -\mu_e. \tag{3.12}$$

Thus electric dipole matrix elements are given by the values in Table 3.2 multiplied by $-\mu_e$.

3.4.2 Magnetic dipole operator

The magnetic dipole term in the Hamiltonian for an atomic state with no orbital angular momentum can be written as $H_B = -\boldsymbol{\mu_B} \cdot \boldsymbol{B} = g\mu_B \boldsymbol{S} \cdot \boldsymbol{B}$. For a Σ state one might naïvely expect that since $\Lambda = 0$, we have $\Omega = S$ and therefore $H_B = g\mu_B \boldsymbol{\Omega} \cdot \boldsymbol{B}$. However the orbital angular momentum perpendicular to the internuclear axis is not necessarily zero. In theory one could expand the molecular state as a linear combination of atomic orbitals and determine an effective g factor from the J-dependent g factors of the atomic orbitals. In practice it is often easier to define an effective $\overleftrightarrow{\boldsymbol{G}}$ tensor in the molecular frame,

$$\overleftrightarrow{\boldsymbol{G}} = \begin{pmatrix} G_\perp & & \\ & G_\perp & \\ & & G_\parallel \end{pmatrix}. \tag{3.13}$$

We write the magnetic interaction as $\mu_B \boldsymbol{B} \overleftrightarrow{\boldsymbol{G}} \boldsymbol{J_e}$, where $G_\perp (G_\parallel)$ is the effective g-factor perpendicular(parallel) to the internuclear axis in the molecule frame. We can treat the product $\overleftrightarrow{\boldsymbol{G}} \boldsymbol{J_e}$ as our

rank-1 tensor in the molecular frame. The matrix elements diagonal in Ω are then

$$\left\langle \Omega \left| \overleftrightarrow{G} \boldsymbol{J}_e \right| \Omega \right\rangle = \langle \Omega | \mu_B G_\parallel J_{e,Z} | \Omega \rangle = \mu_B G_\parallel \Omega. \tag{3.14}$$

3.5 The $a(1)[^3\Sigma^+]$ state of PbO

In this section we delve into the details of the $a(1)[^3\Sigma^+]$ state used in the actual EDM experiment. We follow the notation and much of the discussion in [29].

The $a(1)$ state of PbO is well described by Hund's case (c). The two projections of the electronic angular momentum on the internuclear axis, $\Omega = \pm 1$, are nominally degenerate. However, Coriolis coupling between Ω and the rotational angular momentum split the symmetric and antisymmetric superpositions of these projections. Thus, each rotational line forms an Ω-doublet with an energy splitting of $\Delta_{\Omega_J} = qJ(J+1)$, where $q = 5.6\,\mathrm{MHz}$ [72] is much smaller than the rotational constant $B_r = 7.054\,\mathrm{GHz}$ [68] (see Fig. 3.5).

The field-free states are eigenstates of the parity operator. Since, in general [73],

$$P\,|J, M, \Omega\rangle = (-1)^{J-\Omega}\,|J, M, -\Omega\rangle\,, \tag{3.15}$$

the eigenstates are superpositions of the signed Ω states (see Fig. 3.6). States with parity $(-1)^J$ are labeled e states while states with parity $-(-1)^J$ are f states [73]. We will see in Section 3.5.5 that due to Ω-doubling, the e states are always higher in energy. We denote them by

$$|J, M, |\Omega| = 1, e\rangle = \frac{1}{\sqrt{2}}\left(|J, M, \Omega = +1\rangle - |J, M, \Omega = -1\rangle\right). \tag{3.16}$$

The f states, always lower in energy, are denoted by

$$\left|J, M, |\Omega| = 1, f\right\rangle = \frac{1}{\sqrt{2}}\left(|J, M, \Omega = +1\rangle + |J, M, \Omega = -1\rangle\right). \tag{3.17}$$

In the Stark and Zeeman calculations below, the labeling of e and f states is specific to $\Omega = 1$. However, other than this labeling, the results hold for all states with $\Omega \geq 1$.

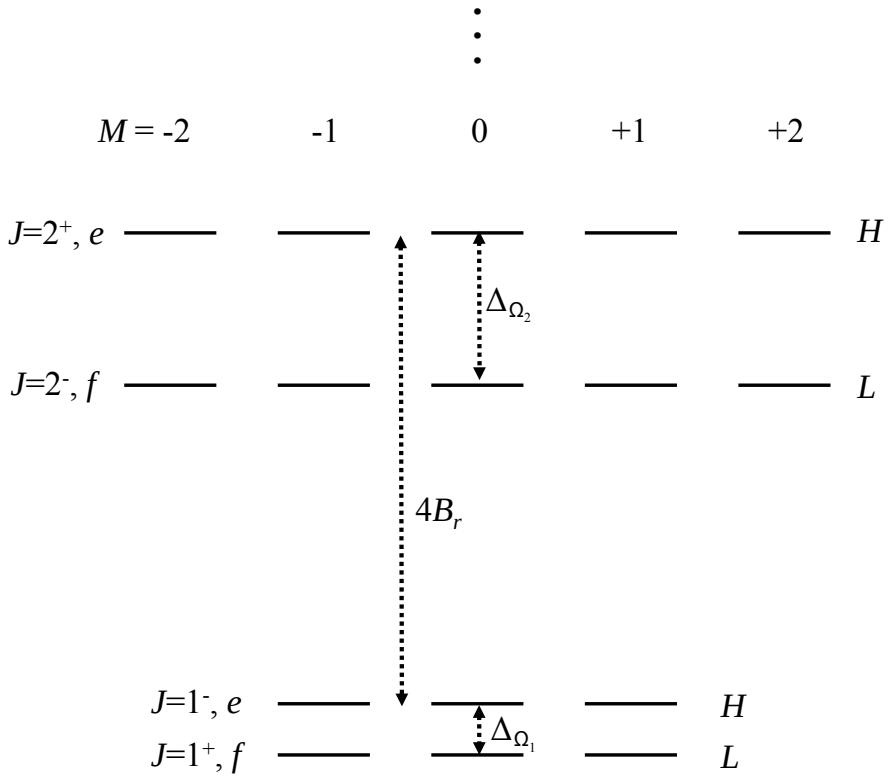

Figure 3.5: The $a(1)$ rotational levels. In a given vibrational level of the $a(1)$ state, the rotational levels have energies $B_r J(J+1)$, with rotational constant $B_r \cong 2\pi \times 7.054\,\mathrm{GHz}$. In the absence of an electric field, Ω-doubling separates the parity eigenstates, e and f, of each rotational sublevel by $\Delta_{\Omega_J} = qJ(J+1)$, where $q \cong 2\pi \times 5.6\,\mathrm{MHz}$. The labels H and L denote the higher and lower energy level of the Ω-doublet regardless of electric field. Note the energy splittings are not drawn to scale.

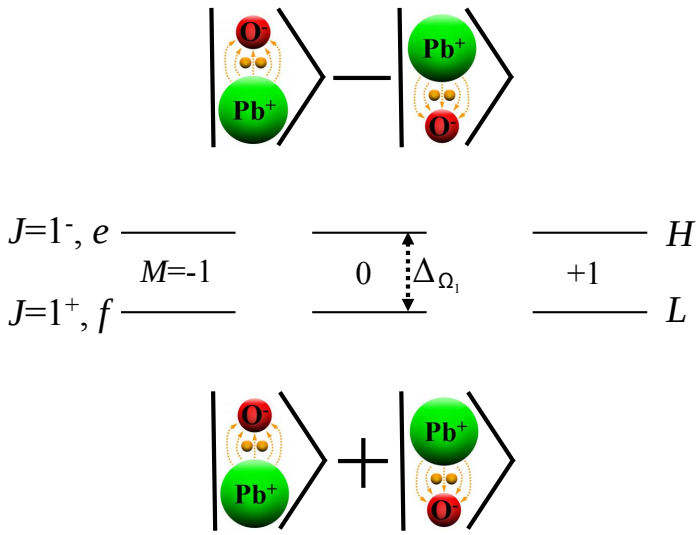

Figure 3.6: Field-free J=1 state. In the absence of magnetic and electric fields, the parity eigenstates, e and f, of the $a(1), J = 1$ state are split by the Ω-doubling energy, Δ_{Ω_1}. The parity states are symmetric or antisymmetric superpositions of states where Ω, the projection of the electronic angular momentum on the internuclear axis, is defined.

3.5.1 Stark effect

The Stark effect in the $a(1)$ state is significantly different than in the $X(0^+)$ state. The e and f states in each Ω-doublet pair can mix and repel in an electric field because they are of opposite parity. Thus, for the same electric field, the $a(1)$ Stark shift is larger than that in the $X(0^+)$ state by the ratio of the rotational splitting to the Ω-doublet splitting or nearly 3 orders of magnitude.

Using Table 3.2, Eq. (3.16), and Eq. (3.17) the Stark Hamiltonian for each M sublevel in the e, f basis is

$$H_{St}^{(J,M)} = \begin{pmatrix} \frac{\Delta_{\Omega_J}}{2} & \frac{-\mu_a \mathcal{E} M |\Omega|}{J(J+1)} \\ \frac{-\mu_a \mathcal{E} M |\Omega|}{J(J+1)} & -\frac{\Delta_{\Omega_J}}{2} \end{pmatrix}, \tag{3.18}$$

where $\mu_a = 1.64\,\mathrm{MHz\,V^{-1}\,cm^{-1}}$ is the molecule-fixed electric dipole moment for the $a(1)$ state [74]. Note that the $M = 0$ states do not mix and therefore remain parity eigenstates regardless of the electric field.

To keep track of the states we use the label $H(L)$ for the higher(lower) energy eigenstate regardless

	No electric field		Arbitrary electric field		Fully polarized		
	$\|e\rangle, \|f\rangle$	$\|\Omega\rangle, \|-\Omega\rangle$	$\|e\rangle, \|f\rangle$	$\|\Omega\rangle, \|-\Omega\rangle$	$\|e\rangle, \|f\rangle$	$\|\Omega\rangle, \|-\Omega\rangle$	$\|n_+\rangle, \|n_-\rangle$
$\|J,+M,H\rangle$	$\begin{pmatrix}1\\0\end{pmatrix}$	$\begin{pmatrix}\frac{1}{\sqrt{2}}\\-\frac{1}{\sqrt{2}}\end{pmatrix}$	$\begin{pmatrix}\cos\frac{\theta}{2}\\\sin\frac{\theta}{2}\end{pmatrix}$	$\begin{pmatrix}\cos\left(\frac{\theta}{2}-\frac{\pi}{4}\right)\\\sin\left(\frac{\theta}{2}-\frac{\pi}{4}\right)\end{pmatrix}$	$\begin{pmatrix}\frac{1}{\sqrt{2}}\\-\frac{1}{\sqrt{2}}\end{pmatrix}$	$\begin{pmatrix}0\\-1\end{pmatrix}$	$\begin{pmatrix}0\\1\end{pmatrix}$
$\|J,-M,H\rangle$	"	"	"	"	$\begin{pmatrix}\frac{1}{\sqrt{2}}\\\frac{1}{\sqrt{2}}\end{pmatrix}$	$\begin{pmatrix}1\\0\end{pmatrix}$	"
$\|J,+M,L\rangle$	$\begin{pmatrix}0\\1\end{pmatrix}$	$\begin{pmatrix}\frac{1}{\sqrt{2}}\\\frac{1}{\sqrt{2}}\end{pmatrix}$	$\begin{pmatrix}-\sin\frac{\theta}{2}\\\cos\frac{\theta}{2}\end{pmatrix}$	$\begin{pmatrix}-\sin\left(\frac{\theta}{2}-\frac{\pi}{4}\right)\\\cos\left(\frac{\theta}{2}-\frac{\pi}{4}\right)\end{pmatrix}$	$\begin{pmatrix}\frac{1}{\sqrt{2}}\\\frac{1}{\sqrt{2}}\end{pmatrix}$	$\begin{pmatrix}1\\0\end{pmatrix}$	$\begin{pmatrix}1\\0\end{pmatrix}$
$\|J,-M,L\rangle$	"	"	"	"	$\begin{pmatrix}-\frac{1}{\sqrt{2}}\\\frac{1}{\sqrt{2}}\end{pmatrix}$	$\begin{pmatrix}0\\1\end{pmatrix}$	"

Table 3.3: $a(1)$ eigenstates in an electric field

of the field. After diagonalizing, $H(L)$ is shifted higher(lower) in energy by

$$\delta_{St} = \sqrt{\left(\frac{\Delta_{\Omega_J}}{2}\right)^2 + \left(\frac{\mu_a \mathcal{E} M\Omega}{J(J+1)}\right)^2} - \frac{\Delta_{\Omega_J}}{2}. \tag{3.19}$$

For small electric fields, i.e. $\delta_{St} \ll \Delta_{\Omega_J}$, this leads to the usual quadratic Stark shift

$$\delta_{St} \approx \frac{1}{\Delta_{\Omega_J}}\left(\frac{\mu_a \mathcal{E} M\Omega}{J(J+1)}\right)^2, \tag{3.20}$$

while for large electric fields, i.e. $\delta_{St} \gg \Delta_{\Omega_J}$, the Stark effect becomes linear,

$$\delta_{St} \approx \left|\frac{\mu_a \mathcal{E} M\Omega}{J(J+1)}\right| - \frac{\Delta_{\Omega_J}}{2}. \tag{3.21}$$

Table 3.3 summarizes the eigenstates for arbitrary electric fields, $\boldsymbol{\mathcal{E}} = \mathcal{E}\hat{z}, |\mathcal{E}| \geq 0$, using the mixing angle notation described in Appendix A with $x = \Delta_{\Omega_J}, y = \frac{-\mu_a \mathcal{E} M|\Omega|}{J(J+1)}$, and $\theta = \arctan\frac{y}{x}$. Note that for $\mathcal{E} > 0$ the mixing angle goes from zero to $\mp\frac{\pi}{2}$ for $\pm M$. From this table one can see that at high electric fields the field-free parity states fully mix and the signed Ω basis states become the energy eigenstates[3] (see Fig. 3.7).

[3]The signs given in Table 3.3 differ from those in [29] and agree with [52]. The relative signs between the states in a given basis set are necessary to correctly change bases.

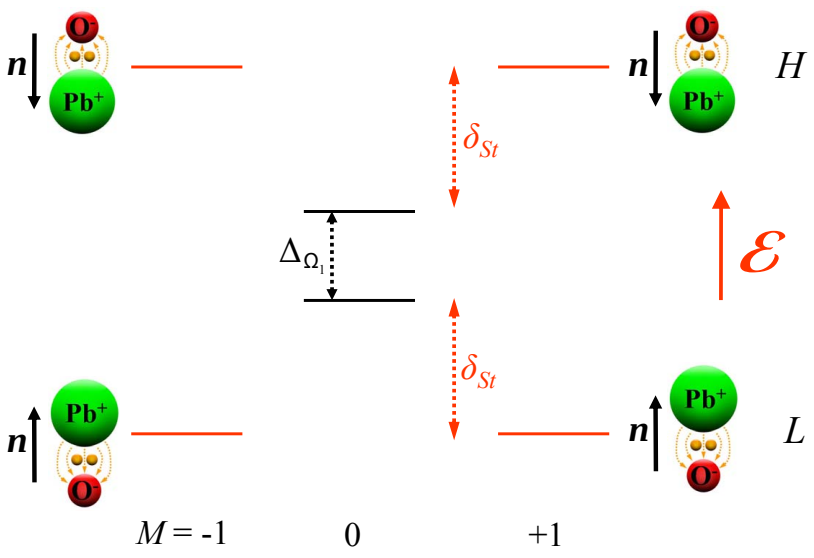

Figure 3.7: The $a(1), J = 1$ state in an electric field. At high electric fields, $\delta_{St} \approx \frac{1}{2}(\mu_a \mathcal{E} - \Delta_{\Omega_1}) \gg \Delta_{\Omega_1}$, the lower(higher) energy state, $L(H)$, for the $M = \pm 1$ sublevels is oriented with(against) the electric field.

Table 3.3 also defines new basis states, $\left|J, M, n_{+(-)}\right\rangle$, corresponding to the states fully polarized with(against) the electric field to give a clearer physical picture and to ease later notation. Using Table 3.2, the average direction of the internuclear axis for a fully polarized state in the laboratory frame is $\langle \hat{\boldsymbol{n}} \rangle = \frac{M\Omega}{J(J+1)} \hat{z}$. Therefore states with $M\Omega > 0$ correspond to the $|n_+\rangle$ state while states with $M\Omega < 0$ correspond to $|n_-\rangle$.

To summarize,

$$\begin{aligned} &\text{Field-free} && |J, M, H\rangle = |J, M, e\rangle \\ &&& |J, M, L\rangle = \left|J, M, f\right\rangle \\ &\text{Fully polarized} && |J, M, H\rangle = |J, M, n_-\rangle \\ &&& |J, M, L\rangle = |J, M, n_+\rangle \,. \end{aligned}$$

3.5.2 EDM shift

The effective electron EDM Hamiltonian, $H_{edm} = -\boldsymbol{d_e} \cdot \boldsymbol{\mathcal{E}}_{eff}$, depends only on the relative direction of the electron spin and the effective internal electric field of the molecule. The effective electric field[4] is typically defined such that $H_{edm} = d_e \mathcal{E}_{eff} \boldsymbol{J_e} \cdot \hat{\boldsymbol{n}} = d_e \mathcal{E}_{eff} \Omega$ [75]. Thus the size of the EDM is

[4]With the internuclear axis $\hat{\boldsymbol{n}}$ defined to be in direction of the dipole moment, $\boldsymbol{\mu_a}$, the internal electric field is expected to be in the opposite direction, $\boldsymbol{\mathcal{E}}_{eff} = -\mathcal{E}_{eff} \hat{\boldsymbol{n}}$.

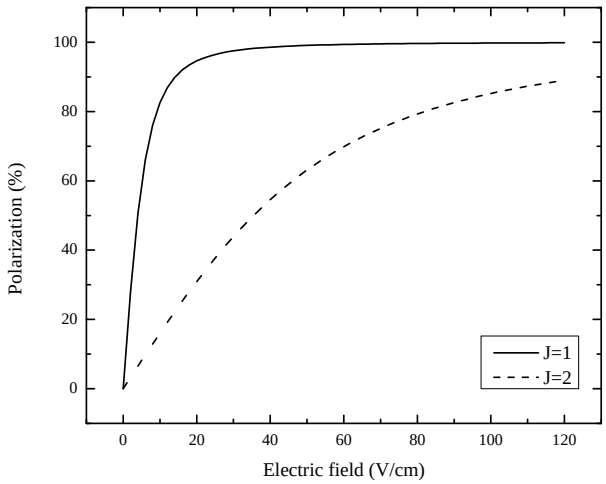

Figure 3.8: The effective polarization, $P = \langle\Omega\rangle / |\Omega|$, for the J=1 and J=2 —M—=1 levels versus applied electric field.

proportional to the expectation value of Ω in the molecular frame. Using Table 3.3, we can define an effective polarization,

$$\begin{aligned} P_{L(H)} &\equiv \frac{\langle\Omega\rangle}{|\Omega|} \\ &= \mp\left[\cos^2\left(\tfrac{\theta}{2}-\tfrac{\pi}{4}\right)-\sin^2\left(\tfrac{\theta}{2}-\tfrac{\pi}{4}\right)\right] = \mp\sin\theta \\ &= \pm\frac{\frac{\mu_a\mathcal{E}M|\Omega|}{J(J+1)}}{\sqrt{\left(\frac{\Delta_{\Omega_J}}{2}\right)^2+\left(\frac{\mu_a\mathcal{E}M|\Omega|}{J(J+1)}\right)^2}}, \end{aligned} \tag{3.22}$$

where the +(−) signs are for the L(H) states (see Fig. 3.8). For arbitrary electric fields, $H_{edm} = Pd_e\mathcal{E}_{eff}$. For fully polarized states, $P_{n_\pm} = \pm sgn(M)$.

3.5.3 Zeeman effect

Using Table 3.2, Eq. (3.14), Eq. (3.16), and Eq. (3.17), the first order Zeeman effect for a magnetic field $\boldsymbol{B} = B\hat{z}$ is (see Fig. 3.9)

$$\delta_Z = \langle J, M, e(f)\left|\, G_\parallel\mu_B B\Omega \,\right|J, M, e(f)\rangle = \frac{G_\parallel\mu_B BM\Omega^2}{J(J+1)}. \tag{3.23}$$

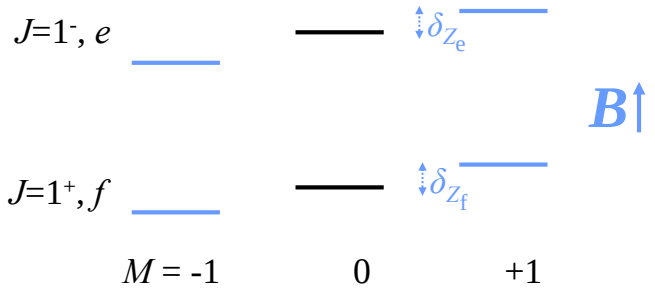

Figure 3.9: The $a(1), J = 1$ state in a magnetic field. The Zeeman shift of the $M = \pm 1$ sublevel is $\delta_{Z_{e(f)}} = g_{e(f)}\mu_B MB$, where $g_{e(f)}\mu_B \approx 2\pi \times 1.30\,\mathrm{MHz\,G^{-1}}$. The g factors, $g_{e(f)}$, of the parity eigenstates differ by $\approx 1.5 \times 10^{-3}$.

For notational ease[5], we define the J=1 g factors, $g_{e(f)} \approx G_\parallel/2 \approx 0.86$ so that

$$\delta_{Z_{e(f)}} = g_{e(f)}\mu_B MB. \tag{3.24}$$

The subscripts reflect the fact that the parity eigenstates, due to Ω-doubling, have slightly different g factors, $g_f - g_e \approx 1.5(4) \times 10^{-3}$ [72].

We can understand this result by considering a simple vector model (refer to Fig. 3.3)[6]. The magnetic moment along $\mathbf{\Omega}$ is by definition $\mu_\Omega = G_\parallel \mu_B \Omega$. The nutation of $\mathbf{\Omega}$ around the total angular momentum $\boldsymbol{J}$ gives an average magnetic moment of

$$\bar{\mu_J} = \mu_\Omega \cos(\mathbf{\Omega}, \boldsymbol{J}) = \mu_\Omega \frac{\Omega}{\sqrt{J(J+1)}} = \frac{G_\parallel \mu_B \Omega^2}{\sqrt{J(J+1)}}. \tag{3.25}$$

The total angular momentum $\boldsymbol{J}$ then precesses around the magnetic field direction giving an average magnetic moment of

$$\bar{\mu_B} = \bar{\mu_J} \cos(\boldsymbol{B}, \boldsymbol{J}) = \bar{\mu_J} \frac{M}{\sqrt{J(J+1)}} = \frac{G_\parallel \mu_B M \Omega^2}{J(J+1)}. \tag{3.26}$$

3.5.4 The EDM measurement states

The EDM measurement involves comparing the energy differences, $\Delta_{n_\pm}$, between the $M = +1$ and $M = -1$ sublevels for both orientations of the molecule, $n_\pm$, in a strong electric field and parallel

[5] Warning! This notation differs from our earlier papers, e.g. [72].
[6] The Stark shift can also be understood with this model.

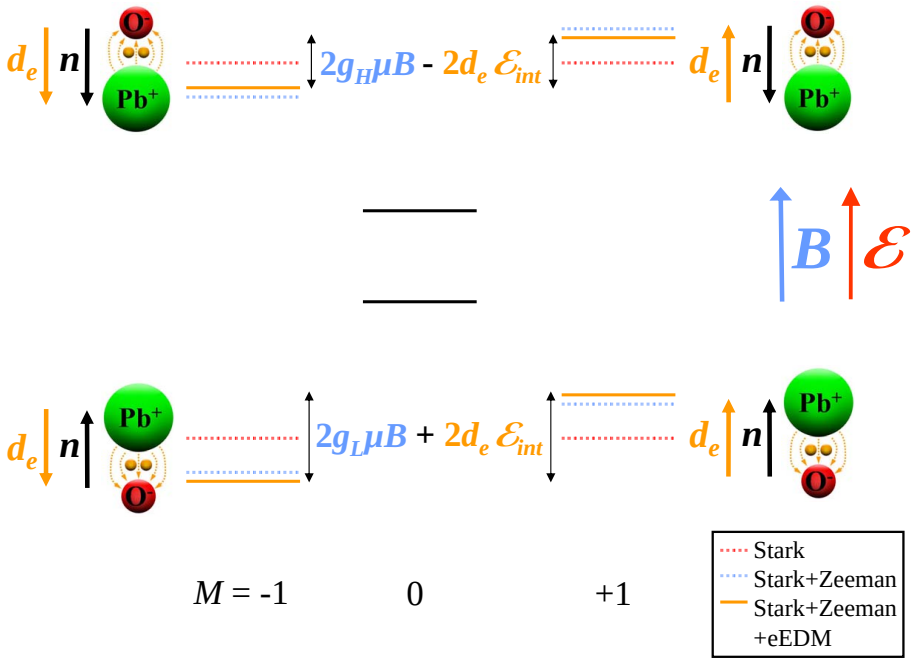

Figure 3.10: The EDM measurement states. The EDM measurement involves comparing the energy differences, $\Delta_{n_\pm}$, between the $M = +1$ and $M = -1$ sublevels for both orientations of the molecule, $n_\pm$, in a strong electric field and parallel magnetic field. In the approximation, $g_H = g_L$, the difference between the two, $\Delta_{EDM,n} = \Delta_{n_+} - \Delta_{n_-} = 4d_e\mathcal{E}_{eff}$, is independent of the magnetic field.

magnetic field (see Fig. 3.10). The Stark shifts for the two magnetic sublevels are identical, while the Zeeman and EDM shifts are opposite in sign. In addition, the EDM shift is of opposite sign for the two orientations $n_\pm$, since the direction of the internal electric field is opposite to the axis of the molecule. Explicitly we can combine the Stark, Zeeman, and EDM shift calculations above to express the total energy shift of a magnetic sublevel as

$$\delta_{n_\pm,M} = \mp\delta_{St} + g_{n_\pm}\mu_B MB \pm d_e\mathcal{E}_{eff}M. \tag{3.27}$$

The splitting between the $M = +1$ and $M = -1$ sublevels is then

$$\Delta_{n_\pm} = \delta_{n_\pm,+M} - \delta_{n_\pm,-M} = 2g_{n_\pm}\mu_B B \pm 2d_e\mathcal{E}_{eff}, \tag{3.28}$$

where $g_{n_\pm} \approx G_\parallel/2$ are the g factors for the $n_\pm$ levels. If $g_{n_+} = g_{n_-}$ the energy difference $\Delta_{EDM,n} = \Delta_{n_+} - \Delta_{n_-} = 4d_e\mathcal{E}_{eff}$ is independent of magnetic field. The cancellation of magnetic effects demonstrates that the two orientations of the molecule act as co-magnetometers.

As we will discuss in Section 3.5.6, the $g_{n_\pm}$ factors are actually different at the 10^{-3} level and depend slightly on the electric field. In this case we have $\Delta_{EDM,n} = 2\Delta g\mu_B B + 4d_e\mathcal{E}_{eff}$, where $\Delta g(\mathcal{E}) = g_{n_+}(\mathcal{E}) - g_{n_-}(\mathcal{E})$. However, with further experimental reversals, for example $B \to -B$, we can eliminate any magnetic field dependence (see Section 6.4).

As an aside, we note that once polarized, all J levels exhibit the same EDM shift. However, the $J = 1$ state is used for two main reasons. First, it has the smallest Ω-doublet splitting and therefore requires the smallest electric field for polarization. The field required for substantial polarization of all non-zero magnetic sublevels is proportional to J^4, making polarization of even $J = 2$ technically difficult. Smaller electric fields reduce leakage currents between the electrodes which can lead to systematic effects. Second, the $J = 1$ state can be excited from the single quantum state $|X, J = 0, m = 0\rangle$. The excitation of multiple incoherent sublevels in higher J levels of the ground state would generally lead to incoherent backgrounds not useful to the EDM measurement.

3.5.5 Ω-doubling

Ω-doubling stems from a "Coriolis"coupling between the rotational angular momentum, N, and the electronic angular momentum, J_e. In Hund's case (c) the rotational quantum number N is not a

good quantum number. Expressing N in terms of the J and J_e the rotational energy is

$$H_{rot} = B_r \boldsymbol{N}^2 = B_r(\boldsymbol{J} - \boldsymbol{J_e})^2 = B_r J^2 + B_r J_e^2 - 2B_r \boldsymbol{J} \cdot \boldsymbol{J_e}. \tag{3.29}$$

The first term is the usual rotational energy and the second term gives a constant energy offset for the electronic state. The last term is the coupling responsible for Ω-doubling. The most general matrix element of this term is

$$M = \langle \gamma', J', M', \Omega' \left| \boldsymbol{J} \cdot \boldsymbol{J_e} \right| \gamma, J, M, \Omega \rangle, \tag{3.30}$$

where γ and γ' represent all other quantum numbers. After expanding the dot product in the spherical basis and inserting the identity as a sum over eigenstates we have

$$M = \sum_q \sum_{\gamma'' J'' M'' \Omega''} (-1)^q \left\langle \gamma', J', M', \Omega' \left| J_q \right| \gamma'', J'', M'', \Omega'' \right\rangle \left\langle \gamma'', J'', M'', \Omega'' \left| J_{e,-q} \right| \gamma, J, M, \Omega \right\rangle. \tag{3.31}$$

Using the Wigner-Eckert theorem twice and the relation [76, (4.168)]

$$\sum_{qM''} (-1)^q \begin{pmatrix} J' & 1 & J'' \\ -M' & q & M'' \end{pmatrix} \begin{pmatrix} J'' & 1 & J \\ -M'' & -q & M \end{pmatrix} = \frac{\delta_{J'J}\delta_{M'M}}{2J+1}, \tag{3.32}$$

we have

$$M = \sum_{\gamma'' J'' \Omega''} (-1)^{J-J''} \frac{1}{2J+1} \langle \gamma', J, \Omega' \left\| J \right\| \gamma'', J'', \Omega'' \rangle \langle \gamma'', J'', \Omega'' \left\| J_e \right\| \gamma, J, \Omega \rangle. \tag{3.33}$$

Using the formula [76]

$$\langle \gamma', J, \Omega' \left\| J \right\| \gamma'', J'', \Omega'' \rangle = \delta_{\gamma'\gamma''}\delta_{JJ''}\delta_{\Omega'\Omega''} \sqrt{J(J+1)(2J+1)}, \tag{3.34}$$

and lab to body-fixed frame transformation Eq. (3.10) for the J_e reduced matrix element we have

$$M = \sum_q (-1)^{J-\Omega'} \sqrt{J(J+1)(2J+1)} \begin{pmatrix} J & 1 & J \\ -\Omega' & q & \Omega \end{pmatrix} \left\langle \gamma', \Omega' \left| J_{e,q} \right| \gamma, \Omega \right\rangle. \tag{3.35}$$

First, we consider diagonal matrix elements that could lead to a first order energy shift. The

field-free parity eigenstates [71] are

$$|J, M, |\Omega|, P = \pm\rangle = \frac{1}{\sqrt{2}}\left(|J, M, \Omega\rangle \pm (-1)^{J-\Omega}|J, M, -\Omega\rangle\right). \tag{3.36}$$

Since J_e is a vector operator, matrix elements between states with Ω and $-\Omega$, having $\Delta\Omega = 2$, must vanish. For the field-free parity eigenstates we are left only with the diagonal elements which also vanish since

$$\langle J, M, |\Omega|, P | \boldsymbol{J}\cdot\boldsymbol{J_e} | J, M, |\Omega|, P\rangle \propto \langle \Omega | J_{e,0} | \Omega\rangle + \langle -\Omega | J_{e,0} | -\Omega\rangle = \Omega + (-\Omega) = 0. \tag{3.37}$$

Next we consider off-diagonal elements which lead to a second order energy shift. Since J_e is a vector operator there are non-vanishing matrix elements between states with $\Delta\Omega = 0, \pm 1$. The closest electronic state to the $a(1)^3\Sigma^+$ state is the $b(0^-)^3\Sigma^+$ state. The splitting between these two states is actually quite small; on the order[7] of 300 cm^{-1} [77–79]. All other electronic states that could mix are much farther away and contribute only negligibly to the Ω-doubling.

As an aside, one can roughly explain the small splitting between these states by analogy to the atomic $^3S_1$ state. Since the electric field does not act on the spin degree of freedom there is no tensor Stark shift to lowest order for the $^3S_1$ state. Similarly the $^3\Sigma_1$ and $^3\Sigma_0$ molecular states, which are analogous to the $m = \pm 1$ and $m = 0$ sublevels of the atomic state, split only due to a second order spin-orbit coupling.

Only levels in $a(1)$ and $b(0^-)$ with the same angular momentum and parity are mixed. Since the $b(0^-)$ levels have parity $-(-1)^J$ and are higher in energy, the f levels of $a(1)$ are shifted downward. Using Eq. (3.35), the second order shift is[8]

$$\begin{aligned}\Delta E &= \frac{\left|\langle J, \Omega = 0 | -2B_r \boldsymbol{J}\cdot\boldsymbol{J_e} | J, |\Omega| = 1, f\rangle\right|^2}{E_{a(1)} - E_{b(0^-)}} \\ &= \frac{(2B_r)^2 J(J+1)\left|\frac{1}{\sqrt{2}}\left(\langle \Omega = 0 | J_{e,-1} | \Omega = 1\rangle - \langle \Omega = 0 | J_{e,+1} | \Omega = -1\rangle\right)\right|^2}{E_{a(1)} - E_{b(0^-)}}.\end{aligned} \tag{3.38}$$

[7] There is significant discrepancy and some uncertainty over the identification of the b state in the literature.

[8] Note that spherical tensor components are related to the usual raising and lowering operators by $J_{e,\pm 1} = \mp\frac{1}{\sqrt{2}} J_{e,\pm}$.

If we assume $J_e = 1$, which, strictly speaking, is not defined for Hund's case (c) [80], we find

$$\Delta E_\Omega = \frac{4B_r^2 J(J+1)}{E_{a(1)} - E_{b(0^-)}} = qJ(J+1). \tag{3.39}$$

Using the experimental values of $B_r = 0.235\,\mathrm{cm}^{-1}$ [68] and $E_{a(1)} - E_{b(0^-)} \approx -300\,\mathrm{cm}^{-1}$ [77] gives $q = -22.1\,\mathrm{MHz}$. The discrepancy with the experimental value of $q = -5.6\,\mathrm{MHz}$ [72] could be due to either misidentification of the $b(0^-)$ levels or our overly simple model that neglects mixing with other states.

3.5.6 Electric field dependence of g factors

As was hinted at in Section 3.5.4, it was found experimentally (see Section 6.3.3) that the g factors, $g_{H(L)}$, of the $|J = 1, M, H(L)\rangle$ states are not equal and depend slightly on the electric field. The difference in the field-free case, $\Delta g = g_f - g_e = 1.5 \times 10^{-3}$, was expected and has the same origin as the Ω-doubling: mixing of the f levels with the $b(0^-)$ state. It was also expected that the mixing of the $|e\rangle$ and $|f\rangle$ levels in electric field would reduce the g factor difference. Using Table 3.3 one can show that

$$\Delta g(\mathcal{E}) = g_L(\mathcal{E}) - g_H(\mathcal{E}) = (g_f - g_e)\cos\theta = \Delta g(0)\frac{\Delta_{\Omega_1}}{\sqrt{(\mu_a \mathcal{E})^2 + (\Delta_{\Omega_1})^2}}. \tag{3.40}$$

Thus the g factor difference should approach zero as the states fully mix.

However, the $J = 1$ and $J = 2$ levels of the $a(1)$ state are also slightly mixed by an electric field. Using perturbation theory we can write the mixed state as

$$|J^*, M, \Omega\rangle = |J, M, \Omega\rangle + \eta(M)\,|J+1, M, \Omega\rangle\,, \tag{3.41}$$

where $\eta(M) = \left\langle J+1, M, \Omega \middle| \boldsymbol{\mu_a} \cdot \boldsymbol{\mathcal{E}} \middle| J, M, \Omega \right\rangle / 2(J+1)B_r$. Using Table 3.2 and Eq. (3.14), the Zeeman shift of the mixed state,[9] to first order in $\mu_a \mathcal{E}/B_r$, is

$$\begin{aligned}\left\langle J^*, M, \Omega \middle| -\boldsymbol{\mu} \cdot \boldsymbol{B} \middle| J^*, M, \Omega \right\rangle &= \left\langle J, M, \Omega \middle| -\boldsymbol{\mu} \cdot \boldsymbol{B} \middle| J, M, \Omega \right\rangle + 2\eta(M) \left\langle J+1, M, \Omega \middle| -\boldsymbol{\mu} \cdot \boldsymbol{B} \middle| J, M, \Omega \right\rangle \\ &= \frac{G_{\|}\mu_B BM}{J(J+1)} + \frac{G_{\|}\mu_B BM}{J(J+1)} \frac{\mu_a \mathcal{E}\Omega J^2 (J+2)\left[(J+1)^2 - M^2\right]}{B_r M (J+1)^2 (2J+1)(2J+3)}\end{aligned} \tag{3.42}$$

[9] Note that in both [52, 81] a factor of J+1 is missing in the denominator.

Recalling that $M\Omega = \pm 1$ for the $|n_\pm\rangle$ states, the effective g factors for the polarized $J = 1$ states are then

$$g_{n_\pm} \approx \frac{G_\parallel}{2}\left(1 \pm \frac{3\mu_a |\mathcal{E}|}{20B_r}\right). \tag{3.43}$$

Combining our results by treating the mixing between the $J = 1$ and $J = 2$ as a small perturbation, the g factor difference to first-order for all fields is

$$\begin{aligned}\Delta g(\mathcal{E}) = g_L(\mathcal{E}) - g_H(\mathcal{E}) &= \cos\theta(g_f - g_e) + \sin\theta\frac{3\mu_a\mathcal{E}}{20B_r}(g_f + g_e) \\ &= \frac{\Delta_{\Omega_1}(g_f - g_e) + \frac{3(\mu_a\mathcal{E})^2}{20B_r}(g_f + g_e)}{\sqrt{(\Delta_{\Omega_1})^2 + (\mu_a\mathcal{E})^2}}.\end{aligned} \tag{3.44}$$

Fig. 3.11 shows the excellent agreement between theory and experiment. This data was obtained by populating both the higher and lower energy EDM states at large electric and magnetic fields. The different g factors for the higher and lower energy levels lead to different Zeeman shifts. Because the quantum beat frequencies are proportional to the Zeeman shift the differing beat frequencies cause "beating" of the beats. From the time of the first node in the envelope of the quantum beats, which occurs when the two beat frequencies are out of phase, one can determine the beat frequency difference.

Note it is inevitable that the change in g factor due to rotational mixing is on the order of and slightly larger than the change due to Ω-doubling. One can show that due to Ω-doubling, $\delta_g \approx gB_r/\Delta_E$, where Δ_E is the energy difference between the $\Omega = \pm 1$ and $\Omega = 0$ states. Rotational mixing gives $\delta_g \approx g\mu_a\mathcal{E}/B_r$. However, when the states are fully polarized $\mu_a\mathcal{E} >> \Delta_\Omega \approx B_r^2/\Delta_E$. Therefore rotational mixing gives $\delta_g > gB_r/\Delta_E$.

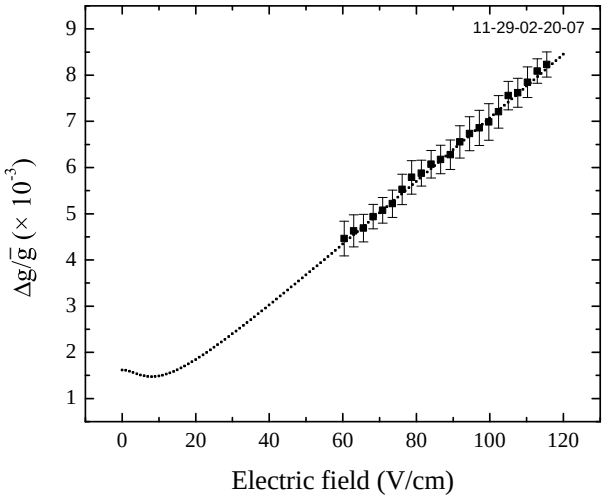

Figure 3.11: Difference between g factors. The dotted line is the theoretical calculation (with no free parameters) of the fractional difference in g factors, $\Delta g/\bar{g} = 2(g_L - g_H)/(g_L + g_H)$, versus applied electric field. The data points were obtained by populating both the higher and lower energy EDM states at large electric and magnetic fields. The different g factors for the higher and lower energy levels lead to different Zeeman shifts. Because the quantum beat frequencies are proportional to the Zeeman shift the differing beat frequencies cause "beating" of the beats. From the time of the first node in the envelope of the quantum beats, which occurs when the two beat frequencies are out of phase, one can determine the beat frequency difference.

Chapter 4

Electron EDM enhancement in atoms and molecules

One might expect that any external electric field is shielded from an electron in an atom or molecule by polarization of its electron cloud. Even though this is strictly correct, relativistic effects can still lead to an enhancement of the electron EDM in heavy atoms or molecules. In atoms, this enhancement is dependent upon polarization of the atom through mixing of s and p orbitals by an external electric field. One can roughly estimate the size and scaling of this effect by calculating the probability for an electron to spend time in the enormous electric field near the nucleus. For simple cases, such as the alkali atoms, the enhancement can be calculated fairly well using analytic relativistic wave functions. Molecular calculations are more complex since there are no simple analytic expressions for molecular orbitals. Instead one expands the molecular orbitals in an appropriate basis set, such as the individual atomic orbitals. The s and p atomic orbitals can then be mixed in a molecular orbital by the strong internuclear electric field. A much smaller external electric field is needed only to orient the molecules. To calculate the EDM enhancement in both heavy atoms and molecules, one can use *ab initio* quantum chemistry methods which attempt to determine the s and p orbital mixing in a given electron configuration from first principles. Alternatively, experimental data on hyperfine constants and fine structure splittings can constrain s and p contributions and be used in a semi-empirical estimate of the EDM enhancement factor.

4.1 Schiff's theorem

At first glance, the idea of using an electron in a neutral atom or molecule for an electron EDM search seems unpromising. From simple electrostatics, for any given electron, an external electric field is exactly canceled by the field due to the other electrons in the atom or molecule. If this were not the case the electron would never reach an equilibrium position. More formally one expects that there can be no first order contribution, linear in the electric field, to an atomic energy level from an EDM. This argument is known as Schiff's theorem[82]. However, as we will see below, relativistic effects can actually lead to a violation of Schiff's theorem and an effective atomic or molecular dipole moment larger than the electron EDM. In atomic systems the ratio of the dipole moments is termed the "enhancement factor".

4.1.1 Shielding of the electric field

One can quickly prove Schiff's theorem by using Ehrenfest's theorem[83],

$$\frac{d}{dt}\langle A\rangle = \frac{1}{i\hbar}\left\langle \psi \middle| [A,H] \middle| \psi \right\rangle, \tag{4.1}$$

where A is an observable and H is the particle Hamiltonian. If $|\psi\rangle$ is an eigenstate of the Hamiltonian the right-side vanishes (regardless of whether A commutes with H) and we see that there is no time dependence for the expectation of any observable in an eigenstate; hence the term "stationary state". For a non-relativistic electron in an electrostatic potential, Φ, the Hamiltonian is $H = \frac{p^2}{2m} - e\Phi$. Considering an energy eigenstate and using Eq. (4.1) with $A = \boldsymbol{p}$ we have[1]

$$\langle \boldsymbol{F}\rangle = \frac{d}{dt}\langle \boldsymbol{p}\rangle = \frac{1}{i\hbar}\langle [\boldsymbol{p},H]\rangle = e\langle [\boldsymbol{\nabla},\Phi]\rangle = e\langle \boldsymbol{\nabla}\Phi\rangle = -e\langle \boldsymbol{\mathcal{E}}\rangle = 0. \tag{4.2}$$

For an atomic system we can split the electric field into internal and external parts, $\boldsymbol{\mathcal{E}} = \boldsymbol{\mathcal{E}}_i + \boldsymbol{\mathcal{E}}_e$ and thus show

$$\langle \boldsymbol{\mathcal{E}}_i\rangle = -\langle \boldsymbol{\mathcal{E}}_e\rangle. \tag{4.3}$$

To show this result also holds for relativistic particles we start with the covariant form of the

[1] Strictly speaking $\boldsymbol{p}$ should be replaced by the kinematical momentum $\boldsymbol{\Pi} = \boldsymbol{p} - e\boldsymbol{A}$ but we are considering the case $\boldsymbol{A} = 0$.

Dirac equation in the presence of an electromagnetic field,

$$\left[-i\hbar c\gamma^{\mu}(\partial_{\mu} - ieA_{\mu}) + mc^2\right]\psi = 0, \tag{4.4}$$

where γ^{μ} are the Dirac matrices, $A_{\mu} = (\frac{\Phi}{c}, \boldsymbol{A})$ is the electromagnetic four-potential, and ψ is a four-component Dirac bispinor. Multiplying on the left by γ^0 and rearranging we find

$$\left\{c\left[\boldsymbol{\alpha}\cdot(\boldsymbol{p} - ie\boldsymbol{A})\right] - e\Phi + mc^2\gamma^0\right\}\psi = i\hbar\frac{\partial\psi}{\partial t}, \tag{4.5}$$

where $\boldsymbol{\alpha} = \gamma^0\gamma^i = \left(\begin{smallmatrix} 0 & \sigma \\ \sigma & 0 \end{smallmatrix}\right)$ and we have made the substitution $\boldsymbol{p} = -i\hbar\boldsymbol{\nabla}$. For a static electric field and no magnetic field the Hamiltonian is then

$$H = c\boldsymbol{\alpha}\cdot\boldsymbol{p} + mc^2\gamma^0 - e\Phi. \tag{4.6}$$

Since $\boldsymbol{p}$ commutes with both $\boldsymbol{\alpha}\cdot\boldsymbol{p}$ and γ^0 we find, similarly to Eq. (4.2),

$$\frac{1}{i\hbar}\langle[\boldsymbol{p}, H]\rangle = -e\langle\boldsymbol{\mathcal{E}}\rangle = 0. \tag{4.7}$$

4.1.2 Evasion of Schiff's Theorem

In fact we can show that the expectation value of the energy due to an electric dipole moment also vanishes in the non-relativistic limit. We first note that an EDM must be either aligned or anti-aligned with the electron spin; otherwise a new quantum number would be needed. Equivalently we could show, using the Wigner-Eckert theorem, that the expectation value of a dipole moment is given only by its projection on the angular momentum of the system. From the energy for a classical dipole in a field, $-\boldsymbol{d}\cdot\boldsymbol{\mathcal{E}}$, we guess the quantum operator for the energy of an electric dipole moment to be $H_{edm} = -d_e\boldsymbol{\Sigma}\cdot\boldsymbol{\mathcal{E}}$, where $\boldsymbol{\Sigma} = \left(\begin{smallmatrix} \sigma & 0 \\ 0 & \sigma \end{smallmatrix}\right)$. One can see that

$$\langle H_{edm}\rangle = -d_e\langle\boldsymbol{\Sigma}\cdot\boldsymbol{\mathcal{E}}\rangle = -d_e\langle[\boldsymbol{\Sigma}\cdot\boldsymbol{p}, H]\rangle = 0, \tag{4.8}$$

since $\boldsymbol{\Sigma}\cdot\boldsymbol{p}$ commutes with $\boldsymbol{\alpha}\cdot\boldsymbol{p}$ and γ^0.

Where then does the enhancement of the electron EDM come from? It turns out that our expression for H_{edm} is incorrect in the relativistic case. To properly derive the operator we follow

Commins *et al.* [84] and first consider the relativistic Lagrangian density for an electric dipole moment [4],

$$\mathcal{L}_{edm} = -i\frac{d_e}{2}\bar{\Psi}\sigma^{\mu\nu}F_{\mu\nu}\gamma^5\Psi = d_e\bar{\Psi}\left[\boldsymbol{\Sigma}\cdot\boldsymbol{\mathcal{E}} + i\boldsymbol{\alpha}\cdot\boldsymbol{B}\right]\Psi. \tag{4.9}$$

$F_{\mu\nu} = \partial_\mu A_\nu - \partial_\nu A_\mu$ is the usual electromagnetic tensor, $\sigma^{\mu\nu} = \frac{i}{2}(\gamma^\mu\gamma^\nu - \gamma^\nu\gamma^\mu)$, and $\gamma^5 = i\gamma^0\gamma^1\gamma^2\gamma^3$. One can show this operator is P- and T-odd as expected (remembering that $\Psi(x,t) \xrightarrow{P} \gamma^0\Psi(-x,t)$ and $\Psi(x,t) \xrightarrow{T} \gamma^1\gamma^3\Psi(x,-t)$ [85]). $\mathcal{L}_{edm}$ is entirely analogous to the P- and T-even anomalous magnetic moment operator $\mathcal{L}_{Pauli} = -\frac{\mu_B}{2}\bar{\Psi}\sigma^{\mu\nu}F_{\mu\nu}\Psi$. The corresponding single-particle EDM Hamiltonian with $\boldsymbol{B} = 0$ is

$$H_{edm} = -d_e\gamma^0\boldsymbol{\Sigma}\cdot\boldsymbol{\mathcal{E}}. \tag{4.10}$$

One can see that, unlike in the non-relativistic case, this operator can not be expressed as a commutator with the Hamiltonian because

$$\left[\gamma^0, H\right] = \left[\gamma^0, \boldsymbol{\alpha}\cdot\boldsymbol{p}\right] \neq 0. \tag{4.11}$$

What then is the physical significance of H_{edm}? Since it involves a fair amount of algebra we quote the result from Commins *et al.*. For the anomalous magnetic moment operator in a uniform magnetic field one can show that

$$\psi^\dagger H_{Pauli}\psi = -\chi^\dagger\boldsymbol{B}\cdot\left(\boldsymbol{\mu} - \frac{\gamma}{1+\gamma}\boldsymbol{\beta}\boldsymbol{\mu}\cdot\boldsymbol{\beta}\right)\chi. \tag{4.12}$$

If μ is the magnetic dipole moment in the rest frame, the factor in parentheses is the Lorentz contracted dipole moment in the lab frame[2]. A similar derivation for H_{edm} gives terms analogous to those in Eq. (4.12). Thus even though *the expectation of the electric field is zero, the expectation value of the Lorentz contracted dipole moment times the electric field is non-zero*. The Lorentz contraction actually makes the dipole moment smaller but, as we'll see below, electric fields in atoms and molecules are enormous. The small asymmetry due to contraction leads to an enhancement of the electron EDM in heavy atoms and molecules.

One might be concerned that the presence of the extra term H_{edm} invalidates our argument about the cancellation of the internal and external electric fields. Adding this term to the Hamiltonian in Eq. (4.7) leads to another force term $[p, H_{edm}] = -d_e\gamma^0\boldsymbol{\Sigma}\cdot\boldsymbol{\nabla}\boldsymbol{\mathcal{E}}$, analogous to the non-relativistic force

[2]The dimensions of the dipole are charge times length; charge is invariant under Lorentz boosts, while the length contracts.

on a dipole, $\boldsymbol{F} = \boldsymbol{d}\cdot\boldsymbol{\nabla}\boldsymbol{\mathcal{E}}$. We find that with an external field, $\boldsymbol{\mathcal{E}}_e = 100\,\mathrm{V\,cm^{-1}}$, an electric field gradient of $\boldsymbol{\mathcal{E}}_{eff}/a_0$, with $\boldsymbol{\mathcal{E}}_{eff} \approx 10\,\mathrm{GV\,cm^{-1}}$, and the limit of $d_e \lesssim 10^{-27} e\cdot cm$,

$$\left|d_e\gamma^0\boldsymbol{\Sigma}\cdot\left(\boldsymbol{\nabla}\boldsymbol{\mathcal{E}}_{eff}\right)\right| \approx 10^{-11}\left|e\boldsymbol{\mathcal{E}}_e\right|. \tag{4.13}$$

While this does lead to a non-zero expectation of the electric field the effect is many orders of magnitude smaller than the effective electric field due to Lorentz contraction.

4.2 Back of the envelope estimate of the effective electric field

To estimate the effective electric field we follow the method in Section 4.8 of Budker *et al.* [86]. The effective electric field that causes the enhancement of an electron EDM in atoms or molecules is largely due from s-wave electrons near a heavy nucleus. Near the nucleus the charge is not screened by the core electrons. For an ion with charge Z the radius of the first Bohr orbit is a_0/Z. The electric field at this radius is roughly $\mathcal{E} = Ze/r^2 = Z^3e/a_0^2 \approx Z^3\times 5\,\mathrm{GV\,cm^{-1}}$.

Above we showed the effective field comes from the Lorentz contraction of the dipole moment, d_e. A classical estimate of the velocity of the electron near the nucleus gives $v \approx Z\alpha c$. The Lorentz contraction of the dipole moment is given by $d_e/\gamma = d_e\sqrt{1-v^2/c^2}$. For $v^2/c^2 \ll 1$ the relative change is approximately $\frac{1}{2}v^2/c^2$. Thus we estimate the relativistic electric field to be

$$\mathcal{E}_{rel} = \tfrac{1}{2}Z^2\alpha^2\frac{Z^3e}{a_0^2} \approx \left(\frac{Z}{8}\right)^5 5\,\mathrm{GV\,cm^{-1}}. \tag{4.14}$$

For Pb, with $Z = 82$, this gives $\mathcal{E}_{rel} \approx 5\times 10^5\,\mathrm{GV\,cm^{-1}}$!

The average electric field on an electron is dominated by the time it spends near the nucleus. We can estimate the probability for the electron to be within a volume, V, of radius, $r \approx a_0/Z$, by

$$\left|\psi_s(0)\right|^2 V \approx \frac{Z}{\pi a_0^3}\frac{4\pi a_0^3}{3Z^3} \approx \frac{1}{Z^2}, \tag{4.15}$$

using an estimate for the s-wave wave function at the origin from Problem 1.12 in Budker *et al.* [86]. The average internal electric field is then

$$\mathcal{E}_{int} \approx \mathcal{E}_{rel}\frac{1}{Z^2} \approx (Z\alpha)^2\frac{Ze}{a_0^2}. \tag{4.16}$$

Finally, if the wave function of the electron is symmetric the field will average to zero. Thus we expect there must be an additional factor, P, to account for the asymmetric polarization of the atom. Putting it all together we have

$$\mathcal{E}_{eff} \approx P \times \mathcal{E}_{int} \approx P \times (Z\alpha)^2 \frac{Ze}{a_0^2} \approx P \times \left(\frac{Z}{27}\right)^3 5\,\mathrm{GV\,cm^{-1}}. \tag{4.17}$$

For Pb we then estimate $\mathcal{E}_{eff} \approx P \times 135\,\mathrm{GV\,cm^{-1}}$. *Ab initio* [87, 88] and semi-empirical calculations [75] give $\mathcal{E}_{eff} \approx 6 - 26\,\mathrm{GV\,cm^{-1}}$. This suggests that the effective polarization in PbO is around 10%.[3] As we will show later, atomic systems are barely polarized in laboratory strength fields (typically $P \lesssim 0.1\%$) and hence give orders of magnitude smaller effective electric fields.

4.3 Introduction to EDM enhancement factor calculations

In this section we briefly sketch the basic principles behind enhancement factors calculations for atoms and molecules. We follow Meyer *et al.* [89] who give a very clear overview for the non-expert in molecular structure calculations.

4.3.1 Enhancement in atoms

Returning to the relativistic operator for an EDM shift, $H_{edm} = -d_e \gamma^0 \boldsymbol{\Sigma} \cdot \boldsymbol{\mathcal{E}}$, we now consider how to calculate its expectation value. Since we previously showed $\langle \boldsymbol{\Sigma} \cdot \boldsymbol{\mathcal{E}} \rangle = 0$, we are free to subtract this term off the relativistic operator. This leaves an operator that acts only on the lower component of the Dirac bispinor (which vanishes in the non-relativistic limit),

$$H_{edm} = -d_e(\gamma^0 - 1)\boldsymbol{\Sigma} \cdot \boldsymbol{\mathcal{E}} = \begin{pmatrix} 0 & 0 \\ 0 & 2d_e \boldsymbol{\sigma} \cdot \boldsymbol{\mathcal{E}} \end{pmatrix}. \tag{4.18}$$

Since this operator is P-odd it can only connect states of opposite parity. For example, in alkali atoms the largest matrix element comes from mixing of the ground s state with the first excited p state by the external electric field. To first order the new ground eigenstate is then $|\psi\rangle = c_s |s\rangle + c_p |p\rangle$,

[3] We will see later that the low effective polarization is mostly due to the lack of s-wave character in the valence electrons, rather than actual low polarization of the molecule

with

$$c_s \approx 1,\ c_p = \frac{\langle s \left| e\boldsymbol{r}\cdot\boldsymbol{\mathcal{E}}_{ext} \right| p\rangle}{\Delta E_{parity}}, \tag{4.19}$$

where we define $E_p - E_s = \Delta E_{parity}$ to bring out an analogy to the molecular case later. The EDM matrix element is then

$$\begin{aligned}\Delta E_{edm} = \langle\psi \left| H_{edm} \right| \psi\rangle = \left(c_s \langle s| + c_p \langle p|\right)|H_{edm}|\left(c_s |s\rangle + c_p |p\rangle\right)\\ = -2c_s c_p d_e \langle s \left| (\gamma_0 - 1)\boldsymbol{\Sigma}\cdot\boldsymbol{\mathcal{E}} \right| p\rangle = 2c_s c_p d_e \left\langle s_L \left| 2\boldsymbol{\sigma}\cdot\boldsymbol{\mathcal{E}} \right| p_L \right\rangle,\end{aligned} \tag{4.20}$$

where s_L and p_L are the lower components of the relativistic wave functions. With the constraint $c_s^2 + c_p^2 = 1$, the factor $c_s c_p$, and thus the EDM energy shift, is maximized for $c_s = c_p = \frac{1}{\sqrt{2}}$; i.e. complete mixing. In the atomic case the electric fields required for complete mixing can not be reached in the laboratory. The matrix element in Eq. (4.20) can be explicitly evaluated (e.g. see section 8.2 of Khriplovich [2]),

$$\left\langle s_{L,1/2} \left| 2\boldsymbol{\sigma}\cdot\boldsymbol{\mathcal{E}} \right| p_{L,1/2} \right\rangle = \left\langle s_{L,1/2} \left| 2\boldsymbol{\sigma}\cdot\left(\frac{Ze\hat{\boldsymbol{r}}}{r^2}\right) \right| p_{L,1/2} \right\rangle = \frac{4(Z\alpha)^2 Ze}{\gamma(4\gamma^2-1)a_0^2(\nu_s\nu_p)^{3/2}} \approx (Z\alpha)^2\frac{Ze}{a_0^2} = \mathcal{E}_{int}, \tag{4.21}$$

where $\gamma = \sqrt{(j+1/2)^2 - Z^2\alpha^2}$ and $\nu_{s,p}$ are the effective principal quantum numbers. Here we see the $(Z\alpha)^2$ relativistic correction we guessed earlier and also note that the roughly $(j+1/2)^{-3}$ dependence of the matrix element confirms our statement that s wave functions lead to larger enhancement. Since the electric field is largest at the nucleus any contribution from the $p_{3/2}$ wave function, which is small at the nucleus, is usually negligible. For $\boldsymbol{\mathcal{E}} = \mathcal{E}\hat{\boldsymbol{z}}$ we now have

$$\Delta E_{edm} \approx 2c_s c_p d_e (Z\alpha)^2\frac{Ze}{a_0^2} \approx \frac{\langle s \left| ez \right| p\rangle \mathcal{E}_{ext}}{\Delta E_{parity}} 2d_e\mathcal{E}_{int}. \tag{4.22}$$

There are two ways to interpret this. First, one can group $d_e\mathcal{E}_{int}$ together and consider the energy shift as being due to the electron EDM in the internal field of the atom suppressed by an effective polarization of the atom. The first order Stark shift of the ground state (neglecting higher lying states) is

$$E_{Stark} = \langle\psi \left| e\boldsymbol{r}\cdot\boldsymbol{\mathcal{E}}_{ext} \right| \psi\rangle = 2c_s c_p \langle s \left| ez \right| p\rangle \mathcal{E}_{ext} \approx \frac{2\left(\langle s \left| ez \right| p\rangle \mathcal{E}_{ext}\right)^2}{\Delta E_{parity}}, \tag{4.23}$$

so we can rewrite the EDM energy shift as

$$\Delta E_{edm} \approx \sqrt{\frac{2E_{stark}}{\Delta E_{parity}}} d_e \mathcal{E}_{int}. \tag{4.24}$$

The Stark shift in atoms is $\frac{1}{2}\alpha\mathcal{E}^2$ where α is the polarizability. For example, the polarizability of the ground state of cesium, a popular atom for EDM searches, is $\sim 400 a_0^3$[90]. The Stark shift in cesium is then

$$E_{Stark} \approx \frac{400}{2} a_0^3 \mathcal{E}^2 \left(\frac{1\,\mathrm{V}}{1\,\mathrm{cm}}\right)^2 \approx \frac{200}{e^2/a_0} \left(\frac{a_0}{1\,\mathrm{cm}}\right)^2 (1\,\mathrm{eV})^2\, \boldsymbol{\mathcal{E}}^2 \approx \boldsymbol{\mathcal{E}}^2 \times 2 \times 10^{-18}\,\mathrm{eV}, \tag{4.25}$$

where $\boldsymbol{\mathcal{E}}$ is the electric field in $\mathrm{V\,cm^{-1}}$. The cesium D1 transition energy is on the order of 1 eV so for the largest lab fields of $50\,\mathrm{kV\,cm^{-1}}$ the suppression factor is

$$\sqrt{\frac{2E_{Stark}}{\Delta E_{parity}}} \approx \sqrt{\frac{2 \times (5 \times 10^4)^2 \times (2 \times 10^{-18}\,\mathrm{eV})}{1\,\mathrm{eV}}} \approx 1 \times 10^{-4}. \tag{4.26}$$

A second way to interpret Eq. (4.22) is to pull out the external electric field term,

$$\Delta E_{edm} \approx \left[\frac{2\langle s \left| ez \right| p\rangle}{\Delta E_{parity}} \mathcal{E}_{int}\right] d_e \mathcal{E}_{ext}, \tag{4.27}$$

and consider the term in brackets to be the "EDM enhancement factor."

4.3.2 Enhancement in molecules

While molecular structure is much more complicated than atomic structure the EDM enhancement still comes from the same mixing of a s and p orbital on a heavy atom. Instead of an external electric field causing the mixing, one can roughly imagine that the internuclear electric field mixes the atomic orbitals that make up a molecular orbital.

Molecular orbitals can be specified by the projection of the orbital angular momentum of the electron on the internuclear axis. For example σ orbitals, with an orbital angular momentum projection of zero, are the analog of atomic s orbitals. A molecular σ orbital can be a linear combination of s, p, and higher momentum atomic orbitals with orbital angular momenta projections on the internuclear axis of zero. More specifically, as we will discuss in Section 4.5.2, the appropriate

linear combination for a σ orbital is

$$|\sigma_{\pm\omega}\rangle = c_s \left|6s_{1/2,\pm\omega}\right\rangle + c_p \left(\mp \frac{2\omega}{\sqrt{3}} \left|6p_{1/2,\pm\omega}\right\rangle + \sqrt{\frac{2}{3}} \left|6p_{3/2,\pm\omega}\right\rangle \right) + c_d \Big(\ldots \Big) + \ldots \tag{4.28}$$

Here ω refers to the projection of the total angular momentum on the molecular axis. Note that the normalization condition is relaxed, $c_s^2 + c_p^2 \leq 1$. Substituting this into Eq. (4.20) as $\left|\psi\right\rangle$ gives

$$\Delta E_{edm} = \pm \frac{4\omega}{\sqrt{3}} c_s c_p d_e \left\langle s_{1/2} \right| 2\boldsymbol{\sigma} \cdot \boldsymbol{\mathcal{E}} \left| p_{1/2} \right\rangle \approx \pm \frac{4\omega}{\sqrt{3}} c_s c_p d_e \mathcal{E}_{int}. \tag{4.29}$$

As in the atomic case the maximum possible value is with full mixing, $c_s = c_p = 1/\sqrt{2}$ (and no admixtures of higher angular momentum states). Note that c_s and c_p, representing mixing of the atomic orbitals, are truly constants of the molecular orbital, independent of the external electric field, unlike in the atomic case.

4.3.3 Molecules do NOT have permanent EDMs

Given the innate mixing of s and p orbitals in a molecular orbital one might wonder why an electric field is needed at all in a molecular electron EDM search. The answer to this question also touches upon a common misconception from high school chemistry: the ball-and-stick picture of a molecule with its attendant "permanent" electric dipole moment. We have already shown that permanent electric dipole moments violate T and P violation so how do we reconcile this picture?

In the absence of an electric field energy eigenstates of a molecule must be parity eigenstates. Since parity flips the direction of the internuclear axis, the parity eigenstates we should be picturing for molecules are symmetric and anti-symmetric combinations of our ball-and-stick molecule pointing in opposite directions (see Fig. 4.1. Applying an electric field mixes the parity eigenstates. When fully mixed we arrive back at our picture of the ball-and-stick molecule. The state with its dipole moment polarized along the electric field lowers in energy and, as we would expect, the state polarized against it rises in energy. We will see later that full polarization occurs when the Stark shift exceeds the energy splitting between the parity eigenstates.

For diatomic molecules this splitting can be anywhere from sub-hertz to the rotational energy scale of gigahertz. For polyatomic molecules opposite parity states are usually nearly degenerate.

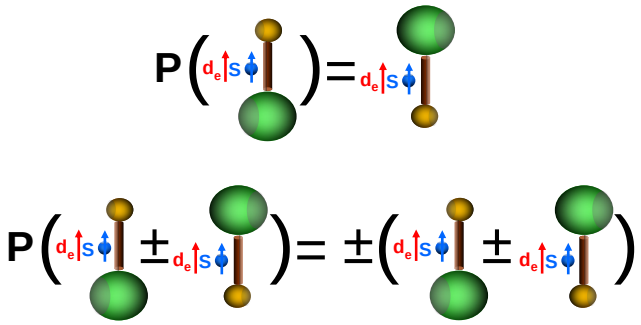

Figure 4.1: Parity eigenstates. In the absence of electric fields, molecules are in parity eigenstates. Since parity operating on a "ball-and-stick" molecule flips the internuclear axis and leaves the electron spin unchanged this can not be a parity eigenstate. The parity eigenstates are superpositions of both orientations.

Laboratory electric fields can readily generate these Stark shifts to orient the molecules.[4]

We can similarly see that the effect of an electron EDM must be zero in the field free parity eigenstates. Since the EDM has a fixed orientation relative to the spin, which does not flip under parity, parity eigenstates are superpositions of the EDM pointing both along and against the internuclear electric field.

4.4 Overview of *ab initio* methods

In Section 4.3.2 we saw that the main task in a molecular enhancement factor calculation is to determine the mixing of the atomic s and p orbitals in a molecular orbital, represented by the constants $c_{s,p}$ in Eq. (4.29). In this section we discuss the *ab initio* method used by Meyer *et al.* [89] to calculate EDM enhancement factors in many molecules and molecular ions of interest to experimentalists. Their methods are generic to many *ab initio* calculations and an overview serves

[4] Intramolecular electric fields experienced during collisions are probably enough to orient molecules with small splittings between parity states during chemical reactions. However, it is more likely that the ball-and-stick picture works well in chemistry because of the timescale of collisions in liquids is faster than the rotational period of molecules. The molecules see only a quick snapshot of each other, oriented in a specific direction. Quantum mechanically the molecules are in a superposition of several rotational states, which alternate in parity, spanning an energy given by the inverse of the collision timescale.

Table 4.1: *Ab initio* methods

Name	Acronym	Description
Hartree-Fock or self-consistent field	SCF	Varies the molecular orbitals and orbital occupation to find the ground state configuration
Multi-configurational self-consistent field	MCSCF	Varies the molecular orbitals and weights of several configurations to find both ground and excited configurations
Configuration interaction	CI	Varies the weights of configurations generated by a fixed number of excitations from the ground state configuration
Multireference configuration interaction	MRCI	CI using several "reference" configurations
Relativistic configuration interaction	RCI	CI using relativistic orbitals; implicitly finds spin-orbit mixing
Coupled cluster	CC	Similar to CI but iterative rather variational. Explicitly uses all excitations due to the first n-electron excitation operators, with n usually 2 or higher.

as a good introduction to the field.

Meyer *et al.* begin with a Hartree-Fock or self-consistent field (SCF) calculation of the ground state wave function and energy. The basic idea is to use the variational method on a multi-electron wave function expanded in an appropriate basis set. Each single-electron molecular orbital, $|\phi_j\rangle$ is expressed as a superposition of the basis wave functions $|f_i\rangle$

$$|\phi_j\rangle = \sum_i c_{ji} |f_i\rangle. \tag{4.30}$$

Atomic orbitals can be used for the basis functions but many *ab initio* methods use more computationally efficient basis sets such as superpositions of Gaussian wave functions centered on each atom. These basis sets have often been optimized beforehand by atomic calculations. Next a given configuration, $|\Phi_k\rangle$, is expressed as an antisymmetrized product of the single-electron molecular orbitals. Antisymmetrization implicitly enforces the Pauli principle and can be expressed with a

Slater determinant,

$$|\Phi_k\rangle = \mathcal{A} \prod_{j=\{j_{k1},\ldots,j_{kN}\}} \phi_j = \mathcal{A} \prod_{j=\{j_{k1},\ldots,j_{kN}\}} \sum_i c_{ji} |f_i\rangle = \frac{1}{\sqrt{N!}} \begin{vmatrix} \phi_{j_{k1}}(\boldsymbol{x_1}) & \phi_{j_{k1}}(\boldsymbol{x_2}) & \cdots & \phi_{j_{k1}}(\boldsymbol{x_N}) \\ \phi_{j_{k2}}(\boldsymbol{x_1}) & \phi_{j_{k2}}(\boldsymbol{x_2}) & \cdots & \phi_{j_{k2}}(\boldsymbol{x_N}) \\ \vdots & \vdots & \ddots & \vdots \\ \phi_{j_{kN}}(\boldsymbol{x_1}) & \phi_{j_{kN}}(\boldsymbol{x_2}) & \cdots & \phi_{j_{kN}}(\boldsymbol{x_N}), \end{vmatrix} \tag{4.31}$$

where the j_{kn} are a set of indices representing the occupied orbitals for the kth configuration. The Hartree-Fock method finds the configuration, i.e. the occupied orbitals given by j_{kn}, and the orbital composition given by c_{ji}, that minimizes the energy.

Implicit in the Hartree-Fock method is the assumption that the total wave function can be represented by a single product of one-electron orbitals only. Correlations between the position of electrons, which are a non-separable function of more than one electron coordinate, can not be accounted for. Most methods that try to account for correlation add more configurations to the wave function. Although usually prohibitive computationally, if every possible configuration built from one-electron orbitals is included, electron correlations can be fully accounted for. This method is referred to as full configuration interaction (full CI), and can be used only for the smallest of systems.

Meyer *et al*. next do a multiconfiguration self-consistent field calculation (MCSCF). Starting with the Hartree-Fock configuration as an initial guess, the energy of the sum of several configurations is simultaneously minimized,

$$\left|\Phi^{MCSCF}\right\rangle = \sum_k d_k |\Phi_k\rangle = \sum_k d_k \mathcal{A} \prod_{j=\{j_k1,\ldots,j_kN\}} \sum_i c_{ji} |f_i\rangle. \tag{4.32}$$

Now excited state energies can be estimated by looking at the energy of a given configuration in the sum with the desired symmetry. Next they perform a multireference configuration interaction (MRCI) calculation. Configurations representing one and two electron excitation from the now fixed MCSCF configurations are added,

$$\left|\Psi^{MRCI}\right\rangle = \sum_m h_m \left|\Phi_m^{MCSCF}\right\rangle. \tag{4.33}$$

The energy is again minimized by varying the h_m while holding the d_k, j_{kn}, and c_{ji} all fixed. After

this spin-orbit mixing is calculated for configurations with the same Ω in terms of a mixing angle χ,

$$|\Phi_{SO}\rangle = \cos\chi\,|\Phi_a, \Omega\rangle + \sin\chi\,|\Phi_b, \Omega\rangle\,. \tag{4.34}$$

At the end of these calculations one has a huge expansion for the molecular wave function. In large scale calculations the number of basis states can be in the tens of millions! To find $c_{s,p}$ the same MCSCF and MRCI calculations are performed for the atomic states. Then one finds the configuration term, $|\Phi_{EDM}\rangle$, in the molecular expansion representing the state of interest and takes its overlap with the atomic s and p orbitals expanded in the same basis

$$c_{s,p} = h_0 \cos\chi\,\langle\Phi_{EDM}\,|\,s, p_{atom}\rangle\,. \tag{4.35}$$

Since the wave functions are output from the calculations one can determine other values of interest. For EDM enhancement calculations it is often useful to calculate hyperfine constants since they also depend heavily on the wave function near the nucleus of the heavy atom and can be compared to experimental values.

4.5 Enhancement in PbO

In this section we review the calculations of the EDM enhancement factor in the $a(1)$ state of PbO. Discussion of the semi-empirical method of DeMille *et al.* [91] necessitates that we first examine the electronic structure of PbO.

4.5.1 Electronic structure of PbO

To determine the electronic structure of a molecule there are two methods that are nearly diametrically opposite to each other in philosophy. The first method starts with the separated states of the constituent atoms and considers what molecular states can be formed as the atoms are moved closer to each other. This method works well for determining the molecular structure at large internuclear distances, i.e. near dissociation. The second method is similar in spirit to the building up principle used in atomic structure. Molecular orbitals are defined and valence electrons are added one by one to determine the electronic configuration. This method typically works for the electronic states

at equilibrium.

Separated atoms

Lead has an electron configuration of $(6s)^2(6p)^2$. The two p electrons give a total spin $S = 0, 1$, and a total angular momentum $L = 0, 1, 2$ leading to the possible atomic terms ${}^3D, {}^1D, {}^3P, {}^1P, {}^3S, {}^1S$. Only ${}^1D, {}^3P$, and ${}^1S$ are antisymmetric in electron exchange.

To find the ground state we follow Hund's rules[92]. The term with the highest S is lowest in energy. Of these terms the one with highest L is lowest. Both rules minimize the overlap of the electrons, lowering the electrostatic repulsion energy. Finally, for shells less than half full the term with lowest $J = |L - S|$ is the ground state. For shells more than half full the term with highest $J = L + S$ is lowest in energy. This rule is due to the spin-orbit interaction. More than half-filled shells can be regarded as shells with holes which have an opposite spin-orbit interaction.

From Hund's rules we conclude the ground term of Pb is ${}^3P_0$ followed by ${}^3P_1$ and ${}^3P_2$.[5] Similarly for oxygen, with four p electrons or two p holes, we conclude the lowest terms are ${}^3P_2$ followed by ${}^3P_1$ and ${}^3P_0$, since multiplets are inverted for more than half-filled shells. The parity of all of these terms is even since we have an even number of electrons with $l = 1$.

When the two atoms are combined an electric field forms between the two nuclei. The projection of the orbital angular momentum of each atom is then quantized along the internuclear axis. The total projection of the orbital angular momentum, Λ, from the two even P states can be 0, 1, or 2 leading to two $\Sigma^+(2)$, one Σ^-, two Π, and one Δ molecular states (see Table 26 in Herzberg [67]). For each of these states we can have $S = 0$, 1, or 2, although the $S = 2$ states are likely repulsive.

For large internuclear distances, or strong coupling between L and S, it is more appropriate to quantize the total angular momentum of each atom along the internuclear axis. For lead ground state, ${}^3P_2$, and oxygen ground state, ${}^3P_0$, we have J=2 and J=0 which leads to possible molecular states with $\Omega = 2, 1, 0^+$. The other terms in the oxygen multiplet lie only a couple hundred cm^{-1} higher (as opposed to the splitting of nearly $8000\,\mathrm{cm}^{-1}$ between ${}^3P_0$ and ${}^3P_1$ of lead). The ${}^3P_1$ of oxygen combined with the lead ground state result in possible states of $\Omega = 1, 0^-$ while the oxygen ${}^3P_0$ state leads to $\Omega = 0^+$.

[5] While this is the correct ordering of the excited states, Hund's rules generally work well only for the ground state

Molecular orbitals

A nearly opposite approach is to build up the electron configuration using molecular orbitals. For a two center system one can define cylindrically symmetric one electron wave functions. These orbitals are designated by n and l as well as the quantum number λ, the magnitude of the projection of l on the internuclear axis. For example an orbital designated $2s\sigma$ has $n = 2, l = 0$, and $\lambda = 0$. For small internuclear distances these quantum numbers are analogous to those of an atom in an electric field with $\lambda = |m_l|$. The molecular shells fill similarly to atomic shells but with two electrons in each σ shell, and four in each $\pi, \delta, \ldots$ shell; two for each sign of m_l.

In limit of large internuclear distance for two like nuclei each orbital can be either symmetric or antisymmetric (labeled g or u, respectively) under a reflection through the origin. For example, if we approximate the lowest molecular orbitals for molecular hydrogen as superposition of the atomic hydrogen orbitals we have $\sigma_{g,u}1s = \sigma 1s_A \pm \sigma 1s_B$. It is clear that for the σ_u orbital, the wave function largely cancels between the two nuclei but for the σ_g orbital, the electron density is highest between the nuclei leading to a stronger bond and lower energy. While the even-odd symmetry is not strictly true in the case of unequal nuclei, there are analogous forms of the orbitals which are called "bonding" and "anti-bonding" orbitals.

For p electrons the lowest energy orbital is a σ bonding orbital. Next comes from the π bonding orbitals, one for each sign of $|m_l|$. The splitting between the σ and π orbitals is essentially the Stark shift from the internuclear electric field of the $|m_l| = 1$ level relative to the $m_l = 0$ level. Next come the π anti-bonding orbitals, denoted by π^*, and finally the σ^* anti-bonding orbital. Their higher energies are due to the asymmetric wave functions which in the limit of small internuclear distance corresponds to an orbital with higher principal quantum number, n.

In PbO we have six valence p electrons. Filling from the bottom this gives a $\sigma^2\pi^4$ configuration for the ground state. Similar to the method of combining separate atoms, to determine the possible molecular terms we can combine the molecular orbital quantum numbers to determine possible terms. Closed shells such as σ^2 and π^4 give ${}^1\Sigma^+$ terms just as in atoms. Thus we conclude the ground state of PbO to be ${}^1\Sigma^+$. The first excited states come from the raising of one of the π electrons to a π^* orbital (see Fig. 4.2). From Table 32 in Herzberg [67] three equivalent π electrons and one nonequivalent π electron give the terms ${}^1\Sigma^+, {}^1\Sigma^-, {}^1\Delta, {}^3\Sigma^+, {}^3\Sigma^-, {}^3\Delta$. From Hund's rules we expect the ${}^3\Sigma$ states to be lowest in energy, followed by the ${}^3\Delta$, and then the singlets. We can also have excited

Table 4.2: PbO configurations and term values

Configuration	(S,Λ) term	(ω,ω) terms
$\sigma^2\pi^4$	$^1\Sigma^+$	0^+
$\sigma^2\pi^3\pi^*$	$^3\Sigma^+$	$0^-, 1$
	$^3\Sigma^-$	$0^+, 1$
	$^3\Delta$	$1, 2, 3$
	$^1\Sigma^+$	0^+
	$^1\Sigma^-$	0^-
	$^1\Delta$	2
$\sigma\pi^4\pi^*$	$^3\Pi$	$0^+, 0^-, 1, 2$
	$^1\Pi$	1

states with the configuration $\sigma\pi^4\pi^*$ which lead to the terms $^1\Pi$ and $^3\Pi$.

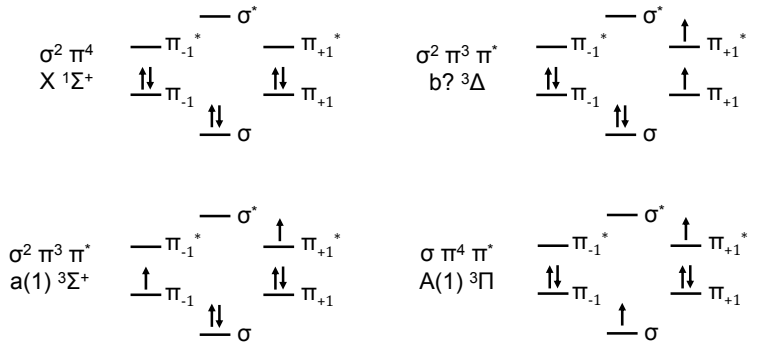

Figure 4.2: Molecular orbital diagrams of a few states of PbO. The ground state, $X^1\Sigma^+$, of PbO fills the σ and π orbitals. Exciting one π electron to a π^* orbital gives Σ and Δ states such as $a(1)^3\Sigma^+$ and $b(1)^3\Delta$. Exciting a σ electron to a π^* orbital gives Π states such as $A(1)^3\Pi$.

For large spin-orbit coupling (Hund's case *c*) S and Λ are no longer good quantum numbers. In this case we use (ω,ω) coupling which is similar to (J,J) coupling in atoms. Ω is the only good quantum number. Table 4.2 all the possible terms in the (ω,ω) coupling scheme along with the corresponding (S,Λ) term. Finally in Table 4.3 we show all the observed states, their assigned terms, and estimates of the mixing of the (S,Λ) based on a theoretical relativistic configuration interaction calculation in Balasubramanian and Pitzer [93].

The ground is dominantly $^1\Sigma^+$, as expected, followed by triplet states. Many of the states have not been observed presumably due to weak coupling to the ground state because of selection rules. $\Sigma^+ - \Sigma^-$ transitions are forbidden (or $0^+ - 0^-$ in Hund's case *c*). For Hund's case *a* only transitions with $\Delta S = 0, \Delta\Sigma = 0$, and $\Delta\Lambda = 0, \pm 1$, are allowed. For both Hund's case *a* and *c* transitions must

Table 4.3: PbO states

Label	(ω,ω) term	(S,Λ) terms	Configuration	Energy (cm^{-1})
X	0^+	$^1\Sigma^+(84\%),^3\Pi_0(0.8\%),^3\Sigma_0^-(3.0\%)$	$\sigma^2\pi^4$	0
a	1	$^3\Sigma_1^+(75\%),^3\Sigma_1^-(25\%),^3\Delta_1(<1\%)$	$\sigma^2\pi^3\pi^*$	16023
b?	0^-	$^3\Sigma_0^+(74\%),^1\Sigma^-(20\%)$	$\sigma^2\pi^3\pi^*$	16335?
?	2	$^3\Delta_2$	$\sigma^2\pi^3\pi^*$	
?	1	$^3\Delta_1$	$\sigma^2\pi^3\pi^*$	
?	2	$^1\Delta_2$	$\sigma^2\pi^3\pi^*$	
?	0^-	$^3\Pi_0(90\%),^3\Sigma_0^+(25\%)$	$\sigma\pi^4\pi^*$	
A	0^+	$^3\Pi_0(\text{mostly}),^1\Sigma^+(\text{small})$	$\sigma\pi^4\pi^*$	19862
B	1	$^3\Pi_1(\text{mostly}),^1\Pi(\text{small}),^3\Sigma_1^-$	$\sigma\pi^4\pi^*$	22282
C	0^+	$^3\Sigma_0^-(\text{mostly}),^1\Sigma^+(\text{small})$	$\sigma^2\pi^3\pi^*$	23795
C′	1	$^3\Sigma_1^-$	$\sigma^2\pi^3\pi^*$	24942
D	1	$^1\Pi$	$\sigma\pi^4\pi^*$	30060
E	0^+	$^1\Sigma^+$	$\sigma^2\pi^3\pi^*$	34443

have $\Delta\Omega = 0, \pm 1$. Strictly speaking only the $D(1)$ and $E(1)$ states have allowed transitions to the ground state. Most of the other observed states are forbidden while the unobserved states are generally doubly forbidden or more.

4.5.2 Semi-empirical calculation

In this section we review the method of Kozlov and DeMille [75] for estimating the EDM enhancement factor in the a(1) state of PbO. The goal is to fill in some of the calculational steps not made explicit in the paper.

The basic idea is to express the molecular orbitals as linear combinations of atomic orbitals (LCAO). The atomic orbitals are first constructed using the Hartree-Fock method on Pb^+, which best represents the lead atom in PbO. By evaluating matrix elements of these molecular orbitals for the spin-orbit splitting between molecular states, hyperfine constants, and the magnetic G factor one can constrain the coefficients of the linear combinations and use these constraints to place limits on the EDM matrix element.

A molecular orbital, $|\lambda_\omega\rangle$, in the case of large spin-orbit coupling is specified only by the quantum numbers $\lambda = |\boldsymbol{L}\cdot\hat{\boldsymbol{n}}|$ and $\omega = |\boldsymbol{J}\cdot\hat{\boldsymbol{n}}|$. To expand a molecular orbital in terms of atomic orbitals we need to make sure that the quantum numbers match. For example, the orbital $\left|\sigma_{\pm 1/2}\right\rangle$ can be expanded only in terms of atomic orbitals with $m_L = 0$ and $m_J = \pm 1/2$. For Pb this means we can use $6s_{1/2,m_j=\pm 1/2}$

and some combination of the $6p_{1/2,m_j=\pm1/2}$ and $6p_{3/2,m_j=\pm1/2}$ orbitals. For the 6p orbitals expressed in the L, S basis the only term that can contribute is $\left|L=1, m_l=0, S=\frac{1}{2}, m_S=\pm\frac{1}{2}\right\rangle$. Following similar reasoning for the $\left|\pi_{\pm1/2}\right\rangle$ orbital and calculating the Clebsch-Gordan coefficients gives

$$\left|L=1, m_l=0, S=\tfrac{1}{2}, m_S=\pm\tfrac{1}{2}\right\rangle = \mp\sqrt{\frac{1}{3}}\left|J=\tfrac{1}{2}, m_j=\pm\tfrac{1}{2}\right\rangle + \sqrt{\frac{2}{3}}\left|J=\tfrac{3}{2}, m_j=\pm\tfrac{1}{2}\right\rangle, \tag{4.36}$$

$$\left|L=1, m_l=0, S=\tfrac{1}{2}, m_S=\pm\tfrac{1}{2}\right\rangle = \pm\sqrt{\frac{2}{3}}\left|J=\tfrac{1}{2}, m_j=\pm\tfrac{1}{2}\right\rangle + \sqrt{\frac{1}{3}}\left|J=\tfrac{3}{2}, m_j=\pm\tfrac{1}{2}\right\rangle. \tag{4.37}$$

$$\tag{4.38}$$

With arbitrary constants the MO LCAO expansion is then

$$\left|\sigma_{\pm1/2}\right\rangle = S_s\left|6s_{1/2,\pm1/2}\right\rangle + S_p\left(\mp\sqrt{\frac{1}{3}}\left|6p_{1/2,\pm1/2}\right\rangle + \sqrt{\frac{2}{3}}\left|6p_{3/2,\pm1/2}\right\rangle\right), \tag{4.39}$$

$$\left|\pi_{i,\pm1/2}\right\rangle = P_i\left(\pm\sqrt{\frac{2}{3}}\left|6p_{1/2,\pm1/2}\right\rangle + \sqrt{\frac{1}{3}}\left|6p_{3/2,\pm1/2}\right\rangle\right), \tag{4.40}$$

$$\left|\pi_{i,\pm3/2}\right\rangle = P_i\left|6p_{3/2,\pm3/2}\right\rangle. \tag{4.41}$$

For the $|\pi_i\rangle$ orbitals $i=1$ refers to ground state orbital while $i=2$ is the excited orbital we previously denoted as π^*. Note the norm of the molecular orbital wave function needs only to be less than or equal to one, allowing the possibility that oxygen orbitals also contribute.

The next step is express the state configurations in terms of the molecular orbitals. To simplify calculations the ground state configuration, $\sigma^2\pi_1^4$, is defined as the vacuum state. Specifying excited states is done by denoting a hole orbital followed by an excited orbital,

$$a(1)[^3\Sigma^+], b(0^-)[^3\Sigma^+], C(0^+)[^3\Sigma^-], C'(1)[^3\Sigma^-], E(0^+)[^1\Sigma^+] \in \sigma^2\pi_1^2\pi_2 \Rightarrow \quad |\pi_1, \pi_2\rangle \tag{4.42}$$

$$A(0^+)[^3\Pi], B(1)[^3\Pi], D(1)[^1\Pi] \in \sigma\pi_1^4\pi_2 \Rightarrow \quad |\sigma, \pi_2\rangle \tag{4.43}$$

One might be concerned that some states will be missed by ignoring the other two π orbitals. A quick check shows that, for example, two non-identical π orbitals form the same states as three identical and one non-identical π orbital.

For the configuration expansions the key once again is to keep track of quantum numbers and symmetries. In particular, there is some subtlety with the $\Sigma^\pm$ states. The $\pm$ here refers only to the parity of the angular part of the wave function. For $\Omega=1$ there are still two nearly degenerate levels

of opposite parity for each rotational line. The $\Omega = 0$ parity states, however, are split in energy (this is also true of the $^3\Pi_{0^\pm}$ states as well). To get the signs correct we use the parity relations (see section 6.9.3-4 of [71]),

$$P\left|\Lambda = \Sigma^\pm\right\rangle = \pm\left|\Lambda = \Sigma^\pm\right\rangle \tag{4.44a}$$

$$P\left|L(l), \Lambda(\lambda)\right\rangle = (-1)^{\Lambda(\lambda)}\left|L(l), -\Lambda(\lambda)\right\rangle \tag{4.44b}$$

$$P\left|S(s), \Sigma(\sigma)\right\rangle = (-1)^{S(s)-\Sigma(\sigma)}\left|S(s), -\Sigma(\sigma)\right\rangle. \tag{4.44c}$$

For example, the $\Sigma^\pm$ states have $\Lambda = 0$ so they must be formed from some linear combination of two π orbitals with $\lambda_1 = -\lambda_2$. One can check that the symmetric combination goes with Σ^+,

$$\begin{aligned} P\left|\Sigma^\pm\right\rangle &= P\left[\frac{1}{\sqrt{2}}\left\{\left|\pi_{1,\lambda=+1}, \pi_{2,\lambda=-1}\right\rangle \pm \left|\pi_{1,\lambda=-1}, \pi_{2,\lambda=+1}\right\rangle\right\}\right] \\ &= \frac{1}{\sqrt{2}}\left\{(-1)^{1-1}\left|\pi_{1,\lambda=-1}, \pi_{2,\lambda=+1}\right\rangle \pm (-1)^{-1+1}\left|\pi_{1,\lambda=-1}, \pi_{2,\lambda=+1}\right\rangle\right\} \\ &= \pm\left|\Sigma^\pm\right\rangle. \quad \checkmark \end{aligned}$$

Now to find the expansion for $a(1)[^3\Sigma^+]$, for example, we simply add the triplet spin function. For the $\Omega = +1$ component we must have $\Sigma = +1$ so

$$\left|a(1)[^3\Sigma^+]\right\rangle = \frac{1}{\sqrt{2}}\left\{\left|\pi_{1,\lambda=1}, \pi_{2,\lambda=-1}\right\rangle + \left|\pi_{1,\lambda=-1}, \pi_{2,\lambda=+1}\right\rangle\right\}|\uparrow\uparrow\rangle = \frac{1}{\sqrt{2}}\left\{\left|\pi_{1,3/2}\pi_{2,-1/2}\right\rangle + \left|\pi_{1,-1/2}\pi_{2,3/2}\right\rangle\right\}. \tag{4.45}$$

Note that this is not a parity eigenstate. Presumably since calculations in this paper only involved differences in electronic energies this distinction was not important since the parity states are nearly degenerate. For $\Omega = 0$ we will have to be more careful since the parity states are quite different in energy.

Let us go over one more example, the $A(0+)[^3\Pi]$ state. Acting on one possible component with the parity operator gives

$$\begin{aligned} P\left|^3\Pi_0, \Lambda = +1, S = 1, \Sigma = -1\right\rangle &= (-1)^{+1}(-1)^{1-(-1)}\left|^3\Pi_0, \Lambda = -1, S = 1, \Sigma = +1\right\rangle \\ &= -\left|^3\Pi_0, \Lambda = -1, S = 1, \Sigma = +1\right\rangle. \end{aligned} \tag{4.46}$$

Table 4.4: PbO $\sigma^2\pi^3\pi^*$ state expansions

	$\lvert\omega_1,\omega_2\rangle = \lvert\pi_{1,\omega_1}\pi_{2,\omega_2}\rangle$									
State	$\lvert\frac{3}{2},\frac{3}{2}\rangle$	$\lvert\frac{3}{2},\frac{1}{2}\rangle$	$\lvert\frac{1}{2},\frac{3}{2}\rangle$	$\lvert\frac{1}{2},\frac{1}{2}\rangle$	$\lvert\frac{3}{2},-\frac{1}{2}\rangle$	$\lvert-\frac{1}{2},\frac{3}{2}\rangle$	$\lvert\frac{1}{2},-\frac{1}{2}\rangle$	$\lvert-\frac{1}{2},\frac{1}{2}\rangle$	$\lvert\frac{3}{2},-\frac{3}{2}\rangle$	$\lvert-\frac{3}{2},\frac{3}{2}\rangle$
$^3\Delta_3$	1									
$^3\Delta_2$		$\frac{1}{\sqrt{2}}$	$\frac{1}{\sqrt{2}}$							
$^1\Delta_2$		$\frac{1}{\sqrt{2}}$	$-\frac{1}{\sqrt{2}}$							
$^3\Delta_1$				1						
$a(1)[^3\Sigma^+]$					$\frac{1}{\sqrt{2}}$	$\frac{1}{\sqrt{2}}$				
$C'(1)[^3\Sigma^-]$					$\frac{1}{\sqrt{2}}$	$-\frac{1}{\sqrt{2}}$				
$b(0^-)[^3\Sigma^+]$							$\frac{1}{2}$	$\frac{1}{2}$	$\frac{1}{2}$	$\frac{1}{2}$
$C(0^+)[^3\Sigma^-]$							$\frac{1}{2}$	$-\frac{1}{2}$	$\frac{1}{2}$	$-\frac{1}{2}$
$E(0^+)[^1\Sigma^+]$							$-\frac{1}{2}$	$\frac{1}{2}$	$\frac{1}{2}$	$-\frac{1}{2}$
$^1\Sigma^-$							$-\frac{1}{2}$	$-\frac{1}{2}$	$\frac{1}{2}$	$\frac{1}{2}$

Thus the positive parity state is given by

$$\begin{aligned}\left|A(0+)[^3\Pi]\right\rangle &= \frac{1}{\sqrt{2}}\left\{|\Lambda=-1,\Sigma=+1\rangle - |\Lambda=+1,\Sigma=-1\rangle\right\}\\ &= \frac{1}{\sqrt{2}}\left\{\left|\sigma,\pi_{2,\lambda=-1}\right\rangle|\uparrow\uparrow\rangle - \left|\sigma,\pi_{2,\lambda=+1}\right\rangle|\downarrow\downarrow\rangle\right\}\\ &= \frac{1}{\sqrt{2}}\left\{\left|\sigma_{1/2}\pi_{2,-1/2}\right\rangle - \left|\sigma_{-1/2}\pi_{2,3/2}\right\rangle\right\}. \end{aligned} \tag{4.47}$$

Tables 4.4 and 4.5 summarize the expansions.

Armed with these expansions the next step is to constrain the coefficients using experimental data. First, Kozlov and DeMille use the spin-orbit multiplet splitting between the $A(0+)[^3\Pi]$ and $B(1)[^3\Pi]$ states. The coefficient for the spin-orbit operator is first determined from the splitting of the $6p$ orbitals in the lead ion,

$$\Delta E_{S-O} = \xi\left\{\langle 6p_{3/2}\left|\, l\cdot s\,\right|6p_{3/2}\rangle - \langle 6p_{1/2}\left|\, l\cdot s\,\right|6p_{1/2}\rangle\right\} = \xi\left(\tfrac{1}{2}-(-1)\right) = \tfrac{3}{2}\xi, \tag{4.48}$$

Table 4.5: PbO $\sigma\pi^4\pi^*$ state expansions

	$\lvert\omega_1,\omega_2\rangle = \lvert\sigma_{\omega_1}\pi_{2,\omega_2}\rangle$				
State	$\lvert\frac{1}{2},\frac{3}{2}\rangle$	$\lvert\frac{1}{2},\frac{1}{2}\rangle$	$\lvert-\frac{1}{2},\frac{3}{2}\rangle$	$\lvert\frac{1}{2},-\frac{1}{2}\rangle$	$\lvert-\frac{1}{2},\frac{1}{2}\rangle$
$^3\Pi_2$	1				
$B(1)[^3\Pi]$		$\frac{1}{\sqrt{2}}$	$\frac{1}{\sqrt{2}}$		
$D(1)[^1\Pi]$		$\frac{1}{\sqrt{2}}$	$-\frac{1}{\sqrt{2}}$		
$A(0^+)[^3\Pi]$				$\frac{1}{\sqrt{2}}$	$-\frac{1}{\sqrt{2}}$
$^3\Pi_{0^-}$				$\frac{1}{\sqrt{2}}$	$\frac{1}{\sqrt{2}}$

where we have used $l\cdot s = \frac{1}{2}\left[j(j+1) - l(l+1) - s(s+1)\right]$. One can also verify that

$$\langle\sigma_{1/2}\left|l\cdot s\right|\sigma_{1/2}\rangle = S_p^2\left\{\frac{1}{3}\langle 6p_{1/2}\left|l\cdot s\right|6p_{1/2}\rangle + \frac{2}{3}\langle 6p_{3/2}\left|l\cdot s\right|6p_{3/2}\rangle\right\} = 0 \tag{4.49}$$

$$\langle\pi_{i,3/2}\left|l\cdot s\right|\pi_{i,3/2}\rangle = P_i^2\langle 6p_{3/2}\left|l\cdot s\right|6p_{3/2}\rangle = \tfrac{1}{2}P_i^2 \tag{4.50}$$

$$\langle\pi_{i,1/2}\left|l\cdot s\right|\pi_{i,1/2}\rangle = P_i^2\left\{\frac{2}{3}\langle 6p_{1/2}\left|l\cdot s\right|6p_{1/2}\rangle + \frac{1}{3}\langle 6p_{3/2}\left|l\cdot s\right|6p_{3/2}\rangle\right\} = -\tfrac{1}{2}P_i^2 \tag{4.51}$$

Returning to the spin-orbit splitting between the A and B states we have,

$$\begin{aligned}\Delta E_{B-A} &= \xi\left\{\langle B(1)\,|\,l\cdot s\,|\,B(1)\rangle - \langle A(0^+)\left|l\cdot s\right|A(0^+)\rangle\right\}\\ &= \xi\left\{\langle\pi_{2,3/2}\left|l\cdot s\right|\pi_{2,3/2}\rangle - \langle\pi_{2,3/2}\left|l\cdot s\right|\pi_{2,3/2}\rangle\right\}\\ &= \frac{\xi P_2^2}{2}.\end{aligned} \tag{4.52}$$

Here we used the expansions in Table 4.5, and the fact that the σ orbitals do not contribute to the spin-orbit splitting (see Eq. (4.49)). Using the experimental values gives

$$P_2^2 = \frac{2\times 2420\,\mathrm{cm}^{-1}}{9450\,\mathrm{cm}^{-1}} = 0.51 \tag{4.53}$$

The next step is to take into account spin-orbit mixing within the configuration. One can show that

the positive eigenvector of a mixing Hamiltonian,

$$H = \begin{pmatrix} \Delta/2 & A \\ A & -\Delta/2 \end{pmatrix}, \tag{4.54}$$

can be expressed as

$$|1'\rangle = \cos\alpha\,|1\rangle + \sin\alpha\,|2\rangle\,, \tag{4.55}$$

where $|1\rangle$ and $|2\rangle$ are the original basis states and the mixing angle $\alpha \approx \frac{A}{\Delta}$ for $A \ll \Delta/2$ (see Appendix A). A similar calculation to Eq. (4.52) gives the mixing angle between the $a(1)$ and $C'(1)$ states,

$$\alpha = \frac{\langle C'(1)\,|\,H_{SO}\,|\,a(1)\rangle}{\Delta E_{aC'}} = \xi\frac{P_1^2 + P_2^2}{2\Delta E_{aC'}}. \tag{4.56}$$

By assuming $P_1 << P_2$ one finds $\alpha \approx 0.3$. Since 1(2) refers to the ground(excited) orbital this assumes the ground state p electrons tend to be on the oxygen atom while the excited p electron moves to the lead atom. The valence bond picture suggests that the lead atom does give up its p electrons to the oxygen atom so this is not unreasonable. In the $\left|\pi_{1,3/2}\pi_{2,-1/2}\right\rangle, \left|\pi_{1,-1/2}\pi_{2,3/2}\right\rangle$ basis the "mixing angle" for the $a(1)$ state was already $\pi/4$. Thus the new expansion, accounting for mixing with $C'(1)$, is

$$|a(1)\rangle = \cos\left(\tfrac{\pi}{4} - \alpha\right)\left|\pi_{1,3/2}\pi_{2,-1/2}\right\rangle + \sin\left(\tfrac{\pi}{4} - \alpha\right)\left|\pi_{1,-1/2}\pi_{2,3/2}\right\rangle. \tag{4.57}$$

Next Kozlov and DeMille take into account mixing with other configurations. These other configurations mix the π orbitals with the σ orbital. For example, the $a(1)$ state has a π_1 hole orbital and π_2 electron orbital. The $B(1)$ and $D(1)$ states instead have σ hole orbitals and π_2 electron orbitals. Mixing with these states thus causes the π_1 orbital to mix with the σ orbital. Mixing with higher energy configurations could similarly cause mixing between π_2 and σ orbitals. To account for this mixing angles for the orbitals are introduced and the $a(1)$ is expressed in terms of these new mixed orbitals,

$$\begin{aligned} \left|\tilde{\pi}_{i,1/2}\right\rangle &= c_i\left|\pi_{i,1/2}\right\rangle + s_i\left|\sigma_{1/2}\right\rangle \\ |a(1)\rangle &= c_\alpha\left|\pi_{1,3/2}\tilde{\pi}_{2,-1/2}\right\rangle + s_\alpha\left|\tilde{\pi}_{1,-1/2}\pi_{2,3/2}\right\rangle \end{aligned} \tag{4.58}$$

Note that this mixing is the key to EDM enhancement. As we saw above, enhancement relies on

mixing of the atomic s and p orbitals. The σ orbital introduced in this mixing is the only source of atomic s orbital in the $a(1)$ wave function.

With the expansion of the $a(1)$ state complete several experimental values can constrain the coefficients. The mixing with the $B(1)$ and $D(1)$ states constrains $s_1 = 2.8 s_\alpha^2 P_1 S_p$ in a calculation similar to Eq. (4.52). The value of the magnetic G tensor parallel to the internuclear axis, $G_\parallel = L_0 + 2S_0$, is straightforward to calculate for the $a(1)$ state and comparison with the experimental value provides the constraint, $s_\alpha^2 s_1^2 + c_\alpha^2 s_2^2 = 0.16$. Finally the hyperfine constant can be calculated with the aid of some radial integrals and compared to experiment.

With the constraints in place the expectation value of the EDM enhancement operator, $W_d = 2\boldsymbol{\sigma}\cdot\boldsymbol{\mathcal{E}}$ is calculated. The result in Kozlov and DeMille is

$$\begin{aligned} W_d &= -c_\alpha^2 W_d^{\tilde{\pi}_2} - s_\alpha^2 W_d^{\tilde{\pi}_1} \\ &= const. \times S_s \left(\sqrt{2} c_\alpha^2 c_2 s_2 P_2 - c_\alpha^2 s_2^2 S_p + \sqrt{2} s_\alpha^2 c_1 s_1 P_1 - s_\alpha^2 s_1^2 S_p \right) \end{aligned} \tag{4.59}$$

The constraints make the first term dominate. An examination of the coefficients show that the first term comes from the matrix element between the p orbital in the $\pi_{-1/2}$ orbital and the s orbital in the σ orbital, all coming from the mixed $\tilde{\pi}_2$ orbital. For this to give large enhancement we would ideally want a large contribution, S_s, from the $6s$ orbital to the σ orbital and strong mixing (s_2, c_2) between the $a(1)$ state and unobserved states in the $\sigma\pi_1^3\pi_2^2$ configurations. The experimental constraints on the coefficients give a final result of $W_d \geq 12 \times 10^{24}\,\mathrm{Hz}\, e^{-1}\,\mathrm{cm}^{-1}$.

4.5.3 *Ab initio* calculations

Meyer *et al.* [89] perform the MRSCF and MRCI calculations described in Section 4.4 for many molecules of interest for EDM experiments including PbO. A more recent version of their method [94] gave results within 25% of the large scale calculations performed for individual molecules. Several other *ab initio* calculations have been performed for PbO only. Isaev *et al.* [88] perform a relativistic coupled cluster calculation to determine the EDM enhancement factor and hyperfine constants. The coupled cluster method is similar in concept to the configuration interaction method. Both start with a reference configuration and add excitations. The coupled cluster method, however, takes into account n-electron excitations to all orders, where n is typically 2 to 4. In addition, the method for generating the excitations allows an iterative rather than variational solution. Petrov

Table 4.6: Effective fields in PbO $a(1)$ state

Reference	$\mathcal{E}_{eff}(GV/cm)$
Kozlov and DeMille [75]	≥ 25
Isaev *et al.* [88]	$6.4 - 13$
Petrov *et al.* [87]	$11 - 16$
Meyer and Bohn [94]	11.5

et al. [87] improve upon this work by using a relativistic configuration interaction calculation. Table 4.6 summarizes the enhancement calculations for the $a(1)$ state of PbO.

Examination of the later *ab initio* calculations suggest the enhancement mechanism is a little more complicated than the semi-empirical model. Configuration mixing is needed to properly take electron correlations into account. When this is done, the contribution from the lead $6s$ state to the σ orbital is actually small. Much of the contribution comes from mixing with the configuration $\sigma\pi^4\sigma^*$. These differences help to explain the discrepancy between the two methods (see Table 4.6).

Chapter 5

Apparatus

The high sensitivity of the PbO experiment comes from two factors which have been never combined in previous EDM experiments: the large enhancement from the internal electric field of a heavy diatomic molecule and the high counting rate of a vapor cell experiment. These factors were never combined for good reason: an EDM measurement requires unpaired electron spins. Molecules with unpaired spins, called free radicals, are extremely chemically reactive, making the use of vapor cells impossible. In the PbO experiment, the electron spins are only briefly unpaired for the EDM measurement by exciting the molecules to a metastable excited state. At all other times the spins are paired making the molecules chemically stable.

Much of the efforts for this experiment focus on the challenges of fabricating and maintaining a high temperature molecular vapor cell and the hardware required to prepare and detect the molecules in the excited metastable state used for the EDM measurement. In addition, as in most EDM experiments, extreme control over magnetic fields in the apparatus is needed. The combination of these unique needs means that commercial equipment is usually inadequate. Nearly every part of the apparatus was designed by grad students and postdocs on the experiment.

This chapter will start with a brief overview of the experimental apparatus and then focus on improvements or attempted improvements made during the course of this dissertation. Greater detail on many other parts of the apparatus are in the theses of Sarah Bickman [81] and Yong Jiang [52]. It is only because of their efforts (and those of previous students and postdocs) that the experiment has reached the stage it is at today.

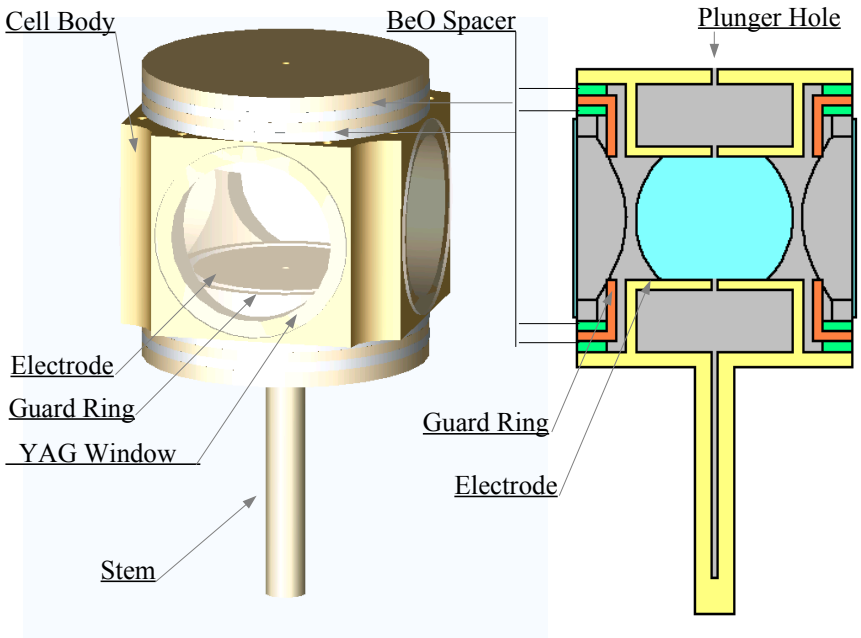

Figure 5.1: Vapor cell. The vapor cell is a high purity alumina frame with gold foil electrodes and guard rings on the top and bottom. YAG windows are sealed to the sides with gold foil. The electrodes and guard rings are electrically isolated with beryllium oxide and sapphire spacers.

5.1 Overview of apparatus

The central piece of the experimental apparatus is a high temperature vapor cell. Design of this vapor cell and the oven used to heat it was technically challenging. To achieve significant PbO vapor pressure, temperatures over 700 °C are needed. Even though PbO is not as reactive as a free radical, it still destroys most materials at these temperatures. It took considerable effort, described in several prior theses [52, 81, 95], to find a suitable vapor cell and heating oven design.

The PbO vapor cell is a hollow rectangular alumina block, 3.5″ wide by 2.5″ high. Four 2″ diameter, 2.5 mm thick, yttrium aluminum garnet (YAG) optical windows are sealed[1] to the sides of the cell with gold foil (see Fig. 5.1). A stack of circular alumina pieces form the top and bottom of the cell. The innermost pieces, 2″ diameter circles covered in bonded gold foil, are the main electrodes. Outside the electrodes are quarter inch thick annular guard rings. Sapphire and/or beryllium oxide spacers electrically isolate the main electrodes from the guard rings and the cell itself. The top and bottom electrode/guard ring pairs project into the cell and are spaced 1.5″ apart

[1]The pieces to be bonded together are held under pressure with the gold foil between them and heated to just below the melting point of gold. See [81] for details.

for maximum uniformity of the electric field. The guard rings are held at 1.8 times the electrode voltage to "push" in the electric fringe fields and create an optimal region of uniformity. Gold foil serves as both the electrical connection to the outside of the cell and a seal between the electrode stack and the spacers. Gold wires are either spot welded[2]or welded with a jeweler's torch to the tabs on the electrode foils.

A stem tube, connected to a small hole in the center of the bottom electrode, is kept cooler than the cell body and, in theory, serves as a reservoir for the PbO. A similar hole in the top of the cell is sealed with a movable polished alumina rod. A home-built non-magnetic linear motion vacuum feedthrough [52] allows this "plunger" rod to be moved from outside the vacuum chamber to open the seal and evacuate the vapor cell at low temperatures.

The cell is heated radiatively by a complex oven structure comprised of resistively heated tantalum foils secured in grooved quartz plates that attach to a quartz frame. The foils are driven with high current audio frequency waveforms generated by a rack of high power stereo amplifiers. The foils are laser cut in a zigzag pattern and connected in pairs with opposing current directions to reduce inductance, which allows us to switch the heating on or off in a fraction of a millisecond. Because of sensitivity to magnetic fields, no heater currents can be present during the EDM measurement. During switching, the amplitude of the heater waveforms is smoothly ramped over a few hundred microseconds to suppress induced eddy currents in metal parts of the oven and vacuum system. There are independent heating elements, comprised of two foils connected in series for each cell side, each cell window, the plunger, and the stem (see Fig. 5.2).

The stem, plunger, and side temperatures are monitored with thermocouples specifically designed for this experiment. Most commercial thermocouples that operate at 700 °C contain magnetic materials or are extremely brittle under the conditions of our experiment. We use thermocouples made from a gold-palladium alloy wire (60% Au, 40% Pd) welded to a pure gold wire with a jeweler's torch. The temperature response was roughly calibrated in vacuum against a set of standard type K thermocouples (see Fig. 5.3). The Au/Au-Pd thermocouples are connected to custom non-magnetic vacuum feedthroughs. To prevent unwanted thermoelectric voltages, the feedthroughs have gold and gold/palladium alloy wires which pass through several inches of epoxy. The feedthrough is also designed to provide strain relief, as the thermocouple wires are prone to breaking after mechanical bending.

[2]For a good bond a #11 welding head should be used with a power setting > 800 and a force setting of 8.0.

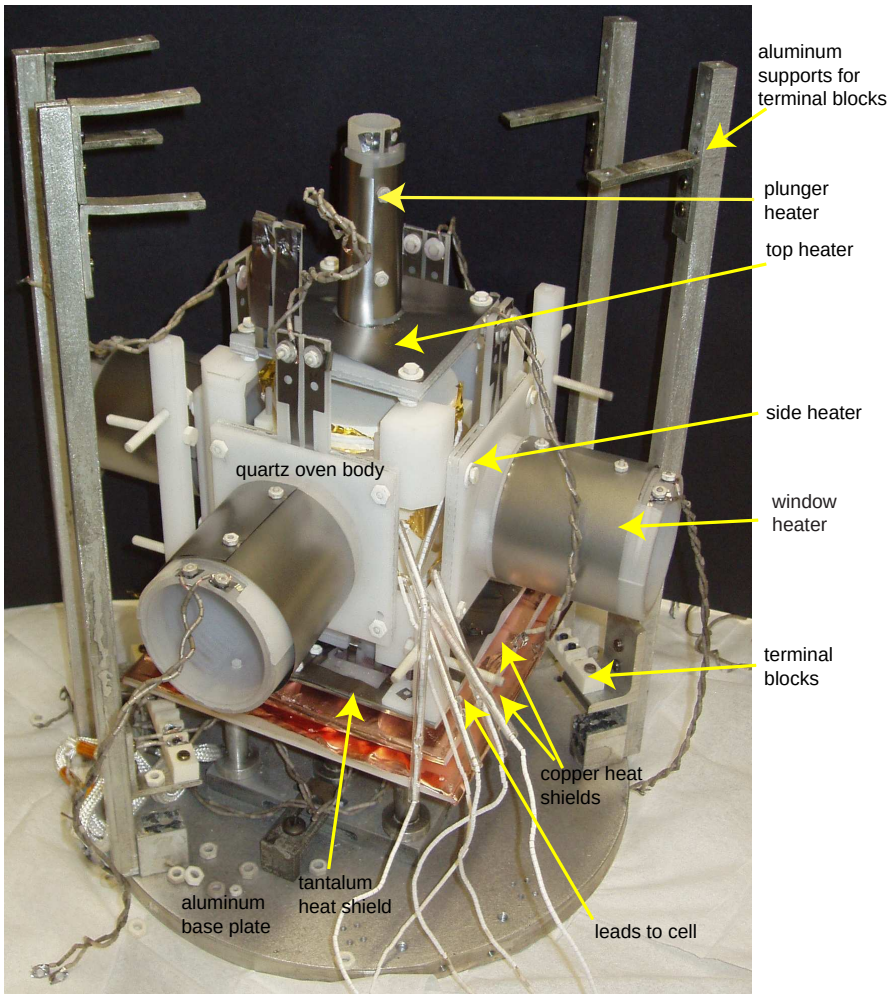

Figure 5.2: Oven. Tantalum heater foils are sandwiched between pieces of quartz, which are attached to a quartz frame surrounding the vapor cell with alumina nuts and screws. Only the leads of the foils are visible. The tantalum foil wrapped around the quartz pieces was a previous attempt at heat shielding. On the bottom, three layers of quartz heat shielding are visible with tantalum foil wrapped on the innermost layer and copper foil on the outer layers. This has since been replaced with insulating ceramic fiber board. The insulating ceramic beads on the twisted wire pairs have also been replaced with woven ceramic sleeving held in place with tantalum or copper crimp-on connectors.

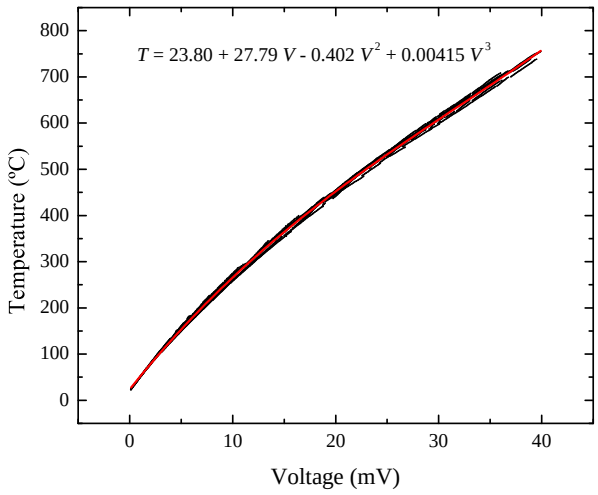

Figure 5.3: Au/AuPd thermocouple calibration. Measured voltages across several thermocouple junctions of a pure gold wire and a 60% gold / 40% palladium wire versus temperature as measured by standard K type thermocouples in vacuum. The red line is a third order polynomial fit.

A 48-channel low speed analog-to-digital board from National Instruments monitors the voltage and current waveforms for each heating element, the thermocouple voltages, electrode currents, and ambient magnetic field as measured by a 3-axis flux-gate magnetometer. Labview software logs the data and displays the time history. Monitoring the heater foil resistances helps us to both identify and predict failures. If systematic effects are identified in the future, this system will facilitate looking for correlations with the housekeeping data.

The oven system is insulated by 1 3/4″ thick layer of ceramic fiber boards held in place by a quartz frame. All electrical connections inside the oven system go to ceramic terminal blocks mounted on the same frame. This entire system sits inside an aluminum vacuum chamber. Connections from the terminal blocks are made to non-magnetic coaxial feedthroughs designed for this experiment (see [52]). The entire vapor cell/oven system is assembled and disassembled outside the vacuum chamber to minimize the risk of breaking electrical connections inside. Once the system has been placed in the vacuum chamber only connections between the terminal blocks, which are easily accessible, and the feedthroughs have to be made (see Fig. 5.4).

The vacuum chamber has copper tubing brazed to it which functions as an open-loop water cooling system. There are also two 300-turn circular magnetic coils (10.5″ ID) mounted in a

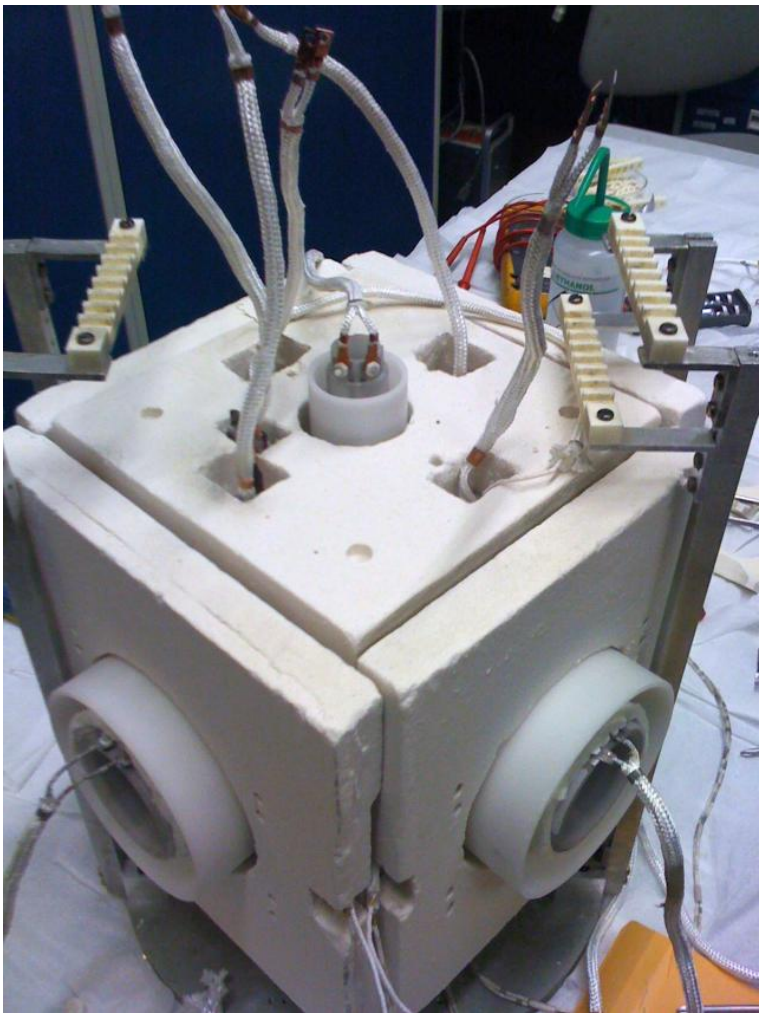

Figure 5.4: Insulation and terminal blocks. The oven assembly is now insulated by 1 3/4″ of ceramic fiber board (Cotronics 360). Ceramic fiber blankets (Cotronics 370) are used to insulate all other exposed parts. The ceramic terminal blocks used to make electrical connections are visible at the top of the picture. The connections are made with twisted wire pairs which are insulated by ceramic fiber sleeving and have crimp-on tantalum connectors on their ends.

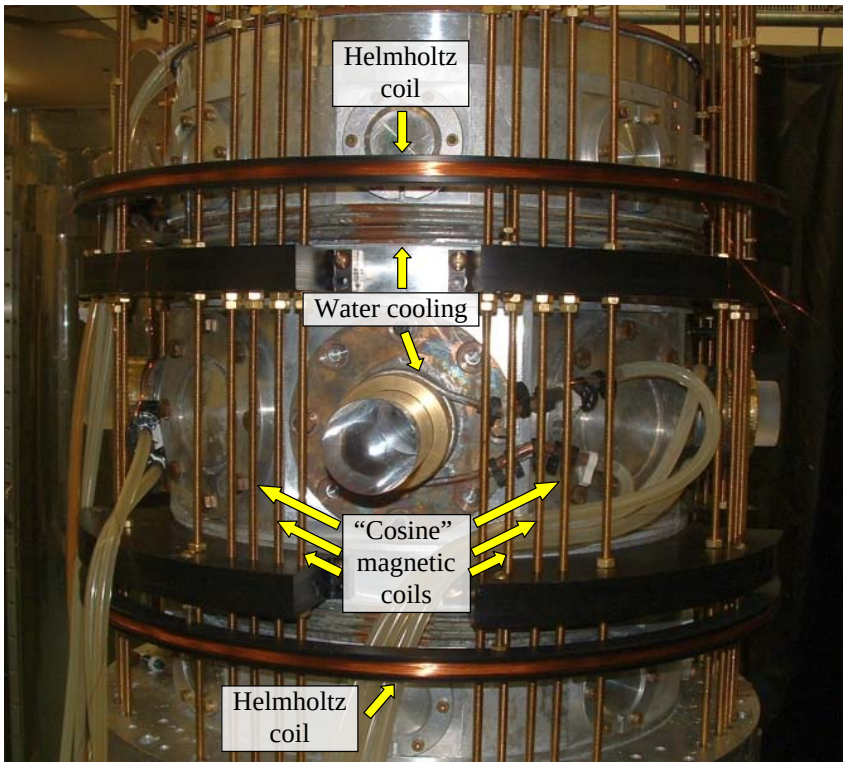

Figure 5.5: The vacuum chamber. Brazed copper tubing provides water cooling for the chamber itself and the light pipe feedthroughs. Two 300-turn magnetic coils mounted in the Helmholtz configuration produce a uniform magnetic field in the vertical direction. Currents run through various combinations of the "cosine" distributed threaded rods produce independently controlled uniform and gradient fields along the two horizontal axes.

Helmholtz configuration to provide a uniform magnetic field in the vertical direction, which we call the laboratory z-axis. A few independent turns of wire are attached to each coil mount for generating a gradient in the z direction, which might be useful during systematic checks. A cage of threaded brass rods in a "cosine" distribution are also mounted to the vacuum chamber. Running current through the rods produces independently controlled uniform and gradient magnetic fields in the x and y directions (see Fig. 5.5). Connections between the rods are made with magnet wire and routed such that supply currents are accompanied by return currents in the opposite direction to eliminate stray magnetic fields. Connections between the current supplies and magnetic coils are made with twisted wire pairs for the same reason.

The vacuum chamber sits inside up to four layers of cylindrical magnetic shielding as shown in Fig. 5.6. An external turbo pump, attached through a pipe entering the bottom of the shields,

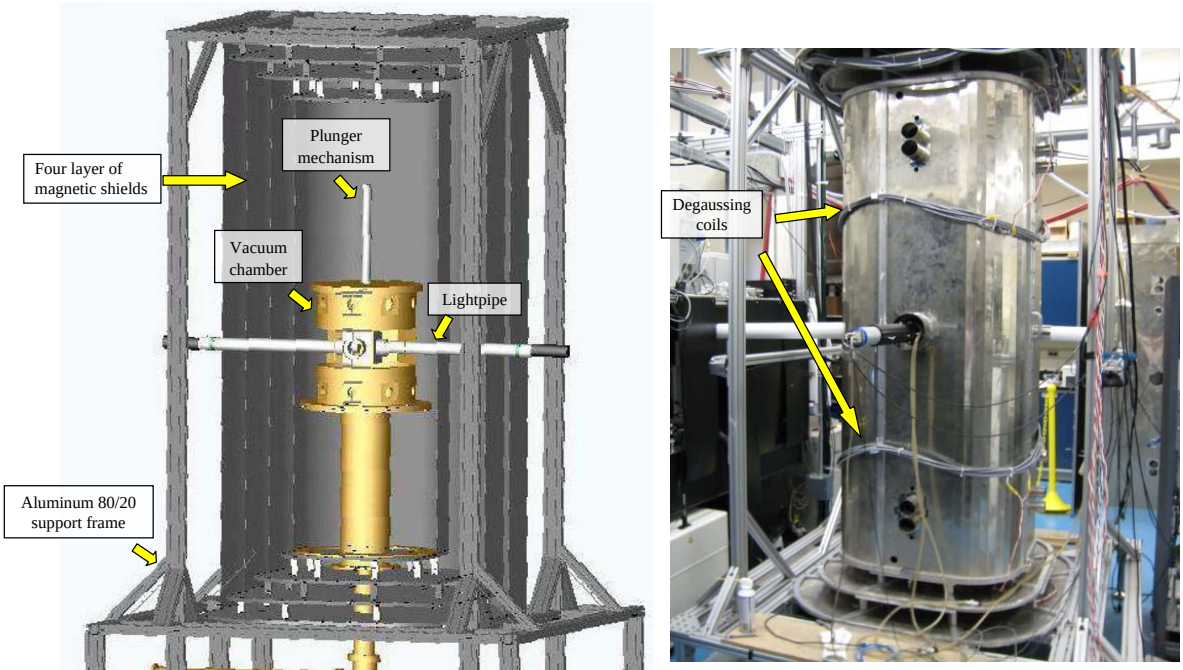

Figure 5.6: Magnetic shields and vacuum chamber. The vacuum chamber sits in up to four layers of roughly cylindrical mu-metal magnetic shields supported by an aluminum 80/20 structure. The aluminum vacuum system exits through the bottom of the shields, connecting to an external turbo pump. Two 60-turn coils wrapped around each shield layer for demagnetization.

evacuates the chamber to $\approx 10^{-6}$ Torr. Electrical connections, either coaxial or twisted pair, pass through holes in the top of the shields. Each layer of magnetic shields has two 60 turn coils wrapped around it for demagnetization (see Section 5.4).

To excite the molecules a pulsed laser system is used which sits on an optical table outside of the magnetic shields. A pulsed Nd:YAG laser (Spectra GCR 190-100), with 100 Hz repetition rate, pumps a Fluorescein 548 dye laser (Lambda Scanmate 2E) which produces 15-25 mJ, 7 ns pulses with a wavelength of 548 nm. This laser drives the $R0$ transition, $|X, v = 0, J = 0\rangle \rightarrow |a, v' = 5, J' = 1\rangle$.[3] The laser propagation direction is defined to be along the laboratory $\hat{y}$ axis as shown in Fig. 5.7. The linear polarization of the laser pulse is set in the $\hat{x} - \hat{z}$ plane by a combination of a high-power half-wave plate and Glan-Laser calcite polarizer. A telescope increases the diameter of the collimated

laser beam to 1.5″.

A home-built microwave system delivering up to 4 W of power at 28.2 GHz drives transitions between the various sublevels of the $|a, J = 1\rangle$ and $|a, J = 2\rangle$ rotational levels.

Four 2″ diameter quartz light pipes serve as vacuum feedthroughs for the laser light, microwaves, and fluorescence. They pass from outside the vacuum chamber, through non-magnetic brass compression feedthroughs, to inside the chamber and oven ending approximately 1/4″ from the cell windows. Two photomultiplier tubes (PMTs) with various colored glass filters, interference filters, and polarizers are mounted on the light pipes in the $\pm\hat{x}$ directions. The high voltage on the first dynode of the PMTs is gated to effectively turn them off during the high intensity laser pulses. The fluorescence signal is then digitized 10 μs after each laser pulse with a 14-bit, 2.5 MHz sampling rate data acquisition board (NI-PCI-6132).[4]

A Labview program automates the tasks of recording the fluorescence and housekeeping data. In addition it runs scripts which control the electrode voltages and microwave pulse parameters used for state preparation. The data is recorded both locally and sent over the Internet via TCP/IP to an analysis program. This program can fit the fluorescence data to a model function which determines the quantum beat frequency in real-time, i.e. in less than 10 ms. It also has a variety of user interfaces for averaging and displaying x-y plots or histograms of specified fit or housekeeping parameters in real time.

The EDM experiment is run at the 100 Hz repetition rate of the pulsed Nd:Yag laser. The Q-switch signal from the laser electronics triggers an eight channel pulse generator (BNC Model 565) every 10 ms. Fig. 5.8 shows the timing sequence for a single "shot" of data. The output of the heater waveform from an arbitrary waveform generator (Agilent 33120A) is triggered $\approx 500\,\mu$s after the trigger. The waveform is ≈ 9 ms long and has smooth on and off transitions. A delayed pulse, 9.99 ms after the laser, triggers a four channel pulse generator (BNC 505). Doing so allows us to send a 10 μs gating pulse to the PMTs 3 μs *before* the laser fires. Other channels trigger the data acquisition system and various parts of the microwave system which will be discussed in Section 5.9.

[3]The $v = 0$ vibrational level in the X state and the $v' = 5$ level in the $a(1)$ state are assumed from this point on unless otherwise specified.

[4]We have recently switched to the 14-bit, 100 MHz NI-PCI-6522.

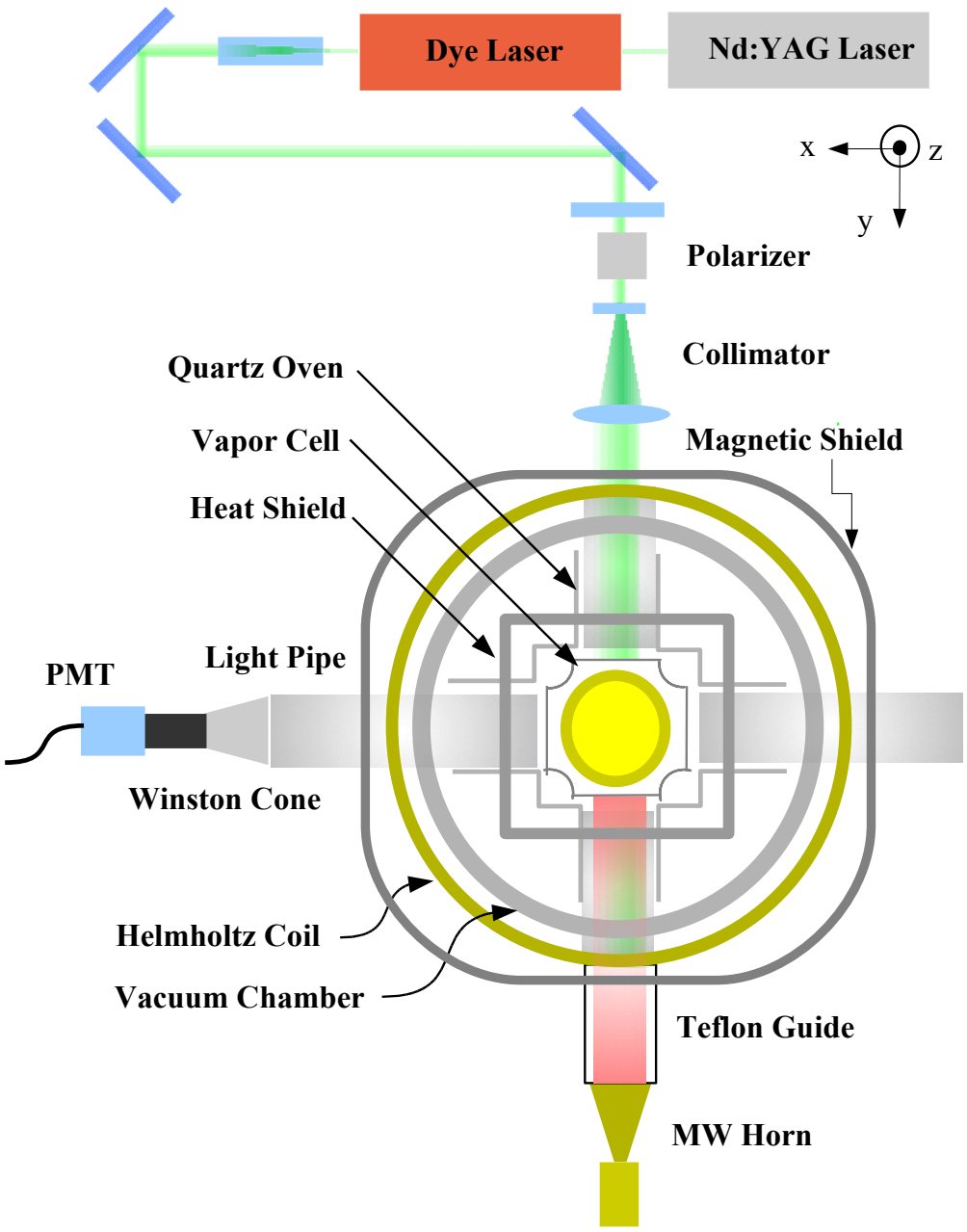

Figure 5.7: Schematic of the optical system. A pulsed Nd:YAG laser, with 100 Hz repetition rate, pumps a Fluorescein dye laser which produces 15-25 mJ, 7 ns pulses at a wavelength of 548 nm. The linear polarization of the laser pulse in the $\hat{x} - \hat{z}$ plane is set by a combination of a high-power half-wave plate and Glan-Laser calcite polarizer. A telescope increases the diameter of the collimated laser beam to 1.5″. Fluorescence is propagated to PMTs via quartz light pipes. Microwaves for driving rotational transitions are coupled to the vapor cell with a solid Teflon guide attached to a quartz light pipe. Helmholtz coils provide a uniform magnetic field inside the magnetic shields surrounding the vacuum chamber.

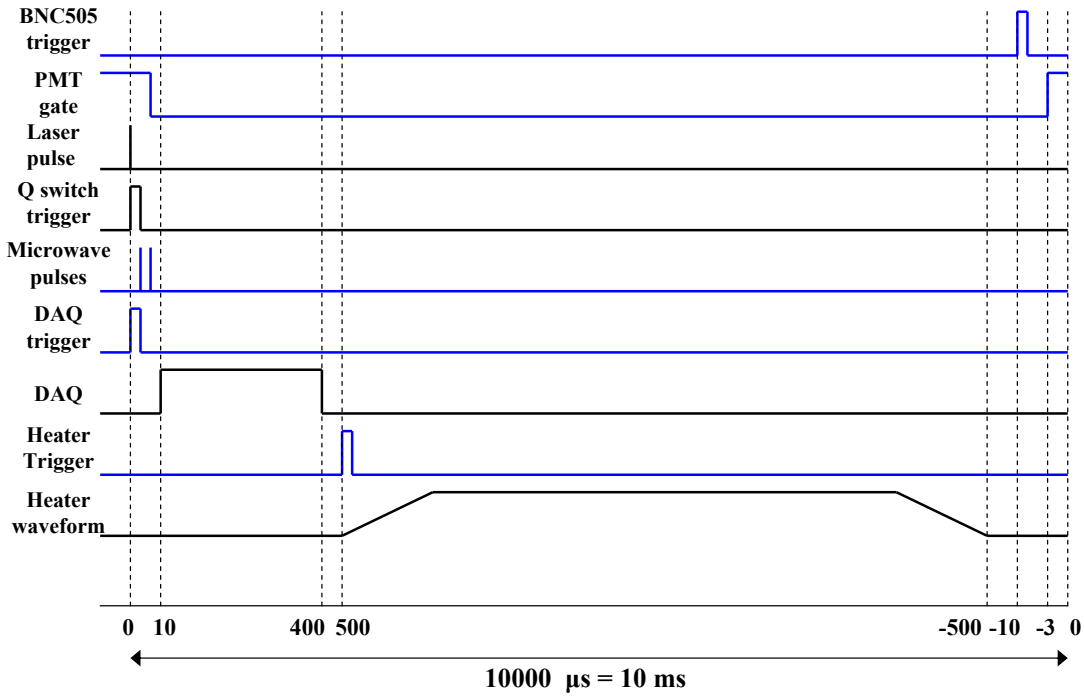

Figure 5.8: Experiment timing schematic. The Q switch trigger from the ND:Yag laser electronics triggers an eight channel BNC 565 pulse generator. Blue pulses are generated by the BNC 565, except for the PMT gates which are generated by the four channel BNC 505 pulse generator. Data acquisition occurs between 10-400 µs. The heater waveform is smoothly ramped on afterwards and then ramped off 0.5 ms before the next laser pulse. The control signals for the microwave system are shown in more detail in Fig. 5.35.

5.2 Electrical connections

In previous generations of the apparatus, one of the limiting factors to experimental run time was the reliability of the electrical connections inside the vacuum chamber. All but the most simple of these failures required removing the oven assembly from the vacuum chamber, a process that generally took close to a full week.

All electrical connections must be made from non-magnetic materials, withstand temperatures of over 700 °C, and withstand contaminants from our tantalum foil oven system. With over 30 connections for the 12 heating elements, 4 electrodes, and 4 or more thermocouples, reliability was key. In the past, we used copper, gold, or tantalum wires, with ceramic beads for insulation. The ceramic beads often shifted, leaving exposed wire that lead to electrical shorts. In addition, over time the wires became extremely brittle. We explored the use of commercial ceramic coated wire as an alternative, but found they all had nickel (i.e. magnetic) coatings.

We now use woven ceramics (Nextel XC) for insulation. Assembly is time consuming. For each connection, several copper wires are threaded through a small ceramic sheath. Two of these bundles are twisted to make a pair and then threaded through a larger ceramic sheath. Crimp-on tantalum or copper connectors, described below, are used to hold the sheaths in place and reduce fraying. The woven ceramics allow flexibility and seem to offer better protection of the wires. Electrical shorts have been eliminated and over several years only one twisted pair has failed.

In the past, to make the electrical connection between the oven foils and wires, tantalum foil tabs were spot-welded to the wires and held against the oven foils with ceramic screws. The other end of the wire was connected to a ceramic terminal block attached to the oven assembly. The spot welds were often the weak point where wires would break. To remedy this, we now use custom-designed crimped connectors (see Fig. 5.9) made of tantalum, for the high temperature oven connections, or copper outside of the oven. The connectors ease assembly and provide strain relief.

5.3 Leakage currents

5.3.1 In-cell leakage currents

Magnetic fields due to stray currents flowing between the electrodes in the vapor cell are a possible source of systematic error. Since the resistance of insulators drops exponentially with temperature,

Figure 5.9: Ceramic insulated twisted wire pairs. All connections to the heaters are made with twisted wire pairs insulated with woven ceramic sleeving. A larger sleeving, seen above, covers the wire pair. A copper or tantalum connector holds the sleeving in place, provides strain relief, and makes the electrical connections more reliable.

isolation of the electrodes is important. Currently, the electrodes are insulated from the guard rings by a beryllium oxide spacer, and the guard rings are insulated from the cell body by a sapphire spacer (see Fig. 5.1).

Leakage currents on the electrodes, guard rings, and cell body are monitored using the five channel floating ammeter circuit described in [81]. High isolation rotary switches have been added to the circuit for selecting the gain of each channel. To determine leakage paths, voltages are applied to each channel one at a time while the other four channels are grounded. The electrical connections from the outside to the inside of the vacuum chamber are made through the center pin of coaxial vacuum feedthroughs. To obtain accurate leakage current readings it is necessary to either apply the same voltage to the coaxial shield of the channel under test or let the shield float. Leakage currents, at the feedthroughs, of up to hundreds of microamps have been observed when the coaxial shield is grounded.

A Labview program ("Leakage current mx.vi") automatically ramps the applied voltage, records the currents, and outputs a log file. The leakage currents are typically on the order of 10 μA for an applied voltage of 150 V at a vapor cell temperature of 700 C (see Fig. 5.10). Leakage paths are usually only seen between an electrode and its guard ring. No currents from the electrodes and guard rings to the cell body have been observed. However, there is usually a substantial difference between the measured currents going into and out of the cell, suggesting there are unidentified leakage paths to ground.

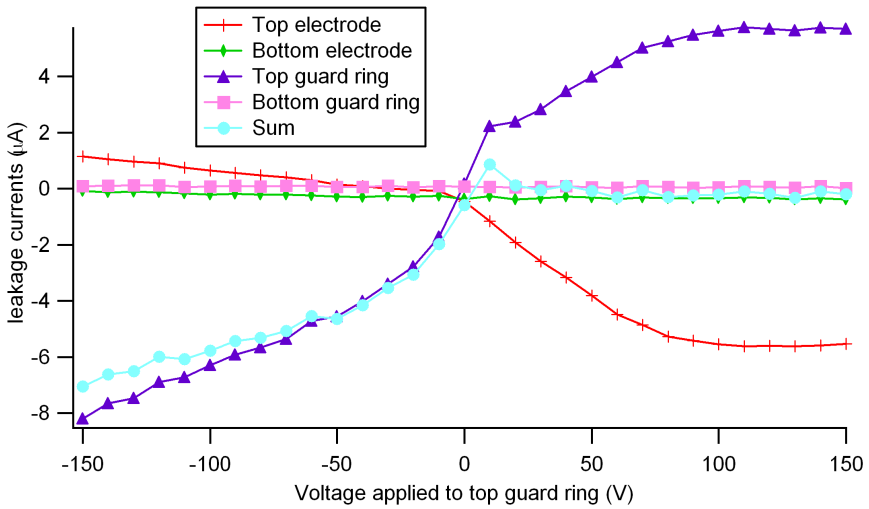

Figure 5.10: In-cell leakage currents. Voltages are applied to the electrodes, guard rings, and cell body one at a time while currents are monitored on all five channels. Shown above is a test with the voltage applied to the top guard ring at a vapor cell temperature of 700 C. For positive voltages the leakage path appears to be to the top electrode, while for negative voltages the path is unknown. Positive currents always refer to currents flowing towards the vapor cell.

The leakage currents are often non-linear in voltage and the shape of the V-I curve depends strongly on the temperature of the vapor cell. One possible explanation for the non-linear currents is thermal emission of electrons, known as thermionic currents, between an electrode and guard ring. For positive top guard ring voltages, the voltage dependence of the current from the top electrode to the top guard ring in Fig. 5.10 is consistent with thermionic emission (also this does not explain the top guard ring currents for negative voltages). At low voltages one expects a $I \propto V^{3/2}$ relationship seen in vacuum diodes [96]. At larger voltages the current emitted per unit area is given by the Richardson equation

$$J = AT^2 e^{-(W-\Delta W)/kT}, \tag{5.1}$$

where $A = 4\pi m_e k^2 e/h^3 \approx 1.2 \times 10^{-6}\,\mathrm{A\,m^{-2}\,K^{-2}}$, W is the surface work function, and $\Delta W = \sqrt{e^3 E/4\pi\epsilon_0}$ with E the applied electric field. The largest electric fields we typically apply between the electrode and guard ring, $E \approx 500\,\mathrm{V\,cm^{-1}}$, give $\Delta W \approx 30$ meV which is negligible compared to the gold work function of $W = 4.0 - 4.9$ eV at 1000 K. A work function of $W = 4$ eV and an electrode area of $\approx 1 \times 10^{-3}\,\mathrm{m^2}$ gives a current of 4 pA. However emission from surface contaminants or contact potentials can reduce the work function. Lowering the work function to 2.5 eV increases the current

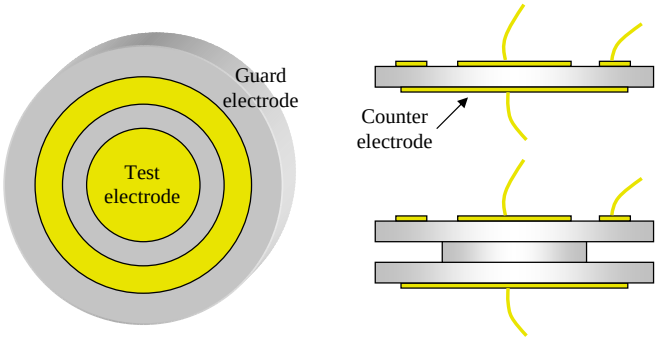

Figure 5.11: Three electrode leakage current measurement. Placing the guard electrode at the same voltage as the test electrode prevents surface currents from the test to counter electrode. Thus measuring the test to counter electrode current determines the volume resistance. The surface resistance is measured through the guard to counter electrode current. Bottom right: A setup to test the theory that making the current path traverse surfaces parallel to the electric field should reduce leakage currents.

to 200 μA![5]

If leakage currents do become a concern in the future, the thermionic emission hypothesis could be tested by looking for leakage currents between two electrodes in a vacuum furnace. If the electrodes are held by mounts which make no contact until outside the hot region of the furnace, surface conduction could be ruled out. If thermionic emission is confirmed, rounding the sharp edges of the cell electrodes could help to reduce locally large electric fields. Other possible improvements are the use of an electrode material with a higher work function, such as platinum, or electrochemical cleaning of the electrodes to remove contaminants. However, if the contamination is due to PbO (e.g. a monolayer on the surface of the electrodes), neither the use of alternative materials nor cleaning will help.

5.3.2 Benchtop leakage current tests

In an effort to understand the source of the vapor cell leakage currents, we measured the high temperature resistivity of sapphire in a ceramic kiln. Fig. 5.11 shows the configuration of the electrodes which were made with gold foil bonded to a 2.5″ diameter, 1/4″ thick sapphire window. A three electrode configuration was needed to separate the effects of surface and volume currents.

[5]Will *et al.* [96] has an excellent discussion of high temperature leakage paths. They observed a surface work function of 2 eV using platinum electrodes which have a 6 eV work function. The lower work function was attributed to contaminant oxides.

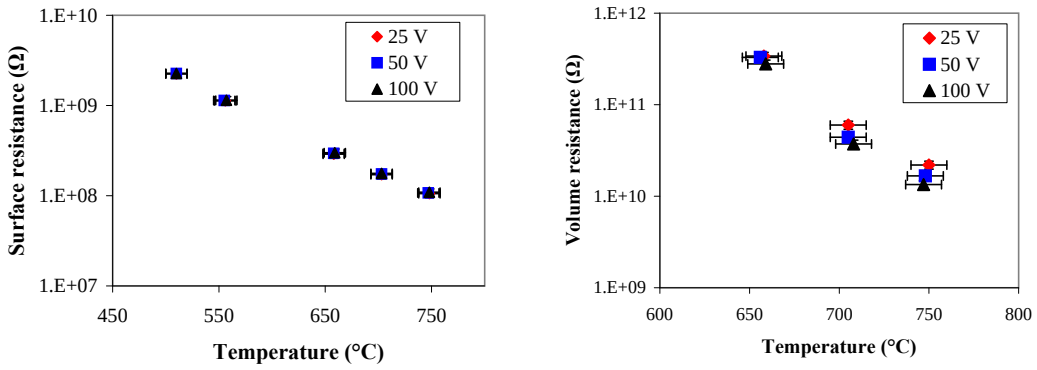

Figure 5.12: Left: Surface resistance of a sapphire window measured in air at several applied voltages. The surface resistivity is ≈ 7 times the resistance. Right: Volume resistance of the sapphire window. The volume resistivity is ≈ 4 cm times the resistance.

A guard electrode surrounds the test electrode. By applying the same voltage to the guard and test electrodes, surface currents can not flow from the test electrode to the counter electrode on the other side of the window. Thus measuring the test to counter electrode current determines the volume resistance. The surface resistance is measured through the guard to counter electrode current. To avoid leakage paths due to poor insulation the electrode wires were threaded through alumina tubes which were suspended by a mount at room temperature outside of the kiln. A digital volt meter (DVM) was wired in series between the electrode under test and ground. The DVM (Fluke 75) voltage reading was divided by its internal resistance, $10^7\ \Omega$, to obtain the current. The lowest possible reading, ≈ 0.5 mV, corresponds to a resistance of $2 \times 10^{12}\ \Omega$ for an applied voltage of 100 V.

The measurements, shown in Fig. 5.12, show that surface currents dominate currents through the bulk of the window. Note that these values of resistivity are orders of magnitude higher than previous measurements in our lab that did not use a guard electrode. However they are still orders of magnitude lower than the data from a careful study in the literature [96]. The difference may be due to the unknown orientation of the crystal axis in our test window. To reduce surface currents we also tried a more convoluted surface (see bottom right of Fig. 5.11), with paths parallel to the electric field, but found this had no discernible effect.

The resistances measured in the test setup were orders of magnitude higher than those currently measured in the vapor cell. This may be due to surface contamination from PbO. It is also very likely that there are leakage paths outside the cell. We did attempt to reduce this possibility by

insulating the electrode wires with beryllium oxide beads and passing them through a quartz tube system (see Jiang [52]) which makes no contact with the apparatus until the tubes are outside of the oven. However, this had little effect on the leakage currents.

5.4 Degaussing system

The magnetic shields are ferromagnetic and thus exhibit hysteresis under changing magnetic fields. To demagnetize the shields we apply a magnetic field, alternating in direction, large enough to saturate the shields and then slowly ramp down the field amplitude to zero. Because the field magnitude required to reach saturation is the same in both directions this procedure should leave the shields completely demagnetized.

To apply the magnetic field we drive 25 amps of alternating current (60 Hz) through each of two 60 turn loops of wire wrapped around the main portion of the shields (see Fig. 5.6). In addition 4 amps of current are driven through loops of 18, 20, and 24 turns wrapped around the endcaps of the first, second, and third shields, respectively. A variac capable of producing 60 amps at 240 volts (Variac Inc. M5011-2S) provides the current. A Labview program ("degaussmx.vi") controls a relay box that switches between the degaussing coils for each shield. After any magnetic field changes, the shields are degaussed from the outermost shield to the innermost shield back to the outermost shield. Note that the coils will melt if not given 5-10 minutes to cool between degaussings.

5.5 Polarization-sensitive detection

In theory, the quantum beat fluorescence is polarized along the $\hat{x}$ axis, while background fluorescence is mostly unpolarized. Past attempts using dichroic polarizers outside the vacuum chamber had shown little background rejection. It was assumed that the light pipes scrambled the polarization of the fluorescence. However, modeling showed that polarization scrambling should be small for our fluorescence angular distribution. After eliminating several sources of birefringence in the apparatus we are now able to use polarization-sensitive detection.

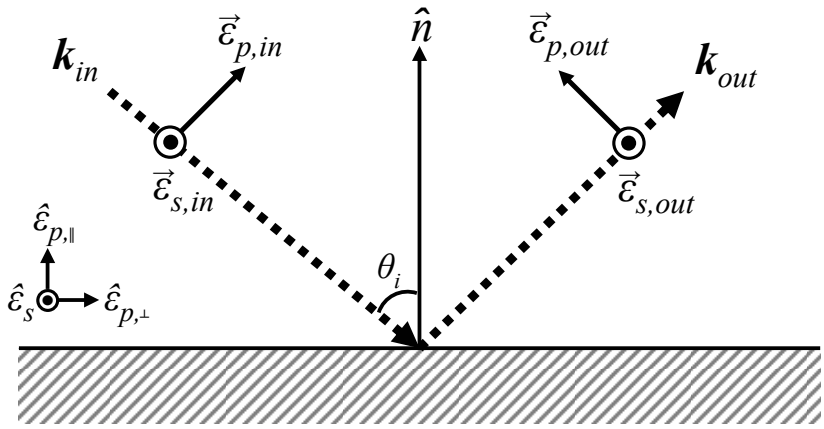

Figure 5.13: Reflection of polarized light. Shown above is the case of external reflection off a metal surface where there is no relative phase shift of the s and p polarization components. In the polarization coordinate basis shown in the lower left, the $\hat{\epsilon}_{p,\perp}$ component flips sign upon reflection while the other two components are unchanged. For internal reflection there can be a phase change between the s and p components dependent on the angle of incidence, θ_i.

5.5.1 Polarization in light pipes

Consider a light ray bouncing off a surface (see Fig. 5.13). From elementary optics [97, 98] there can be a relative phase shift between the electric field component parallel to the plane of incidence, called the p polarization, and the component perpendicular to the plane of incidence, called the s polarization.[6] If the polarization is either completely s or p, the relative phase shift has no physical effect. Polarization scrambling occurs only when both components are present. For external reflections off a metal surface the relative phase shift is zero and all polarizations "follow" the reflected ray as expected. If we define a coordinate system (see Fig. 5.13) for the polarization with $\hat{\epsilon}_s = \hat{k} \times \hat{n}$, $\hat{\epsilon}_{p,\parallel} = \hat{n}$, and $\hat{\epsilon}_{p,\perp} = \hat{n} \times (\hat{k} \times \hat{n})$ then the relations between the incoming and outgoing components for external reflection are

$$\epsilon_s \to \epsilon_s, \quad \epsilon_{p,\parallel} \to \epsilon_{p,\parallel}, \quad \epsilon_{p,\perp} \to -\epsilon_{p,\perp} \tag{5.2}$$

For internal reflections above the critical angle the phase shift is 180 degrees. Below the critical

[6] s stands for the German word for perpendicular, *senkrecht*. This will probably not help you to remember which is which.

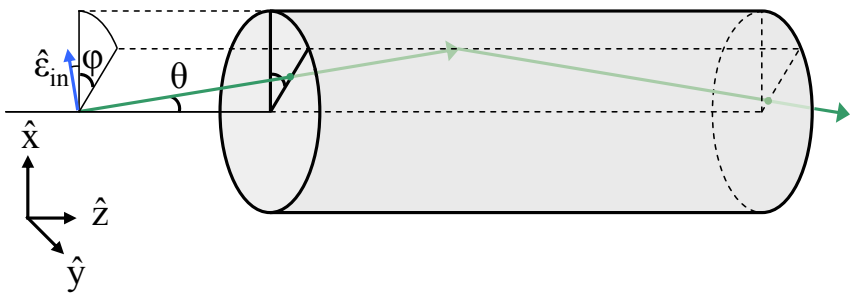

Figure 5.14: Geometry for light pipe polarization calculation. A ray, parameterized by the angles θ and ϕ starts on the light pipe axis with polarization in the $\hat{x} - \hat{z}$ plane. The change in polarization is calculated for a single bounce and the transmission through a polarizer oriented to reject the $\hat{y}$ polarization is calculated.

angle, i.e. total internal reflection, the phase shift varies with angle of incidence [98] as

$$\tan \delta/2 = \cos \theta_i \frac{\sqrt{sin^2\theta_i - (1/n)^2}}{sin^2\theta_i}. \tag{5.3}$$

For arbitrary phase shift the relation between the incoming and outgoing polarization components is then

$$\epsilon_s \rightarrow \epsilon_s, \quad \epsilon_{p,\parallel} \rightarrow e^{i\delta}\epsilon_{p,\parallel}, \quad \epsilon_{p,\perp} \rightarrow -e^{i\delta}\epsilon_{p,\perp} \tag{5.4}$$

In this polarization coordinate basis the magnitudes of the polarization components are unchanged. Therefore if we want to preserve the polarization in the laboratory coordinate system we should align it with one of the polarization coordinate axes. However, only the axis pointing in the direction of the normal, $\hat{\epsilon}_{p,\parallel} = \hat{n}$, is fixed in the laboratory frame for arbitrary ray direction $\hat{k}$. Thus only the normal component of the polarization can be preserved for an arbitrary ray. Since two surfaces with different normals are needed for a light pipe, a polarization preserving light pipe is impossible.

Given the above relations it is straightforward to calculate the polarization of an arbitrary ray after total internal reflection in a light pipe. Fig. 5.14 shows the geometry for rays starting on the light pipe axis, parameterized by the two angles θ and ϕ. To determine the degree of polarization scrambling the initial polarization is set in the $\hat{x} - \hat{z}$ plane, as if the rays had passed through a polarizer on the face of the light pipe oriented to reject the $\hat{y}$ polarization. We then calculate the

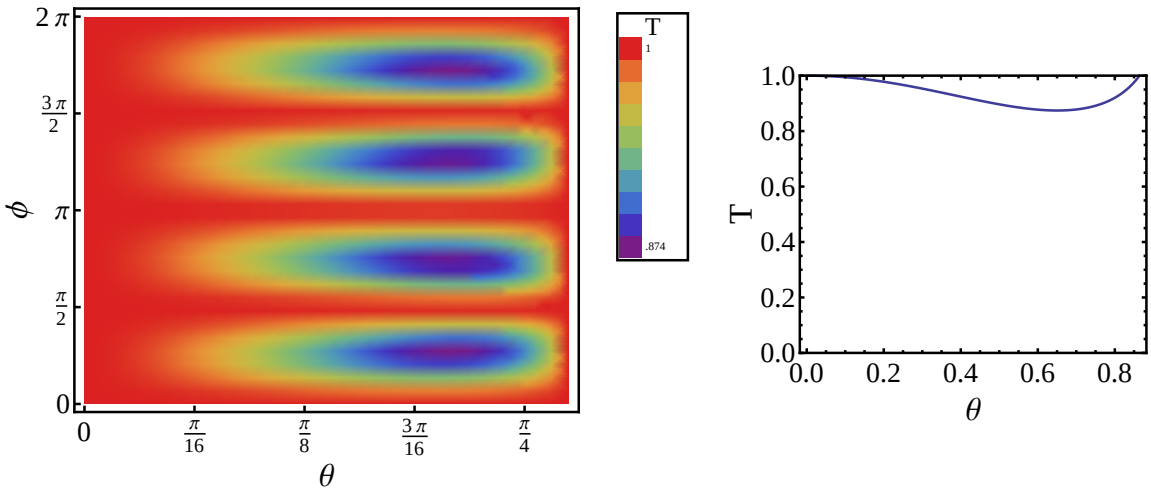

Figure 5.15: Benchtop test of polarization after a light pipe. The color indicates the theoretical transmission through parallel polarizers before and after a light pipe. Note the lowest color corresponds to ≈ 87%. Rays start on the light pipe axis and are parameterized by the angle, θ, between their propagation direction and the light pipe axis and the azimuthal angle, ϕ. Only one bounce is calculated. The angular distribution in our experiment peaks around $\theta = \pi/9$. A cut through the worst azimuthal angle, $\phi = \pi/4$, is plotted on right.

transmission through a polarizer on the exit face of the light pipe also oriented to reject the $\hat{y}$ polarization. Note the transmission is not the square of the component the polarizer passes, in this case $(\hat{\epsilon} \cdot \hat{x})^2$, rather it is one minus the square of the rejected component, $1 - (\hat{\epsilon} \cdot \hat{y})^2$. Fig. 5.15 shows the transmission as determined by Mathematica,

$$T = 1 - \left| \frac{\left(-1 + e^{i\delta}\right) \cos\theta \cos\phi \sin\phi}{\sqrt{\cos^2\theta + \cos^2\phi \sin^2\theta}} \right|^2 . \tag{5.5}$$

Since the fluorescence angular distribution peaks at $\theta \approx \pi/9$ in our experiment this calculation suggests the polarization should be well preserved. However these analytical results neglect multiple bounces and skew rays. A ray tracing program by Amar Vutha predicts that, for our angular distribution, the polarization will be 80 – 90% preserved even after a few bounces.

We confirmed these models by observing light from a diverging source passing through a light pipe with crossed polarizers on either end. If a point source is used, a lens placed after the light pipe will focus the rays from successive bounces into concentric ring patterns (see Fig. 5.16). The rings clearly showed the four-fold pattern of polarization scrambling which increased with each

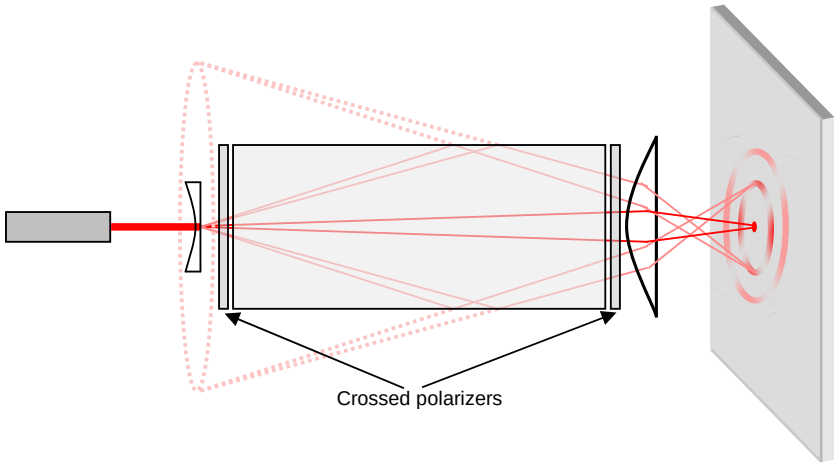

Figure 5.16: Polarization scrambling in a light pipe. Diverging light from a point source can be imaged into a series of concentric rings which increase in size for each bounce in the light pipe. The dashed lines show the virtual source on the left for a a few rays representative of a single bounce. Extinction in the ring images show increasing polarization scrambling for each bounce at 45 degree angles to the crossed polarizers' orientations.

bounce.

5.5.2 Sources of birefringence

After a renewed investigation into sources of polarization scrambling in our apparatus, a few changes were made.

First, the sapphire windows on the vapor cell were replaced with YAG windows. The sapphire windows were cut along the c-axis of the crystal to eliminate birefringence. This was essential to preserve the polarization of the collimated excitation laser. However, even c-cut sapphire is birefringent for light at non-normal incidence. This scrambled the polarization of the fluorescence light, foiling previous attempts at polarization-sensitive detection.

YAG is not birefringent regardless of the angle of incidence due to its cubic crystal structure. It is also one of a few materials that can withstand PbO vapor. To reduce reflections of microwaves [99], the 1.5 mm thickness of the new windows corresponds to roughly half the wavelength, in YAG, of the microwaves used in the experiment, after taking into account the changing refractive index of YAG with wavelength and temperature [100].

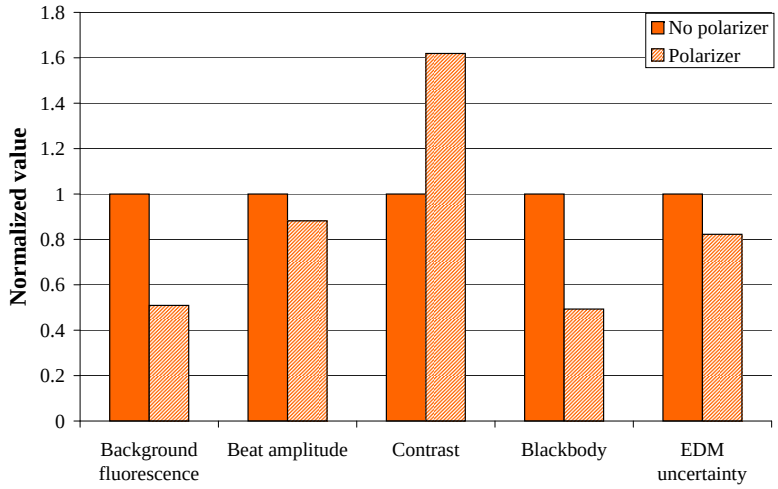

Figure 5.17: Effect of wire grid polarizer. The unpolarized background fluorescence and blackbody radiation are reduced by 50%. The beat amplitude change is consistent with the transmission of the polarizer and loss from Fresnel reflections. Since the EDM uncertainty improves as the square root of signal-to-noise (i.e. beat amplitude to background) the polarizer gives a modest improvement. Even a perfect polarizer would only reduce the uncertainty to $\frac{1}{\sqrt{2}} \approx 70\%$. However, higher contrast will improve the reliability of our fitting program and/or reduce the number of averages needed before fitting.

Second, a small aluminum ring is attached with caulk (Elmer's Stix-all, at Larry Hunter's suggestion) to the light pipes to keep them from being pushed into the vacuum chamber. Atmospheric pressure pushes the light pipes with 44 lbs of force. In the past, o-rings in a compression mount prevented the light pipes from slipping. Observing light through crossed polarizers on the ends of a light pipe confirmed that the compression mounts cause stress-induced birefringence.

We also found that the plastic light pipes used outside of the vacuum chamber are extremely birefringent. Hence the analyzing polarizer must precede them in the optical path. IR blocking colored glass and the CaF_2 windows, previously used to cool the colored glass, are not birefringent.

5.5.3 Observations with wire grid polarizers

For polarization-sensitive detection of the fluorescence we use the relatively new technology of visible wire-grid polarizers which have high transmission (> 90%) and large angular acceptance. Polarizers typically used in laser optics accept a very small solid angle. Dichroic polarizers have large angular acceptance but typically have transmissions below 50%.[7] We use 2″ circular wire-grid polarizers from Moxtek (PPL05C) which have a typical transmission of 92.5% for p-polarized light and 0.52% for s-polarized light. The polarizers are mounted after the heat blocking colored glass filters on the air side of the detection light pipes. As shown in Fig. 5.17, the background fluorescence and blackbody radiation are reduced 50% by the polarizer as expected for unpolarized light. The beat amplitude change is consistent with the transmission of the filter after accounting for Fresnel reflections. Since the EDM uncertainty improves as the square root of signal-to-noise (i.e. beat amplitude to backgrounds) the polarizer gives only a modest improvement. Even a perfect polarizer would only reduce the uncertainty to $\frac{1}{\sqrt{2}} \approx 70\%$. However, the higher contrast should improve the reliability of our fitting program and/or reduce the number of averages needed before fitting.

5.6 Oven and heat shielding

In the past, the tantalum foils of the vapor cell oven become brittle after a couple months of usage and eventually broke. Replacing the foils required complete disassembly and reassembly of the apparatus which took a few weeks of time. In search of a more reliable material we explored alternatives to tantalum.

Other metals were eliminated because of either their magnetic properties, high vapor pressure at 700 C, incompatibility with the quartz oven parts, higher brittleness, or excessive cost. We tried nickel foils, assuming that heating them above their Curie point ($\approx 500\,^{\circ}\mathrm{C}$) would render them non-magnetic. The foils were less brittle but evaporated over time. The heating element alloy KANTHAL (a FeCrAl alloy) required less power to reach a given temperature (see Fig. 5.20) but we were concerned by its considerable outgassing in vacuum, even after annealing in air.

Previously, up to 4 kW of power was needed to heat the oven and vapor cell to 700 C. To put this

[7] In exploring polarization-sensitive detection for shorter wavelengths we did find one company, Boulder Vision Optik, that produces dichroic polarizers with a peak transmission > 80% at 530 nm and good transmission in the 400-500 nm range.

in perspective, given the total surface area of the heater foils, $A \approx 1800\,\mathrm{cm}^2$, and the total emissivity of tantalum, $\epsilon_{1000\,\mathrm{K}} = 0.14$ [101], the power output for a completely unshielded oven with the foils at 700 °C is only 1.4 kW. If we assume heat shielding reduces the power load by a factor 1.5-2 (see below) the observed power load implied a foil temperature of 1100-1200 C. This caused several problems. First, it was difficult to find stereo amplifiers that would not overheat when run for weeks at a time at the powers required, even though the foils were designed to have impedances similar to audio speakers. Second, as mentioned above, the tantalum foils would eventually become brittle and break. Lastly, blackbody radiation from the ovens dominated our signal, even with colored glass and narrow band interference filters.

The original oven design had three layers of heat shielding made from clear quartz painted with high emissivity paint. In the second version opaque quartz replaced the clear quartz.[8]The power required by the oven to reach a given temperature greatly increased. Tantalum and copper foils were wrapped around the quartz heat shields in an effort to reflect the heat back towards the cell. This helped somewhat but the power required was still more than in the original oven.

To gain some understanding of the physics, we consider a simple model for the heater consisting of one hot and one cold infinite plane at temperatures $T_{H(C)}$ with emissivities, $\epsilon_{H(C)}$ and reflectivities $\rho_{H(C)}$. Blackbody body radiation from plane H gives a power flux of $\epsilon_H \sigma T_H^4$. If we denote the total flux of power leaving each plane as $J_{H(C)}$ (as shown in Fig. 5.18), plane H also reflects back ρJ_C towards plane C. By conservation of energy the difference in the two fluxes must be equal to the flux, F, leaving plane C to the right. Thus we have the three relationships

$$J_H = \epsilon_H \sigma T_H^4 + \rho_H J_C \tag{5.6}$$

$$J_C = \epsilon_H \sigma T_C^4 + \rho_C J_H \tag{5.7}$$

$$F = J_H - J_C \tag{5.8}$$

If the planes are opaque, i.e. $\epsilon = 1 - \rho$, then solving for F gives

$$F = \frac{\sigma\left(T_H^4 - T_C^4\right)}{1/\epsilon_H + 1/\epsilon_C - 1} = \epsilon_{HC}\sigma\left(T_H^4 - T_C^4\right), \tag{5.9}$$

[8]Both the high emissivity paint and opaque quartz were used in attempt to bathe the vapor cell in more spatially uniform blackbody radiation.

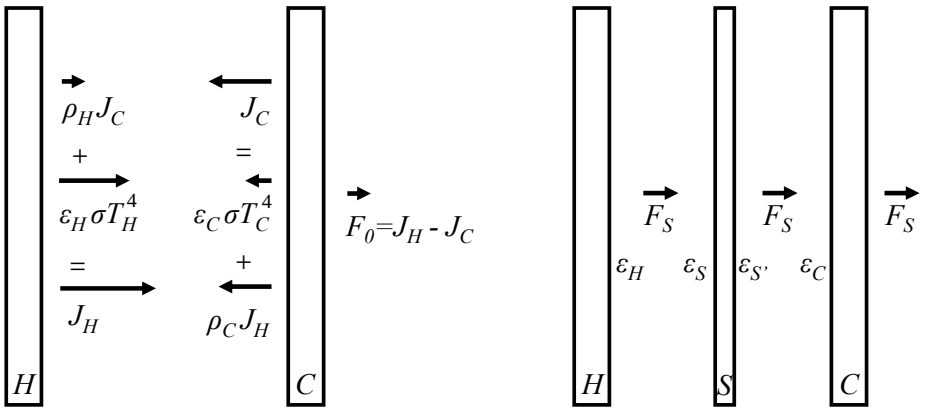

Figure 5.18: Heat shields. On left: One hot (H) and one cold (C) opaque infinite plane are in thermal equilibrium. The total flux of power radiated from the $H(C)$ plane, $J_{H(C)}$, is the sum of the blackbody power radiated, $\epsilon_{H(C)}\sigma T_{H(C)}^4$, and the power reflected from incoming radiation, $\rho_{H(C)}J_{C(H)}$, where $\epsilon_{H(C)}$ and $\rho_{H(C)}$ are the total emissivity and reflectance, respectively. On right: When a shielding layer with possibly different emissivities, ϵ_S and $\epsilon_{S'}$, of its two sides is inserted between the hot and cold planes the flux is reduced to F_S.

where we have used an effective emissivity, $\epsilon_{ij} \equiv \frac{1}{1/\epsilon_i + 1/\epsilon_j - 1}$. To examine heat shielding we will consider H to be our oven and C to be a perfect room temperature blackbody with $\epsilon_C = 1$. In this case $\epsilon_{HC} = \epsilon_H$ and

$$F_0 = \epsilon_H \sigma \left(T_H^4 - T_C^4\right). \tag{5.10}$$

Now consider what happens if a third plane, S, is placed between the other two. For generality let the side of S facing H have emissivity ϵ_S , while the side facing C has emissivity $\epsilon_{S'}$. The net flux going from plane H to plane S must be equal to the net flux from plane S to plane C therefore

$$F_{H\to S} = F_{S\to C} = F_S = \epsilon_{HS}\sigma \left(T_H^4 - T_S^4\right) = \epsilon_{S'}\sigma \left(T_S^4 - T_C^4\right). \tag{5.11}$$

Eliminating T_S gives

$$F_S = \frac{\epsilon_{S'}\epsilon_{HS}}{\epsilon_{S'} + \epsilon_{HS}} \sigma \left(T_H^4 - T_C^4\right), \tag{5.12}$$

and the shielding factor is

$$SF = F_0/F_S = \frac{\epsilon_H(\epsilon_{S'} + \epsilon_{HS})}{\epsilon_{S'}\epsilon_{HS}}. \tag{5.13}$$

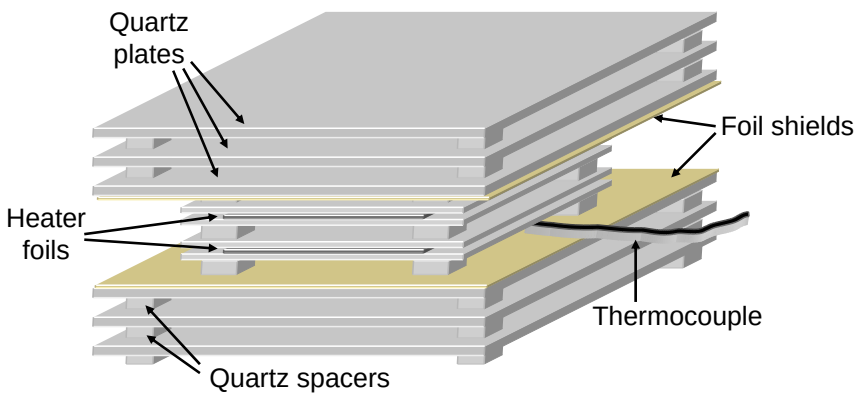

Figure 5.19: Mock oven for heat shield testing. Two heater foils were placed in the middle of a stack of opaque quartz plates separated by quartz spacers. Various metal foils or plated pieces were placed on top of the quartz plates nearest to the oven. Thermocouples recorded the temperature the "oven" reached for a given input power.

Now we can consider several limiting cases. First, consider $\epsilon_S = \epsilon_{S'} \ll \epsilon_H \ll 1$, i.e. the shield is a good reflector. In this case $\epsilon_{HS} \approx \epsilon_S$ and $SF = 2\epsilon_H/\epsilon_S$. Using the total emissivity of tantalum for the hot plane, $\epsilon_H \approx 0.15$ [101, 102], and assuming a shield reflectivity of 95% gives $SF = 6$. One can show similarly that n such shields give $SF = 2n\epsilon_H/\epsilon_S$.

Next consider $\epsilon_S = \epsilon_{S'} = 1$, i.e. S is a blackbody. In this case $\epsilon_{HS} = \epsilon_H$ and $SF = 1 + \epsilon_H \approx 1.15$. Clearly reflective shields should work significantly better than high emissivity shields. One can show that n blackbody shields give $SF = 1 + n\epsilon_H$.

Last, consider the case where one side of S is reflective and the other side is a blackbody. For either orientation one can show that $SF = \epsilon_H/\epsilon_R$, where ϵ_R is the emissivity for the reflective side. A high emissivity side thus reduces the effectiveness of a reflective shield by a factor of two.

Returning to our apparatus, we hypothesize that the foil shields did not help significantly because thermal insulation between the layers of the heat shields was poor. The mounting of the foils was necessarily crude so there were points of contact between foils of adjacent layers (see Fig. 5.2). However, this could be remedied by using a metal plating instead of foil. To test this idea we made a mock version of the oven in a small test chamber (see Fig. 5.19). We focused on gold because of its high reflectivity, low vapor pressure, and resistance to oxidation. We tried gold coating quartz and alumina but found that it scratched easily. The difficulty of assembling the oven precludes gentle handling of the heat shields. Next we tried gold coated copper plates. At high

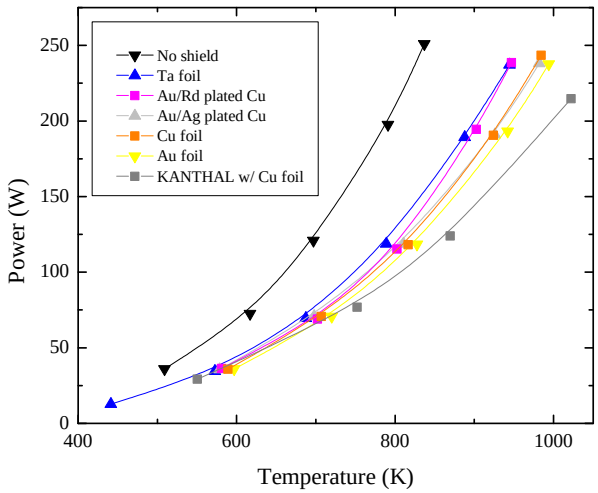

Figure 5.20: Tests of metal foil heat shields. The power required by the mock oven to reach a given temperature is lessened by nearly a factor of two using foil heat shields. However, this is less shielding than predicted by theory. The lowest curve is a test using KANTHAL rather tantalum for the heating elements. Although KANTHAL is more efficient, it was never used because it outgasses significantly in vacuum.

temperatures (above ≈ 800 K) the gold migrated into the copper. A gold plating company suggested a barrier layer of rhodium or silver to prevent the gold diffusion. Neither of these helped. Fig. 5.20 shows a summary of our tests. The metal shields lessened the power required to reach a given temperature by a factor of two, which was less shielding than expected. This was probably partly due to the shielding not completely surrounding the foils, which is also a problem in the actual oven. In retrospect, lack of thermal insulation may have also contributed, even in the test setup. Even though the thermal conductivity of quartz is low, a $300 - 400$ K drop across the four spacers gives a heat flow of over 50 W, which was a significant fraction of the input power. In the oven used in the EDM apparatus, alumina nuts were used to separate the shield layers. This certainly contributed to heat loss as alumina has a conductivity nearly 10 times that of quartz.

In the end, we abandoned the heat shields and now use a combination of ceramic fiber board and blankets (Cotronics 360HS and 370) to insulate the oven (see Fig. 5.4). Despite being extremely porous, testing has shown that they are compatible with the typical vacuum pressure of $\approx 1 \times 10^{-6}$ Torr in our apparatus. Their thermal conductivity is over 10 times smaller than that of quartz, which is considered a good insulator itself. The temperature, T_c, on the cold side of the

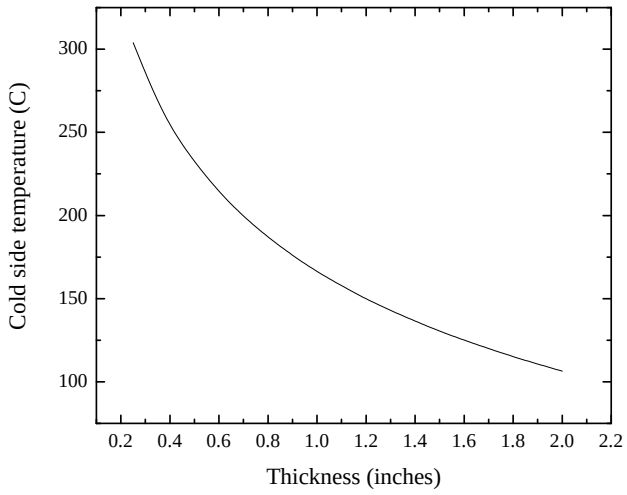

Figure 5.21: Thermal insulation. Cold side temperature versus thickness for a Rescor 360 board with a hot side temperature of 700 °C. An average thermal conductance of $C = 0.7\,\mathrm{W\,m^{-1}\,K^{-1}}$ is assumed based on the datasheet from Cotronics, Inc.

ceramic board can be estimated by equating the blackbody power radiated per unit area on the cold side to the power per unit area that thermally conducts through the board,

$$\frac{(T_h - T_c)C}{L} = \sigma T_c^4, \tag{5.14}$$

where L is the thickness of the board, T_h is the hot side temperature, and C is the thermal conductance. Fig. 5.21 shows the cold side temperature as the board thickness is varied with $T_h = 700$ °C. For even 1″ of insulation the outside temperature drops to 150 °C. If the outside of the oven is treated as a 10″ blackbody cube, this corresponds to a power output of only 700 W. Doubling the thickness reduces the power by a factor of 5. Tests in a small vacuum chamber confirmed that ceramic insulation gave higher temperatures for the same power input compared to reflective shielding (see Fig. 5.22).

Using the ceramic fiber board and blanket insulation reduced the oven power load by a factor of four. In addition the blackbody background was reduced by a factor of 5-10 which allowed us to switch to wider interference filters for fluorescence detection. Putting tantalum foils around the ends of the light pipe nearest the cell also helped to block blackbody radiation going directly from the heater foils into the light pipe. The blackbody background seen in the detectors is now typically

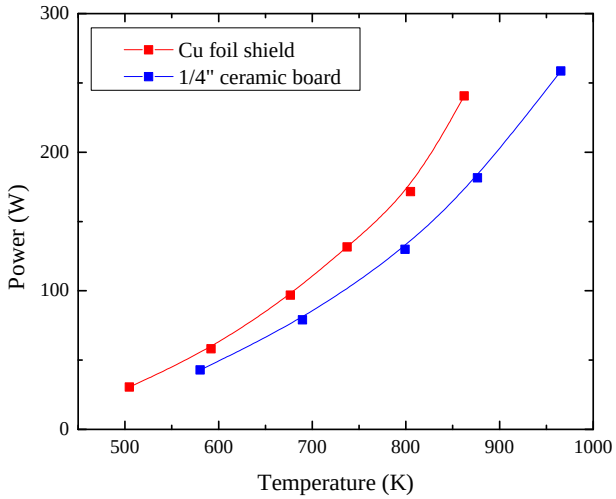

Figure 5.22: Ceramic insulation versus metal foil heat shield. An insulating 1/4″ thick ceramic fiber board lowered the oven power requirement to reach a given temperature versus a copper foil heat shield. In theory the power drops an addition factor of 5 for each doubling of the insulation thickness. 1 3/4″ of fiber board are used in the actual apparatus.

similar in size to the fluorescence signal.

5.7 Spectral filters

The large angular spread and source size of our fluorescence make the use of interference filters tricky. The bandpass of an interference filter shifts with angle of incidence. Thus even with monochromatic radiation a larger bandpass is needed to collect all angles of incidence.

In the past, modeling had suggested that narrow bandpass interference filters should give the optimal signal-to-noise, i.e. the optimal ratio of fluorescence collection versus blackbody background. Several changes necessitated a re-evaluation. First, the improved insulation of the oven reduced the blackbody background substantially. Second, with a new gating circuit[9]the PMTs recover from scattered light well enough that we can detect fluorescence at the same wavelength as the excitation laser pulse. This allowed us to switch from excitation along $|X, v = 1\rangle \rightarrow |a, v' = 5\rangle$ transition to excitation on the $|X, v = 0\rangle \rightarrow |a, v' = 5\rangle$ transition. The larger population of the ground vibrational level increased the signal size by a factor of 3. Lastly, experience had shown that the signal and

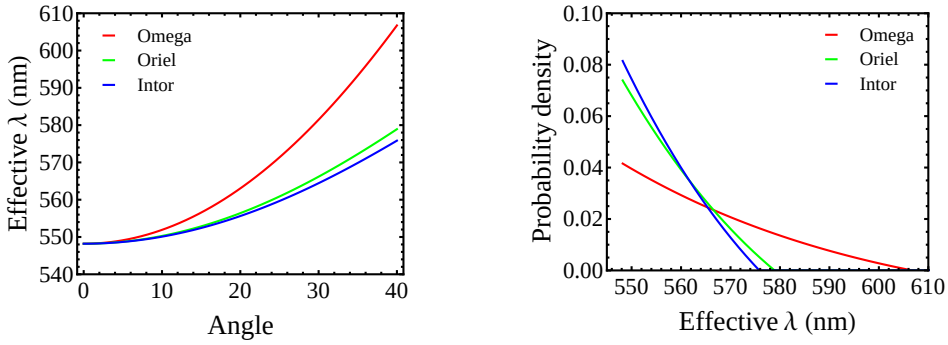

Figure 5.23: Effective wavelength and probability density for interference filters. On left: The effective wavelength for 548 nm light passing through an interference filter at varying angles of incidence. On right: The probability distribution assuming the angular distribution of light is $\propto \sin(2.25\theta)$, which peaks at 20 degrees. The various filters show different responses because of their effective indices of refraction.

background transmissions predicted by a previous ray tracing simulation for interference filters did not agree with experimental observations.

To determine the optimal filter we first took data with several interference filters of varying central wavelength and bandwidth. The signal size, background size, beat contrast, and beat frequency fit uncertainty (aka EDM uncertainty) were recorded for each filter. In addition, the same values were recorded with the second PMT using a fixed filter combination. To correct for changes in experimental conditions, e.g. cell temperature changes, laser frequency drift, etc., all parameters were normalized to the reference PMT data.

Next we tried two methods for modeling the effect of interference filters. The first method created a simple filter function based on the manufacturer's specified central wavelength, transmission, and bandwidth. We then calculated the "effective" wavelength for a given angle of incidence,

$$\lambda_{eff} = \frac{\lambda_0}{\sqrt{1 - \left(\frac{\sin\theta}{n_{eff}}\right)^2}}, \tag{5.15}$$

where n_{eff} is the effective index of refraction of the interference filter. Given the probability distribution for the angle of incidence of the fluorescence we can calculate the probability distribution

[9]The current circuit is based on [103] (see discussion in [81]). Hunter Smith is currently working on a PCB layout of a new, more modular version [104].

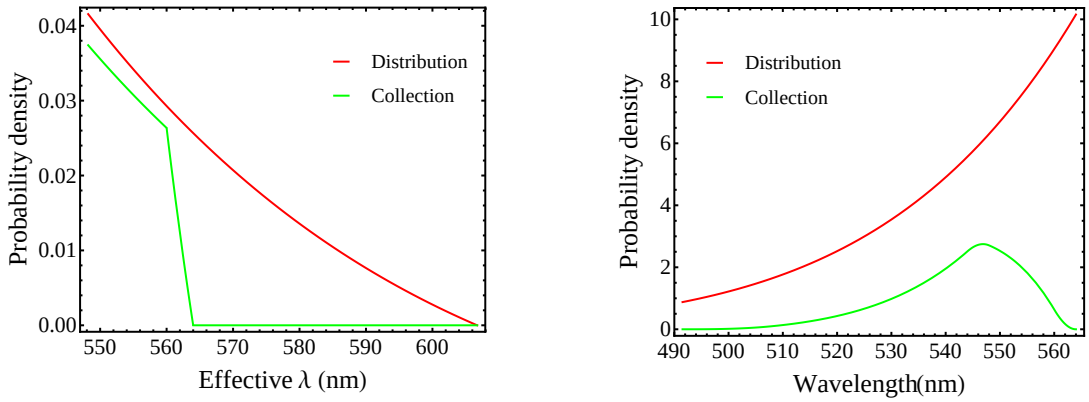

Figure 5.24: Modeled transmission of an Omega interference filter. On left: The red curve is the modeled probability distribution for fluorescence from a 548 nm line with an angular distribution peaked at 20 degrees. The green curve is the probability distribution multiplied by the model transmission of the interference filter, in this case an Omega 16 nm bandpass filter centered at 554 nm. The total transmission of 44% is the area under the green curve. On right: The red curve is the modeled blackbody distribution. The green curve is the transmission of the blackbody through the filter integrated over the angular distribution.

for the effective wavelength,

$$p(\theta)d\theta = p(\lambda_{eff})d\lambda_{eff} \Rightarrow p(\lambda_{eff}) = p(\theta)\frac{d\theta}{d\lambda_{eff}}. \tag{5.16}$$

Fig. 5.23 shows the effective wavelength and probability distribution for 548 nm light from the $|a, v' = 5\rangle \rightarrow |X, v = 0\rangle$ transition. We assume the fluorescence angular distribution is $\propto \sin(2.25\theta)$, which peaks at 20 degrees. The total transmission of a filter is given by

$$T = \int T(\lambda)p(\lambda_{eff})\, d\lambda. \tag{5.17}$$

Fig. 5.24 shows the result for one filter along with a similar calculation of the blackbody transmission. The blackbody background was assumed to have a spectrum given by the Wien law. The slope of the intensity versus wavelength in previous observations [81] of the blackbody was consistent with a temperature of 1200 K. We also tried the typical vapor cell temperature of 1000 K for comparison. Because relative transmissions will be compared in the end, the results are only sensitive to the slope of the blackbody curve and not the absolute height.

Fig. 5.25 shows a relative comparison between the modeled predictions and experimental ob-

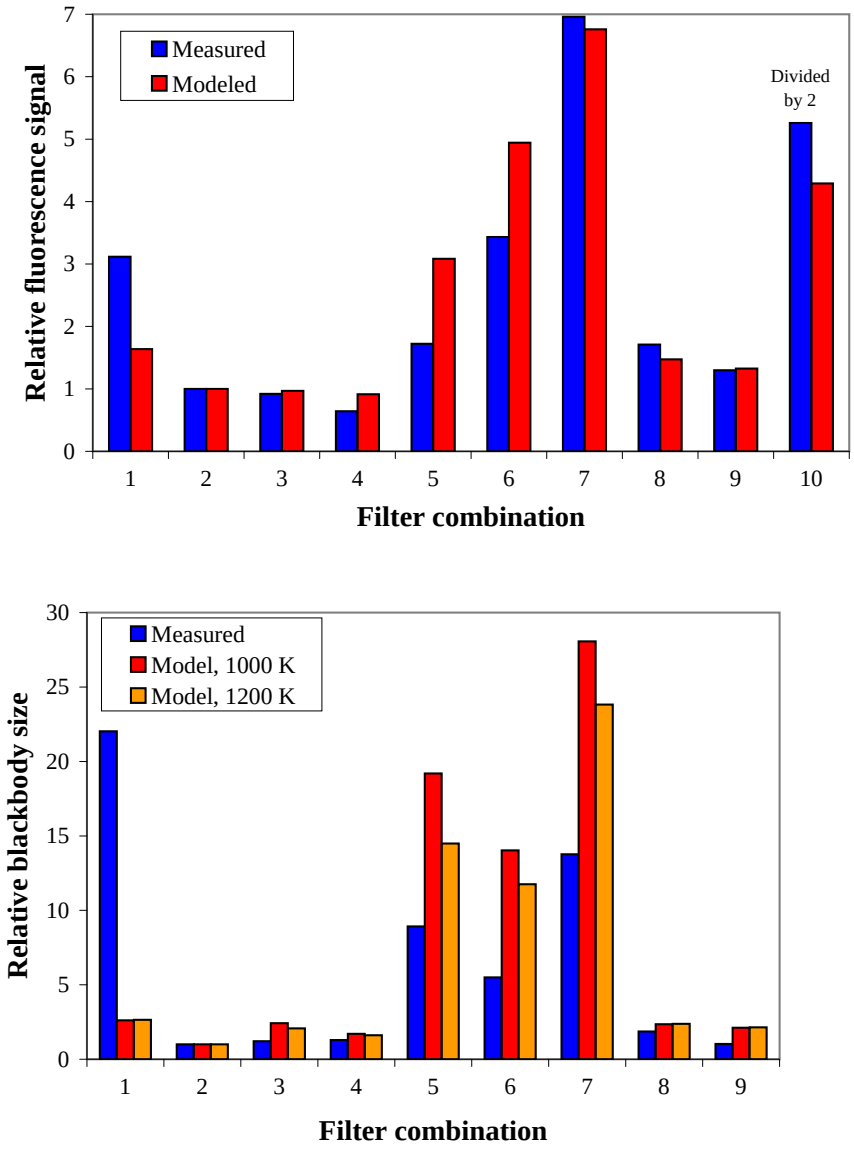

Figure 5.25: Top: Fluorescence signal sizes. Bottom: Blackbody background sizes. All measured values are first normalized to the signal size measured simultaneously with a reference PMT, then scaled to the measured filter 2 value. All modeled values are scaled to the modeled filter 2 value. Filters(company, central wavelength in nm, bandpass in nm, peak transmission): 1 - Omega, 554, 16, 90%; 2 - Intor, 550.5, 8.3, 58.5%; 3 - Intor, 570, 9, 62%; 4 - Oriel, 560, 10, 60%; 5 - Intor, 587, 29, 83%; 6 - Intor, 571, 36, 83%; 7 - Omega, 554, 104, 90%; 8 - 1 and 7; 9 - 1 and two of 7; 10 - No filters with PMT gain reduced but corrected for.

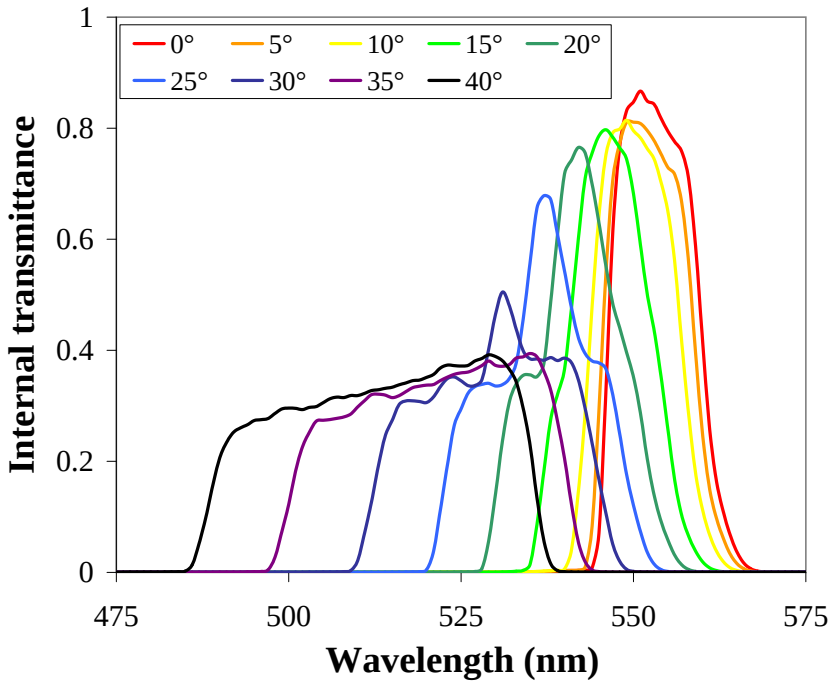

Figure 5.26: Transmission of IF at varying angles of incidence. The angle of incidence changes both the central wavelength, bandwidth, and transmission of an interference filter. Shown above is the measured transmittance, i.e. the transmission corrected for Fresnel reflections, for an Omega 16 nm bandpass filter centered at 554 nm with a nominal peak transmittance of 90%.

servations for a variety of filters. Both the modeled and experimental values are scaled to their respective values for filter 2. The agreement between model and experiment is not particularly convincing. The enormous blackbody for filter 1, the Omega 16 nm bandpass filter, was expected because it was designed to be used with a broader filter to block the red and infrared.

After this comparison it was not clear that we could reliably predict the transmission of the fluorescence and blackbody from a filter's specifications. In particular we were concerned that the modeling of the interference filters was inaccurate for large angles of incidence. We also had some concerns that blackbody radiation in the near infrared might be leaking through the combination of colored glass and interference filters normally used in the experiment.

To reduce our uncertainty we set up an automated system for measuring filter transmission versus incidence angle. A photodiode recorded the transmission through an interference filter mounted on a computer controlled rotation stage. The wavelength was scanned using a computer

controlled monochromator with a xenon arc lamp as the source light. We measured transmission curves for a few colored glass filters to verify the setup. The results agreed well with their known transmission curves. The interference filter transmissions were measured out to 1000 nm to allow modeling of blackbody leakage outside the filter passband. The measured transmission curves did change significantly at large angles of incidence (see Fig. 5.26).

Next, we performed the same analysis as above, only now numerically integrating over the measured transmission curves. In addition we included the effects of colored glass IR blocking filters. Past measurements had used KG4, but we hoped the sharper cutoff of BG39 and BG40 might reduce the blackbody. For the blackbody analysis we took into account the quantum efficiency of our PMT versus wavelength. Fig. 5.27 shows the results of this analysis grouped by color glass filter.

The agreement is excellent for both signal and blackbody sizes, except for the 16 nm bandpass Omega filter which still shows anonymously high blackbody transmission with the KG1 and KG4 colored glass. The good agreement for BG39 and BG40 colored glass, which completely block light above 600 nm, suggests the blackbody leaks through at longer wavelengths. However, the measured filter transmission is essentially zero up to 750 nm at which point the PMT quantum efficiency is specified to be negligible.

Fig. 5.28 shows the measured and modeled EDM sensitivity for the various filter combinations.[10] The optimal sensitivity is with the large bandpass filters which can collect fluorescence from decays to both the $v = 0$ and $v = 1$ vibrational levels in the ground state (about 50% of the decays go to each level). The gray bar is a model filter (based on scaling of the measured transmissions) where we have varied the central wavelength and bandwidth in an attempt to find the ideal filter. In the past we used the 104 nm bandpass Omega filter with two 16 nm bandpass Omega filters (which would be worse than the purple bars in the figure). Based on these results switching to the 104 nm bandpass Omega filter by itself increased our EDM sensitivity by a factor of 2. In addition, it does not appear we could design a custom filter that would give a further improvement.

[10]Note this data was taken at zero electric field and assumed the uncertainty in the frequency fits during the EDM measurement would be two times larger, as it is when using the beat erasure method (see Section 6.3.2).

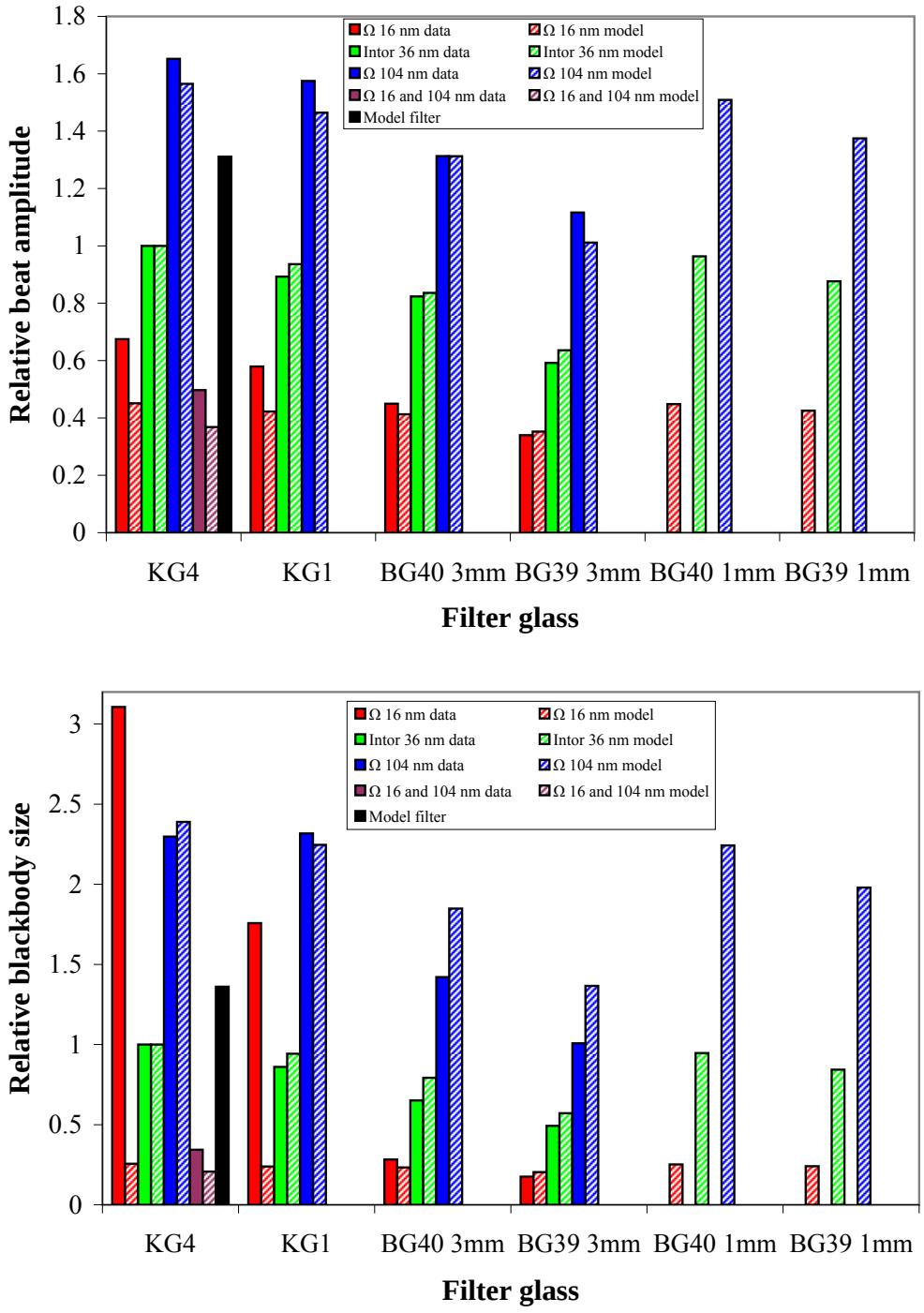

Figure 5.27: Modeled fluorescence and blackbody sizes are based on the measured transmission of the interference and colored glass filters over wavelength and angle of incidence. Both modeled and experimental values are scaled to their respective values for the Intor 36 nm bandpass filter. The experimental values are also first scaled to a reference PMT with a fixed filter combination.

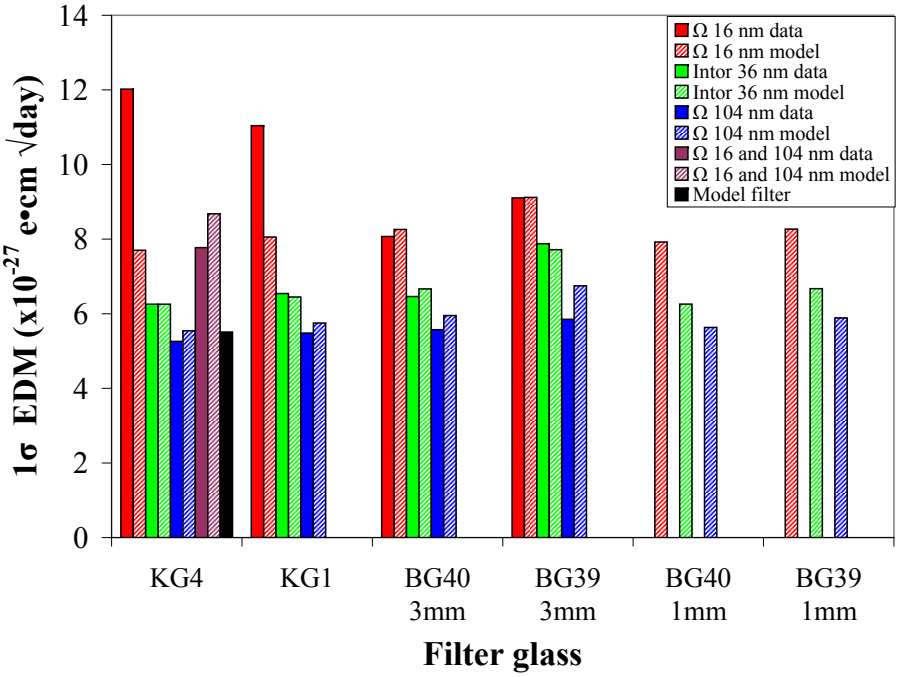

Figure 5.28: The measured EDM sensitivity is based on a measurement at zero electric field and assumes the quantum beat frequency uncertainty will increase by a factor of 2, as it does using the beat erasure method. Modeled values are based on the scaling of the relative signal and blackbody sizes in Fig. 5.27 and the measured EDM sensitivity using the Intor 36 nm bandpass filter.

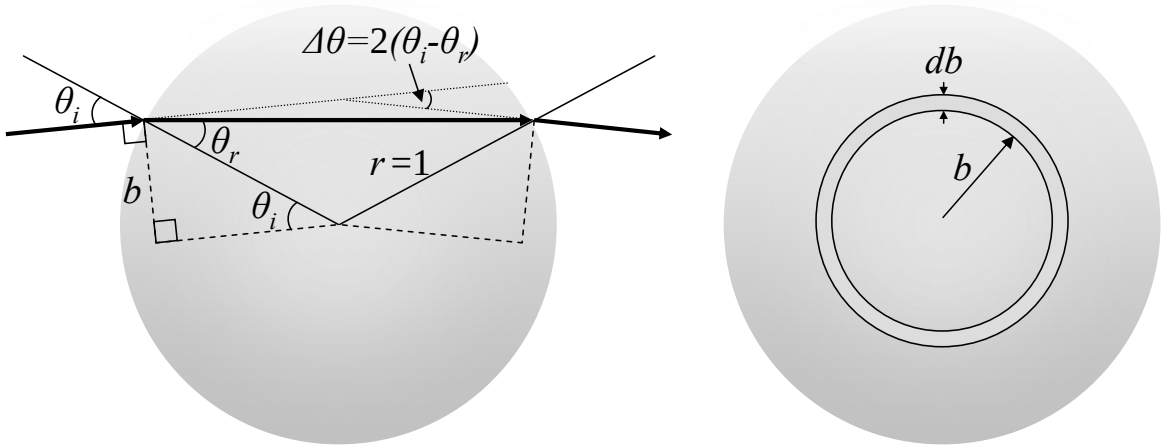

Figure 5.29: Scattering via refraction in a sphere. On left: A ray refracts twice as it enters and exits the dielectric sphere. On right: The probability of impact parameter b is the ratio of the annulus to the total cross-sectional area.

5.8 Christiansen filters

We also explored the possibility of using Christiansen filters [105]. Unlike interference filters, the bandpass of Christiansen filters does not change with angle of incidence. We hoped that an extremely narrow Christiansen filter would pass the fluorescence from one decay transition, which is monochromatic but has a large angular spread, and reject the broadband blackbody radiation.

A Christiansen filter consists of a liquid filled with scatterers, typically small spheres of glass. If the index of refraction of the liquid is adjusted, usually via temperature, to match the index of the scatterers, light passes through unimpeded. If the indices differ, the light is deflected slightly due to refraction. After many deflections the light can be completely scattered. In real materials there is dispersion, i.e. wavelength dependence, of the index of refraction. Therefore for any given temperature there will be a small range of wavelengths where the indices are close enough that the light is transmitted with little scatter. A larger difference in the dispersion of the two materials gives a narrower filter.

Hunter Smith tried implementing a filter using a long tube filled with glass spheres (30-270 micron Duraspheres from Mo-Sci) and index matching liquids (Cargille) without success. To get a rough idea of the requirements for a practical filter we considered a simple analytic model. The

basic principle is to determine the average angle scattered by a single sphere and then treat many such scatters as a random walk in angle. From Fig. 5.29, the angles of incidence, θ_i and refraction, θ_r, for a ray with impact parameter of b on a sphere of radius 1 are

$$\begin{aligned} \theta_i &= \sin^{-1} b \\ \theta_r &= \sin^{-1} \frac{n_i}{n_r} \sin\theta_i = \sin^{-1} \frac{n_i}{n_r} b. \end{aligned} \tag{5.18}$$

For small differences in the index refraction, $n_i/n_r = n_i/(n_i + \Delta n) \approx 1 - \Delta n/\bar{n}$. The total change in angle is then

$$\begin{aligned} \Delta\theta &= 2(\theta_i - \theta_r) \\ &= 2\left[\sin^{-1} b - \sin^{-1}\left(b - b\frac{\Delta n}{n}\right)\right] \\ &\approx 2\frac{d}{db}(\sin^{-1} b) b\frac{\Delta n}{n} = \frac{2b}{\sqrt{1-b^2}}\frac{\Delta n}{n}. \end{aligned} \tag{5.19}$$

where in the last step we have approximated the difference as a derivative.[11] From Fig. 5.29 we can see that the probability distribution of b for a sphere with radius, $r = 1$, is

$$p(b)db = \frac{2\pi b\, db}{\pi r^2} = 2b\, db \tag{5.20}$$

The average change in angle is then

$$\overline{\Delta\theta} = \int_0^1 \Delta\theta\, p(b)\, db = 4\frac{\Delta n}{n}\int_0^1 \frac{b^2}{\sqrt{1-b^2}} = \frac{\Delta n}{n}\pi. \tag{5.21}$$

If we consider a random walk in angle with a step size of $\overline{\Delta\theta}$, we would expect that after N such steps the angular distribution should be a Gaussian with variance, $\sigma_N^2 = N(\overline{\Delta\theta})^2$. For a random walk of varying step sizes with variance, σ_θ^2, the resulting distribution is a Gaussian with variance, $\sigma_N^2 = N\sigma_\theta^2$. This agrees well with an exact calculation by Roberts and Ursell [106] who considered a random walk on a sphere consisting of angular steps with a given probability distribution. Fig. 5.30

[11] This approximation is good for $b\Delta n/n \ll 1 - b$. For large $\Delta n/n$ the divergence near $b = 1$ causes later results to be correct to within a factor of a few.

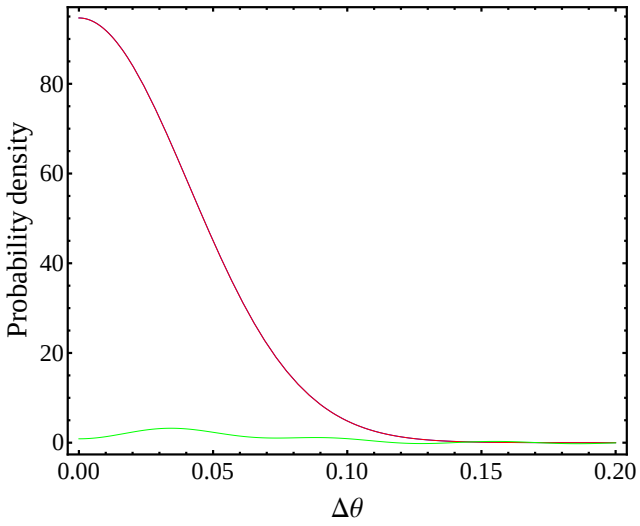

Figure 5.30: Random angular walk. Blue: First 100 terms of the exact solution for 10000 scatters with an index of refraction difference of 10^{-3}. Red: Gaussian approximation. Green: Difference between the approximation and exact solution [106] times 100.

shows the excellent agreement between the Gaussian approximation,

$$p_{Gauss}(\Delta\theta) = \frac{1}{\pi\sigma_N^2} e^{-\Delta\theta^2/\sigma_N^2} \tag{5.22}$$

and the first 100 terms (which are needed for convergence) of the exact result,

$$p_{exact}(\Delta\theta) = \sum_n \frac{2n+1}{4\pi} e^{-\frac{1}{4}n(n+1)\sigma_N^2} P_n(\cos\Delta\theta), \tag{5.23}$$

where P_n are Legendre polynomials, $N = 10000$ steps, and $\Delta\theta = \pi\Delta n/n \approx 3 \times 10^{-3}$. The Gaussian has a variance of one half the step size variance which may be due to the two-dimensional nature of the angular walk.

The next step is to relate the angular probability distribution to an experimental observable. As a crude estimate, we take the transmission of the filter to be the total probability that a ray is scattered less than some angle, α, determined by the detection solid angle. In one example in the literature [107], the incident light was collimated from a point source, passed through the filter, then focused onto the slit of a spectrometer. In this case the detection focal length and the slit size would

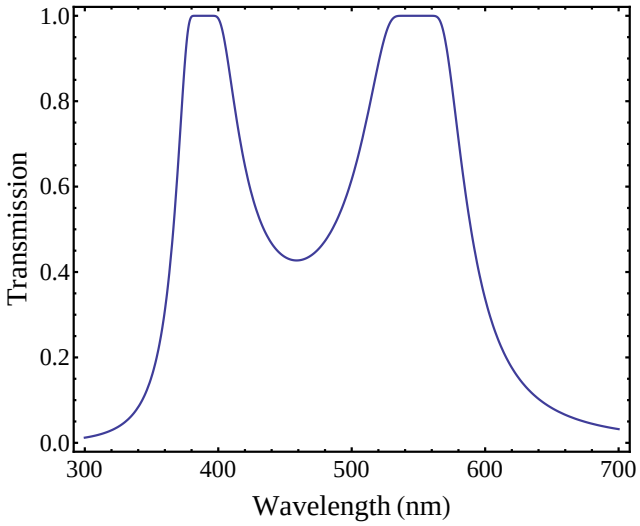

Figure 5.31: Theoretical transmission of the Christiansen filter test setup assuming a 30 cm long tube filled with 30 μm glass spheres and an index matching liquid from Cargille, 5,000 scatters, and a detection angle of 0.2 radians.

determine the solid angle. Using (5.22) with $\alpha \ll 1$ the transmission is

$$T = \int_0^{2\pi} \int_0^{\alpha} \frac{1}{\pi\sigma_N^2} e^{-\Delta\theta^2/\sigma_N^2} \sin(\theta)\, d\theta\, d\phi \approx 1 - e^{-\alpha^2/\sigma_N^2} \tag{5.24}$$

For $\alpha > \sigma_N$, i.e. a detection angle larger than the scatter, T rapidly approaches one. For $\alpha \ll \sigma_N$ the transmission decreases as α^2/σ_N^2 giving a dependence of

$$T \propto \frac{1}{\sigma_N^2} \approx \frac{1}{\pi^2 N(\Delta n/n)^2} \propto \frac{n^2}{dLr^2} \left(1 \Big/ \frac{dn}{d\lambda}\right)^2, \tag{5.25}$$

where we have used $N = dL\pi r^2$, d is the number density of the scatterers, L is the filter length, r is the scatterer radius, and $dn/d\lambda$ is the differential dispersion. This dependence agrees with Clarke [108], who treat the Christiansen filter as a series of phase scatterers on an incoming plane wave and calculate the outgoing coherent power. However, they predict an exponential rather than asymptotic decay.

Returning to our experimental efforts, Fig. 5.31 shows the expected transmission for the 30 cm long tube filled with 30 μm glass spheres and an index matching liquid, assuming 5,000 scatters and a detection angle of 0.2 radians. The filter rejection in the visible is quite small which could explain

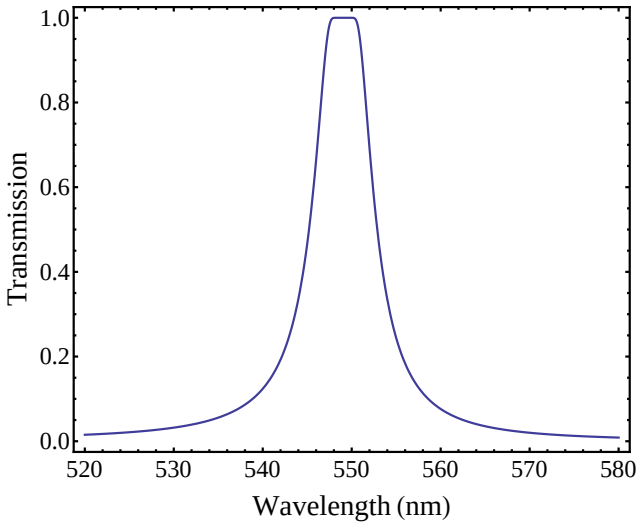

Figure 5.32: Theoretical transmission of a 1-m long filter filled with 10 micron spheres, assuming 100,000 scatters, 10 times the dispersion of the test setup, and a detection angle of 0.75 radians. Even in this extreme case, the FWHM of 10 nm is hardly better than an interference filter.

why no effect was observed. The index matching liquid was used to avoid the need to control the temperature of the tube. However the difference in dispersion between the glass spheres and the liquid was quite small. Other filters in the literature [107, 109] have used liquids with an order of magnitude higher dispersion.

For the PbO experiment, the fluorescence comes from an extended source with an angular distribution that peaks at ≈ 0.4 radians. With this large angular spread, using a Christiansen filter that acts as a light pipe might be advantageous. For a quartz light pipe any light that enters through the end of the light pipe must undergo total internal reflection on the sides.[12] Thus only rays that have been scattered by the filter above the critical angle will be lost. For a long filter, this obviates the need to have the filter and detector diameter increase as the source light diverges. Fig. 5.32 shows the best case result for a one meter long filter, filled with 10 μm beads and a liquid with 10 times higher dispersion. The bandwidth is no better than our interference filters.

For a practical Christiansen filter for the PbO experiment, a higher dispersion is needed. Hunter Smith did briefly explore the use of rare earth solutions as the liquid. In theory their dispersion near absorption lines can be very large. Sarah Bickman had previously identified several absorption lines

[12] This is true for any material with an index of refraction greater than $\sqrt{2}$.

near our fluorescence wavelength when she explored the possibility of using rare earth solutions as absorptive filters [81].

In summary, although the passband of Christensen filters have no dependence on the angle of the incoming light, their typical usage in the literature was either for collimated light or light from a point source. In both cases a lens and a spatial filter on the detection side can reject light scattered by a very small angle. An extended source, such as in our experiment, requires a larger scattering angle which in turn requires a filter length that is not practical.

5.9 Microwave system

In our experiment microwaves are used mainly for driving rotational transitions in the $a(1)$ state. Initially we planned to use two frequency chirped microwave pulses to prepare the EDM state (see Section 6.3.1). To preserve quantum beat coherence the microwave transitions must take place much faster than a quantum beat period, which is typically on the order of microseconds. In addition the central frequencies of the double pulses are changed at the 100 Hz repetition rate of the EDM experiment . After finding no reasonably priced (< 60k$) commercial microwave generators that could produce double pulses with large frequency modulation on these time scales, we built our own system.

The basic principle of our system is to transfer the enormous flexibility and low cost of arbitrary waveform generators (AWG) at radio frequencies (RF), ≈ 31 MHz in our case, to microwave frequencies. We do this by a combination of frequency multiplication and mixing. This method certainly sacrifices some stability and spectral purity compared to commercial microwave generators. However, RF generators are typically stable to a ppm and with microwave line widths on the order of tens of kilohertz in our experiment, this is good enough.

The hardware of our system (see Figs. 5.33 and 5.34) is controlled by a Labview program ("set mw mx.vi"), written by Yong Jiang and myself, which lets the user select pulse widths, delays, separation times, amplitudes, central frequencies, frequency chirp amplitudes, frequency chirp directions, and polarization axes. The Labview program also automates real-time data collection, averaging, analysis, logging, and display while varying any of these parameters (or several other experimental parameters) over a specified range.

Fig. 5.35 shows an example timing diagram of the microwave system. First, the software

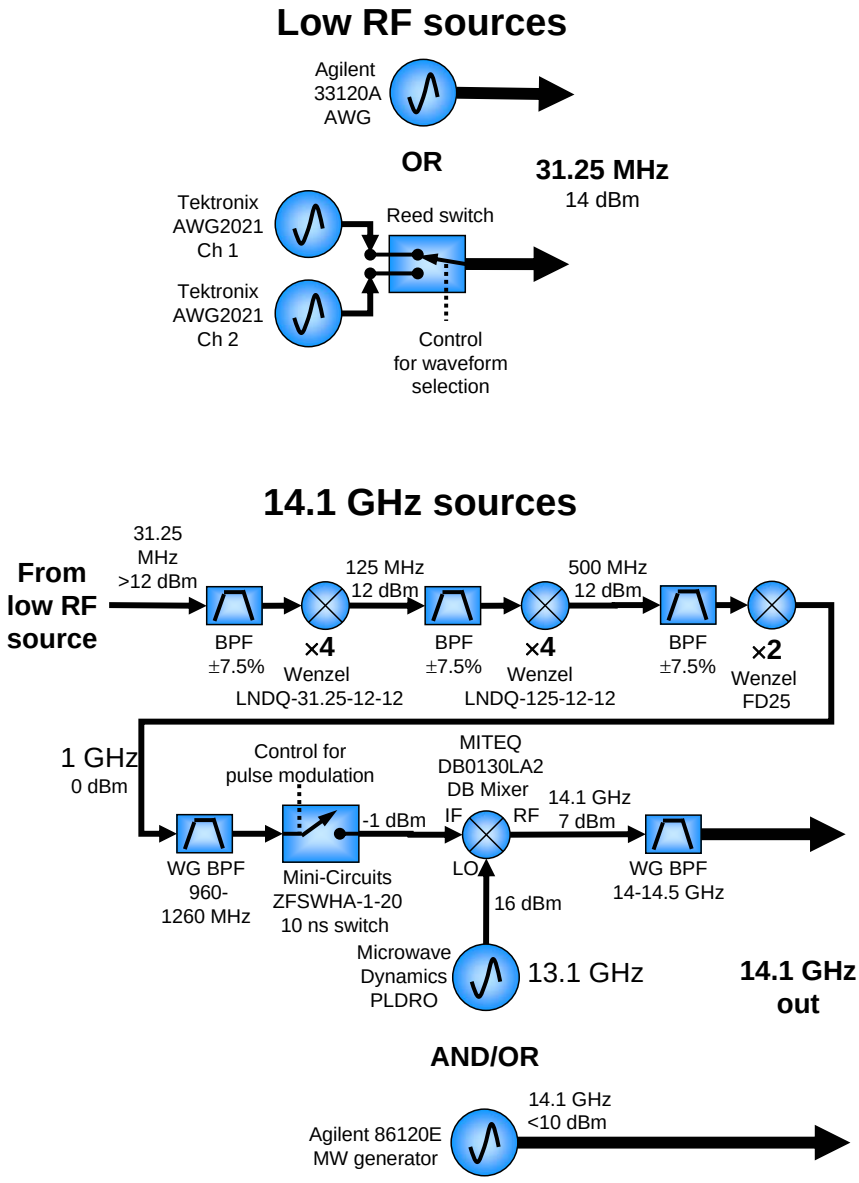

Figure 5.33: Microwave system schematic. A RF arbitrary waveform generators produces an initial frequency modulated waveform at 31.25 MHz. This waveform is frequency multiplied to 1 GHz, pulse modulated with a switch, and then mixed with a 13.1 GHz microwave reference to produce output pulses at 14.1 GHz. An Agilent microwave generator can also produce the 14.1 GHz pulses or be used as an independent second channel.

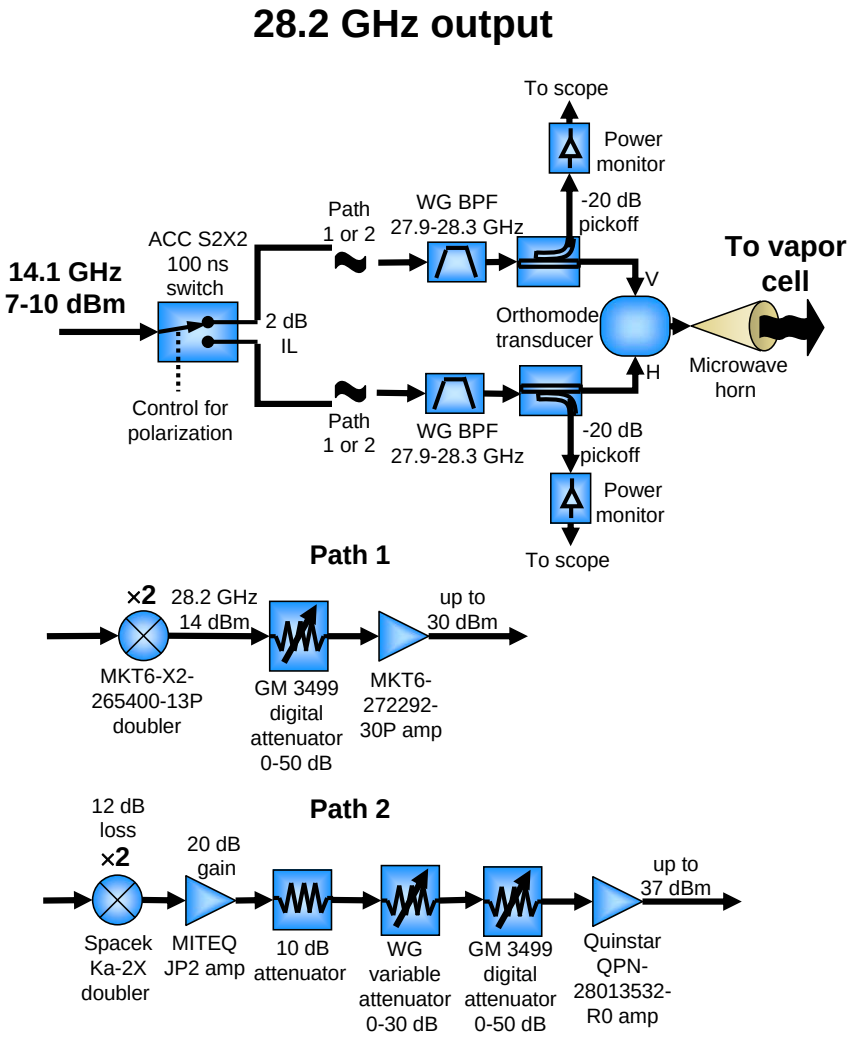

Figure 5.34: Microwave system schematic. For single channel operation a high speed switch selects a path for each pulse. Each path has a frequency doubler, digitally controlled attenuator to set the output amplitude, and a high power amplifier. Directional couplers pick off a fraction of the output for monitoring. An orthomode transducer couples each path to orthogonal microwave polarizations in a circular waveguide. A conical horn outputs the microwaves.

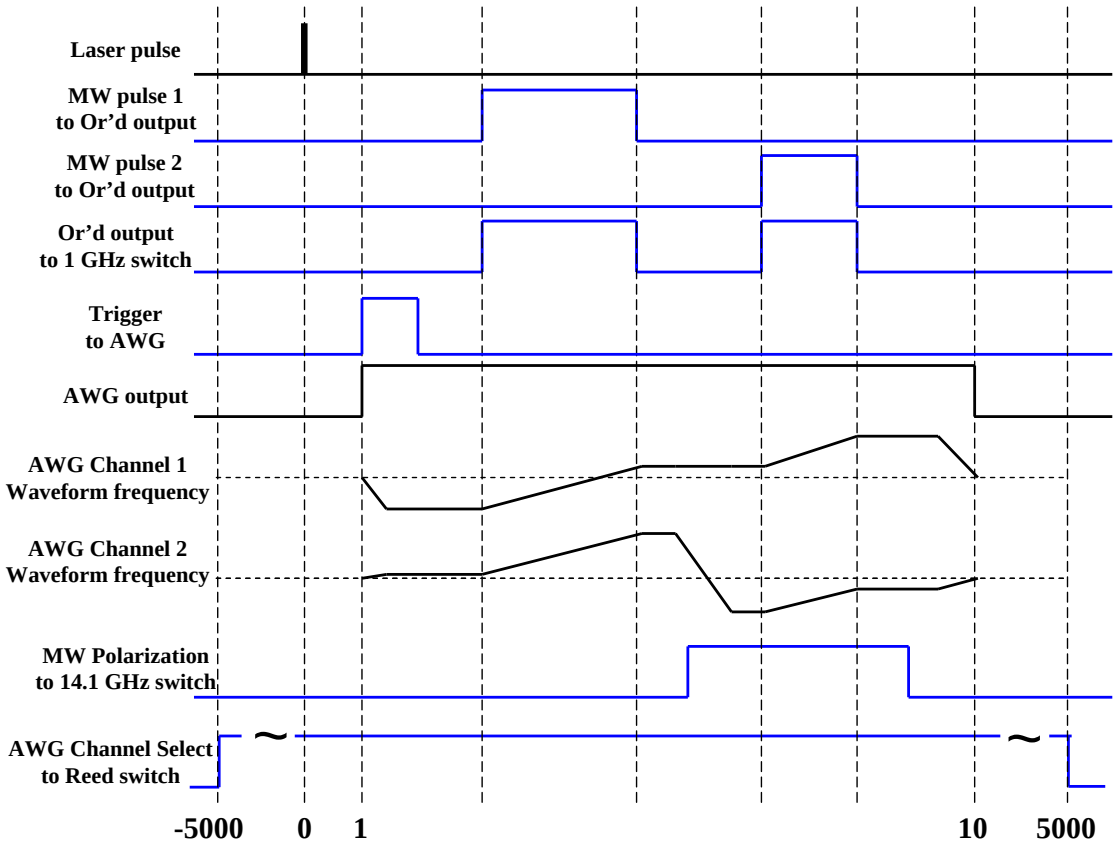

Figure 5.35: The timing of the microwave system is achieved through programming of a BNC 565 8-channel pulse generator which is triggered by the Nd:YAG laser (blue pulses come from the BNC 565). The output of the two microwave pulse channels are added with a logical OR. When using an RF AWG as a source, a long sine waveform is output and pulse modulated by a switch at 1 GHz after frequency multiplication. Each AWG channel can be programmed with a different time dependence of the microwave frequency. The waveforms are programmed so that the frequencies are smoothly varied to minimize distortion. A pulse to a Reed switch 5 ms before the laser pulse selects one of the two AWG channels for output. A pulse to a switch at 14.1 GHz can select separate polarizations for each of the two pulses in a waveform. If the Agilent microwave generator is used as a source the OR'd microwave pulse channel is sent to the pulse modulation input and the RF AWG sends waveforms similar to those shown above to the frequency modulation input. All timing and frequency parameters are set by the user in a Labview program.

generates a quasi-continuous sine waveform with the desired time dependence of the microwave frequency and sends it to an AWG. The central frequencies at this point are in the range of 31.25 ± 2.5 MHz. For EDM data we wish to alternate preparing the molecules oriented with or against the electric field each laser shot. This requires using a different set of frequencies for the microwave pulses every other shot. To do this we load separate waveforms into two channels of a Tektronix AWG2021. The AWG is triggered to output the waveforms after every laser shot. A digitally controlled single pole-double throw (SPDT) Reed switch is used to select one channel for output each shot.

Next, the waveform passes through two frequency quadruplers and a doubler. Before each stage there are filters with a bandpass of ±7.5% of the central frequency to eliminate harmonics. A waveguide bandpass filter removes harmonics at the output frequency of ≈ 1 GHz. At this point a digitally controlled Mini-Circuits switch (ZFSWHA-1-20) is used to set the pulse widths, delays, and separation. In the past we had used pulsed waveforms at the input of the multiplication chain but found that the sharp edges in the waveform caused distortion and propagation delays on the output because of the bandpass filters. The Labview program now generates longer waveforms that start and end well before and after the desired output pulses. In addition, for frequency changes between pulses or for frequency chirps the waveform is programmed to have a continuous phase. Discrete jumps in phase also generated distortion.

Next, a 13.1 GHz phase-locked dielectric resonator oscillator (Microwave Dynamics) serves as the local oscillator for a double balanced frequency mixer (MITEQ DB0130LA2). After mixing with the 1 GHz waveform, the output at 14.1 GHz goes through a waveguide bandpass filter to eliminate the 12.1 GHz sideband. A digitally controlled SPDT microwave switch (Advanced Control Components S2X2) sends the waveform along one of two paths which correspond to different microwave polarizations at the output. The switch is fast (< 100 ns switching time) so that the polarization can be switched between the two microwave pulses.

Each path has a frequency doubler, a digitally controlled attenuator which sets the output power, and some combination of fixed attenuators and amplifiers. At the output are two high power solid state amplifiers, a Millitech MKT series and a Quinstar QPN series, with 1 dB saturation powers of 1 watt and 5 watts, respectively. Note these amplifiers are designed only for microsecond scale pulses and should not be used continuously at full power.

After the high power amplifier each path passes through a waveguide filter and a 20 dB direc-

tional coupler. The coupler picks off 1% of the power which goes to a diode detector for monitoring. Each path goes into a port of an orthomode transducer, a device which converts microwaves from two rectangular waveguides into orthogonal linear polarizations in a circular waveguide. From here the microwaves exit through a conical horn and then propagate through a solid cylindrical piece of Teflon attached to one of the the quartz light pipes in our apparatus. Both the Teflon and quartz light pipe act as oversized waveguides for the microwaves.

There are several alternative configurations for our microwave system when we do not need as much flexibility.

For single pulses without frequency modulation or the quasi-continuous operation used in absorption measurements (see Section 7.4) we use a single channel Agilent 33250B AWG as our 31.25 MHz source. In this case the AWG outputs a continuous sine wave at the specified frequency and the switch at 1 GHz generates the pulse modulation. The frequency shift keying (FSK) feature of this AWG is convenient for quickly changing the microwave frequency between laser shots.

We also initially used an Agilent 86120B microwave generator as our 14.1 GHz source. This generator accepts a pulse modulation input and an analog frequency modulation input. Because the central frequency of the generator can only be changed every 20 ms we used the frequency modulation input for changing both the central frequencies and chirps of the microwave double pulses. In this configuration the Labview program sends waveforms to the RF AWG for the pulse modulation and frequency modulation inputs of the Agilent microwave generator. This method of using the frequency modulation worked fairly well but, as discussed in Jiang [52], the central microwave frequency shifted systematically for large frequency chirps. In addition the frequency modulation input had a limited bandwidth of 10 MHz and the frequency modulation depth was limited to 16 MHz. By using an AWG the modulation depth in our system is limited only by the bandpass filters to ≈ 300 MHz. The modulation frequency is limited by the output frequency of the AWG to ≈ 40 MHz.

The Agilent microwave generator could also be used as an independent second channel. Simultaneous pulses could be used to produce circular polarization, although the reference frequencies of the generators would have to be locked to each other. Two channel operation could also be useful for stimulated Raman adiabatic passage (STIRAP) which requires two overlapping pulses of orthogonal polarizations.

5.10 Dye laser system

The original laser system in this experiment was extremely simple compared to most AMO experiments (see Section 5.1 and Fig. 5.7). This was mostly due to the high temperature of our vapor cell. Large Doppler widths for the molecular transition lines meant our laser frequency stability and linewidth requirements were modest.

To quickly reprise, our system started with a frequency doubled Nd:YAG laser (Spectra GCR 190-100) which generated 100 mJ pulses with 6-7 ns width at a repetition rate of 100 Hz. The YAG pumped a dye laser (Lambda Physik Scanmate 2E) which used Fluorescein 548 dye to produce $\approx 10\,\text{ns}$, $15-25$ mJ pulses with a wavelength of 548.2 nm. An intracavity étalon in the dye laser nominally limited the frequency width of the pulses to 1 GHz.

5.10.1 Laser line width problem

We had long suspected that the frequency widths of the dye laser pulses were much larger than the 1 GHz manufacturer's specification. Scanning the dye laser over rotational lines in the $a(1)$ state produced a fluorescence excitation spectrum with line widths closer to 2 GHz. Some of the excess width was due to the convolution of the laser line shape with the Doppler profile of the rotational lines, which has a FWHM of $\approx 800\,\text{MHz}$. More concerning was the large background fluorescence observed between well separated rotational lines (see the black curve in the top of Fig. 5.36). It was difficult to find any frequency at which no fluorescence was observed. However, at that point it was unclear whether this was due to the laser or some effect of the molecules.

The key to unlocking this mystery was the use of quantum beats. For the EDM measurement we observe quantum beats between the $|a, J = 1, m = \pm 1\rangle$ sublevels. The "beats" are the intensity modulation of the fluorescence with a frequency given by the Zeeman energy splitting between the sublevels. Because the Zeeman shift is different for each rotational line (see Section 3.5.3) the beat frequency is unique to each line. Thus the line shape of even completely overlapped lines can be measured by monitoring the amplitude of the quantum beats for each of the lines. In fact, calculations had suggested that when we tuned to the $J = 1$ line for the EDM measurement the amplitude of the $J = 1$ quantum beats should be one half the fluorescence size, i.e. 50% contrast. We had long attributed the fact that we observed $10-15\%$ contrast to either background fluorescence from other nearby rotational lines or a broad background in the laser.

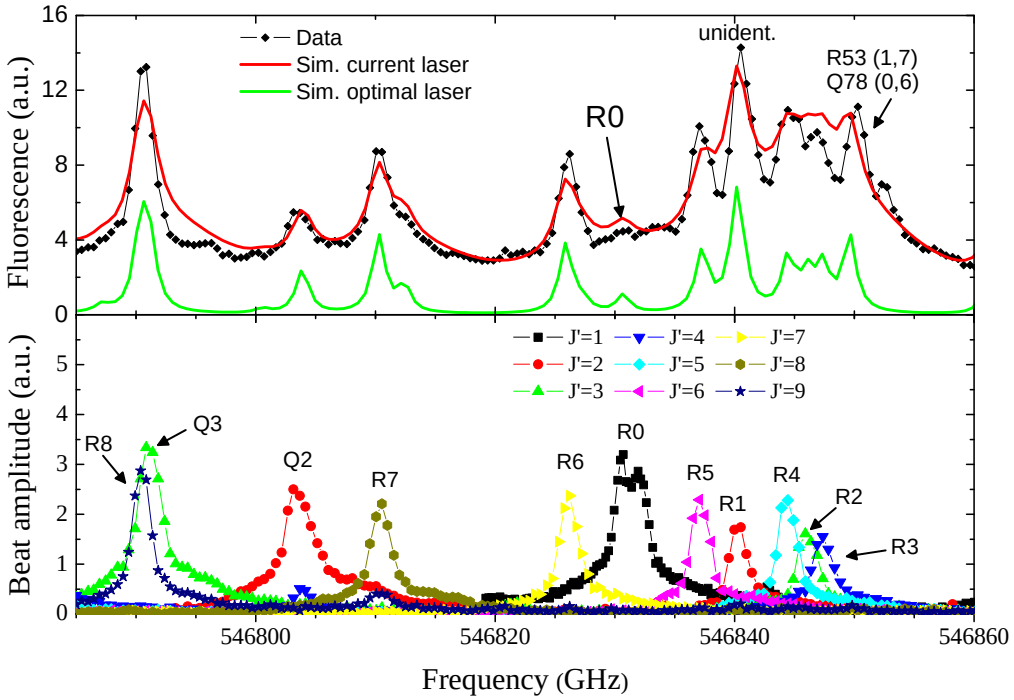

Figure 5.36: Top: Fluorescence spectra from a scan of the dye laser frequency. The black points are data, the red curve is a simulation using the laser line shape inferred from the quantum beat spectra below, and the green curve is a simulation using an optimal laser line shape with a FWHM of 800 MHz. Note the small bump labeled R0 is the transition used for the EDM measurement. Bottom: Quantum beat spectra of the same lines. The frequency of quantum beats (intensity modulations in the fluorescence) are unique for each rotational level. Each curve is the amplitude of the quantum beats at the associated beat frequency for the denoted rotational line. All nine curves can be obtained in a single laser scan. Labels above the peaks indicate the rotational transitions from the ground state.

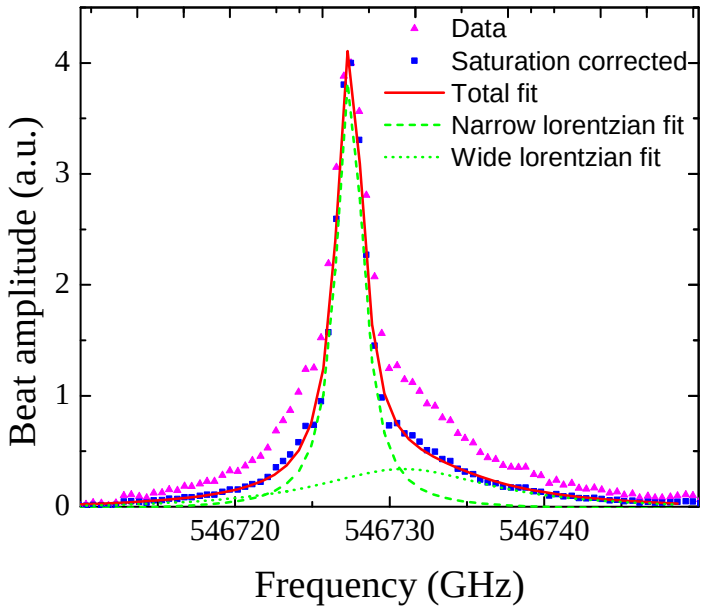

Figure 5.37: Dye laser spectrum from quantum beat spectroscopy. The purple triangles are the quantum beat amplitudes for the $J = 5$ line as the laser is scanned over the Q5 transition. The blue squares are a curve corrected for saturation of the transition (a peak saturation parameter of 4 is assumed). The line shape is well approximated by the sum, the line in red, of two Lorentzians with widths of 2 GHz, shown in dashed green, and 14 GHz, shown in dotted green.

To measure the amplitude of the quantum beats at different frequencies the fluorescence signal is Fourier transformed. Peaks in the Fourier transform are visible for each of the rotational beat frequencies. By monitoring each of the peak heights during a laser scan, background free line profiles are obtained. The bottom half of Fig. 5.36 shows the beat frequency amplitudes as the laser was scanned over several rotational lines. The line shapes have a narrow central peak but unexpectedly long tails. Fig. 5.37 shows the fit for the sum of two Lorentzians to an isolated line profile. The line shape is first corrected for saturation of the transition. For all lines we consistently observe a narrow central peak with a FWHM of ≈ 2 GHz and an offset broader peak with a FWHM of $10-14$ GHz. The top half of Fig. 5.36 shows the good agreement between the observed fluorescence spectra and a simulation based on the fitted line profile. The long tail accounts for the fluorescence seen when the laser is not resonant with any of the lines. The small peak marked R0 is the transition used for the EDM experiment. The background is over four times the useful signal size. The green curve is a simulation using an optimal Lorentzian line shape with 800 MHz FWHM. With this theoretical line shape the background fluorescence for the EDM measurement is nearly completely eliminated.

Because the dye laser line width without the intracavity étalon was similar to the width of the broad peak seen in the quantum beat spectrum, we initially attributed the broad peak to the design of the dye laser. We attempted to insert a second étalon into the laser cavity to improve filtering. A broader bandwidth étalon had no discernible effect while the loss from a narrower étalon pushed the laser below threshold.

5.10.2 Laser excitation efficiency problem

In addition to the line width problems, we had also long suspected that the number of molecules driven to the excited state by the dye laser was lower than what was expected from calculations. Extensive modeling of the collection efficiency of our detection system (see [81]) allowed us to convert the number of fluorescence photons detected into an estimate of the number of molecules excited. We could also calculate the density of lead oxide in our cell using vapor pressure curves and the measured temperature of the cell. A comparison of the two estimates gave an excitation efficiency, i.e. the fraction of available molecules excited, of much less than 1%.

Later, using microwave absorption (see Section 7.5.3), we directly measured the PbO density

and found that vapor pressure curves we had previously used were roughly an order of magnitude high. Even with this correction we estimated the dye laser excitation efficiency was $2-4\%$. Further microwave absorption measurements of the ground and excited state population densities immediately after laser excitation inferred an efficiency of $\approx 10\%$.

We can estimate the probability of excitation given the absorption cross section, σ, for the $|X, \nu = 0, J = 0\rangle \rightarrow |a(1), \nu' = 5, J' = 1\rangle$ transition. The cross section is related to the natural line width and the laser line width by [86]

$$\sigma = \frac{\lambda^2}{2\pi} \frac{2J'+1}{2J+1} \frac{\xi\gamma_0}{\gamma_{laser}}, \tag{5.26}$$

where λ is the transition wavelength; $2J'+1$ and $2J+1$ are the degeneracies of the excited and ground state levels; ξ is the branching ratio or fraction of molecules which decay back to the bottom state of the transition; γ_0 is the natural line width; and γ_{laser} is the laser line width. The branching ratio, ξ, is the product of the Franck-Condon and the Honl-London factors which give the branching ratios to vibrational and rotational levels in the ground state, respectively. The Franck-Condon factor for this transition is $\approx 1/2$. The forbidden nature of this electronic transition prevents a direct calculation of the Honl-London factor. We estimate the Honl-London factor to be 1/3 from observations of the relative fluorescence sizes of various rotational levels [52]. Using the lifetime of the $a(1)$ state, $\tau_a = 80\,\mu s$, a laser line width of $2\pi \times 2\,GHz$, and a transition wavelength of $550\,nm$ gives $\sigma = 2.4 \times 10^{-16}\,cm^2$. The excitation rate is the absorption cross multiplied by the photon flux, Φ. Therefore the probability of excitation is

$$P = \sigma\Phi T, \tag{5.27}$$

where T is the laser pulse length. A 10 mJ pulse, 6 ns long with a beam diameter of 1.5" corresponds to a flux of $\Phi = 4 \times 10^{23}$ photons $cm^{-2}\,s^{-1}$. This gives $P \approx 35\%$ which is 3.5 times higher than any of the estimates based on observed signal sizes.

Adding to the confusion, measurements of the fluorescence size versus laser power suggested an excitation efficiency of nearly 50%. At low laser powers, the fluorescence size should be proportional to the laser power as the excitation rate from the ground state increases. At higher laser powers a significant population builds up in the excited state and stimulated emission can drive the molecules

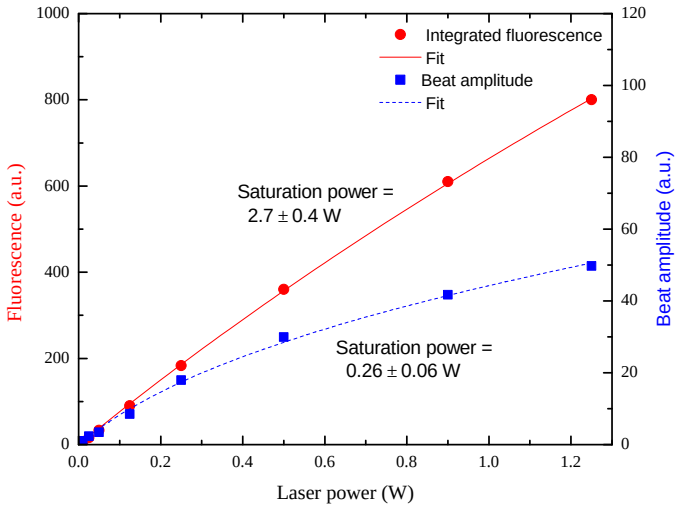

Figure 5.38: Saturation of quantum beats. Measuring the integrated fluorescence signal and the quantum beat amplitude versus dye laser power shows that the fluorescence increases roughly linearly with power while the quantum beat amplitude increases in a manner consistent with a saturation power of 0.26 W.

back to the ground state. At this saturation point the fluorescence size increases only as the square root of the laser power and the populations in the ground and excited states approach an equilibrium of 50%.

Fig. 5.38 shows the total fluorescence size and quantum beat amplitude versus laser power with the laser tuned to $|X, J = 0\rangle \rightarrow |a, J = 1\rangle$ transition. The linear dependence of the total fluorescence is consistent with excitation of nearby rotational lines by the broad but lower power tails of our laser spectrum. The square root dependence of the beat amplitude, which is proportional to the number of molecules excited to the $J = 1$ state only, is consistent with a saturation power of 0.26 W.

We now believe that the narrow 2 GHz peak in the dye laser spectrum is the result of averaging many individual laser pulses of 1-3 narrower lines, each of which could be as small as the Fourier transform limit of 30 MHz. This behavior is typical of pulsed dye lasers [110–112] and is due to different longitudinal modes of the laser cavity dominating each laser shot. Each of the modes saturates a small velocity class in the Boltzmann distribution of the molecules while leaving the others unexcited. In this case the excitation fraction is roughly given by the ratio of the area of the narrower line width(s) to the Doppler width. This model could explain both the low excitation

efficiency and the saturation behavior (i.e., signal $\propto \sqrt{\text{power}}$) of the beat amplitude with increased laser power.

5.11 Seeded dye laser

To eliminate both the broad line width and low excitation efficiency problems with the commercial dye laser, we built our own seeded dye amplifier system [113]. In an unseeded dye laser system a cavity is placed around a dye cell. The pump laser excites the dye molecules and as the first molecules spontaneously decay they emit light into the cavity over a broad wavelength range, typically tens of nanometers. Some type of spectral filter introduces loss in the cavity for all but the desired frequency. The remaining photons pass through the dye cell and stimulate emission into the cavity which leads to gain and lasing at the desired frequency.

In a seeded dye amplifier, a continuous wave (CW) laser at the desired frequency passes through the dye cell. When the pump pulse excites the dye molecules the CW laser stimulates emission and after further gain the frequency spectrum of the output pulse matches the frequency spectrum of the CW laser (albeit transform-broadened due to the finite duration short pump pulse). The line width of commercial CW diode lasers is on the order of megahertz but can be broadened using frequency modulation of the control current to match the Doppler width of the molecular transition lines. Thus by using a seeded dye amplifier we have exquisite control over the output frequency spectrum.

CW seed laser

In theory, to seed our dye laser at 548 nm there are two options. The first is to use a CW dye laser to seed the pulsed dye amplifier. CW dye lasers are expensive and notoriously difficult to use. In addition there is no easy way to broaden the line width to match the Doppler width.

The second option is to use a diode laser. In the last decade there has been an enormous increase in the wavelength range covered by CW diode lasers. Unfortunately, it is notoriously difficult to manufacturer diodes at the green wavelengths we use.[13] Thus, to make the seed laser, we have to frequency double an infrared (IR) diode laser with a nonlinear crystal.[14] With CW lasers it is difficult

[13] Most green laser pointers have a frequency doubled solid state laser that emits at a fixed wavelength.
[14] A fiber laser could also be used, but at that time there were no off-the-shelf fiber lasers at 1096 nm.

to get significant power at the doubled frequency because doubling efficiency is proportional to the square of the input laser intensity. To give some idea of the problem, the doubling efficiency of the pulsed YAG is about 30% and the peak intensity during the 6 ns pulse for a 1 cm diameter beam is 60 MW cm^{-2}! Typically the solution for CW lasers is to place the doubling crystal in a high finesse cavity and focus the laser as tightly as possible inside the crystal. However, a high finesse cavity also has a narrow resonant line width. This is incompatible with the relatively broad line width of 800 MHz needed to match the Doppler width of the excitation transition.

Fortunately, the relatively new technology of optical waveguides made from periodically poled doubling crystals offers single pass doubling efficiencies up to tens of percent for CW lasers. The efficiency of doubling in bulk crystals is ultimately limited by diffraction which causes the laser to diverge more quickly the tighter it is focused. By confining the beam to an optical waveguide less than 5 μm wide, the laser intensity remains high along the entire length of the crystal. Periodic poling ensures that the doubled light from different parts of the crystal remains in phase, preventing destructive interference.

5.11.1 High power infrared laser

Our seed laser system (see Fig. 5.39) begins with an infrared 1096 nm laser diode in a DL PRO mount from Toptica with a maximum output power of 150 mW. The laser frequency is stabilized in the DL PRO with a proprietary external cavity design which minimizes beam deflection as the frequency is tuned. The laser frequency can be coarsely adjusted by changing the voltage to a piezo which tilts a diffraction grating in the external cavity. Adjusting the laser diode current gives more precise frequency control. The electronics for the DL PRO have a feedforward adjustment which automatically changes the laser current in proportion to the piezo voltage. By adjusting the feedforward we have been able to tune the laser over 65 GHz without mode hops using external control of the piezo voltage. Note that the optimal feedforward adjustment is highly dependent on the piezo voltage sweep rate. The current over a 65 GHz scan can change by more than 25% which causes heating of the laser diode. If the current is changed significantly in less than the few seconds it takes for temperature stabilization, the tuning properties of laser diode change.

At the output of the DL PRO a beam shaping anamorphic prism pair changes the elliptical beam to a roughly circular cross section. Two optical isolators prevent reflections from entering the laser

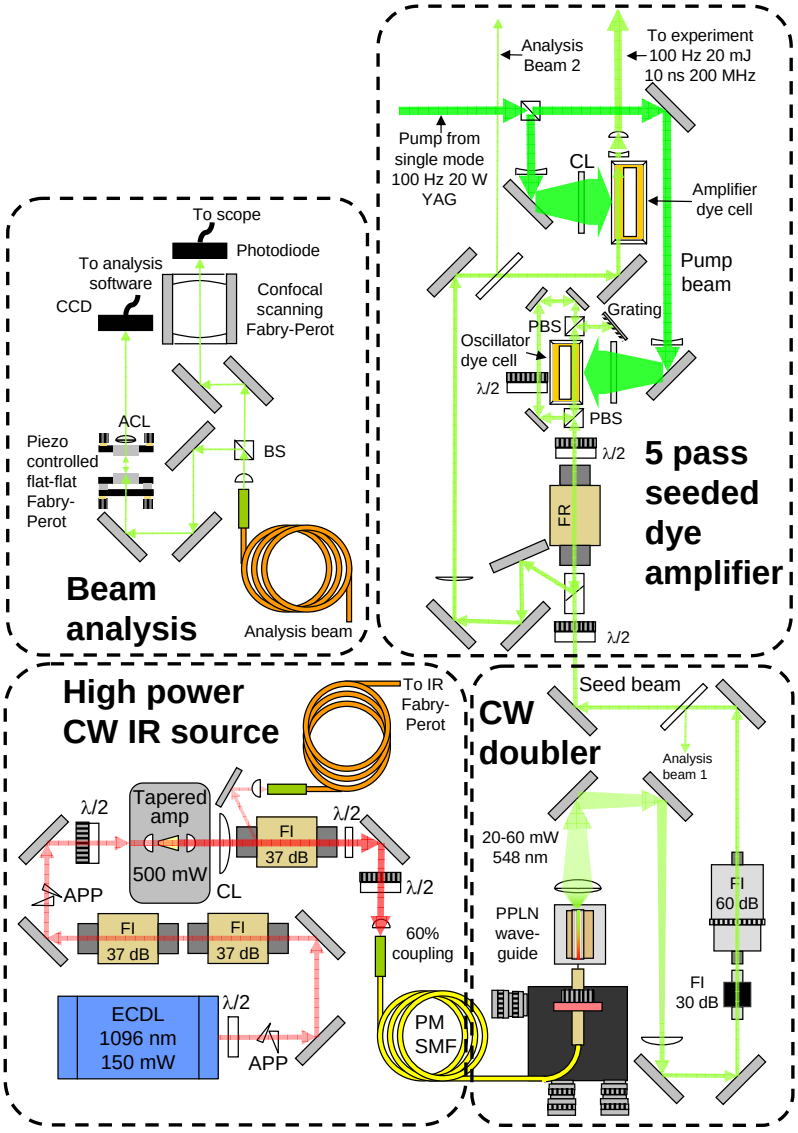

Figure 5.39: Green seeded dye laser system. ECDL: external cavity diode laser, APP: anamorphic prism pair, FI: Faraday isolator, $\lambda/2$: half-wave waveplate, CL: cylindrical lens, PM SMF: Polarization maintaining single mode fiber, PPLN: periodic poled lithium niobate, FR: Faraday rotator, PBS: polarizing beamsplitting cube, BS: beamsplitting cube, ACL: achromatic lens doublet. Description: A Toptica 1096 nm diode laser is amplifier by a tapered amplifier chip to an output power of 500 mW. This is launched via a bare SMF PM fiber into a PPLN waveguide doubling chip. 20-60 mW of green power are used as the seed for a four pass dye amplifier pumped by a fraction of the power from an Nd:YAG laser. The output of the four pass amplifier makes one pass through a larger dye cell pumped by the remainder of the power from the YAG laser. The output pulses are 10 ns long, 200 MHz wide, with powers of 10-20 mJ at a repetition rate of 10 Hz. A flat-flat Fabry Perot measures single shot frequency spectra of the output pulses.

cavity which can cause instability and possibly damage the laser diode. A second anamorphic prism pair shapes the beam profile to roughly match the profile of the beam coming from the input side of a tapered amplifier chip. A $\lambda/2$ waveplate is used to rotate the polarization for optimal amplification.

The tapered amplifier is in a mount with two adjustable aspherical lenses for coupling into the chip and collimating the output.[15] The mount is on a temperature controlled aluminum block. To achieve the maximum output power of 500 mW the temperature of the mount is kept well below room temperature by a thermoelectric cooler (TEC). A thermistor mounted near the amplifier chip provides feedback to a temperature controller which runs the TEC. The entire amplifier system was originally set up by Lucas Willis.

Only one axis of the output beam from the tapered amplifier is collimated by the aspheric lens. The second axis is collimated with a cylindrical lens. With the proper choice of focal length the collimated beam is roughly circular. Positioning the beam in the center of both lenses is crucial to obtaining a decent output beam shape.

Next the amplified beam passes through an optical isolator. The rejected light from the isolator is picked off and fiber coupled to a confocal Fabry-Perot cavity for monitoring of the frequency and to determine if the diode laser is running single mode. The isolator rotates the polarization to a 45° angle between horizontal and vertical. A $\lambda/2$ waveplate rotates the polarization back to vertical or horizontal before it reaches a dielectric mirror.

After the mirror, a second $\lambda/2$ waveplate on a rotation stage is used to align the polarization with one of the axes of a polarization maintaining (PM) single mode fiber. An adjustable mirror mount holds a fiber collimator (Thorlabs CFC-5X-C), which has a z-axis adjustable collimating lens. Note that if the beam polarization is not horizontal or vertical when it hits the dielectric mirror the polarization after the mirror is elliptical. When coupled into the PM fiber, the elliptical polarization makes the output power strongly temperature dependent regardless of the orientation of the PM fiber axis.[16]

[15] See Appendix C for alignment hints.
[16] See Appendix C for alignment hints.

5.11.2 Optical waveguide frequency doubler

The output end of the PM fiber is mounted on a 3-axis sub-micron positioning stage (Thorlabs MAX312) with differential adjustment knobs and piezo actuators. For efficient coupling the bare fiber must be placed within a few microns[17] of the MgO doped periodic poled lithium niobate (MgO:PPLN) waveguide doubling chip (HC Photonics).

For a given wavelength there is one temperature at which the doubling efficiency of the PPLN chip is maximized. For our particular chip this temperature is $60 - 70\,^{\circ}\mathrm{C}$ for a doubled wavelength of 548.2 nm. The chip temperature is controlled by an oven designed and machined by Emil Kirilov. A brass piece heated by a small thermoelectric cooler (TEC) holds the chip. This piece sits inside a brass enclosure which itself sits on a large aluminum block. A large TEC run with a current supply provides course temperature control over the aluminum block, while the smaller TEC maintains the chip temperature. A thermistor mounted on the brass piece near the chip provides feedback to a TEC controller (Wavelength Electronics) for the small TEC. The original oven from HC Photonics is no longer used because its temperature servo relied on pulse modulation of the heater current. Periodic thermal expansion led to changes in both the coupling efficiency, causing output power fluctuations of up to 40%, and the pointing of the output beam.

There are 16 waveguide channels, less than 5 μm wide, in two groups of 8 which lie on the top of the doubling chip. The channel specified for use is the 11th from the left (see Fig. 5.40). We believe that in the manufacturing process the channels are each given a slightly different poling period. Testing determines which is optimal for the customer. The 8 channels on the right all work well albeit at slightly different temperatures for a given wavelength. We have avoided using the 11th channel thus far to save it for actual data taking. This was fortunate because, as we will discuss below, the output coating on the 10th channel was destroyed.

An achromatic lens brings the output beam of the PPLN chip to a slight focus. After the lens, the second and third mirrors in the beam path have coatings which separate the remaining fundamental frequency from the doubled frequency by reflecting the green and transmitting the IR. A second lens collimates the beam at a diameter of $\approx 2\,\mathrm{mm}$. The green power should always be measured after the two harmonic separator mirrors as the remaining IR power at the output of the PPLN chip is larger than the green power. The green beam then passes through two isolators providing

[17] See Appendix C for alignment hints.

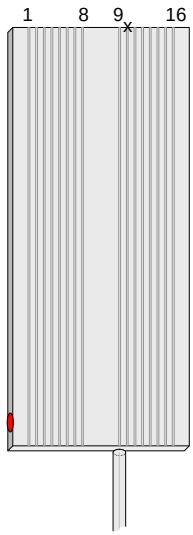

Figure 5.40: Periodic poled lithium niobate waveguide chip. There are 16 waveguide channels in two groups of 8 on the top surface of the chip. A red dot defines the orientation of the chip. Channel 11 was spec'd by the manufacturer. The coating on the output of channel 10 has been destroyed. The right group of channels seem to work the best, although at different temperatures.

approximately 90 dB of isolation.

Before the isolators we have measured green powers > 60 mW with an input IR power to the PPLN chip of $\approx 250mW$. Initially the output power changes significantly with a temperature change of a couple degrees. However after several days the output power slowly drops to below $\approx 20mW$ and is relatively insensitive to temperature changes. We suspect this is due to photorefractive damage. Papers in the literature [114–116] suggest the reduced doubling efficiency is due to formation of charge centers which change the index of refraction in the waveguide. The manufacturer's specified output power was 20 mW for an input power of 150 mW. After contacting the manufacturer they agreed it is most likely a photorefractive effect and suggested we keep the green power below 20 mW. They also said newer versions of the chip with different dopings are less susceptible to this effect.

For considerations in future purchases, many crystal manufacturers now suggest that using a phase matching temperature (which is set by the poling period) near 200 °C can reduce or eliminate photorefractive effects. Using stoichiometric rather than congruent lithium niobate also helps [114]. As a last recommendation, one can get a fiber pigtailed directly to the waveguide chip eliminating

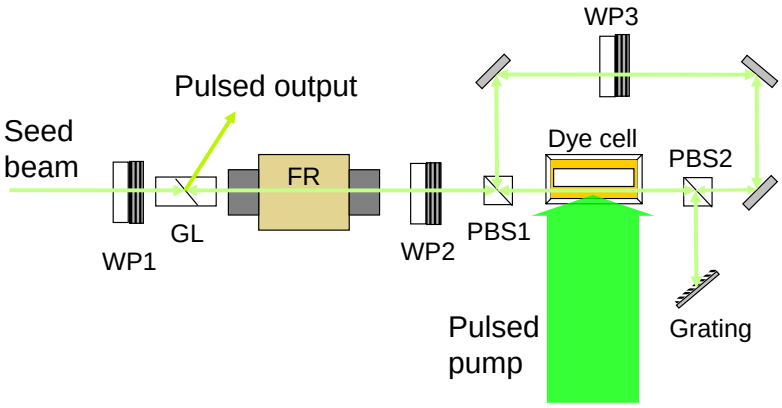

Figure 5.41: Four pass seeded dye amplifier. WP = $\lambda/2$ waveplate, GL = Glan laser polarizer, FR = Faraday rotator, PBS = polarizing beam splitter, HP = horizontal polarization, VP = vertical polarization. The polarizers transmit HP and deflect VP. The CW seed beam enters from the left with VP. WP1 rotates to HP and the beam passes through the GL polarizer. The FR rotates the polarization 45 degrees and WP2 rotates the polarization 45 degrees back to HP. The beam passes through PBS1, the dye cell and PBS2. WP3 rotates to VP and the beam is now deflected by PBS1 for a second pass through the dye cell. PBS2 deflects the beam to a diffraction grating which is aligned so that the first order retroreflects. PBS2 deflects the beam for a third pass through the cell and PBS1 deflects the beam upwards. WP3 rotates to VP and the beam now passes through PBS2 for a fourth pass through the dye cell. The beam continues through PBS1 and is rotated 45 degrees by WP1 and an additional 45 degrees by the FR (which rotates the same direction independent of the beam polarization) to VP. The GL polarizer deflects the beam for output.

alignment to the chip.

The damage we observed may be reversible by heating the chip to 200 °C overnight. Note that heating to 200 °C requires disassembly of the current PPLN mount as indium foil was used to make thermal contact between the small TEC and the brass piece. Indium was used rather than thermal grease to prevent vapors from possibly contaminating the PPLN chip.

5.11.3 CW seeded dye amplifier

After the isolators the beam enters a seeded dye amplifier based on the designs in [117, 118]. Through clever use of polarization (see caption for Fig. 5.41) the beam passes through the dye cell in both directions with horizontal and vertical polarizations for a total of 4 passes.[18] A grating after the second pass provides some frequency selectivity so that amplified spontaneous emission (ASE) can be separated from the amplified seed beam on the output. The dye cell is pumped from the

[18]See Appendix C for alignment hints.

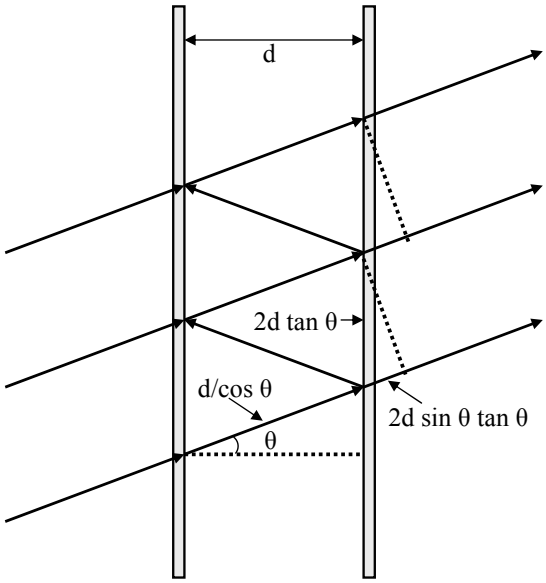

Figure 5.42: Fabry Perot. Transmission of monochromatic light through two parallel mirrors occurs at discrete angles when there is constructive interference between the rays from multiple bounces. Constructive interference occurs when the path length difference of two rays is an integer multiple of the wavelength.

side with 7-10 mJ of the pulsed YAG. After four passes we obtain 1-2 mJ pulses, 10 ns pulses at the frequency of the CW seed laser. This represents a gain of over 10^7.

From the pulsed dye amplifier the beam is slightly expanded and passes through a second larger dye cell for further amplification. This dye cell is pumped with the remainder of the power from the pulsed YAG. The YAG beam is split between the two dye cells using a high power $\lambda/2$ waveplate in a rotation mount and polarized beam splitting cube. The power split is adjusted to optimize the the size of the quantum beats in the fluorescence signal. The path length of the YAG to the second dye cell was adjusted so that the pump pulse arrives within a nanosecond of the output pulse from the first dye cell. Pulse energies as high as 20 mJ can be obtained but we see better results with energies below 10 mJ.

5.11.4 Fabry Perot

To analyze the frequency spectrum of our pulsed laser system on the benchtop, we use a flat-flat Fabry Perot which is nothing more than flat mirrors mounted parallel to each other. Fig. 5.42 shows the principle of the device. A plane wave entering at an angle can be transmitted through

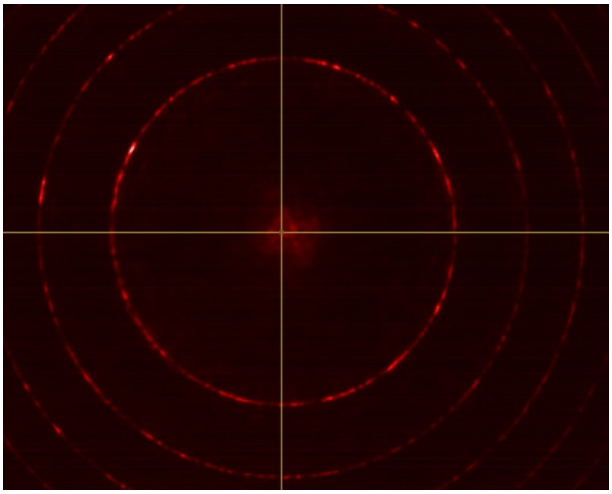

Figure 5.43: Fabry Perot image. The raw Fabry Perot image of a single pulse from the four pass seeded dye amplifier. The radial coordinate is a non-linear function of frequency. The frequency range between each ring is $\approx 14\,\mathrm{GHz}$.

the two mirrors when there is constructive interference between the rays from multiple bounces. Constructive interference occurs when the path length difference for two rays is an integer multiple of the wavelength,

$$\frac{2d}{\cos\theta} - 2d\sin\theta\cos\theta = n\lambda \rightarrow \cos\theta = \frac{n\lambda}{2d}. \tag{5.28}$$

Thus if monochromatic light is sent towards the mirrors at all angles it will only be transmitted at the specific angles given above. If a lens is placed after the mirrors, a ring is formed in the focal plane for each of the angles. From Eq. (5.28) one can derive a relationship between the radius of a point in the focal plane and frequency.

The main motivation for using a flat-flat Fabry Perot is that it allows measurement of the entire frequency spectrum of the laser in a single shot. Most other methods measure a single frequency per shot and thus only give an average spectrum.

Our Fabry Perot consists of two ultra-flat mirrors ($\lambda/20$ from CVI) mounted in ultra-stable mirror mounts with differential adjustment knobs (Thorlabs KS2D). For even finer adjustment small piezo rings have been placed underneath the adjustment screws. A piece of ground glass is mounted before the input mirror to scatter the incoming light. An achromatic lens is mounted on the back mirror to form the spectrum image (see Fig. 5.43). A Mightex CCD camera captures the image and a Labview program allows the user to interactively mark the position of a ring and correct

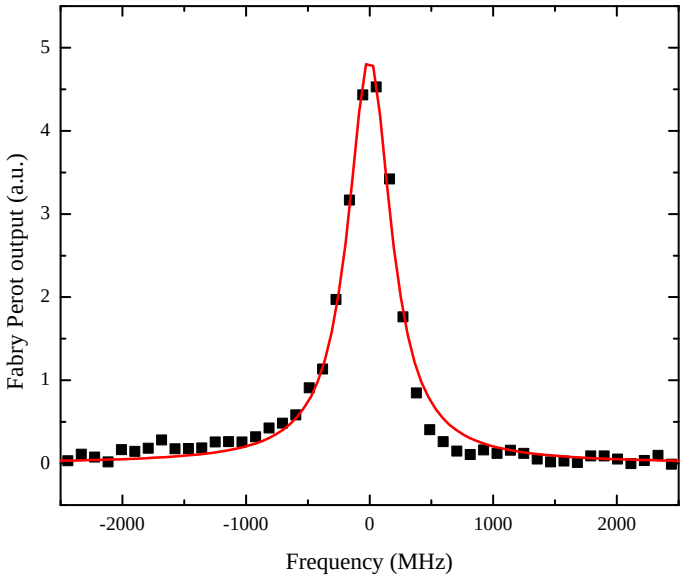

Figure 5.44: Frequency spectrum of the seeded dye laser using the flat-flat Fabry Perot. The fitted line width of 420 MHz is consistent with the resolution of the Fabry Perot for this measurement. The data comes from scaling, radial binning, and averaging one of the rings in Fig. 5.43.

for ellipticity. The pixels are then scaled, binned radially, and averaged to give a linear frequency spectrum.

5.11.5 Results with the new laser system

The raw image of the output from the Fabry Perot for a single pulse of the four pass seeded dye amplifier is shown in Fig. 5.43. The Lorentzian fit of the resulting frequency spectrum, shown in Fig. 5.44, gives an upper limit for the line width of less than 420 MHz, which is over five times narrower than the line width of the commercial dye laser we had previously used. The resolution of the Fabry Perot for this measurement was estimated to be 400 MHz.

Next we sent the output of the seeded dye laser into the vapor cell and scanned the laser frequency over several rotational lines while monitoring the amplitude of the quantum beats in fluorescence (as described in Section 5.10.1). Fig. 5.45 shows the resulting spectra using the four pass amplifier only, on the left, and the four pass amplifier plus the second amplifier dye cell,

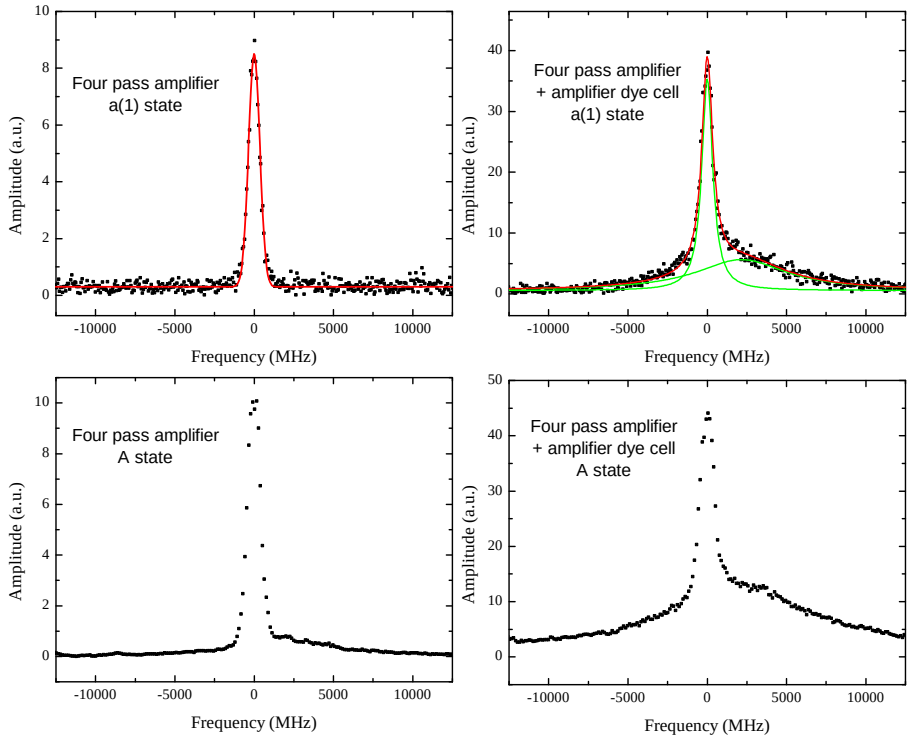

Figure 5.45: Quantum beat spectra with seeded dye laser. Top left: $a(1)$ state transition using the four pass amplifier only. The fit is a Gaussian with a FWHM of 830 MHz which is consistent with the Doppler width. Top right: $a(1)$ state transition using the four pass and second dye cell amplifier. The fit is two Lorentzians with FWHM of 1000 MHz and 8000 MHz. Bottom left: A state transition using the four pass amplifier only. Because this transition is stronger and saturates at a lower power the broad tail is evident even at low power. Bottom right: A state transition using four pass and second dye cell amplifier. Note the relative height is meaningful between left and right graphs only.

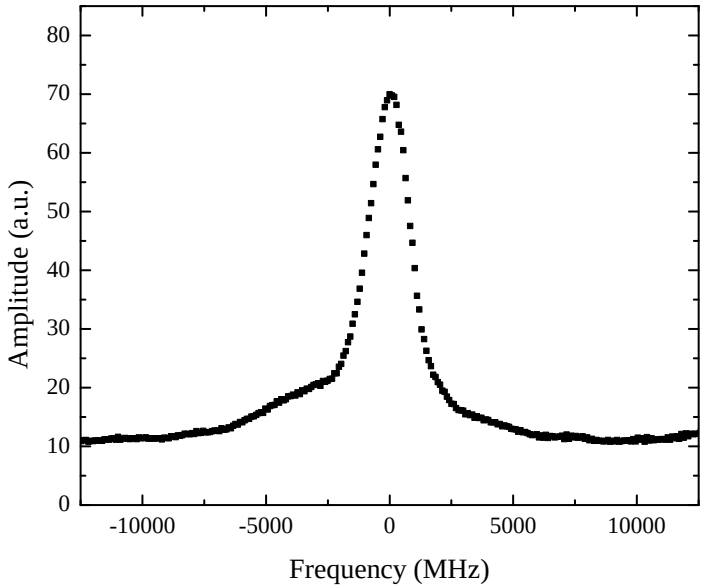

Figure 5.46: With higher power the broad spectral tail is evident in the Fabry Perot spectrum of the four pass dye amplifier. The tail is on the correct side to explain the tails seen in fluorescence spectra. Note that the 2 GHz FWHM of the central peak is limited by the low resolution of this particular measurement.

on the right. The top and bottom graphs are scans over a rotational line in the $a(1)$ and A states respectively. The narrow peaks are consistent with the Doppler width which suggests the laser line width is significantly smaller than the Doppler width. However it is also clear that there is a broad tail very similar to that seen in the spectra using the commercial dye laser (compare with Fig. 5.37). Because the A state transition is stronger and thus easier to saturate, the tail is evident even when using only the low power four pass amplifier.

The fact that we see the same shape in transitions to two different electronic states and many rotational levels makes it very unlikely this is an effect due to the molecules. It is also difficult to imagine a molecular mechanism that could lead to a line width of many gigahertz, which implies a timescale of hundreds of picoseconds. Collisions occur at kilohertz frequencies in the vapor cell. Stark shifts from stray electric fields would decrease with rotational level.

To confirm that the broad spectral tail was due to the laser we revisited our measurements of the spectra using the flat-flat Fabry Perot. Because the molecular transition is saturated the height

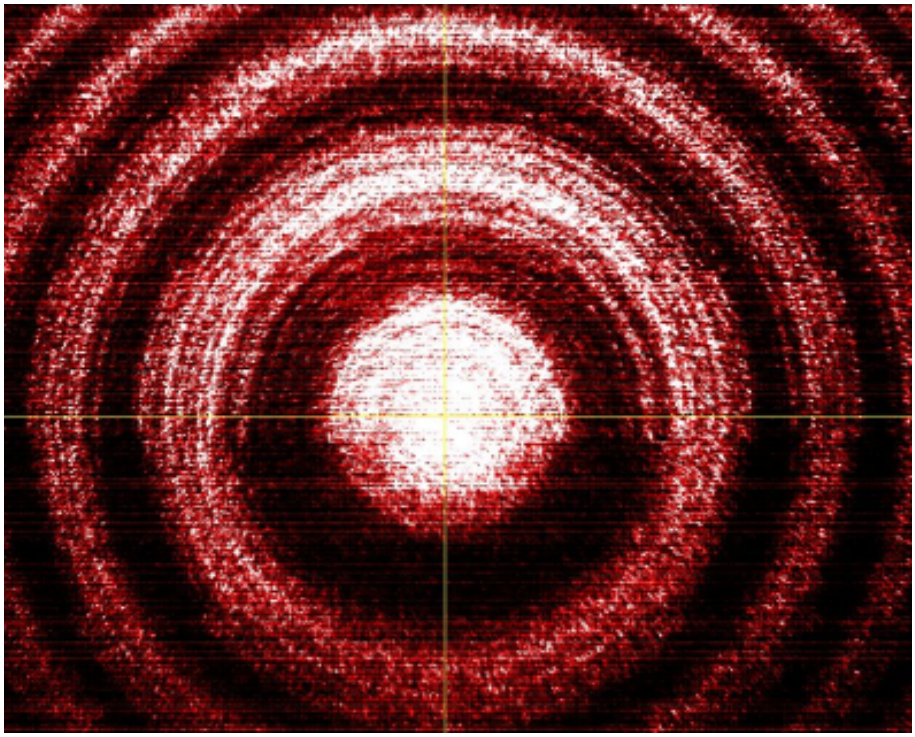

Figure 5.47: Fabry Perot image of YAG pulse. The frequency range between groups of rings is $\approx$ 27 GHz. The Spectra YAG is specified to have a line width of 30 GHz. Because of the way the CCD shutter and readout work, each line in the image is the result of a single pulse but the whole image has several pulses. The change in modes between two pulses is evident between the top and bottom of the image.

of the spectral tail relative to the central peak is enhanced in the fluorescence spectra. In the first measurement (see Fig. 5.43) we had fiber coupled a small fraction of the output beam to the Fabry Perot. The peak height of the rings was only 5 ADC counts. Fig. 5.46 shows a spectra with a much stronger signal, but lower frequency resolution. The 2 GHz FWHM of the peak is due to the resolution of the Fabry Perot in this measurement. Even with the poor resolution a broad tail is evident. The tail is also on the correct side for explaining the fluorescence spectra.

5.11.6 The YAG laser

One common element between the seeded dye laser system and the commercial dye laser we previously used was the YAG laser used to pump the dye. After searching the literature we found several papers (e.g. [119, 120]) which mentioned frequency broadening of dye laser pulses due to amplitude fluctuations in the pump pulse. Amplitude fluctuations in the pump imprint

amplitude fluctuations in the dye pulse which show up as frequency sidebands in the spectrum. In particular multimode YAG lasers often exhibit beating between longitudinal modes in the few gigahertz frequency range[120]. Additionally, changes in the excited state population of the dye, during amplitude fluctuations of the pump, can modulate the index of refraction of the dye and lead to phase fluctuations in the output pulse. Some combination of the both amplitude and phase modulation is needed to explain the one-sided nature of the observed spectrum.

The Spectra-Physics Nd:YAG laser we use as a pump has a specified line width of 30 GHz. Fig. 5.47 shows the image of a YAG laser pulse after the flat-flat Fabry Perot. The frequency range between sets of rings is ≈ 27 GHz. The individual modes are clearly visible and the large line width could easily lead to mode beating well over 10 GHz.

We have now traded in the Spectra-Physics YAG for a used Coherent Infinity YAG laser. The Infinity has twice the output power of the Spectra-Physics YAG and is designed to be inherently single mode. If this laser does remove the spectral tail from the dye laser pulses, the elimination of background fluorescence should improve our EDM sensitivity by a factor of 2. In addition, if the seeded dye laser line width is matched to the Doppler line width, an improvement to 50% excitation efficiency would give another factor of 2 increase in EDM sensitivity. If both these improvements are realized, our statistical sensitivity would surpass that of the Berkeley Tl limit in less than one day of integration.

Chapter 6

EDM measurement methods and results

In this chapter we will delve into more detail of the state preparation and detection methods used in the EDM measurement. We will follow much of the discussion and notation in a previous paper[29]. After discussing these methods we will present the first results of the experiment. While the limit placed on the electron EDM from these results was over an order of magnitude worse than the current experimental limit, the sensitivity was ultimately limited by statistics. Several possible systematics were examined and found to be consistent with zero. Limits placed on these systematics suggest they should not be an issue as the statistical sensitivity of the experiment is improved.

Note that much of the discussion below will use the notation and assume the results in Section 3.5, which discussed the structure of the $|a(1), J = 1\rangle$ state.

6.1 Fluorescence detection of quantum beats

The EDM measurement starts with excitation of the transition $|X, v = 0, J = 0, M = 0\rangle \rightarrow |a, v' = 5, J' = 1\rangle$ by a pulsed dye laser. If the polarization of the laser pulse is in the $\hat{x}$ direction, transition matrix elements ensure that a coherent superposition of the sublevels, $\frac{1}{\sqrt{2}}(|a, J = 1, M = +1\rangle - |a, J = 1, M = -1\rangle)$, is initially populated. In the absence of an electric field the transition must be between states of

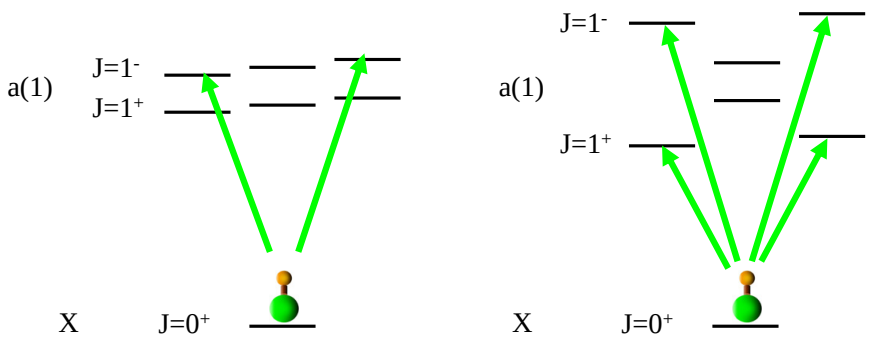

Figure 6.1: Pulsed dye laser excitation to the a(1) state. Left: In the absence of an electric field, the energy levels are parity eigenstates. From the $|X, J = 0\rangle$ state only the odd parity levels of the Ω-doublet are populated by a $\hat{x}$-polarized laser pulse. Right: In an electric field, the $|a, J = 1, M = \pm 1\rangle$ sublevels are of mixed parity and all four sublevels are populated by the laser pulse.

opposite parity. Since the X states have parity $(-1)^J$ only the negative parity levels of the Ω-doublet are populated (see Fig. 6.1) when exciting from $|X, J = 0\rangle$. In a magnetic field the initial state evolves according to

$$|\Psi(T)\rangle = \frac{1}{\sqrt{2}}\left(e^{-i\delta_Z T}\,|a, J = 1, M = +1, P = -1\rangle - e^{-i\delta_Z T}\,|a, J = 1, M = +1, P = -1\rangle\right), \tag{6.1}$$

where δ_Z is the Zeeman shift. Parity selection allows decays only to the positive parity J=0 and J=2 levels of the ground state. The fluorescence intensity, S, for detection along the $\hat{x}$ axis (see Fig. 5.7), is given by

$$S(T) \propto \sum_{J''=0,2} \sum_{M''} \sum_{\epsilon=\hat{y},\hat{z}} |\langle X, J'', M''\,|\,\boldsymbol{\epsilon}\cdot\boldsymbol{r}\,|\,\Psi(T)\rangle|^2\,, \tag{6.2}$$

where $\boldsymbol{\epsilon}$ is the polarization of the fluorescence. Decays to $M = 0$, which require $\hat{y}$ polarization, give rise to quantum beats (see Fig. 6.2. For example, with $M_{J''} \equiv \langle X, J'', M = 0\,|\,y\,|\,a, J = 1, M = 1\rangle = \langle X, J'', M = 0\,|\,y\,|\,a, J = 1, M = -1\rangle$,

$$S_{qb}(T) \propto \sum_{J''=0,2} M_{J''}\left|e^{-i\delta_Z T} - e^{i\delta_Z T}\right|^2 \propto 1 - \cos(2\delta_Z T). \tag{6.3}$$

Thus these decays give rise to fluorescence which is 100% modulated. The fluorscence from decays to other sublevels does not exhibit quantum beats. Given the fraction of decays, c, to the $M = 0$

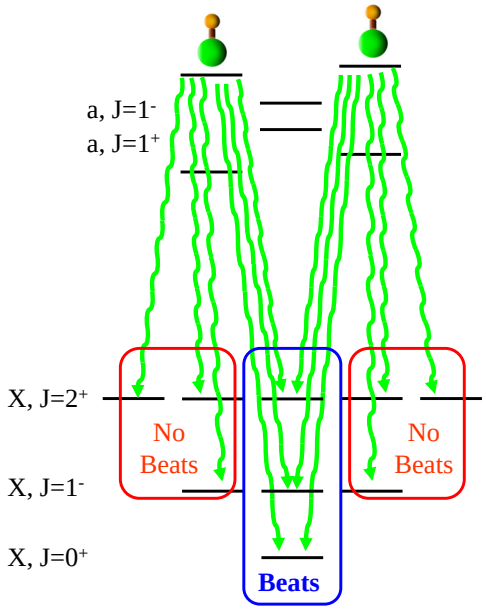

Figure 6.2: Decay paths leading to quantum beats. In an electric field the $|J = 1, M = \pm 1, P-\rangle$ levels are of mixed parity and can decay to the $J = 0, 1$, and 2 levels of the ground state. Only decays to the $M = 0$ sublevels exhibit quantum beats. In the absence of an electric field decays to the $J = 1$ level of the ground state are forbidden.

sublevels the total fluorescence signal is then

$$S(T) = Ae^{-T/\tau} \left[1 - c\cos(2\delta_Z T)\right], \tag{6.4}$$

where A is the total signal size and τ is the lifetime of the excited state. Borrowing from terminology used in interferometry, we call c the contrast of the quantum beats.

The fraction of decays to the $M = 0$ sublevels is determined by the branching ratio for the decays to the $|X, J = 0\rangle$ and $|X, J = 2\rangle$ states. Because the $a \rightarrow X$ transition is forbidden this value can not be calculated. However, observations of the relative fluorescence size from several rotational lines suggests that $c = 50\%$ (see discussion in [52] for more details). The observed value of $c = 10 - 15\%$ is most likely due to background from excitation of nearby rotational lines by the dye laser.

In an electric field, the $|a, J = 1, M = \pm 1\rangle$ states are of mixed parity and additional decays are allowed to the $|X, J'' = 1\rangle$ levels (see Fig. 6.2). The only effect on the fluorescence is a slight reduction in contrast due to the change in the fraction of decays to $M = 0$ sublevels.

Note that because there are no vibrational selection rules, decays generally go to several vibra-

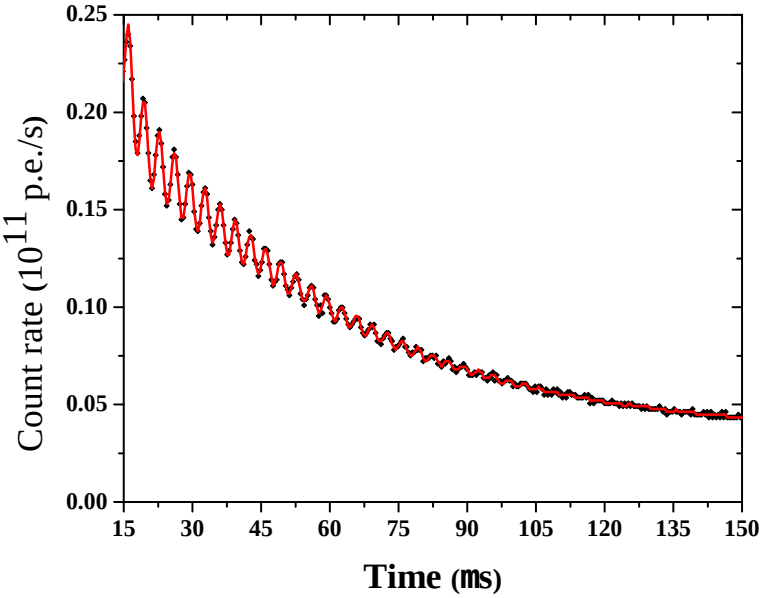

Figure 6.3: Fit of quantum beat data. The data points are the average fluorescence from four laser shots. The red line is a fit to Eq. (6.5).

tional levels in the ground state. The relative branching ratio of the vibrational decays is given by the Frank-Condon factor, which is a measure of the overlap of the radial wavefunctions. For the $|a, v' = 5\rangle$ state about 50% of the molecules decay back to the $|X, v = 0\rangle$ state with fluorescence wavelength 548 nm and 50% go to the $|X, v = 1\rangle$ level with wavelength 572 nm. In the past narrow interference filters in front of the PMTs transmitted only one of these transitions. We have recently switched to wider interference filters that capture both transitions (see Section 5.7).

6.2 Data fitting

The fluorescence data in the experiment is fit (see Fig. 6.3) to a slightly more complicated function than Eq. (6.4),

$$S_{model}(T) = \alpha I(T)\left[1 + ce^{-T/T_b}\cos(\omega_b T + \phi)\right] + d. \tag{6.5}$$

Here the beat shortening time T_b accounts for spin-decohering collisions, ϕ is the starting phase, and d is the dc background due to blackbody radiation. The "scrambled" data, $I(T) \approx e^{-T/T_1}$, is

essentially the fluorescence signal without quantum beats.[1] T_1 is the $a(1)$ state lifetime in the cell, which is determined by the natural lifetime, $\tau_a \approx 80\,\mu s$, and the collisional quenching rate. Optimal sensitivity is obtained when these two rates are approximately equal, which gives $T_1 \approx 40\,\mu s$. The data is fit in real-time with free parameters α, c, T_b, ω_b, and ϕ using a Levenburg-Marquardt algorithm written in C. The routine is compiled in a dynamic link library called by a Labview program which allows the user to interactively see histogram or x-y plots of the fit parameters, uncertainties, and various other experimental parameters. Because of electrical transients from the pulsed YAG laser and short lived background fluorescence from a nearby level of the A state, the data fit is usually started $10 - 15\mu s$ after the laser shot (see Fig. 6.3).

The uncertainty, $\delta\omega_b$, in the fitted value of the beat frequency, $\omega_b \approx 2g\mu B + 2d_e\mathcal{E}_{eff}$, determines our uncertainty in the EDM, $\delta d_e \approx \delta\omega_b/(2\mathcal{E}_{eff})$. From the uncertainty principle we expect that $\delta\omega = 1/T$ where T is the measurement time. For shot noise limited detection the uncertainty is improved by the signal-to-noise ratio, $S/N = cN/\sqrt{N}$. When α is in units of a counting rate, we then estimate

$$\delta\omega_b = \frac{1}{cT\sqrt{N}} = \frac{1}{cT\sqrt{\alpha T}}. \tag{6.6}$$

An analytic calculation using the fitting function Eq. (6.5), discussed in detail in Appendix D, gives a shot-noise limited sensitivity of

$$\delta\omega_b = \frac{\sqrt{2}}{c\sqrt{\alpha T_1^3}}\xi\left(\tfrac{T_1}{T_b}, \tfrac{d}{\alpha}\right) = \frac{\sqrt{2}}{cT_1\sqrt{N}}\xi\left(\tfrac{T_1}{T_b}, \tfrac{d}{\alpha}\right). \tag{6.7}$$

The function $\xi\left(\frac{T_1}{T_b}, \frac{d}{\alpha}\right) = \sqrt{\left(1 + 2\frac{T_1}{T_b}\right)^3 + 8\left(1 + \frac{T_1}{T_b}\right)^3 \frac{d}{\alpha}}$ is a correction factor which accounts for the beat shortening time, T_b, and the dc background, d. The current optimal configuration (100 nm bandpass interference filter and KG4 IR blocking glass) gives $d/\alpha \approx 0.5$, $\alpha = 3.5 \times 10^{11}$photoelectrons/s, $c = 0.08$, and $T_1 \approx T_2 \approx 40 \times 10^{-6}\,\mu s$. Using Eq. (6.7) gives a single shot uncertainty estimate of $\delta\omega = 2\pi \times 144\,\text{Hz}$. This agrees well with the actual uncertainty (determined from a histogram of the fit frequencies) of $2\pi \times 148\,\text{Hz}$. Note these values are for zero electric field without EDM state preparation.

[1] See Appendix D.2 for a discussion of the various methods used to obtain this data.

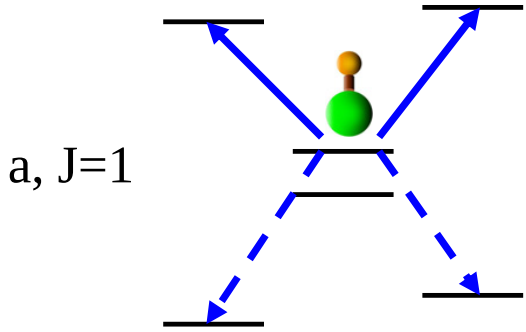

Figure 6.4: RF EDM state preparation. A $\hat{z}$-polarized laser pulse drives the molecules to the state $|a, J = 1, M = 0\rangle$. An RF magnetic field selectively prepares either the higher or lower EDM state.

6.3 EDM state preparation

In an electric field the $|a, J = 1, M = \pm 1\rangle$ energy eigenstates are no longer parity eigenstates. Because the laser line width is much broader than the Stark splitting, a $\hat{x}$-polarized laser pulse populates all four $|a, J = 1, M = \pm 1\rangle$ levels (see Fig. 6.1).

To selectively prepare either the higher or lower EDM state, the initial plan was to start with a $\hat{z}$-polarized laser pulse and populate the $|a, J = 1, M = 0, P-\rangle$ level. Next, a RF magnetic field drives a transition to either the higher or lower EDM state (see Fig. 6.4). Yong Jiang carried out extensive experiments investigating this method [52]. The RF transitions were driven by a 1 kW RF pulse amplifier connected to square Helmholtz coils mounted near the vapor cell using an impedance matching network that could be switched for the two RF frequencies. It was found, in the reverse process, that driving the RF transitions could effectively destroy the beat coherence if a $\hat{x}$-polarized laser pulse was used to initially populate all four of the $M = \pm 1$ sublevels. However, when the RF transition was used to selectively populate one of the EDM states, measurements of the beat contrast implied a population transfer of only 20%.

6.3.1 Microwave state preparation

Next we tried driving two step microwave Raman transitions using the higher $J = 2$ rotational level as an intermediate state (see Fig. 6.5). Yong Jiang's thesis [52] has an excellent discussion of the details of our experimental investigations of the these transitions and his analytic calculations of the transition dynamics. As this method was also eventually abandoned, I will only summarize a

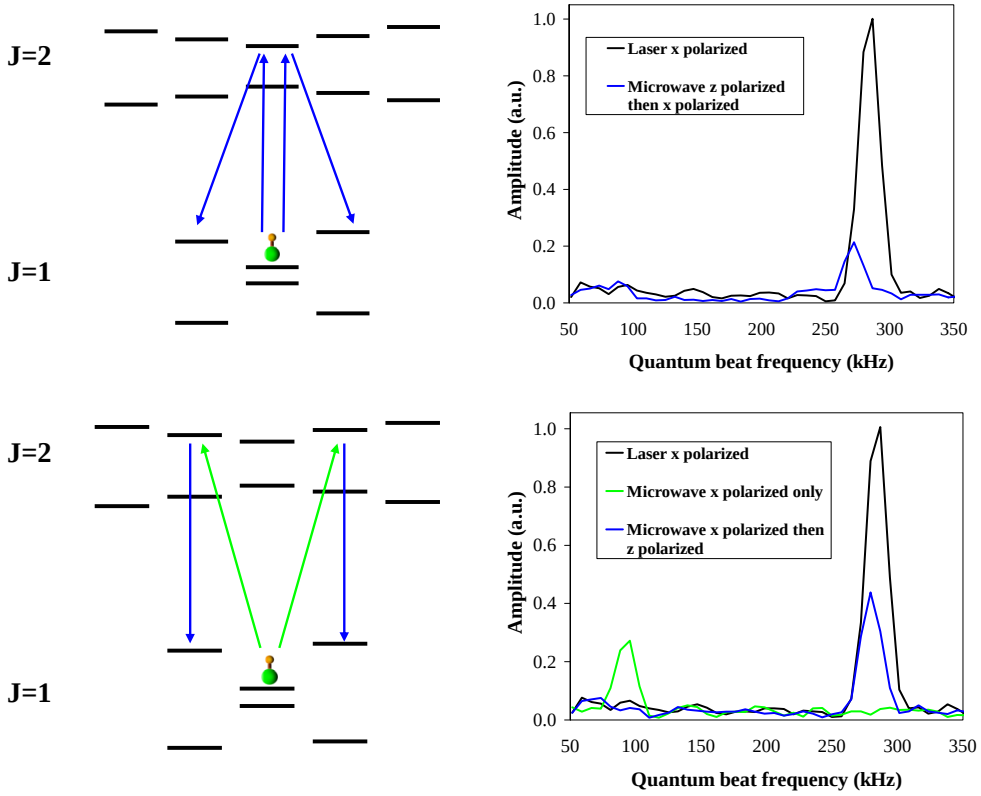

Figure 6.5: Microwave Raman EDM state preparation. Left: Two excitation pathways were investigated for preparing the EDM states. For the zx path, on top, a $\hat{z}$-polarized microwave pulse drives the molecules to $|J = 2, M = 0, P+\rangle$. A second $\hat{x}$-polarized pulse is tuned to the transition for either the higher or lower EDM state. The xz path, on bottom, consists of a $\hat{x}$-polarized microwave pulse which drives the molecules to $|J = 2, M = \pm 1, H\rangle$ followed by a z-polarized pulse tuned to the transition for the EDM states. Right: Excitation efficiencies of the individual steps were monitored via quantum beats. The Fourier transform of the fluorescence data shows peaks at beat frequencies for the $J = 1$ states, near 300 kHz, and the $J = 2$ states, near 100 kHz. The intermediate state in the zx pathway exhibits no quantum beats and could not be monitored.

few of the results.

At the 28.2 GHz frequency of the rotational transition, the Doppler width is ≈ 40 kHz. Thus the various sublevels, which are separated by Stark shifts on the order of tens of megahertz, are easily resolvable. The microwave pulses were generated using a homebuilt source described in Section 5.9 and coupled to the vapor cell via a Teflon tube attached to the quartz light pipe opposite to the laser excitation side of the apparatus.

Excitation efficiencies of the microwave transitions were monitored via quantum beats in the fluorescence. Because the Zeeman shift in the $J = 2$ state is one-third that of the $J = 1$ state the quantum beats from the two states have unique frequencies. By taking the Fourier transform of the fluorescence data and monitoring the amplitudes at the two beat frequencies, the populations in superpositions of the $M = \pm 1$ levels in either rotational state could be inferred (see Fig. 6.5). To determine efficiencies, the amplitudes were normalized to the beat amplitudes observed when $\hat{x}$-polarized laser excitation was used to populate the final state.

There were large inhomogeneities in the microwave power due to the divergence of the microwave beam once it left the light pipe. In addition, for $\hat{x}$-polarized pulses boundary conditions require the field to vanish at both electrodes. Because of these inhomogeneities, attempts to observe Rabi flopping were unsuccessful. Generally the excitation efficiency of a transition increased with microwave pulse area to a maximum slightly above $\approx 50\%$ and then decreased to a plateau near $\approx 50\%$, consistent with the behavior of an inhomogeneously broadened transition. Using the maximum available microwave power, we estimated average π pulse times of 100-300 ns for the various transitions.

Adiabatic passage

The excitation efficiency of an inhomogeneously broadened transition can often be increased by chirping the excitation frequency through the resonant frequency of the transition. In classical magnetic resonance this technique, known as adiabatic passage, can be pictured as a slow flipping of the effective magnetic field seen by the spins in the frame rotating at the RF frequency. If the change in direction of the effective magnetic field is slow enough, the spins adiabatically follow the field and flip.

There are two requirements for high efficiency in adiabatic passage (see discussions in [52, 86]). The first requirement is that the excitation frequency must start and end far off resonance, where

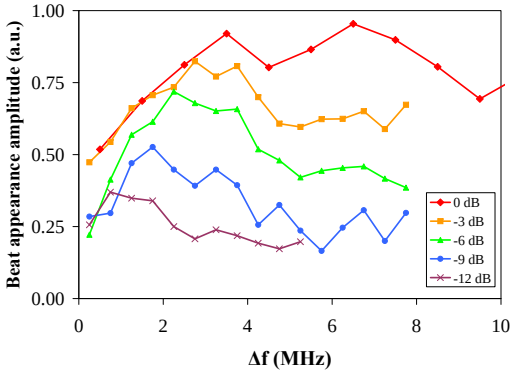

Figure 6.6: Population transfer by a frequency chirped microwave pulse. Appearance of quantum beats indicate population transfer via a frequency chirped microwave pulse. The legend indicates the relative microwave power for each of the curves. The microwave pulse width is fixed and the chirp amplitude, $\Delta f = \Delta\omega/2\pi$, is varied. As the Rabi frequency is increased, via the microwave power, the population transfer increases. Increasing the chirp amplitude increases the transfer up to the point that the rapid frequency change becomes non-adiabatic.

far means the frequency chirp amplitude, $\Delta\omega$, is large compared to the resonant Rabi frequency, i.e. $\Delta\omega \gg \Omega_R$. Second, the effective field direction must be changed adiabatically, which translates to the condition $d\omega/dt \ll \Omega_R^2$, where ω is the instantaneous microwave frequency. If, as a minimum requirement, we assume $\Delta\omega \geq 2\Omega_R$ and $d\omega/dt \leq \frac{1}{2}\Omega_R^2$, the pulse length, T_P, and Rabi frequency must obey the relation, $\Omega_R \geq 8/T_P$. Fig. 6.6 shows the unnormalized population transfer versus frequency chirp amplitude for a fixed pulse width at several microwave powers. One can see that as the Rabi frequency is increased, via the microwave power, the population transfer increases. Increasing the chirp amplitude increases the transfer up to the point that the frequency change becomes non-adiabatic.

Inhomogeneous microwave power in the cell leads to more stringent requirements. The horn used to launch the microwaves has a 3 dB beam width of $\approx$ 20 degrees. Over the 8 cm length of the cell, the intensity of the diverging microwave beam, which starts with a 2″ diameter, drops by a factor of 4. Thus Ω_R, which is proportional to the field strength, drops by a factor of 2 across the cell. For an average Rabi frequency, Ω_{ave}, the range of Rabi frequencies is approximately $0.6\Omega_{ave} - 1.2\Omega_{ave}$. Assuming the same two conditions above are met for all Rabi frequencies leads to the condition

$\Omega_{ave} \geq 27/T_p$. In general, the microwave pulses should be much faster than the quantum beat period, which is typically 3 μs, to avoid dephasing effects. A 1 μs pulse length requires a Rabi frequency, $\Omega_{ave} \geq 27$ MHz, which corresponds to a π-pulse time of 100 ns. Because we observed π-pulse times in the range of 100-300 ns, it is likely that the adiabatic passage efficiency was limited by the microwave power.

Results

The EDM state preparation scheme started once again with a $\hat{z}$-polarized laser pulse to initially populate the $|J = 1, M = 0, P-\rangle$ sublevel. Next two microwave transitions were driven to populate either the higher or lower EDM state. Two different paths were investigated. To reach the $M = \pm 1$ sublevels of the EDM states the two pulses had to have polarizations of $\hat{x}$ and $\hat{z}$.

The first path, the xz sequence, used a $\hat{x}$-polarized microwave pulse, which populates an intermediate state $|J = 2, M = +1, H\rangle - |J = 2, M = -1, H\rangle$, followed by a $\hat{z}$-polarized microwave pulse which populates either the higher or lower EDM state. The second path, the zx sequence, used a $\hat{z}$-polarized microwave pulse, which populates the $|J = 2, M = 0, H\rangle$ level , followed by a $\hat{x}$ pulse to populate the higher or lower EDM state.

Pulse frequency, width, power, frequency chirp, and delays were all optimized by maximizing beat frequency amplitudes when possible. For example, the pulse parameters of the first step of the xz sequence were optimized by maximizing the size of the $J = 2$ beats. The second step was optimized by initially populating a superposition of the $|a, J = 2, M = \pm 1\rangle$ levels with a $\hat{x}$-polarized laser pulse and optimizing the appearance of $J = 1$ beats.

The xz sequence had three disadvantages. Because quantum beats are produced in the intermediate state, imperfect population transfer from $J = 2$ to $J = 1$ in the second step left residual $J = 2$ quantum beats which could complicate data fitting and analysis. Second, the time evolution of the phase of the intermediate state superposition was concerning. The timing of the second microwave pulse was critical and its duration had to be much smaller than the beat period to prevent decoherence. Third, because the $J = 2$ Ω-doubling is three times larger than in the $J = 1$ state, the $|J = 2, M = \pm 1\rangle$ sublevels are not fully polarized. The microwave pulse parameters therefore had to be optimized for each electric field strength.

The zx sequence always had its disadvantages. Because neither the initial state or the intermediate state produce quantum beats, the first microwave pulse could not be directly optimized. The

second step was optimized by using a $\hat{z}$-polarized laser pulse to populate the $|J = 2, M = 0\rangle$ level and maximizing the appearance of $J = 1$ beats. This step had a small transition amplitude which limited transfer efficiency.

Fig. 6.5 shows the optimized results for using both sequences to populate the higher EDM state. Generally single step excitation efficiencies were $\geq 50\%$ using frequency chirped pulses. Without frequency chirping the efficiency dropped to $\approx 30-40\%$. Two step sequences had typical efficiencies of $\geq 30\%$. Transfer efficiency to the lower EDM state was systematically lower than that of the upper EDM state.

6.3.2 Microwave erasure

After trying two methods to coherently transfer the entire molecular population from the $|J = 1, M = 0\rangle$ state to the EDM states, we decided next to take the opposite tack. First, with an electric field applied, a $\hat{x}$-polarized laser pulse populates all four $|J = 1, M = \pm 1\rangle$ sublevels. The initial state is a coherent superposition of the four sublevels,

$$\left|\Psi_{\mathcal{E}}^{(x)}(T)\right\rangle = \frac{1}{\sqrt{2}}\left(e^{-i\omega_S T}\left|\Psi_{EDM,n_+}^{(x)}\right\rangle - e^{+i\omega_S T}\left|\Psi_{EDM,n_-}^{(x)}\right\rangle\right), \tag{6.8}$$

with $\omega_s = \delta_{St} + \Delta_{\Omega_1}/2$ and

$$\left|\Psi_{EDM,n_\pm}^{(x)}\right\rangle = \frac{1}{\sqrt{2}}\left(e^{+i\delta_{Z_{n_\pm}}}|J = 1, M = -1, n_\pm\rangle - e^{-i\delta_{Z_{n_\pm}}}|J = 1, M = +1, n_\pm\rangle\right), \tag{6.9}$$

are the n_+ and n_- EDM superpositions with an initial phase in the $\hat{x}$ direction. However, because of the electric field inhomogeneity in the vapor cell ($\delta\mathcal{E}/\mathcal{E} \approx 1\%$), the varying phase factors ω_S, which are dominated by the Stark shift, cause rapid decoherence. For a typical electric field of $50\,\mathrm{V\,cm^{-1}}$, the two EDM states decohere relative to each other in a few microseconds. Thus by the time data taking begins at 10-15 μs after the laser pulse, the resulting state is an incoherent mixture of the states $\left|\Psi_{EDM,n_\pm}\right\rangle$.

However, for EDM data taking we typically would like to measure only one of the EDM states each laser shot. To do this, the beat erasure method simply destroys the coherence of one of the EDM states while leaving the other intact (see Fig. 6.7) . Immediately after the laser pulse and before data-taking begins, a 10 μs microwave pulse is applied resonant with the transition

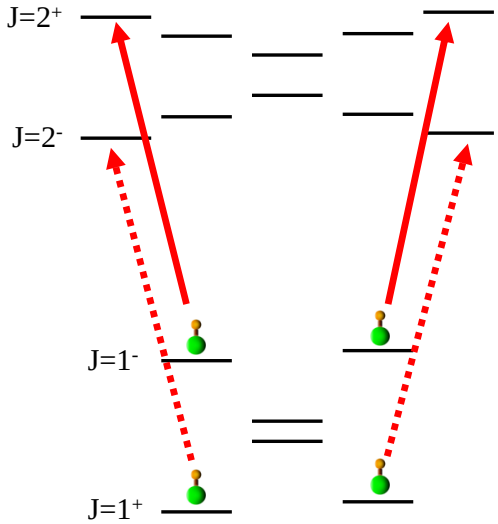

Figure 6.7: Microwave erasure. A $\hat{x}$-polarized laser pulse populates all four $M = \pm 1$ sublevels of the $J = 1$ state, which evolve to an incoherent mixture of the two EDM states. A long microwave pulse, applied before data taking, is tuned to the transition $|J = 1, M = \pm 1, H(L)\rangle \rightarrow |J = 2, M = \pm 2, H(L)\rangle$ shown by the solid(dashed) arrows. Rabi flopping during many quantum beat periods erases the coherence of the higher(lower) EDM state.

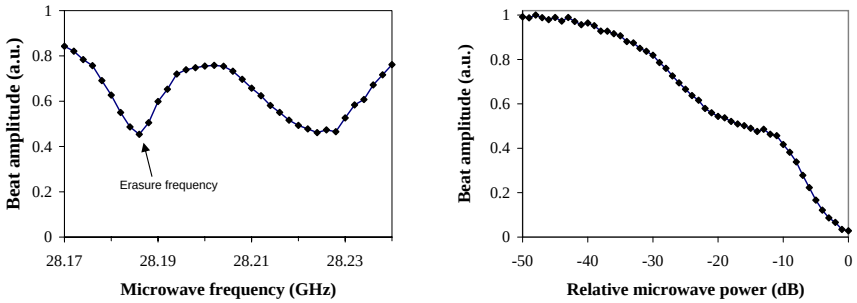

Figure 6.8: Microwave erasure evidence. Left: The beat amplitude drops to one half showing erasure of an EDM state as the microwave frequency is tuned across the $|J = 1, M = \pm 1, H(L)\rangle \rightarrow |J = 2, M = \pm 2, H(L)\rangle$ transitions. In the absence of microwaves the beat amplitude was 1. Right: With the microwave frequency at the point indicated on the left, the microwave power is increased. From -10 to -15 dB a plateau in the beat frequency, at one half its initial value, shows the erasure of one of the EDM states. Increasing the microwave power further broadens the transition until the second EDM state is also erased.

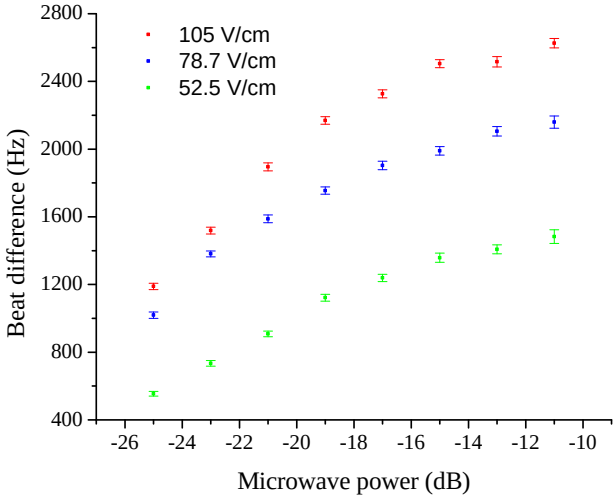

Figure 6.9: The apparent difference in the beat frequencies of the higher and lower EDM states is shown versus microwave power. The procedure for optimizing the microwave erasure, shown in Fig. 6.8, suggested erasure of one EDM state in the range of -20 to -14 dB. If the erasure was complete at these powers, the beat frequency difference should plateau rather than continue to rise.

$|J = 1, M = \pm 1, H(L)\rangle \rightarrow |J = 2, M = \pm 2, H(L)\rangle$, which is chosen for its large Clebsch-Gordon coefficient. Rabi flopping between the $J = 1$ and $J = 2$ states for many beat periods destroys the coherence of the selected EDM state. In addition, inhomogeneity of the microwave power causes different molecules to Rabi flop a different number of times. Fig. 6.8 shows the typical procedure for determining the erasure frequency and power. First the microwave frequency is scanned and the center of the desired transition is found. Next the microwave power is increased until the observed beat amplitude plateaus at one half its original value, indicating erasure of one of the EDM states.

This method, which effectively gives 50% transfer efficiency, was used during the EDM run described in the next section. However a more recent investigation has cast doubt on the claim that the selected EDM state is completely erased. Fig. 6.9 shows the difference in the measured beat frequencies, using erasure of either the upper or lower EDM state, versus microwave power. At low powers no erasure occurs and the two measurements should be nearly identical. As the power is increased we expect to see the difference plateau as one state is completely erased in each measurement. Using the same optimization method of Fig. 6.8 showed a plateau in the beat amplitude in the range of -14 to -20 dB. The beat frequency difference continues to increase at this point. By the time the microwave power is -10 dB the beat amplitude was less than 25% of its

original value, rendering the erasure method no more efficient than the microwave Raman transfer method. We do note however that to first order the unerased beats may not cause systematic effects. If the value of the fitted beat frequency is equal to a weighted average of the actual beat frequencies and the weights are unchanged throughout experimental reversals, one can show that the unerased beats only reduce the sensitvity.

6.3.3 Two frequency fitting

After the reliability of the microwave erasure method was put into question, we considered an even more radical alternative for state preparation. With the realization that the inhomogeneity of the electric field led to an incoherent mixture of the two EDM states after excitation with a $\hat{x}$-polarized laser pulse, we considered the possibility of simply doing nothing and measuring both beat frequencies simultaneously.

This method was first considered after the discovery of the electric field dependence of the magnetic g factor. Because the g factors for the higher and lower energy levels of the Ω-doublet diverge, at high enough electric and magnetic fields the beat frequencies of the two EDM states can be resolved, i.e. their frequency difference is greater than one over the $a(1)$ state lifetime. The first observations of this effect used a windowed Fourier transform of the fluorescence data. At high fields the quantum beat frequency peak split into two peaks. However modeling showed that for barely resolvable frequencies the measured separation between the two peaks in the Fourier transform was an extremely poor measure of the actual frequency difference. Because of this observation, we presumed the fitting of two frequencies would not work.

Extensive modeling in MATLAB of two frequency fitting of simulated fluorescence data with shot noise has shown that not only is fitting accurate and robust, it actually improves the sensitivity of an EDM measurement. Simulated data is fit to the function

$$S(T) = e^{-T/T_1}\left[1 + c_1 e^{-T/T_b}\cos(\omega_1 t + \phi) + c_2 e^{-T/T_b}\cos(\omega_2 t + \phi)\right] + d. \tag{6.10}$$

Because the initial phase of the quantum beats is set by the laser polarization, only one phase parameter is needed. Fig. 6.10 shows the error in the two frequency fitting routine versus both the blackbody-to-signal ratio and the beat frequency difference. Above a beat frequency difference of $\approx 4\,\mathrm{kHz}$ the errors appear to be random. After varying all other fit parameters similarly, the

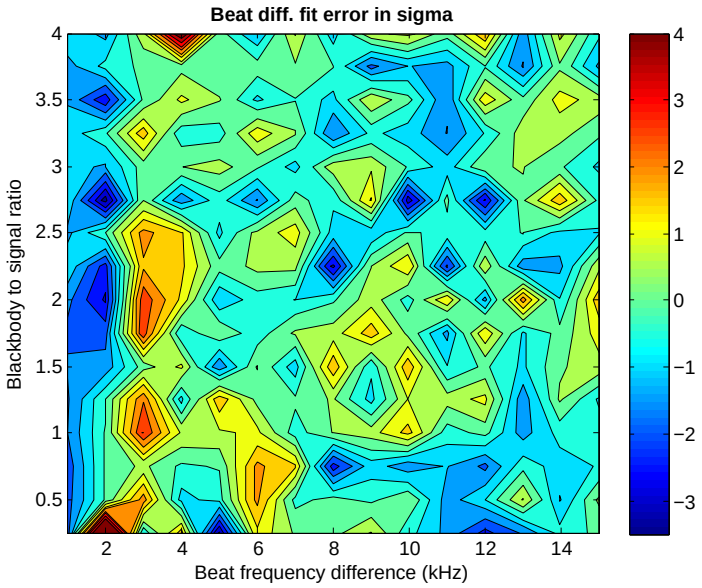

Figure 6.10: Accuracy of two frequency fitting. Two frequency data is simulated with shot noise and fit to Eq. (6.10). The color scale shows the difference between the fitted beat frequency difference and the actual beat frequency difference used in the simulation. The differences are expressed in units of the $1-\sigma$ uncertainty in the frequency difference.

two frequency fit routine appears robust as long as the beat frequency difference is approximately greater than $1/(2\pi T_1)$, which is perhaps not too surprising. In addition, the uncertainty in the fitted frequencies is consistently $\sqrt{2}$ times lower than an analogous fit with the usual one frequency routine. We speculate that this increased senstivity is due to the fact that only one phase is needed for both beat frequencies.

6.4 Reversals and rejection of systematics

The beat frequency from a given measurement during the EDM experiment is dependent on three experimental parameters: the direction of the laboratory electric field, the direction of the laboratory magnetic field, and whether the measurement was made in the higher or lower energy EDM state. By combining measurements from various combinations of these parameters, limits can be placed on systematic effects.

During an EDM measurement the molecules are fully polarized so the lower(higher) energy state of the Ω-doublet always corresponds to the state polarized with(against) the electric field,

$n_+(n_-)$. For notational convenience below we define $N = +1$ for the n_+ state and $N = -1$ for the n_- state. The laboratory electric and magnetic fields are defined to be positive when pointing upwards along the laboratory z axis.

The energy of a given sublevel in the EDM state (see Chapter 3), including the electric field dependence of g is

$$E(M,N,\mathcal{E},B) = \left[\overline{g} + \eta\,|\mathcal{E}|\,\mathrm{sgn}(N)\right]M\mu B + d_e\mathcal{E}_{int}M\,\mathrm{sgn}(N)\,\mathrm{sgn}(\mathcal{E}) - \mathrm{sgn}(N)\delta_{St}(|\mathcal{E}|). \tag{6.11}$$

where $\overline{g} \approx G_{parallel}/2 = 0.93$ is the average g factor; $\eta = 3.2\times10^{-5}\,\mathrm{cm\,V^{-1}}$ gives the g factor dependence on $\mathcal{E}$; $\mathcal{E}_{int} = -6.1\times10^{24}\,\mathrm{Hz/(e\cdot cm)}$ is the effective internal electric field; and $\mathrm{sgn}(N)\,\mathrm{sgn}(\mathcal{E}) = \mathrm{sgn}(\mathcal{E}_{int})$ is the sign of the internal electric field in the laboratory frame. The measured beat frequencies are the magnitudes of the difference in energy of each $M = \pm1$ pair

$$\begin{aligned}\omega(N,\mathcal{E},B) &= |E(M=+1,N,\mathcal{E},B) - E(M=-1,N,\mathcal{E},B)| \\ &= \left|2\overline{g}\mu B + 2\eta\mu\,|\mathcal{E}|\,B\,\mathrm{sgn}(N) + 2d_e\mathcal{E}_{int}\,\mathrm{sgn}(N)\,\mathrm{sgn}(\mathcal{E})\right| \\ &= 2\overline{g}\mu\,|B| + 2\eta\mu\,|\mathcal{E}|\,|B|\,\mathrm{sgn}(N) + 2d_e\mathcal{E}_{int}\,\mathrm{sgn}(N)\,\mathrm{sgn}(\mathcal{E})\,\mathrm{sgn}(B).\end{aligned} \tag{6.12}$$

In the last line we have used the fact that the magnitude of the first term is always largest and $\left|x+y\right| = |x| + \mathrm{sgn}(x)\left|y\right|$ for $|x| > \left|y\right|$. Written in this manner we can explicitly see the dependence of the various terms on the experimental reversals. For example, the EDM term is odd, i.e. changes sign, with all three reversals $N, \mathcal{E}$, and B.

Eq. (6.11) gives the energy of the sublevels in the absence of experimental imperfections. Here we consider three systematic effects: non-reversing components along the z axis of the magnetic field, B_{nr}, and electric field, $\mathcal{E}_{nr}$, and an additional magnetic field, $B_{leak} = \alpha\mathcal{E}$, along the $\hat{z}$ axis due to leakage currents following a helical path between the electrodes. Using the replacement $B \to B + B_{nr}$, the non-reversing magnetic field component leads to extra terms in Eq. (6.12),

$$\delta\omega_{B_{nr}} = 2\overline{g}\mu B_{nr}\,\mathrm{sgn}(B) + 2\eta\mu\,|\mathcal{E}|\,B_{nr}\,\mathrm{sgn}(N)\,\mathrm{sgn}(B). \tag{6.13}$$

The replacement $\mathcal{E} \to \mathcal{E} + \mathcal{E}_{nr}$ affects only the second term of Eq. (6.12) and leads to the extra term

$$\delta\omega_{\mathcal{E}_{nr}} = 2\eta\mu\mathcal{E}_{nr}\,|B|\,\mathrm{sgn}(\mathcal{E})\,\mathrm{sgn}(N). \tag{6.14}$$

An additional term arises from the cross term of both non-reversing components,

$$\delta\omega_{\mathcal{E}_{nr},B_{nr}} = 2\eta\mu\mathcal{E}_{nr}B_{nr}\,\mathrm{sgn}(N)\,\mathrm{sgn}(\mathcal{E})\,\mathrm{sgn}(B). \tag{6.15}$$

The leakage currents contribute an additional magnetic field and give rise to the two terms

$$\delta\omega_{B_{leak}} = 2\overline{g}\mu\alpha\,|\mathcal{E}|\,\mathrm{sgn}(\mathcal{E})\,\mathrm{sgn}(B) + 2\eta\mu\alpha\mathcal{E}^2\,\mathrm{sgn}(N)\,\mathrm{sgn}(\mathcal{E})\,\mathrm{sgn}(B). \tag{6.16}$$

Next we consider combinations of all eight beat frequencies which are even or odd in each reversal,

$$\Delta\omega(P_N,P_\mathcal{E},P_B) = \sum_{\mathrm{sgn}(N)}\sum_{\mathrm{sgn}(\mathcal{E})}\sum_{\mathrm{sgn}(B)}(P_N)^{-\mathrm{sgn}(N)}(P_\mathcal{E})^{-\mathrm{sgn}(\mathcal{E})}(P_B)^{-\mathrm{sgn}(B)}\omega\Big(\mathrm{sgn}(N)\,|N|\,,\mathrm{sgn}(\mathcal{E})\,|\mathcal{E}|\,,\mathrm{sgn}(B)\,|B|\Big), \tag{6.17}$$

where P_X is the parity of the $X = N,\mathcal{E},B$ reversal, i.e +1 for an even combination and −1 for an odd combination. For example, the EDM combination, which is odd in all three reversals, is explicitly

$$\begin{aligned}\Delta\omega(-1,-1,-1) &= \sum(-1)^{(-\mathrm{sgn}\,N-\mathrm{sgn}\,\mathcal{E}-\mathrm{sgn}\,B)}\omega\Big(\mathrm{sgn}(N)\,|N|\,,\mathrm{sgn}(\mathcal{E})\,|\mathcal{E}|\,,\mathrm{sgn}(B)\,|B|\Big)\\ &= \omega\Big(+1,+|\mathcal{E}|\,,+|B|\Big)-\omega\Big(-1,+|\mathcal{E}|\,,+|B|\Big)-\omega\Big(+1,-|\mathcal{E}|\,,+|B|\Big)\\ &\quad+\omega\Big(-1,-|\mathcal{E}|\,,+|B|\Big)-\omega\Big(+1,+|\mathcal{E}|\,,-|B|\Big)+\omega\Big(-1,+|\mathcal{E}|\,,-|B|\Big)\\ &\quad+\omega\Big(+1,-|\mathcal{E}|\,,-|B|\Big)-\omega\Big(-1,-|\mathcal{E}|\,,-|B|\Big).\end{aligned} \tag{6.18}$$

One can quickly check that, for a given combination, only terms with the same parity as the combination will appear. As an example, the N-odd, B-odd combination only has terms proportional to $\mathrm{sgn}(N)\,\mathrm{sgn}(B)$.

Table 6.1 summarizes the surviving terms for each of the combinations using Eq. (6.12) and the terms from non-reversing magnetic and electric fields [Eq. (6.13),Eq. (6.14), and Eq. (6.15)], and magnetic fields due to leakage currents [Eq. (6.16)]. Many of the combinations can be used to directly place a limit on systematic effects. The suppression by the Ω-doublet reversal, i.e. odd N combinations, is evident by their dependence on the g factor difference of the $n_\pm$ states, $\Delta g = 2\eta\,|\mathcal{E}|$. At a typical electric field of $50\,\mathrm{V\,cm^{-1}}$, $\Delta g = 3\times10^{-3}$. Finally, one can see that in the

Table 6.1: Beat frequency combinations and systematic effects

N	$\mathcal{E}$	B	Terms	Derived quantity
+	+	+	$16\overline{g}\mu\,\lvert B\rvert$	$\lvert B\rvert$
+	+	-	$16\overline{g}\mu B_{nr}$	B_{nr}
+	-	+	0	
+	-	-	$16\overline{g}\mu B_{leak}$	B_{leak}
-	+	+	$8\Delta g\mu\,\lvert B\rvert$	$\lvert\mathcal{E}\rvert$
-	+	-	$8\Delta g\mu B_{nr}$	
-	-	+	$16\eta\mathcal{E}_{nr}\mu\,\lvert B\rvert$	$\mathcal{E}_{nr}$
-	-	-	$16d_e\mathcal{E}_{int} + 16\eta\mathcal{E}_{nr}\mu B_{nr} + 8\Delta g\mu B_{leak}$	d_e

EDM combination,

$$\Delta\omega_{EDM} = \Delta\omega(-1,-1,-1) = 16d_e\mathcal{E}_{int} + 16\eta\mathcal{E}_{nr}\mu B_{nr} + 8\Delta g\mu B_{leak}, \tag{6.19}$$

the terms from systematic effects are the product of two or three small numbers.

To estimate the size of the systematic terms we assume that the magnetic field can be reversed to a part per thousand. With the current sensitivity of the experiment a typical magnetic field, $B = 100\,\text{mG}$, can be measured to better than a part per thousand in a single shot. We estimate the electric field reversal at $\mathcal{E} = 50\,\text{V cm}^{-1}$ to be accurate to 10^{-4}. Yong Jiang [52] has built and extensively tested a high voltage source for the electric field that can reverse to better than 2.5×10^{-5}. With these assumptions the second term, $16\eta\mathcal{E}_{nr}\mu B_{nr}$, after dividing by the eight measurements, gives a shift per measurement of $\approx 50\,\mu\text{Hz}$ or a false EDM of 4×10^{-30} e·cm. For the third term, a typical leakage current of $10\,\mu\text{A}$ in a 8 cm loop around the cell body gives a magnetic field, $B_{leak} = 200\,\text{nG}$. This leads to a shift per measurement of $\Delta g\mu B_{leak} = 900\,\mu\text{Hz}$ or a false EDM of 7×10^{-29} e·cm.

More important is the fact that we do not have to rely on these estimates of the systematic effects in the EDM combination. Limits can be directly placed on each of the factors, B_{leak}, $\mathcal{E}_{nr}$, and B_{nr}, using the other beat frequency combinations. Because these factors are suppressed by two to three orders of magnitude in the EDM combination, *as the sensitivity of the experiment is improved, non-zero values for any of these factors will be well measured before they can lead to a systematic effect*.

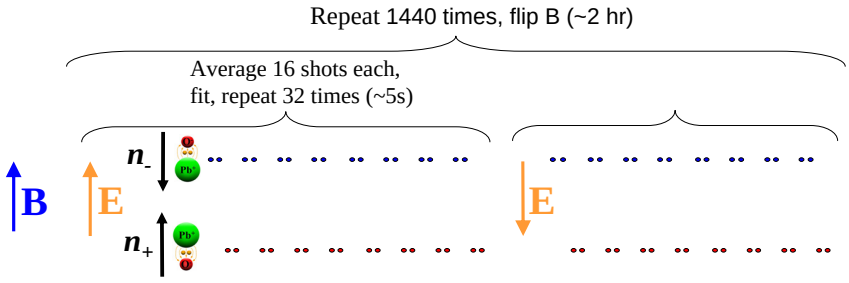

Figure 6.11: Order of reversals during EDM data taking. Every other laser shot the microwave erasure frequency was switched to change between the n_+ and n_- EDM states. 16 shots of each state were averaged and fit. This was repeated 16 times for a total time of about 5 s. This procedure was repeated 1440 times with the electric field reversed each iteration. This constitutes a single dataset. Next, the magnetic field was reversed and the magnetic shields degaussed. The entire process then repeated.

6.5 EDM data and results

In 2008, we took 43 hours of EDM data to verify that systematic errors in the experiment were under control. At that time the sensitivity was significantly lower than it is today. The molecules were excited on the 572 nm transition, $|X, v = 1\rangle \rightarrow |a, v' = 5\rangle$, and detected on the transition $|a, v' = 5\rangle \rightarrow |X, v = 1\rangle$ at 548 nm. Two narrowband interference filters centered at 554 nm were used along with a wideband IF filter and KG4 IR blocking glass. The blackbody size was significantly larger than the signal size, as we were still using foil heat shields on the oven. Two magnetic shields were installed.

The data taking procedure was as follows: Every other laser shot the microwave erasure frequency was switched to change between the n_+ and n_- EDM states. After 16 shots of each state the data was averaged and fit. This process was repeated 16 times for a total time of about 5 s. Next the electric field direction was switched. The electrode voltage is generated by a high voltage amplifier connected to a programmable precision voltage standard (EDC 501J). Software ensured that the voltage was smoothly ramped over a few tens of milliseconds to prevent significant currents, due to the capacitance of the cables, which could magnetize the magnetic shields. After the electric field direction was switched, data taking is paused for 100 ms to let any charging currents subside (no significant currents have been observed). This process was repeated 1440 times to give one dataset of about 2 hours. A gaussian is fit to the histograms of each of the four possible even or

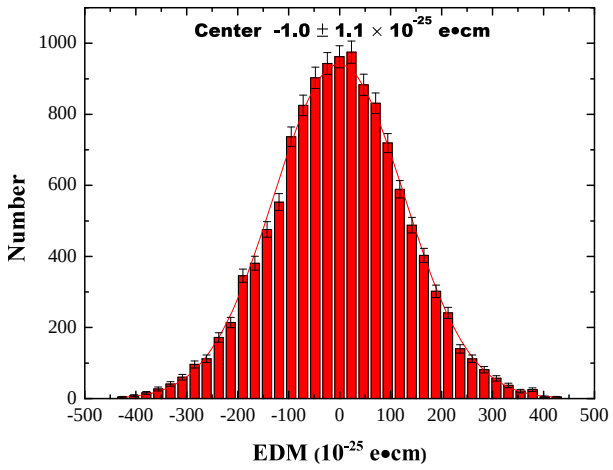

Figure 6.12: Histogram of the $\mathcal{E}$-odd, N-odd combination for a dataset in the 2008 EDM run. In general, the Gaussian fits to the histograms were very good, with reduced χ-squared values close to 1.

odd combinations of the $\mathcal{E}$ and N reversals (see Fig. 6.12). The combinations odd in the electric field are subtracted pairwise in the order they were recorded. The central value and uncertainty are recorded for each fit parameter. After this, the magnetic field direction is reversed and the shields are degaussed. The process then starts all over.

Fig. 6.13 shows the final result from the 2008 EDM run with each point representing a pairwise subtraction of the $\mathcal{E}$-odd, N-odd combination for datasets with oppositely directed magnetic fields. Averaging the values from all datasets with the same magnetic field first, and then subtracting did not change the result significantly. The 1-σ statistical EDM uncertainty of 2×10^{-26} e· cm is over an order of magnitude worse than the Berkeley limit. In addition, we estimate that imperfections in the microwave erasure method reduces the actual EDM sensitivity by a factor of 25%. However, using the other beat frequency combinations we placed limits on systematic effects: $\mathcal{E}_{nr} < 90\,\mathrm{mV\,cm^{-1}}$, $B_{nr}/B < 1\%$, and $B_{leak} < 400\,\mathrm{nG}$, all at 95% confidence level. In the EDM combination this leads to a limit on a false EDM of $< 9 \times 10^{-28}$e·cm (95% c.l.). Combined with the statistical uncertainty, the final result is $\delta d_e = (-19 \pm 25 \pm 0.5) \times 10^{-27}$e·cm.

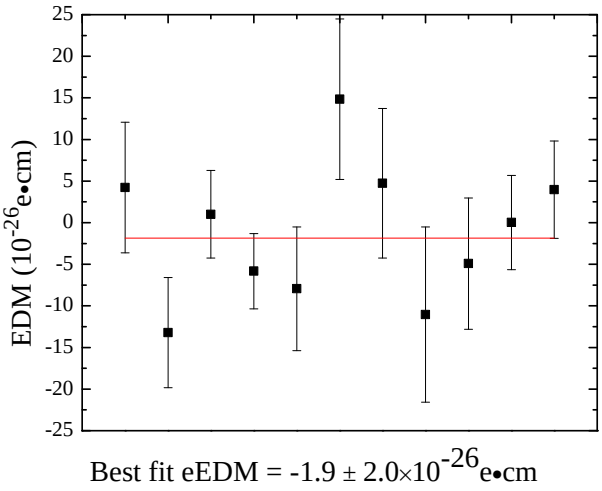

Figure 6.13: EDM results from the 2008 data run.

Chapter 7

Microwave absorption

In this chapter, I discuss a proposed second generation of the PbO experiment based on detection via microwave absorption. This proposal requires a completely new apparatus with several technically challenging requirements. The predicted statistical sensitivity is orders of magnitude better than that of the current apparatus. As a proof-of-principle we measured microwave absorption in the excited $a(1)$ state with the current apparatus. In the end it was decided that the ThO beam experiment [30], which is technically easier and predicted to have an even higher sensitivity, was a better focus of manpower and resources. However, the microwave absorption techniques turned out to be useful for characterizing the PbO vapor pressure and pulsed laser excitation efficiency. Both values were measured and found to be much smaller than originally expected.

7.1 Basic principle

The main idea of the second generation experiment is to replace the current detection method of fluorescence light collection with an absorption measurement. Instead of passively observing interference between spontaneous decay paths that lead to a common ground state, interference would be seen as the quantum beat states were driven to a common excited state (see Fig. 7.1).

Fluorescence detection is typically inefficient for several reasons. First, it requires a large collection solid angle. In the current apparatus the walls of the vapor cell were designed to be as thin as was structurally possible. Our collection solid angle is limited only by the size of the cell windows. Maintaining the same solid angle is difficult as the size of the vapor cell increases. Even with

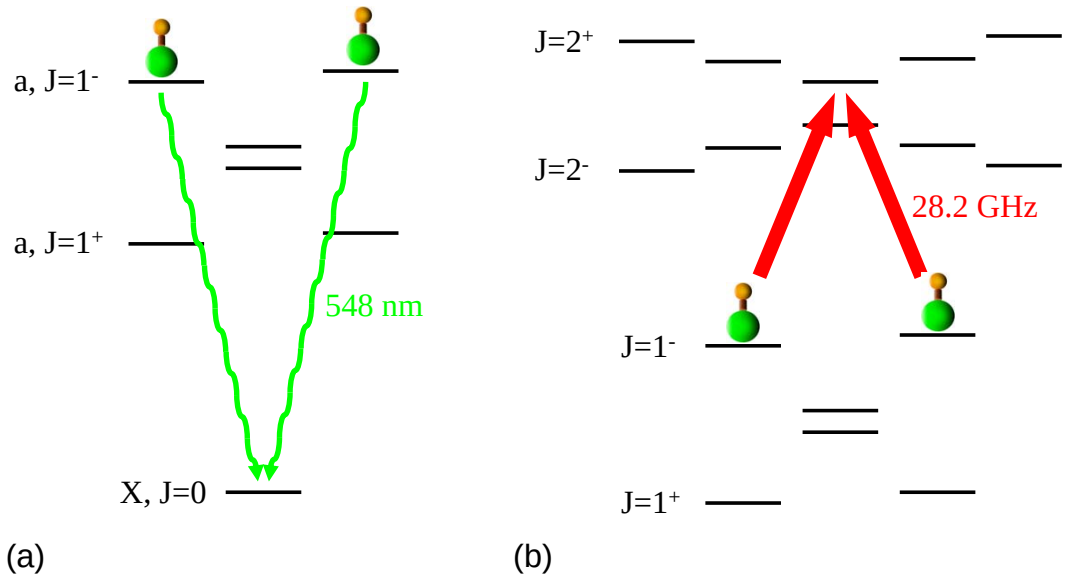

Figure 7.1: Spontaneous optical decay versus microwave absorption detection schemes. (a) Quantum beats are seen in fluorescence from the interference of two spontaneous decay pathways to a common ground state. (b) Similar beats occur in microwave absorption due to the interference of two excitation pathways to a common final state.

efficient light collection there are many other inefficiencies downstream in the detection process. Every surface the light passes through (e.g. lightpipes, cell windows, filters, etc.) contribute Fresnel reflection losses. The high temperature of our apparatus precludes the use of anti-reflection coatings on many of the surfaces. A spectral filter is required to eliminate background from blackbody radiation emanating from the hot surfaces of the vapor cell (and possibly the heating foils themselves). Finally the detector itself is usually inefficient. We use the best available photomultiplier tubes (PMT) which have a quantum efficiency of only 15%. In the end, we collect light from less than 10^{-3} of the molecules in the EDM state (see [81] for a complete discussion of detection choices).

Absorption measurements eliminate many of these difficulties. Detection solid angle is not an issue since the absorption beam is fully collected by the detector. Increasing the cell length or using a resonant cavity increases the efficiency to which the molecules are used. Backgrounds are still a concern, but narrowband filters can be used since detection occurs at a single wavelength. Finally the small solid angle used allows one to focus the absorption beam onto a smaller, more efficient detector.

Originally it was proposed to use laser absorption in the second generation PbO experiment

to increase detection efficiency. A search was carried out for states with strong coupling to a state of PbO. No states were found with a coupling sufficient for an absorption measurement [91]. The Thomas-Reiche-Kuhn sum rule of oscillator strengths and known transitions suggests such a state much exist [76]. It is possible that this unknown state is simply out of the reach of convenient laser wavelengths.

While exploring the possibility of using microwave Raman transitions for state preparation (see Section 6.3.1), it was realized that the microwave coupling between rotational lines is very strong. In fact, as we will show in Section 7.4, absorption can be seen in the current vapor cell. In theory, a longer cell with a microwave cavity around it could give absorption signals on the order of a few percent and an increase in signal-to-noise by orders of magnitude.

7.2 Signal to Noise

In this section we go through a detailed derivation of the signal-to-noise ratio for some common detection schemes used in microwave absorption measurements. We start with a few formal mathematical definitions and then delve into the details of detection with a square law ("power") detector for both constant and amplitude modulated signals with background noise. We consider the relative importance of thermal and shot noise. In retrospect, calculation of the theoretical signal to noise can be simply estimated. However, a couple differences between microwave and optical absorption experiments made our initial attempts confusing. First was a difference in terminology. Most of the literature on microwave technology is in engineering books. Differences in the definition of signal-to-noise between physicists and engineers made it unclear whether we cared about the signal-to-noise of the output voltage or power on our detector. Second, being used to optical experiments, we did not realize that the dominant source of noise in microwave measurements comes from thermal noise (or more specifically a cross term between the thermal noise and signal) rather than shot noise. To verify that our calculations were correct we carried out an in-depth analysis borrowing heavily from Chapter 12 of Davenport & Root [121].

7.2.1 Definitions

First let us give a few definitions and notations. The statistical average of a random process is defined and denoted by

$$\mathrm{E}[y(x_t)] \equiv \int_{-\infty}^{\infty} y(x_t)p(x_t)\,dx_t \tag{7.1}$$

where x_t is a random variable at time t and $p(x_t)$ is the probability density of x_t. The autocorrelation function is denoted by

$$R_y(t_1, t_2) \equiv \mathrm{E}(y_{t_1} y_{t_2}). \tag{7.2}$$

If y_t is stationary (i.e. the probability density is independent of t) then we can define $\tau = t_1 - t_2$ and

$$R_y(\tau) \equiv R_y(t_1, t_2). \tag{7.3}$$

From the Wiener-Khinchin theorem the power spectral density (PSD) is given by the Fourier Transform of the autocorrelation function

$$S_y(f) \equiv \int_{-\infty}^{\infty} R_y(\tau)e^{-i2\pi f\tau}\,d\tau. \tag{7.4}$$

The units of S_y are $[y]^2/Hz$. Note that we will be using the double sideband (DSB) power spectral density throughout this chapter unless otherwise noted. Also note that for a random variable with zero mean the variance is given by

$$R_y(0) = \mathrm{E}\left(y^2\right) = \sigma_y^2 = \int_{-\infty}^{\infty} S_y(f)\,df. \tag{7.5}$$

7.2.2 Square Law Detector

General signal with noise

Now we consider a square law detector, that is a detector with a response $y(t)$ to a signal $x(t)$ given by

$$y(t) = x^2(t). \tag{7.6}$$

To find the autocorrelation we use the relation (see 8-121 in [121])

$$\mathrm{E}(x_1x_2x_3x_4) = \mathrm{E}(x_1x_2)\mathrm{E}(x_3x_4) + \mathrm{E}(x_1x_3)\mathrm{E}(x_2x_4) + \mathrm{E}(x_1x_4)\mathrm{E}(x_2x_3). \tag{7.7}$$

Thus for the output we have

$$\mathrm{E}(y_1y_2) = \mathrm{E}\left(x_1^2x_2^2\right) = \mathrm{E}\left(x_1^2\right)\mathrm{E}\left(x_2^2\right) + 2\left[\mathrm{E}(x_1x_2)\right]^2. \tag{7.8}$$

The autocorrelation of the output is then

$$R_y(\tau) = \mathrm{E}(y_1y_2) = \sigma_x^4 + 2R_x^2(\tau). \tag{7.9}$$

Using Eq. (7.4) the PSD of the output is

$$\begin{aligned} S_y(f) &= \sigma_x^4\delta(f) + 2\int_{-\infty}^{\infty} R_x^2(\tau)e^{-i2\pi f\tau}\,d\tau \\ &= \sigma_x^4\delta(f) + 2\int_{-\infty}^{\infty} S_x(f')e^{i2\pi f'\tau}\,df' \int_{-\infty}^{\infty} R_x(\tau)e^{-i2\pi f\tau}\,d\tau \\ &= \sigma_x^4\delta(f) + 2\int_{-\infty}^{\infty} S_x(f')S_x(f-f')\,df', \end{aligned} \tag{7.10}$$

i.e. a DC power level of σ_x^4 and a PSD given by the convolution of S_x with itself.

Now let $x(t) = s(t) + n(t)$ where $s(t)$ and $n(t)$ represent the signal and noise, respectively. For simplicity assume both have zero mean and are statistically independent random processes. The autocorrelation of the output is

$$\begin{aligned} R_y(t_1,t_2) &= \mathrm{E}\left[(s_1+n_1)^2(s_2+n_2)^2\right] \\ &= \mathrm{E}\left(s_1^2s_2^2\right) + 4\mathrm{E}(s_1s_2)\mathrm{E}(n_1n_2) + \mathrm{E}\left(s_1^2\right)\mathrm{E}\left(n_2^2\right) + \mathrm{E}\left(s_1^2\right)\mathrm{E}\left(n_2^2\right) + \mathrm{E}\left(n_1^2n_2^2\right), \end{aligned} \tag{7.11}$$

where we used the fact that s and n are statistically independent and have zero means. This gives

$$R_y(\tau) = R_{s^2}(\tau) + 4R_s(\tau)R_n(\tau) + 2\sigma_s^2\sigma_n^2 + R_{n^2}(\tau), \tag{7.12}$$

using the definition $R_{a^2}(\tau) \equiv \mathrm{E}\left[a_1^2a_2^2\right]$. Thus the autocorrelation of the output contains three types of

terms

$$R_y(\tau) = R_{s\times s}(\tau) + R_{s\times n}(\tau) + R_{n\times n}(\tau). \tag{7.13}$$

Each term results from the interaction of

$$\text{signal with signal} \qquad R_{s\times s}(\tau) \equiv R_{s^2}(\tau), \tag{7.14a}$$

$$\text{signal with noise} \qquad R_{s\times n}(\tau) \equiv 4R_s(\tau)R_n(\tau) + 2\sigma_s^2\sigma_n^2, \tag{7.14b}$$

$$\text{noise with noise} \qquad R_{n\times n}(\tau) \equiv R_{n^2}(\tau). \tag{7.14c}$$

The output PSD can be separated similarly into three parts by taking the Fourier transform of the autocorrelations

$$S_y(f) = S_{s\times s}(f) + S_{s\times n}(f) + S_{n\times n}(f). \tag{7.15}$$

Constant sine wave with noise

Now consider the case of a sine wave signal with Gaussian noise

$$x(t) = s(t) + n(t) = \sqrt{2}V\cos(\omega_c t + \theta) + n(t), \tag{7.16}$$

where V is the constant RMS amplitude, and θ is a random variable uniformly distributed over $[0, 2\pi]$. Note, as we will see below, θ is just a tool to help with taking expectation values; it is not the noise itself.

First the autocorrelation and the PSD of the signal are

$$\begin{aligned} R_s(t_1, t_2) &= 2V^2\mathrm{E}[\cos(\omega_c t_1 + \theta)\cos(\omega_c t_2 + \theta)] \\ &= V^2\cos[\omega_c(t_1 - t_2)] + V^2\frac{1}{2\pi}\int_0^{2\pi}\cos[\omega_c(t_1 + t_2) + 2\theta]\, d\theta \\ &= V^2\cos\omega_c\tau \end{aligned} \tag{7.17}$$

$$\Rightarrow S_s(f) = \frac{V^2}{2}\left[\delta(f - f_c) + \delta(f + f_c)\right]. \tag{7.18}$$

Half of the power is at f_c and half is at $-f_c$ as expected. Then from Eq. (7.14b) we have

$$R_{s\times n}(\tau) = 4V^2\cos(\omega_c\tau)R_n(\tau) + 2V^2\sigma_n^2 \tag{7.19}$$

$$\Rightarrow S_{s\times n}(f) = 2V^2[S_n(f-f_c) + S_n(f+f_c)] + 2V^2\sigma_n^2\delta(f). \tag{7.20}$$

Using Eq. (7.14a) the signal with signal autocorrelation and PSD are

$$\begin{aligned} R_{s\times s}(\tau) &= 4V^4\mathrm{E}\Big[\cos^2(\omega_c t_1+\theta)\cos^2(\omega_c t_2+\theta)\Big] \\ &= V^4 + \frac{V^4}{2}\cos(2\omega_c\tau) \end{aligned} \tag{7.21}$$

$$\Rightarrow S_{s\times s}(f) = V^4\delta(f) + \frac{V^4}{4}\left[\delta(f-2f_c) + \delta(f+2f_c)\right]. \tag{7.22}$$

Finally, from Eq. (7.10), the noise with noise PSD is

$$S_{n\times n} = \sigma_n^4\delta(f) + 2\int_{-\infty}^{\infty} S_n(f')S_n(f-f')\,df'. \tag{7.23}$$

The above results hold for any noise source. Now let S_n be a constant A over an input bandwidth B_{in} centered on f_c (see Fig. 7.2b). In this case, from Eq. (7.20) and Eq. (7.23), we have

$$S_{s\times n}(f) = 4V^2AB_{in}\delta(f) + \begin{cases} 4V^2A & \text{if } -B_{in}/2 < f < B_{in}/2, \\ 2V^2A & \text{if } -B_{in}/2 < |f| - 2f_c < B_{in}/2, \\ 0 & \text{otherwise,} \end{cases} \tag{7.24}$$

$$S_{n\times n}(f) = (2AB_{in})^2\delta(f) + \begin{cases} 4A^2(B_{in}-|f|) & \text{if } -B_{in} < f < B_{in}, \\ 2A^2(B_{in}-\big||f|-2f_c\big|) & \text{if } -B_{in} < |f| - 2f_c < B_{in}, \\ 0 & \text{otherwise,} \end{cases} \tag{7.25}$$

where we have used

$$\sigma_n^2 = \int_{-\infty}^{\infty} S_n\,df = 2AB_{in}. \tag{7.26}$$

Combining Eq. (7.22), Eq. (7.24), and Eq. (7.25) and dropping high frequency terms which can be

filtered at the output we have

$$S_y(f) = \left(V^2 + 2AB_{in}\right)^2 \delta(f) + \begin{cases} 4V^2A + 4A^2(B_{in} - |f|) & \text{if } 0 < |f| \leq B_{in}/2, \\ 4A^2(B_{in} - |f|) & \text{if } B_{in}/2 < |f| \leq B_{in}, \\ 0 & \text{otherwise.} \end{cases} \tag{7.27}$$

Note that this is the PSD of the output voltage, i.e., it has units power per hertz. We are interested in the output voltage since it is proportional to input power. The input signal power is $P_s \equiv V^2$ and the input noise power is $P_{n,in} \equiv 2AB_{in}$. Thus the output DC voltage of $V^2 + 2AB_{in}$ is simply the sum of the input signal and noise powers as we would expect for a "power" detector.

We can interpret the output of the square law detector simply as the result of mixing input frequencies. The quadratic output multiplies two sine waves which is equivalent to summation of two sine waves at the sum and difference of the two frequencies. In the $s \times s$ output we see just this: a DC term and a term at twice the input frequency. Similarly the $n \times n$ output consists of a DC term from the mixing of equal noise input frequencies and a convolution that is simply the summation of each pair of input noise frequencies at a given difference in frequency. This gives some intuition to the shape of the output (see Fig. 7.2). For example, the fact that convolution term in the $n \times n$ output is largest at $f_{out} = 0$ and drops linearly to zero at $f_{out} = \pm B_{in}$ is simply because there are fewer and fewer "pairs" of input frequencies, i.e. those at $f_c - f_{out}/2$ and $f_c + f_{out}/2$, that can mix to give an output at f_{out}.

Since we detect near DC and the output bandwidth of our detector is much smaller than the input bandwidth we can essentially use the PSD at $f = 0$ over some small output bandwidth B_{out} (making sure to include a factor of 2 for positive and negative f). The contribution to the output noise power from $S_{s\times n}$ is then

$$\sigma^2_{s\times n} = 8V^2AB_{out} = 4P_sP_{n,out}, \tag{7.28}$$

and the contribution from $S_{n\times n}$ is

$$\sigma^2_{n\times n} = 8A^2B_{in}B_{out} = 2P_{n,in}P_{n,out}, \tag{7.29}$$

where we have defined the output noise power $P_{n,out} \equiv 2AB_{out}$. To be more precise $P_{n,out}$ is the power from the input noise PSD over the output bandwidth. Note that in some engineering texts

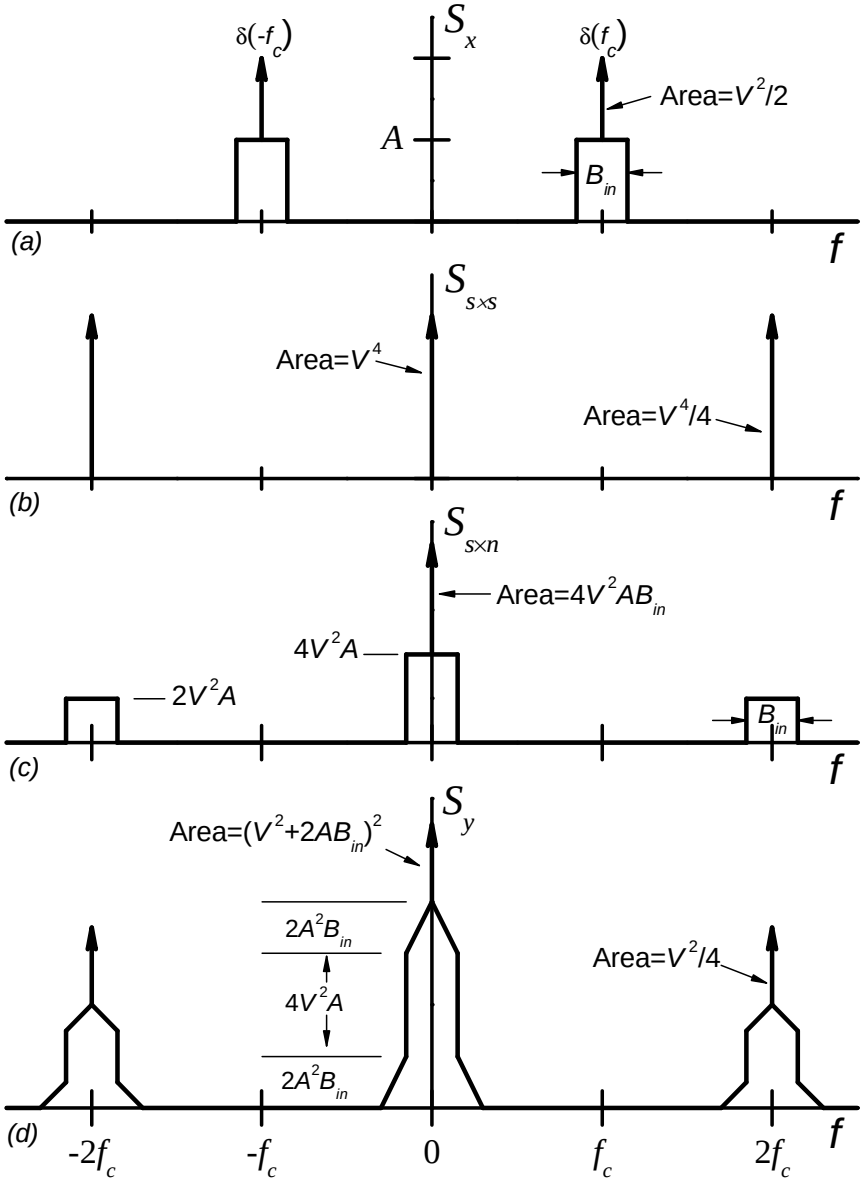

Figure 7.2: Square law detector PSD functions for a sinusoidal input with noise. a) Input signal at f_c and constant noise over a bandwidth B_{in}. b) Signal × signal term on the output. c) Signal × noise term on the output. d) Total output of b), c), and a noise × noise term.

this can be alternatively expressed as

$$\sigma_{n\times n} = 2AB_{eq} \tag{7.30}$$

with $B_{eq} = \sqrt{2B_{in}B_{out}}$ called the equivalent noise bandwidth.

Since

$$\left(\frac{S}{N}\right)_{in} = \frac{P_s}{P_{n,in}} \tag{7.31}$$

we see that

$$\frac{\sigma^2_{s\times n}}{\sigma^2_{n\times n}} = \frac{4P_sP_{n,out}}{2P_{n,in}P_{n,out}} = 2\frac{P_s}{P_{n,in}} = 2\left(\frac{S}{N}\right)_{in}. \tag{7.32}$$

Thus the output noise contribution from $s \times n$ dominates as $(S/N)_{in}$ increases.

The output signal-to-noise depends only on the input signal-to-noise and the input and output bandwidths.

$$\left(\frac{S}{N}\right)_{out} = \frac{P_s^2}{4P_sP_{n,out} + 2P_{n,in}P_{n,out}} = \frac{1}{2}\left(\frac{S}{N}\right)_{in}\frac{(S/N)_{in}}{1 + 2(S/N)_{in}}\frac{B_{in}}{B_{out}} \tag{7.33}$$

For $(S/N)_{in} >> 1$

$$\left(\frac{S}{N}\right)_{out} \approx \frac{1}{4}\left(\frac{S}{N}\right)_{in}\frac{B_{in}}{B_{out}} \tag{7.34}$$

Note here we are following the engineering convention of always using ratios of powers for signal-to-noise. For a square law detector the power of the output is proportional to the input power squared. In our experiment, the uncertainty comes from fitting a curve to the output voltage so *we must use the signal-to-noise on the output voltage*. On the output voltage

$$\left(\frac{S}{N}\right)_{out,V} \approx \frac{1}{2}\sqrt{\left(\frac{S}{N}\right)_{in}\frac{B_{in}}{B_{out}}} = \frac{1}{2}\sqrt{\frac{P_s}{P_{n,out}}} \tag{7.35}$$

Modulated sine wave plus noise

Now consider a modulated sine wave plus Gaussian noise

$$x(t) = \sqrt{2}v(t)\cos(\omega_c t + \theta) + n(t). \tag{7.36}$$

Assuming v is statistically independent of θ the autocorrelation of the signal is

$$\begin{aligned} R_s(\tau) &= 2\mathrm{E}(v_t v_{t+\tau})\mathrm{E}\{\cos(\omega_c t+\theta)\cos[\omega_c(t+\tau)+\theta]\} \\ &= R_v(\tau)\cos(\omega_c\tau) \qquad (7.37) \\ \Rightarrow S_s(f) &= \frac{1}{2}[S_v(f-f_c)+S_v(f+f_c)]\,. \qquad (7.38) \end{aligned}$$

The $s\times n$ autocorrelation and PSD are

$$\begin{aligned} R_{s\times n}(\tau) &= 4R_s(\tau)R_n(\tau)+2\mathrm{E}\left(s^2\right)\sigma_n^2 \\ &= 4R_v(\tau)R_n(\tau)\cos\omega_c\tau+2R_v(0)\sigma_n^2 \qquad (7.39) \\ \Rightarrow S_{s\times n}(f) &= 4\int_{-\infty}^{\infty}R_v(\tau)R_n(\tau)\cos 2\pi f_c e^{-i2\pi f_c\tau}\,d\tau+2\mathrm{E}\left(v^2\right)\sigma_n^2\delta(f) \\ &= 2\int_{-\infty}^{\infty}S_n(f')[S_v(f-f_c-f')+S_v(f+f_c-f')]\,df'+2\mathrm{E}\left(v^2\right)\sigma_n^2\delta(f). \qquad (7.40) \end{aligned}$$

Compared to Eq. (7.20), $S_{s\times n}$ now has the convolution of S_v with S_n instead of a constant V. The $s\times s$ autocorrelation and PSD are

$$\begin{aligned} R_{s\times s}(\tau) &= 4\mathrm{E}\left(v_t^2 v_{t+\tau}^2\right)\mathrm{E}\left\{\cos^2(\omega_c t+\theta)\cos^2[\omega_c(t+\tau)+\theta]\right\} \\ &= R_{v^2}(\tau)+\frac{1}{2}R_{v^2}(\tau)\cos 2\omega_c\tau \qquad (7.41) \\ \Rightarrow S_{s\times s}(f) &= S_{v^2}(f)+\frac{1}{4}[S_{v^2}(f-2f_c)+S_{v^2}(f+2f_c)]\,. \qquad (7.42) \end{aligned}$$

Compared to Eq. (7.22), $S_{s\times s}$ now has S_{V^2} instead of δ-functions. The $n\times n$ autocorrelation and PSD are the same as the unmodulated case above.

Amplitude modulation

Now consider the case of AM modulation. Since the quantum beat signal in the actual experiment is an AM modulated signal this case is very relevant. To first order we can treat the incoming amplitude as

$$s(t) = \sqrt{2}v(t)\cos(\omega_c t+\theta) = \sqrt{2}V(1+m\cos\omega_m t)\cos(\omega_c t+\theta). \qquad (7.43)$$

The PSD of the amplitude $v(t)$ is

$$S_v(f) = V^2\left\{\delta(f) + \frac{m^2}{4}[\delta(f - f_m) + \delta(f + f_m)]\right\}. \tag{7.44}$$

Using Eq. (7.40) the signal × noise PSD is

$$S_{s\times n}(f) = 4V^2\left(1 + \frac{m^2}{2}\right)AB_{in}\delta(f) + \begin{cases} 4V^2\left(1 + \frac{m^2}{2}\right)A & \text{if } -B_{in}/2 < f < B_{in}/2, \\ 2V^2\left(1 + \frac{m^2}{2}\right)A & \text{if } -B_{in}/2 < |f| - 2f_c < B_{in}/2, \\ 0 & \text{otherwise.} \end{cases} \tag{7.45}$$

This is the same as the unmodulated case Eq. (7.24) with an additional $O\left(m^2\right)$ term from the power in the sidebands. Dropping the higher order term the noise variance in a bandwidth B_{out} near DC is the same as in Eq. (7.28)

$$\sigma^2_{s\times n} = 8V^2AB_{out} = 4P_sP_{n,out}. \tag{7.46}$$

To find the output signal we first compute the square of the amplitude $v(t)$ to $O(m)$

$$v^2(t) = V^2(1 + 2m\cos\omega_m t) \tag{7.47}$$

which has a PSD of

$$S_{v^2}(f) = V^4\left\{\delta(f) + m^2[\delta(f - f_m) + \delta(f + f_m)]\right\}. \tag{7.48}$$

Using Eq. (7.42) the output power at f_m is

$$P_{f_m} = 2m^2V^4 = 2(mP_s)^2. \tag{7.49}$$

Using Eq. (7.49) and Eq. (7.46) the signal to noise is

$$\left(\frac{S}{N}\right)_{V_{fm}} = \sqrt{\frac{P_{f_m}}{\sigma^2_{s\times n}}} = \frac{m}{\sqrt{2}}\sqrt{\frac{P_s}{P_{n,out}}}. \tag{7.50}$$

Compared to the unmodulated case Eq. (7.35) there is an additional factor of $\sqrt{2}m$. The absorption fraction x is equal to the peak to peak modulation of the power, $4m$. In terms of absorption fraction x,

$$\left(\frac{S}{N}\right)_{V_{fm}} = \frac{x}{4\sqrt{2}}\sqrt{\frac{P_s}{P_{th}}\frac{B_{in}}{B_{out}}}. \tag{7.51}$$

Actual noise sources

Now we are in a position to compare the actual experimental noise sources.

Shot noise, due to the discrete nature of photons, is on the input power which makes the above analysis problematic. To a first approximation we can use the usual derivation of shot noise and assume the PSD of the output voltage reproduces the PSD due to shot noise. The signal power is

$$P_s = hf\dot{N} = \frac{hfN}{\Delta t} = 2hfNB_{out}, \tag{7.52}$$

where $\dot{N} = N/\Delta t$ is the photon rate. With a sampling time Δt (and therefore a bandwidth $B_{out} = 1/2\Delta t$) we observe N photons on average and we can find the variance of the output from

$$S_{shot} = \frac{\sigma^2_{P_s}}{2B_{out}} = \frac{1}{2B_{out}}(2hfB_{out}\sigma_N)^2 = 2(hf)^2B_{out}\sigma_N^2 = 2(hf)^2B_{out}N = hfP_s. \tag{7.53}$$

This is analogous to the well-known Schottky formula [122] for the SSB PSD of shot noise on electrical current, $S_i = 2ei$.

Thermal noise (Johnson noise) is independent of frequency so we can use the analysis above with the substitution $A = \frac{1}{2}kT$ (for DSB PSD).

Summarizing the three major noise sources

Thermal noise [see Eq. (7.29)]	$\sigma_{th} = \sqrt{2P_{th,in}P_{th,out}}$	(7.54a)
Signal thermal cross term [see Eq. (7.28)]	$\sigma_{s\times th} = 2\sqrt{P_sP_{th,out}}$	(7.54b)
Shot noise [see Eq. (7.53)]	$\sigma_{shot} = \sqrt{2hfP_sB_{out}}$	(7.54c)

where $P_s = V^2$ and $P_{th,in(out)} = kTB_{in(out)}$. One can see that the cross term will dominate the thermal noise term as long as the signal power is larger than the input thermal noise power. Even without

filtering on the input this will always be the case since

$$P_{th,in} = kTB_{in} = (1.4 \times 10^{-23}\,\mathrm{J\,K^{-1}})(300\,\mathrm{K})(10^{10}\,\mathrm{Hz}) \approx 40\,\mathrm{pW} \tag{7.55}$$

and P_s is typically on the order of microwatts. Comparing the cross term Eq. (7.54b) with the shot noise term Eq. (7.54c)

$$\frac{\sigma_{s\times th}}{\sigma_{shot}} = \frac{2\sqrt{P_s P_{th,out}}}{\sqrt{2hfP_s B_{out}}} = \sqrt{\frac{2kT}{hf}} = \sqrt{\frac{2(1.4 \times 10^{-23}\,\mathrm{J\,K^{-1}})(300\,\mathrm{K})}{(6.6 \times 10^{-34}\,\mathrm{J\,s})(30 \times 10^{9}\,\mathrm{Hz})}} \approx 20 \tag{7.56}$$

shows that thermal cross term dominates. The temperature T used here is a typical noise temperature of the amplification electronics (see discussion in Section 7.3).

This result depends only on the detection frequency and is independent of the power. One could alternatively derive this by starting from the Bose-Einstein statistics of photons and deriving the mean squared fluctuation in photon number. There are in fact two terms: one due to quantum or particle fluctuations and the other due to wave interference or thermal fluctuations. Optical experiments ($hf \gg kT$) typically ignore the thermal fluctuation term while RF experiments ($hf \ll kT$) ignore the particle term (see Chapter 2 in [123] for a detailed discussion).

7.2.3 Homodyne detection

In this section we consider the alternative of homodyne detection with a mixer. The output from the mixer is given by

$$y(t) = x_{RF}(t)x_{LO}(t) \tag{7.57}$$

where

$$x_{RF}(t) = s_{RF}(t) + n_{RF}(t) \tag{7.58a}$$

$$x_{LO}(t) = s_{LO}(t) + n_{LO}(t) \tag{7.58b}$$

$$s_{RF}(t) = \sqrt{2}V_{RF}\cos\omega_c t \tag{7.58c}$$

$$s_{LO}(t) = \sqrt{2}V_{LO}\cos(\omega_c t + \theta). \tag{7.58d}$$

We define $P_{RF} \equiv V_{RF}^2$, $P_{LO} \equiv V_{LO}^2$, and $P_{th,RF}$ and $P_{th,LO}$ to be the total thermal noise over the input bandwidth on the RF or LO port, respectively, of the mixer. These bandwidths are determined only by the mixer or waveguide if no filters or amplifiers are used before the mixer. Substituting into Eq. (7.57)

$$\begin{aligned} y(t) = 2[&V_{RF}V_{LO}\cos\omega_c t\cos(\omega_c t+\theta) + n_{RF}(t)V_{LO}\cos(\omega_c t+\theta) \\ &+ n_{LO}(t)V_{RF}\cos\omega_c t + n_{RF}(t)n_{LO}(t)] \end{aligned} \tag{7.59}$$

First consider the term analogous to the signal × signal term for the square law detector

$$2V_{RF}V_{LO}\cos\omega_c t\cos(\omega_c t+\theta) = V_{RF}V_{LO}[\cos\theta + \cos(2\omega_c t+\theta)]. \tag{7.60}$$

The expectation value of the second term is zero and with proper phase control we can set $\theta = 0$ so

$$V_{s\times s} = \sqrt{P_{RF}P_{LO}}. \tag{7.61}$$

Now each of the cross terms have the same form as in the square law detector case so, using Eq. (7.28),

$$\sigma_{s\times n} = \sqrt{2(P_{RF}P_{th,LO} + P_{LO}P_{th,RF})}. \tag{7.62}$$

The thermal noise terms are usually comparable, while $P_{LO} \gg P_{RF}$ which gives

$$\sigma_{s\times n} = \sqrt{2P_{LO}P_{th,out}}. \tag{7.63}$$

This leads to a signal to noise on the output of

$$\left(\frac{S}{N}\right)_{V_{out}} = \sqrt{\frac{P_{RF}P_{LO}}{2P_{LO}P_{th,out}}} = \sqrt{\frac{P_{RF}}{2P_{th,out}}}. \tag{7.64}$$

Compared to square law detection Eq. (7.35) we gain a factor of $\sqrt{2}$ from one of the signal × noise terms being suppressed by the low RF power. One can quickly see that the same analysis holds for an amplitude modulated RF signal, since the output term at the modulation frequency comes from multiplying the AM sidebands by $\cos\omega_c t$, which in turn comes from the local oscillator.

7.3 Microwave absorption EDM measurement

In this section we calculate the theoretical sensitivity of our experiment to an electron EDM using microwave absorption with actual parameter values. To use the signal-to-noise ratio formulas calculated above, we first need to determine the expected absorption fraction and the optimal microwave absorption beam power.

7.3.1 Expected absorption fraction

To calculate the absorption fraction we first need to calculate the dipole transition matrix element. Using Table 3.2 and Table 3.3, the matrix element for the EDM transition is

$$M_{EDM} = \frac{1}{\sqrt{2}} \langle J=2, m=0, e| - \mu_x \left(|J=1, M=-1, n_-\rangle + |J=1, M=+1, n_-\rangle\right) = \frac{\mu_a}{2\sqrt{10}}, \tag{7.65}$$

where $\mu_x = \frac{1}{\sqrt{2}}(-\mu_{-1} + \mu_{+1})$. This gives an absorption cross-section of (see discussion in Appendix B)

$$\sigma_{abs} = \frac{8\pi\omega}{c} \frac{1}{\gamma\hbar} M_{EDM}^2 = 1.9 \times 10^{-12}\,\mathrm{cm}^2, \tag{7.66}$$

where $\omega = 2\pi(28.2\,\mathrm{GHz})$ is the transition frequency and $\gamma = \frac{1}{\tau} = \frac{1}{50\,\mu\mathrm{s}} = 2\pi(3.2\,\mathrm{kHz})$ is the natural linewidth. Doppler broadening reduces the cross section to (see 3.155 and 3.150 in [86])

$$\sigma_D = 0.89 \frac{\gamma}{\Gamma_D} \sigma_{abs} = 2 \times 10^{-13}\,\mathrm{cm}^2, \tag{7.67}$$

where

$$\Gamma_D = \frac{\omega}{c}\sqrt{\frac{2kT}{M}} = 2\pi(26.6\,\mathrm{kHz}) \tag{7.68}$$

at $T = 1000\,\mathrm{K}$. The inhomogeneous linewidth, Γ_E, due to the electric field further reduces the cross-section by Γ_D/Γ_E. To fully polarize the molecules we apply a field of $50\,\mathrm{V\,cm^{-1}}$ which causes a Stark shift of $\approx 40\,\mathrm{MHz}$. An inhomogeneity of χ_E reduces the cross-section by

$$\frac{\Gamma_{D,FWHM}}{40\,\mathrm{MHz}\cdot\chi_E} = \frac{2\sqrt{\ln 2}\cdot 26.6\,\mathrm{kHz}}{40\,\mathrm{MHz}\cdot\chi_E} \approx \frac{10^{-3}}{\chi_E}. \tag{7.69}$$

For the current vapor cell $\chi_E \approx 0.01$, therefore $\sigma = 2 \times 10^{-14}\,\mathrm{cm}^2$.

The absorption fraction is given by

$$x = n\sigma L \tag{7.70}$$

For the current vapor cell, with $L = 5\,\text{cm}$ and $n = 1 \times 10^{10}\,\text{cm}^{-3}$, we have

$$x = f \cdot 1 \times 10^{10}\,\text{cm}^{-3} \cdot 2 \times 10^{-14}\,\text{cm}^2 \cdot 5\,\text{cm} = f \cdot 10^{-3}, \tag{7.71}$$

where f is the efficiency of the $|X, v = 0, J = 0\rangle \rightarrow |a, v = 5, J = 1\rangle$ excitation process. In general

$$x = f\frac{10^{-5}}{\chi_E}\Big(\frac{L}{5\,\text{cm}}\Big). \tag{7.72}$$

This is valid down to an electric field inhomogeneity of $\chi_E = 10^{-3}$ at which point the line broadening is comparable to the Doppler width.

7.3.2 Optimal absorption beam power

The signal-to-noise increases as the microwave power increases. However, at a certain power population transfer begins to limit the absorption signal. To avoid this we assume the power is small enough that it drives less than one-tenth of a π pulse during the state lifetime

$$\frac{1}{\hbar}\mu_{edm}\mathcal{E}\tau < \frac{\pi}{10}. \tag{7.73}$$

This gives an allowed flux of $S = 2 \times 10^{-8}\,\text{W}\,\text{cm}^{-2}$. For the current cell a circular 2 inch diameter microwave beam gives

$$P = \pi(2.54\,\text{cm})^2 S = 0.4\,\mu\text{W}. \tag{7.74}$$

The microwave power can be increased if the linewidth is broadened to match any inhomogeneous broadening of the absorption line. Electric field broadening increases the maximum power by $\frac{\Gamma_E}{\gamma} = \frac{400}{3.2} \approx 125$ or

$$P \approx 50\,\mu\text{W} \quad \text{for the current cell.}$$

For the best case, when $\Gamma_E < \Gamma_D$ we can use $\frac{\Gamma_D}{\gamma} = \frac{26.6}{3.2} = 8.3$ times more power or

$$P \approx 3\,\mu\text{W} \quad \text{for a Doppler limited linewidth.}$$

7.3.3 Signal-to-noise ratio using the current apparatus

From the full analysis of an amplitude modulated absorption signal with a modulation of x on the power detected by a square-law detector the signal-to-noise is

$$\left(\frac{S}{N}\right)_{sq.law} = \frac{x}{4}\sqrt{\frac{P}{kT_{eff}B_{out}}}. \tag{7.75}$$

Homodyne detection was a factor of $\sqrt{2}$ better

$$\left(\frac{S}{N}\right)_{homodyne} = \frac{x}{2}\sqrt{\frac{P}{2kT_{eff}B_{out}}}. \tag{7.76}$$

T_{eff} is the effective temperature of the microwave receiver. There are two main contributions to the temperature. First is the brightness temperature in the field of view of the detection antenna. In our experiment the quartz lightpipes act as waveguides between the transmitting and receiving horns. Thus, without some trick, such as cooling the transmitting horn or possibly coating it with low emissivity paint, the receiving antenna mostly "sees" the room temperature surface of the transmitting horn. There are also thermal noise contributions from any hot surfaces in the field of view of the antenna and from the hot PbO gas itself. The gas contributes an effective temperature given by the physical temperature times the absorption. With small absorption, it was verified experimentally that the detected noise power was significantly below that of a 1000K blackbody. The second contribution to the effective noise temperature is the electronic noise of the detection amplifier. The gain of the amplifier makes noise from electronic components further downstream negligible. The effective temperature for an amplifier is,

$$T_{amp} = (F-1)T_0 \tag{7.77}$$

where F is a noise figure specification and T_0 is a "standard" temperature of 290 K. Putting all of this together we have

$$T_{eff} = T_{bright} + T_{elec} = [x \times 1000\,\mathrm{K} + (1-x)293\,\mathrm{K}] + (F-1)290\,\mathrm{K}. \tag{7.78}$$

Any loss in power, ℓ, from the vapor cell to the detector will further reduce the S/N by $\sqrt{\ell}$. For

example with a square law detector

$$\begin{aligned} S &\propto P_{det} = P_{in}/\ell \\ N &\propto \sqrt{P_{det}} = \sqrt{P_{in}/\ell} \\ \Rightarrow \frac{S}{N} &\propto \sqrt{\frac{P_{in}}{\ell}} \end{aligned} \tag{7.79}$$

Finally, for our current cell, using $kT_0 \approx 4 \times 10^{-21}\,\mathrm{W\,Hz^{-1}}$, assuming $\ell \approx 10$ dB, a noise figure of $F = 2.8$ dB= 1.9 (typical for low-noise amplifiers), an input power of 50 μW, an excitation efficiency of 1%, and an absorption fraction of $X = 1\% \cdot 10^{-3}$, we have

$$\frac{S}{N} = \frac{10^{-5}}{2}\sqrt{\frac{50\,\mu\mathrm{W}}{2 \cdot 2.9(4 \times 10^{-21}\,\mathrm{W\,Hz^{-1}})(3.2\,\mathrm{kHz})10}} \approx 1.3 \tag{7.80}$$

7.3.4 EDM sensitivity with present apparatus

The frequency shift due to an EDM in our experiment is given by $\delta f = 2d_e W_d$, with $W_d = 6.1 \times 10^{-24}\,\mathrm{Hz}\,e^{-1}\,\mathrm{cm}^{-1}$ [87]. Therefore the statistical sensitivity of our experiment is

$$\delta d_e = \frac{\delta f}{2W_d} = \frac{1}{2W_d}\frac{\frac{1}{2\pi\tau}}{(S/N)\sqrt{N_{shots}}} = \frac{8.9 \times 10^{-26}\,e\,\mathrm{cm}\sqrt{\mathrm{day}}}{(S/N)}, \tag{7.81}$$

where we have assumed an experimental repetition rate $N_{shots} = 100\,\mathrm{Hz}$ and a coherence time $\tau = 50\,\mu\mathrm{s}$. Using the current cell with a signal-to-noise of only 1.3 per shot, over 4000 days would be needed to reach $10^{-27}e\,\mathrm{cm}$.

7.3.5 Second generation absorption cell

Next we consider a second generation absorption cell (see Fig. 7.3). This cell will be a 50 cm long cylinder with gold coated sapphire rods for electrodes. Each end will be sealed with sapphire or YAG windows. The cell will be heated with coaxial tantalum wires wrapped around the circumference of the cylinder (which is significantly simpler than the current heating system). A free space microwave cavity can be placed around the cell. The microwaves are launched and received by horns with microwave lens for proper focusing. Before the transmitting horn a waveguide magic-T splits the power. With a variable phase shifter and attenuator (not shown) the power can be

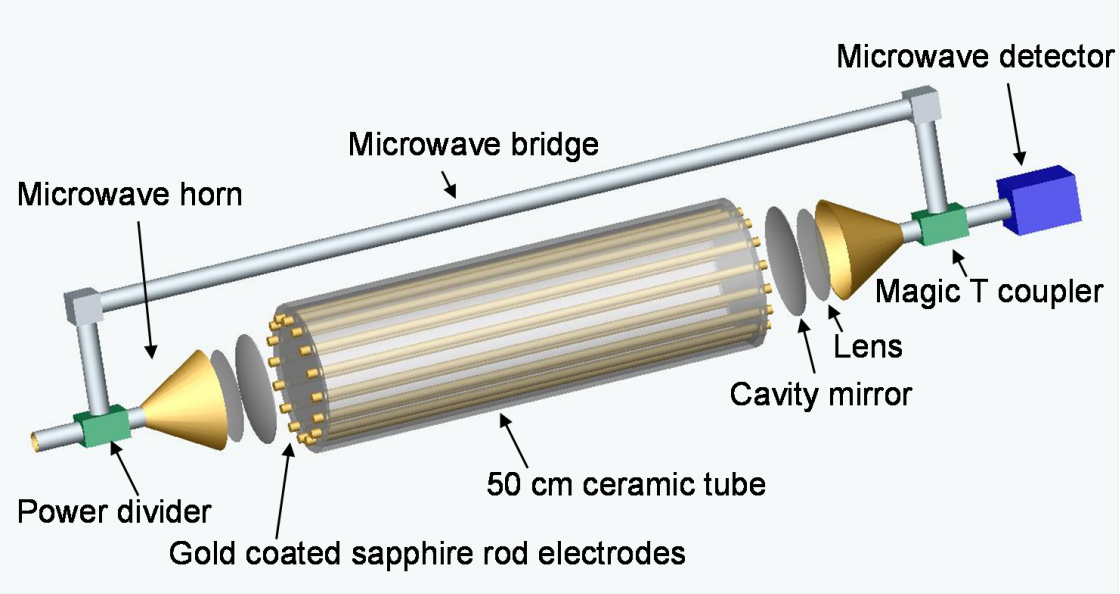

Figure 7.3: Microwave absorption cell setup. Microwave power is split by a magic tee, sent through a horn and focused into a microwave cavity surrounding the high temperature absorption cell. A mirror image lens and horn collect the microwaves and recombine with the split power to cancel off the DC signal. In the actual experiment variable phase shifters and attenuators will be used to minimize the DC offset. The absorption signal passes through a low noise amplifier before reaching a square law detector. Gold coated sapphire rods produce a homogeneous electric field.

recombined after the receiving horn for homodyne detection.

This cell substantially increases the signal-to-noise of the experiment. Increasing the length to 50 cm increases the path length and absorption fraction by a factor of 10.

Modeling of rod electrodes with a cosine voltage distribution show that the electric field homogeneity can be controlled to 10^{-3}; the level where the linewidth is dominated by Doppler broadening. This increases the cross section by a factor of 10 but requires 10 times lower power to prevent saturation for a total increase in signal-to-noise of $\sqrt{10}$.

Modeling of the microwave cavity mode shows that loss in the cavity will be negligible. We also expect that with proper load matching, loss from the cell to the detector will be negligible.

Use of a cryogenic detector with a noise temperature of ≈ 30 K, such as the Quinstar QCA series, lowers the electronic noise temperature by 520 K.

Placing a microwave cavity around the absorption cell increases the path length by the finesse, $\mathcal{F}$, but requires $\mathcal{F}$ less power to prevent saturation. The increase in the signal-to-noise is then $\sqrt{\mathcal{F}}$. For a free space cavity with room temperature copper mirrors a quality factor, Q, of 10^5 is possible

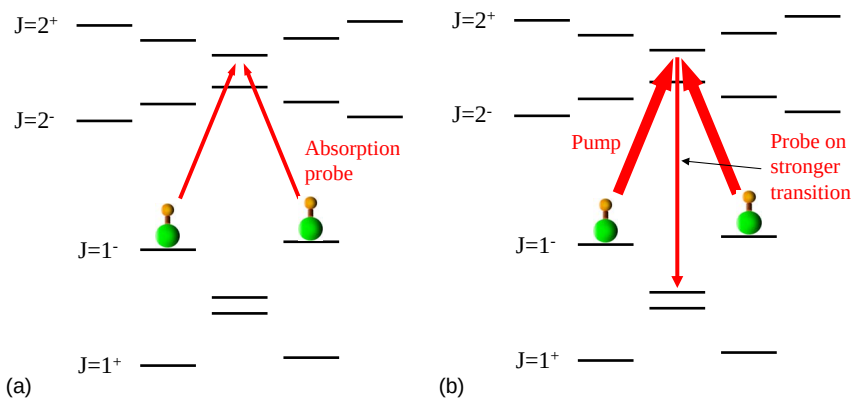

Figure 7.4: Microwave pump-probe scheme. Compared to the direct absorption measurement, on left, a pump-probe measurement, on right, could increases the effective absorption cross-section by a factor of 8. The dipole matrix element for the $|J=1, m=0\rangle \rightarrow |J=2, m=0\rangle$ transition is a factor of $2\sqrt{2}$ larger than the EDM transition dipole matrix element.

[124]. The high temperature cell must be sealed so the external cavity will have to pass through sapphire or YAG windows on either end of the cell. Resistive loss in the windows will be small and reflections can be mostly eliminated by using a window of $(2n+1)\lambda/4$ thickness. To be conservative we consider $Q = 10^4$. The quality factor and finesse for a confocal cavity are related by

$$\mathcal{F} = \frac{cQ}{4Lf} \approx \frac{3\times10^{10}\,\mathrm{cm\,s^{-1}}\times10^4}{4\times50\,\mathrm{cm}\times(30\times10^9\,\mathrm{Hz})} = 50. \tag{7.82}$$

With this finesse and the improvements mentioned above, the absorption, x, will still be on the few percent level. Thus we expect the brightness temperature seen by the detection horn to remain close to room temperature.

Lastly, use of a pump-probe scheme could further increase the absorption cross section. The dipole matrix element for the $|J=1, m=0\rangle \rightarrow |J=2, m=0\rangle$ transition is a factor of $2\sqrt{2}$ larger than the EDM transition dipole matrix element. One could imagine using a strong microwave beam to pump the molecules to the $|J=2, m=0\rangle$ state and then probe on the $m=0$ transition (see Fig. 7.4).

These improvements, summarized in Table 7.1, give a total increase in the signal-to-noise of ≈ 10000, which gives an EDM sensitivity of $9\times10^{-30}\,e\,\mathrm{cm}\,\sqrt{\mathrm{day}}$.

Table 7.1: Signal-to-noise improvements from absorption cell

Improvement	Description	Gain in S/N
50 cm cell length	Increases absorption	10
Rod electrodes with cosine voltage distribution	Increased homogeneity which reduces linewidth, increases cross section, but requires lower power	$\sqrt{10}$
Free space cavity matched to detector	Lowers loss	$\sqrt{10}$
Cryogenic amplifier	Lower electronic noise	2
Pump probe	Probe on stronger transition increases cross-section	$2\sqrt{2}$
Microwave cavity	Increases effective path length by finesse, $\mathcal{F}$, but requires reduced power to avoid saturation	$\sqrt{50}$
Improved laser excitation	Increases excited state density	$2-3$
	Total gain	≈ 10000

7.4 Excited state absorption

To test our understanding of a microwave absorption measurement, we looked with our current apparatus for an absorption signal in the a state after pulsed laser excitation from the ground state (see Fig. 7.5 and Fig. 7.6).

Specifically we looked for absorption on the transition $|a, J = 1, M = 0\rangle \Rightarrow |a, J = 2, M = 0\rangle$ immediately after a dye laser shot tuned to the R0 transition, $|X, J = 0\rangle \rightarrow |a, J = 1\rangle$. There was no applied electric field and a magnetic field of 100 mG. An Agilent 33250A arbitrary waveform generator (AWG) was used as the source for our homebuilt 28 GHz frequency setup (see Section 5.9). The frequency shift key (FSK) modulation feature of the AWG changed the output frequency from on resonance to 200 kHz off resonance every other laser shot. A Labview program automatically took the difference of a pair of shots to reduce background transients due to the laser power supply that showed up on the microwave detection electronics. After the detection horn there were two microwave amplifiers before an Agilent R422C crystal detector. Fig. 7.7 shows a calibration curve, $V(P)$, of the detector using a 40 GHz Agilent microwave generator in the Schoelkopf lab. We use a numerical derivative of this curve, $\frac{dV}{dP}$, to estimate the response to AC power changes[1].

[1]The frequency response of the detector to power changes was verified to be flat out to several hundred kilohertz using

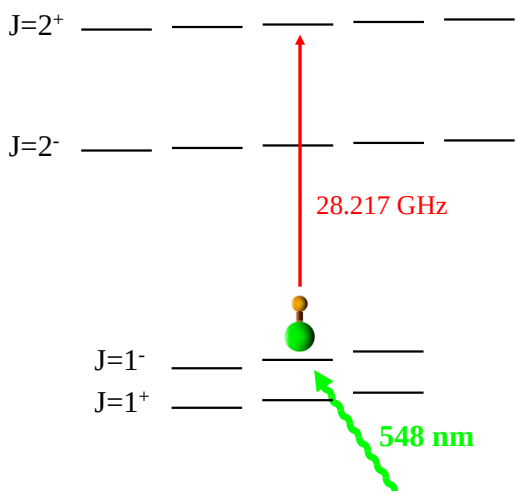

Figure 7.5: Microwave absorption proof of principle measurement. After pulsed laser excitation from the ground state, we looked for transient absorption on the $|a, J = 1, m = 0\rangle \rightarrow |a, J = 2, m = 0\rangle$ rotational transition.

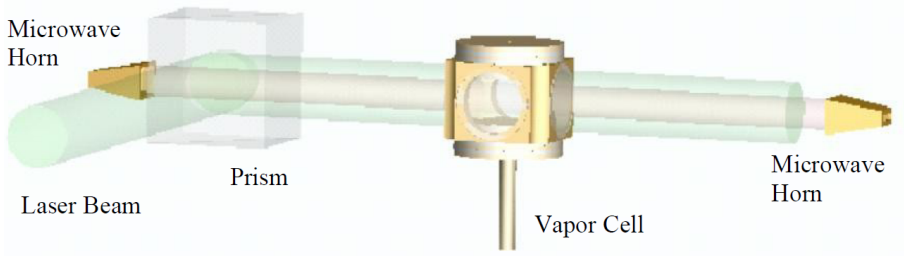

Figure 7.6: Microwave absorption setup. Both the pulsed laser excitation and microwave absorption beams passed through quartz lightpipes into the vapor cell. An air-gap beamsplitting prism allowed us to send the excitation laser beam in from the side while leaving the microwave beam unaffected. Microwave horns on both sides of the apparatus served as either the source or receiver of the absorption beam.

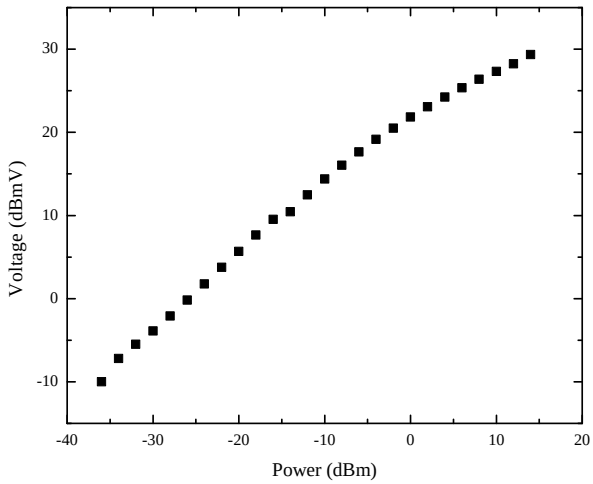

Figure 7.7: Voltage versus microwave power on the Agilent R422C diode detector. At powers below ≈ -15dBm the output is linear and the diode behaves as a "power law" detector.

Before each series of absorption measurements, the DC power level on the detector was first recorded. Afterwards the detector signal was fed to a SRS low-noise preamplifier with selectable bandpass filters and gain, G. The output of the preamp was then digitized with a Labview DAQ board. An analytical simulation in Mathematica of the RC filters' responses to an exponential signal determined the ratio, R, of the observed peak height to the peak height before the filters. Fig. 7.8 shows typical data along with the modeled filter response and the inferred input signal. The peak microwave absorption fraction is related to the peak signal voltage by

$$x = \frac{V_{peak}}{RG} \frac{1}{\frac{dV}{dP} P}\bigg|_{P=P_{DC}}. \tag{7.83}$$

Fig. 7.9 shows an example of the absorption lineshape as the microwave frequency was scanned across the $|a, J = 1, m = 0\rangle \rightarrow |a, J = 2, m = 0\rangle$ transition. The line width of 43(2)kHz is consistent with the expected Doppler width of 43 kHz for the 740 °C vapor cell.

a microwave generator.

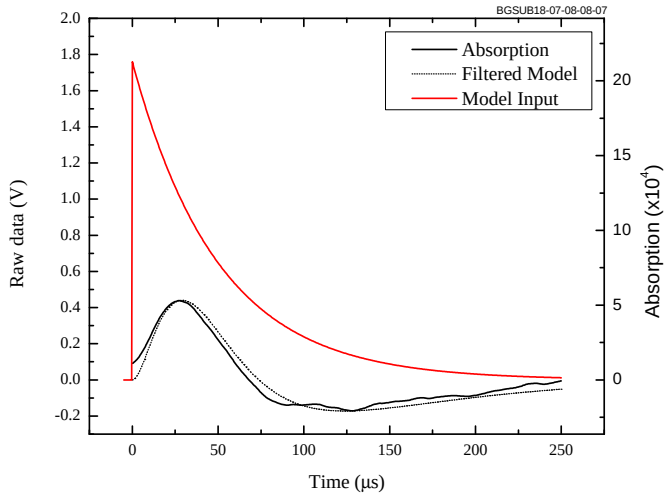

Figure 7.8: Time domain microwave absorption signal in the $a(1)$ state. The black line is the average of 500 laser shots of data for the transition $|a, J = 2\rangle \rightarrow |a, J = 1\rangle$ with z-polarized microwaves. The microwave frequency is shifted on and off resonance every other shot. Pairs of shots are automatically subtracted to eliminate electronic noise. Although this particular example is stimulated emission, it is exactly analogous to the absorption measurements discussed in the text.

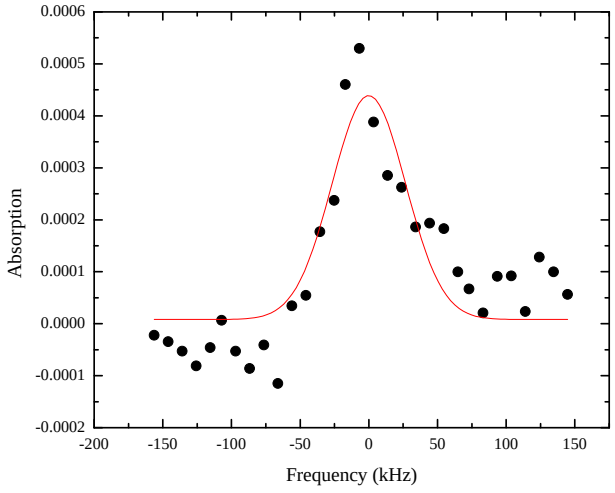

Figure 7.9: Microwave absorption lineshape in the $a(1)$ state. Each data point is the integrated absorption from a measurement at a given microwave frequency, such as that shown in Fig. 7.8. The Gaussian fit gives a FWHM of 43(2)kHz consistent with the expected Doppler width of 43 kHz for the 740 °C vapor cell.

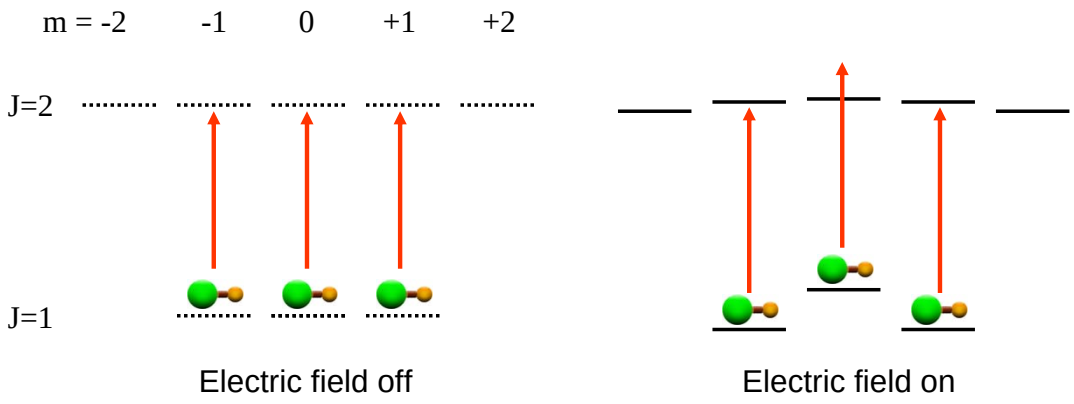

Figure 7.10: Stark modulation. Modulation of the electric field causes a tensor Stark shift of the $X, J = 1$ and $J = 2$ sublevels (see Section 3.3.1). As the microwave frequency is scanned over the $J = 1 \rightarrow J = 2$ transition it comes on resonance at three frequencies: once at the field-free transition frequency for all three sublevels (shown on left) and twice at the Stark shifted frequencies of the $m = 0$ and $|m| = 1$ transitions (only the $|m| = 1$ resonance is shown on the right).

7.5 Ground state absorption

After the proof-of-principle absorption measurement in the excited state we realized that, without significant modification to the apparatus, we could also look for absorption in the ground state. Since the absorption cross section is well understood, this measurement enables a fairly direct determination of the vapor density and hence the vapor pressure of PbO. The low fluorescence yields we had detected over the years led us to suspect that the PbO vapor pressure may not be as high as the standard CRC reference[125] suggested. In addition by performing measurements both before and after the laser excitation pulse we could directly measure the laser excitation efficiency.

7.5.1 Stark modulation

The long measurement times possible in the ground state allowed us to use the lock-in technique for detection. The lock-in technique roughly consists of modulating a parameter that affects the output signal and then measuring the amplitude of the output signal at the modulation frequency. If an experimental background changes slower than the modulation frequency it is suppressed at the lock-in output.

We initially attempted frequency modulation of the absorption beam but reflections and étalon

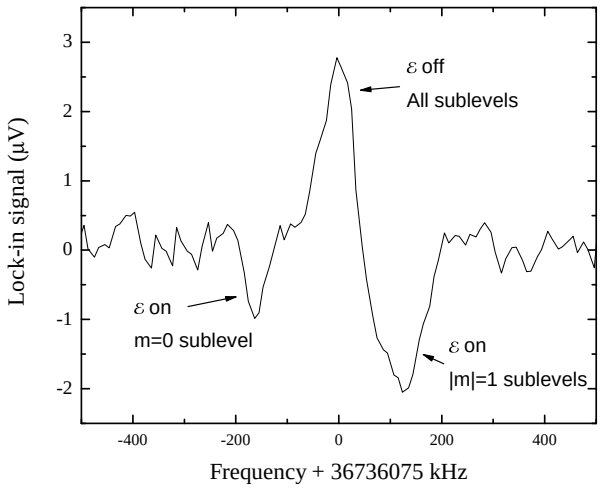

Figure 7.11: Stark modulation signal. The Stark modulation output signal is essentially the difference between the absorption with or without an applied electric field. An electric field causes a tensor Stark shift of the $X, J = 1$ and $X, J = 2$ sublevels (see Fig. 3.4). As the microwave frequency is scanned over the $J = 1 \rightarrow J = 2$ transition it comes on resonance with all three m sublevels when the electric field is off, and the Stark shifted levels when the field is on.

effects in the lightpipes and cell windows made this difficult. Stark modulation [69] proved to be much easier. By modulating the electric field, via the voltage on the cell electrodes, the tensor Stark shift of the Zeeman sublevels moved the microwave absorption frequency on and off resonance (see Fig. 7.10). High resolution data on the $J = 1 \rightarrow J = 2$ lines in the $v = 0, 1$ vibration levels from the NIST diatomic spectral database[126, 127] were key to initially locating the narrow lines. We then varied the modulation depth and modulation frequency to confirm that our home-built precision voltage supply for the electrodes could handle the rapid changes. The absorption signal changed little with modulation depth and only dropped off above modulation frequencies of 3 kHz, presumably due to the bandwidth of the high voltage source. The microwave power was also adjusted to avoid saturation (see Fig. 7.11 for typical data). The peak absorption began to drop at a microwave power of ≈ -37 dBm (see Fig. 7.12). This agrees fairly well with a rough estimate of -39 dBm for the saturation power based on Eq. (7.73) and Eq. (7.74), with a correction for the collision induced lifetime of 20 μs at a cell temperature of 750 °C.

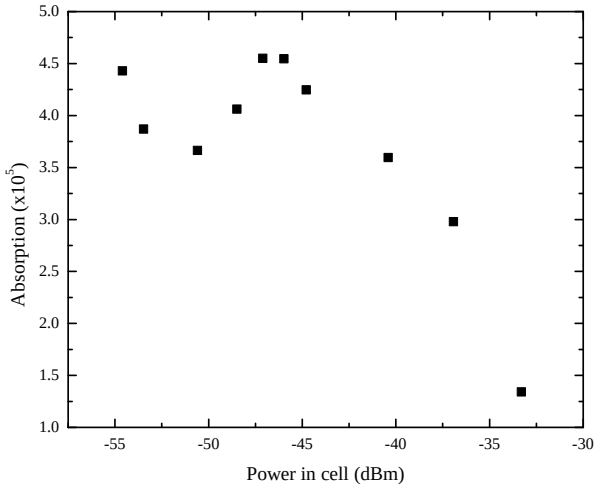

Figure 7.12: Saturation of the ground state microwave absorption. High microwave power causes transitions to the upper state which lead to stimulated emission and a reduction of the absorption signal. The approximate saturation power of -37 dBm agrees well with an estimate of -39 dBm based on the estimated in-cell microwave power, transition dipole moment, and estimated state lifetime.

7.5.2 Ground state dipole moment

By determining the position of the Stark-shifted transition frequencies at several electric fields we could measure the dipole moment of the ground state, μ_X. From Eq. (3.6) the Stark shift for a given magnetic sublevel is

$$\Delta E^{(2)}_{stark} = \frac{\mu_X^2 \mathcal{E}^2}{2B_r J(J+1)} \frac{J(J+1) - 3M^2}{(2J-1)(2J+3)}. \tag{7.84}$$

Using the literature values of the dipole moment, $\mu_X = 4.64(30)$ D [128], and the rotational constant, $B_r = 9.17\,\mathrm{GHz}$[68], gives differential Stark shifts of

$$\Delta E_{st,m=0} = -\frac{8}{105}\frac{\mu_X^2 \mathcal{E}^2}{B} = -45\mathrm{Hz}\left(\frac{\mathcal{E}}{\mathrm{V\,cm^{-1}}}\right)^2, \tag{7.85}$$

and

$$\Delta E_{st,|m|=1} = \frac{13}{210}\frac{\mu_X^2 \mathcal{E}^2}{B} = 37\mathrm{Hz}\left(\frac{\mathcal{E}}{\mathrm{V\,cm^{-1}}}\right)^2. \tag{7.86}$$

Fig. 7.13 shows the absorption at several different modulation depths. The measured line positions suggest a dipole moment of $\mu_X = 4.35$ D, consistent with the published value.

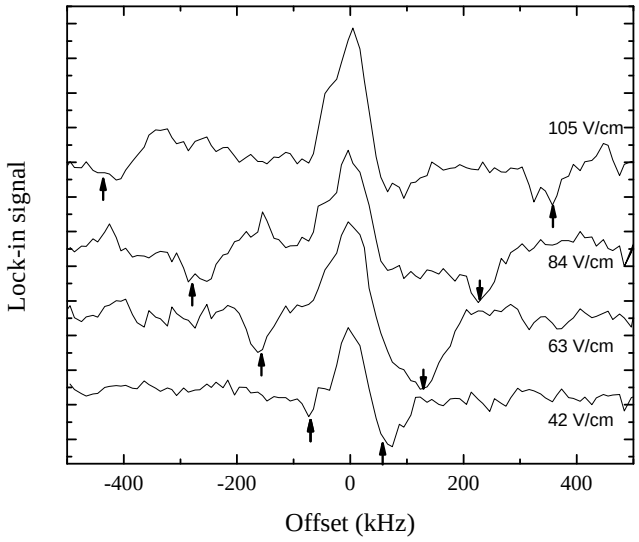

Figure 7.13: Stark modulation at several field strengths. The markers depict the expected Stark-shifted transition frequencies for a dipole moment of μ_X = 4.35 D, consistent with the literature value of 4.64(30) D. Offsets are inserted for each field for clarity.

7.5.3 Vapor pressure

The pressure in our vapor cell is related to the number density via the ideal gas law,[2]

$$PV = NkT \Longrightarrow P = nkT, \tag{7.87}$$

where n is the number density of the gas. We have already seen in Eq. (7.70) that the absorption fraction, x, is also related to the number density via $x = n_x \sigma L$, where σ is the absorption cross section and L is the path length. However, here n_x refers to the difference in population between the upper and lower states of the absorption transition. To relate n_x to n we need to calculate two factors: the fraction of molecules in a given rovibrational level and the fractional difference in population between the upper and lower states.

At thermal equilibrium the fraction of molecules in a given vibrational state is the normalized

[2]The high temperature and relatively low pressure of the vapor cell make this a good approximation.

Boltzmann factor of the vibrational energy,

$$f_v = \frac{e^{\frac{-w_e v}{kT}}}{\sum_{n=0,\cdots} e^{\frac{-w_e n}{kT}}} \approx \frac{e^{\frac{-w_e v}{kT}}}{1 - e^{\frac{-w_e}{kT}}}. \tag{7.88}$$

Similarly, the fraction of molecules in a given rotational state is

$$f_J = \frac{(2J+1)e^{\frac{-BJ(J+1)}{kT}}}{\sum_{n=0,\cdots} (2n+1)e^{\frac{-Bn(n+1)}{kT}}} \approx \frac{B}{kT}(2J+1)e^{\frac{-BJ(J+1)}{kT}}. \tag{7.89}$$

The density of the upper state of the absorption transition is simply the density of the lower state multiplied by the Boltzmann factor of the transition energy. Therefore the fractional difference is

$$f_{ul} = 1 - e^{-\frac{\hbar\omega_0 bs}{kT}}. \tag{7.90}$$

To determine the cross section we use the dipole matrix elements calculated in Section 3.3.1 for the ground state Stark shift. With no electric or magnetic fields the magnetic sublevels are all degenerate. Averaging over the sublevels, the square of the transition matrix element is then

$$|\langle d_X \rangle|^2 = \frac{1}{2J+1} \sum_{m=-J}^{J} \mu_X^2 \frac{(J+1)^2 - m^2}{(2J+1)(2J+3)} = \mu_X^2 \frac{J+1}{3(2J+1)}. \tag{7.91}$$

Using the literature value of $\mu_X = 4.64$ D and Eq. (B.1), the cross section is then $\sigma_X = 4.4 \times 10^{-11}$ cm^2. The Doppler-broadened cross section , using Eq. (7.67), is $\sigma_D = 3.7 \times 10^{-12}$ cm^2.

Finally, combining all of these factors we find

$$P = \frac{xkT}{f_J f_v f_{ul} \sigma_D L}. \tag{7.92}$$

Fig. 7.14 shows the measured values along with several vapor pressure curves from the literature. Our older papers based sensitivity estimates on the CRC curve [125] which is a factor of 10-50 higher than the measured values. More recent data from Popovič *et al.* [129] and Lopatin *et al.* [130] are based on mass spectrometry measurements that can separately identify not only PbO, but also its dimers and tetramers in the vapor (see Fig. 7.15). The CRC curve is based on much older data which assumed the total vapor pressure over solid PbO was due solely to gaseous PbO.

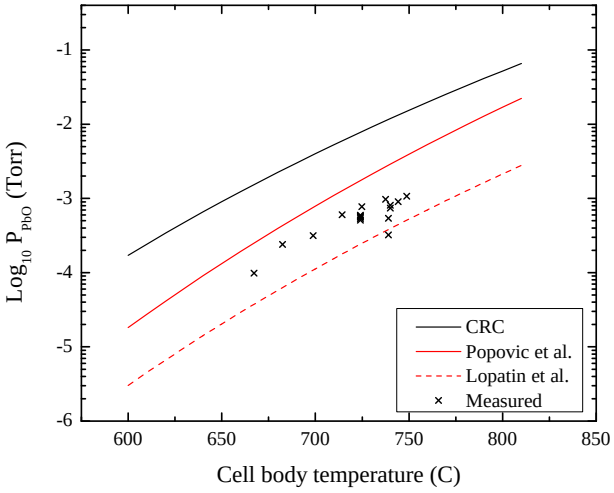

Figure 7.14: PbO partial vapor pressure. The measured data points are inferred from microwave absorption. The standard CRC reference suggested a vapor pressure 10-50 times higher than the measured values. More recent measurements (Popovič *et al.* [129] and Lopatin *et al.* [130]) that single out the partial pressure of PbO monomers show better agreement with the data.

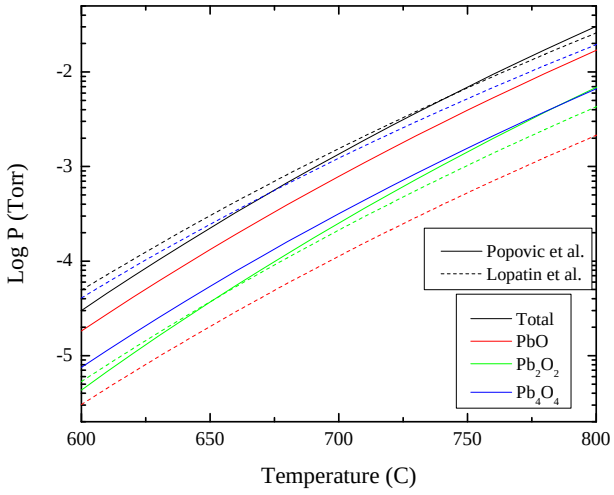

Figure 7.15: Partial and total vapor pressure for PbO polymers above solid PbO. Vapor pressure curves from Popovič *et al.* [129] and Lopatin *et al.* [130] for monomer, dimer, and tetramer PbO over solid PbO. Note the substantial difference between the black lines, which are the total vapor pressures, and the red lines, which are the monomer PbO vapor pressures.

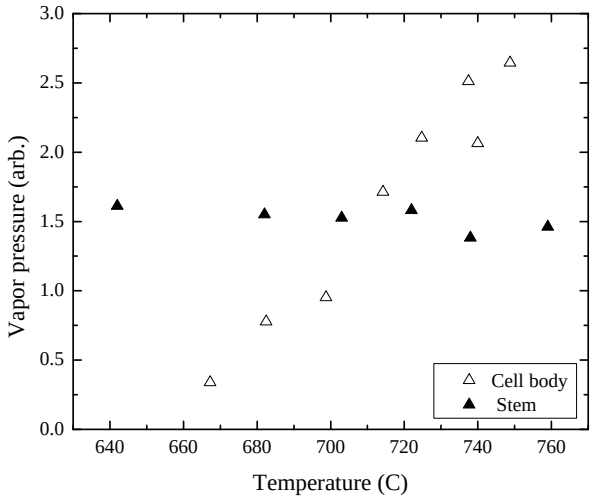

Figure 7.16: Vapor pressure versus cell body and stem temperatures. The PbO vapor cell has a small stem tube which was designed as a reservoir for the PbO vapor. In theory the stem temperature, when lower than the cell body temperature, should determine the PbO vapor pressure. In practice it appears only the cell body temperature matters.

Finally we note that the vapor pressure measurements also enabled a better understanding of our control over the cell temperature. The vapor cell was designed with a small stem that was supposed to act as a reservoir of the PbO, by keeping its temperature lower than the rest of the cell. As shown in Fig. 7.16, the temperature measured with thermocouples near the stem had little correlation with the vapor pressure. Instead the cell body temperature seems to determine the vapor pressure. This is probably due to significant absorption of PbO into the vapor cell body. We had seen previous indications of this when we switched from naturally abundant PbO to isotopically enriched PbO. Even after cleaning the cell body with solvents, the isotope composition of the PbO vapor upon heating remained the same.

7.6 Pulsed dye laser excitation efficiency

Microwave absorption measurements also proved useful for determining the excitation efficiency of our pulsed dye laser from the ground state, X, to the excited $a(1)$ state. For this measurement we tuned the dye laser to the R1 transition, i.e. $|X, v = 1, J = 1\rangle \rightarrow |a, v = 5, J = 2\rangle$. No electric or magnetic

field was applied, leaving the magnetic sublevels degenerate. An initial microwave absorption measurement on the transition $|X, v = 1, J = 1\rangle \rightarrow |X, v = 1, J = 2\rangle$ determined the number density in the $|X, v = 1, J = 1\rangle$ state. After the dye laser excitation pulse, measurement of the microwave stimulated emission on the $|a, v = 5, J = 2\rangle \rightarrow |a, v = 5, J = 1\rangle$ transition determined the number density of molecules transferred to the excited state (see Fig. 7.17). Note, a stimulated emission measurement is exactly analogous to an absorption measurement.[3]

To relate the fractional absorption to the number density, cross sections were needed for both states. The ground state absorption cross section, calculated in Section 7.5.3, was $\sigma_X = 3.7 \times 10^{-12}\,\mathrm{cm}^2$. A similar calculation for the $|a, J = 2\rangle \rightarrow |a, J = 1\rangle$ cross section, averaged over the magnetic sublevels and corrected for Doppler broadening, gives $\sigma_a = 1.3 \times 10^{-12}\,\mathrm{cm}^2$. The observed absorption signals imply an excitation efficiency of $\approx 10\%$. If the dye laser saturated the $X \rightarrow a$ transition we would expect an excitation efficiency of 50%. In practice, the longitudinal modes of the dye laser reduce the efficiency. A rough estimate suggests suggests the actual efficiency should be in the $10 - 20\%$ range (see Section 5.10.2 for further discussion).

In addition, we also measured the microwave absorption in the ground state after the dye laser pulse to verify that all of the molecules leaving the $|X, J = 1\rangle$ state ended up in $|a, J = 2\rangle$. The inferred number density change in the ground state was actually a factor of two smaller than what appeared in the excited state. This is most likely due to a slight frequency dependent response of the microwave detector, which could change the conversion factors for determining the absorption fraction (see Eq. (7.83)). The frequency of the microwave beam in the ground and excited states was 28.2 GHz and 36.5 GHz, respectively.

[3]The number density inferred from the original absorption measurement on the $|a, J = 1, m = 0\rangle \rightarrow |a, J = 2, m = 0\rangle$ transition did agree with the stimulated emission measurement.

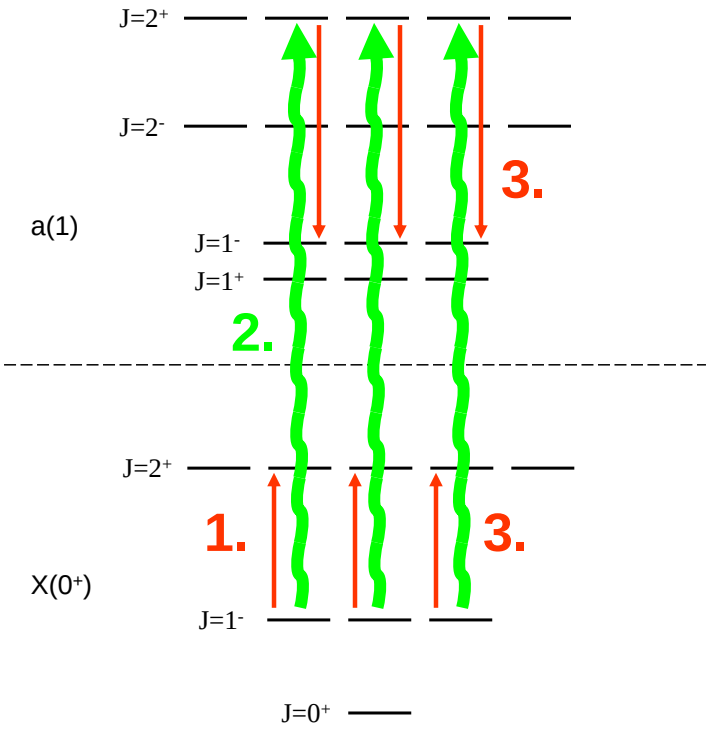

Figure 7.17: Excitation efficiency measurement. 1. Microwave absorption in the ground state determines the number density of the $|X, J = 1\rangle$ state. 2. A pulsed dye laser excites the molecules from $|X, J = 1\rangle$ to $|a, J = 2\rangle$. 3. Microwave absorption in the excited state determines the number density in the $|a, J = 2\rangle$ state. The ratio of the number densities gives the excitation efficiency. In addition, an absorption measurement in the ground state confirms the number density of molecules that left the $|X, J = 1\rangle$ state.

Chapter 8

Conclusions and Future Directions

The current sensitivity of the PbO experiment is not high enough to place a new limit on the electron EDM. Without EDM state preparation we have achieved beat frequency sensitivities of $\approx 105\,\mathrm{Hz}/\sqrt{N_{sh}}$, where N_{sh} is the number of laser shots. With an EDM state preparation efficiency of 100%, this corresponds to a sensitivity of $\delta d_e = 3 \times 10^{-27}\mathrm{e{\cdot}cm}/\sqrt{T}$, where T is the integration time in days. To reach the current experimental limit would require over 16 full days of integration.

At this point the highest state preparation efficiency achieved was 50%, with the microwave erasure method. A recent analysis has shown that this method may not be reliable. Computer modeling of a new method based on fitting two beat frequencies predicts it will give an effective efficiency a factor of $2\sqrt{2}$ higher than the microwave erasure method. However, this method has not been tested with actual experimental data. In addition, since it only works at high electric and magnetic fields, we may not have much flexibility for testing systematic effects.

The new laser system should improve the excitation efficiency and reduce the background fluorescence. The excitation efficiency is currently estimated to be 10% and the background fluorescence is likely 3-4 times the fluorescence from the J=1 state. If we conservatively assume the excitation efficiency is increased by a factor of 2 and the background fluorescence is reduced by a factor of 2 this should give an increase to the EDM sensitivity of 2.

With both the two beat frequency fitting and new laser system improvements we project a sensitivity of $\delta d_e = 1 \times 10^{-27}\mathrm{e{\cdot}cm}/\sqrt{T}$, where T is the integration time in days. Integrating for 2 days would match the current experimental limit. The apparatus has been successfully run continuously for 48 hours. In addition, it has been run several hours a day for months without

technical problems. Integrating continuously for a few weeks should pose no problems.

The seeded laser system has been used to take fluorescence data with the old YAG laser. The new YAG still needs to be integrated into the system but this should be straightforward. The seed laser should be broadened to match the Doppler width of 800 MHz for optimal excitation. Using the flat-flat Fabry Perot we have successfully observed ≈ 300 MHz sidebands on the output pulses of the seeded dye laser system by modulating the bias-T current input of the IR seed laser. However, these observations were averaged over several pulses. In addition, we would ideally like to use noise modulation to make a smoother lineshape.

There are not too many things left on the rest of the apparatus that could be further optimized. The analysis in Section 5.7 suggests the optical filters are now near optimal. Alternative detectors and detection schemes were extensively explored in previous theses[52, 81]. The second generation microwave absorption cell discussed in Chapter 7 would offer much higher sensitivity than the current apparatus. However, the ThO beam experiment, which is being pursued instead, uses standard AMO techniques and is projected to offer even higher sensitivity along with the promise of a less delicate experimental apparatus.

For the most part, the main thing left to do is to take EDM data![1]

[1] ..and, being a precision experiment, investigate systematic effects more extensively.

Appendix A

Mixing in a two level system

Consider a two-level Hamiltonian of the form

$$H = \begin{pmatrix} x & y \\ y & -x \end{pmatrix}. \tag{A.1}$$

Defining $r \equiv \sqrt{x^2 + y^2}$, $\theta \equiv \arctan(y/x)$ we can rewrite this as

$$H = \begin{pmatrix} r\cos\theta & r\sin\theta \\ r\sin\theta & -r\cos\theta \end{pmatrix}. \tag{A.2}$$

One can quickly check that the unnormalized eigenvectors of H are $\begin{pmatrix} \sin\theta \\ \pm 1 - \cos\theta \end{pmatrix}$ with eigenvalues $\pm r$. After some algebra one finds the normalized eigenvectors are

$$\frac{1}{\sqrt{2}} \begin{pmatrix} \pm\sqrt{1 \pm \cos\theta} \\ \sqrt{1 \mp \cos\theta} \end{pmatrix} \text{ or } \begin{pmatrix} \cos\theta/2 \\ \sin\theta/2 \end{pmatrix}, \begin{pmatrix} -\sin\theta/2 \\ \cos\theta/2 \end{pmatrix}. \tag{A.3}$$

In the limit of small mixing, $y/x \to 0$, we have $\theta \to 0$, eigenvalues of $x, -x$, and eigenvectors $\begin{pmatrix} 1 \\ 0 \end{pmatrix}, \begin{pmatrix} 0 \\ 1 \end{pmatrix}$. In the limit of strong mixing, $y/x \to \pm\infty$, we have $\theta \to \pm\frac{\pi}{2}$, eigenvalues of $y, -y$, and eigenvectors $\frac{1}{\sqrt{2}} \begin{pmatrix} 1 \\ \pm 1 \end{pmatrix}, \begin{pmatrix} \mp 1 \\ 1 \end{pmatrix}$.

Appendix B

Comparison of cross section calculations

At first glance, different textbooks seem to give different formulas for the absorption cross section. We will show below these differences are only in notation or assumptions. All are equivalent to the formula

$$\sigma = \frac{8\pi}{\hbar c}\frac{\omega}{\gamma}\left|\langle d\rangle\right|^2, \tag{B.1}$$

where ω is the angular frequency of the transition, γ is the natural linewidth in angular frequency equal to $1/\tau$, and $|\langle d\rangle|^2$ is the transition dipole matrix element squared. Hopefully this will prevent future students from struggling through factors of 2 and π.

B.1 Budker, Kimball, and Demille [86]

The final cross-section formulas in this book (hereafter BKD) tend to be stated in terms of reduced matrix elements or partial widths and include averages over polarizations. This is often appropriate for optical transitions where transition matrix elements can be difficult to calculate but makes it difficult to compare to more tractable cases such as rf transitions.

The derivation starts with the statement of Fermi's golden rule (3.73)

$$dW_{fi} = \frac{2\pi}{\hbar}\left|\left\langle f\right|H'\left|i\right\rangle\right|^2 \rho_f(E)P(E)\,dE, \tag{B.2}$$

where $\rho_f(E)$ is the density of states. For a Lorentzian lineshape the energy distribution, $P(E)$ is given by

$$P(\omega) = \frac{\gamma/2\pi}{(\omega - \omega_0)^2 + (\gamma/2)^2} \tag{B.3}$$

where $\gamma = 1/\tau$ is the FWHM of the angular frequency spread. Assuming monochromatic light we can substitute the resonant value of $P(\omega_0) = \frac{2}{\pi\gamma}$ for the integration over energy into Eq. (B.2) which gives

$$W_{eg} = \frac{4}{\gamma\hbar^2} \left|\langle f \left| H' \right| i\rangle\right|^2 \tag{B.4}$$

From 3.123,

$$\left|\langle f \left| H' \right| i\rangle\right|^2 = \frac{2\pi\hbar\omega_0 n}{V} \left|\langle d\rangle\right|^2, \tag{B.5}$$

where $|\langle d\rangle|^2 = |\langle d \cdot \hat{\epsilon}\rangle|^2$, with $\hat{\epsilon}$ the light polarization, n is number of photons in the electromagnetic mode, and V is the volume. Since the photon flux is

$$\Phi = \frac{nc}{V} \tag{B.6}$$

we have

$$\left|\langle f \left| H' \right| i\rangle\right| = \frac{2\pi\hbar\omega_0\Phi}{c} \left|\langle d\rangle\right|^2. \tag{B.7}$$

This gives a cross section of

$$\sigma_{BKD} = \frac{W_{eg}}{\Phi} = \frac{8\pi}{\hbar c} \frac{\omega_0}{\gamma} \left|\langle d\rangle\right|^2 \tag{B.8}$$

B.2 Sakurai [131]

With an assumption of monochromatic excitation we start with (S 5.7.22)

$$\sigma_{abs} = 4\pi^2\alpha\omega_{ni} \left|\langle n \left| x \right| i\rangle\right|^2 \delta(\omega - \omega_{ni}) \tag{B.9}$$

Similar to BKD we substitute the resonant value of a Lorentzian lineshape Eq. (B.3) for the δ-function (the limit $\gamma \to 0$ of a Lorentzian is one analytical expression for a δ-function). Note that γ is also

defined as $1/\tau$ and is again equal to FWHM of the angular frequency. This gives

$$\sigma_{Sak} = 4\pi^2 \frac{e^2}{\hbar c} \omega_{ni} \left|\langle n \left| x \right| i \rangle\right|^2 \frac{2}{\gamma\pi} = \frac{8\pi}{\hbar c} \frac{\omega_{ni}}{\gamma} \left|\langle d \rangle\right|^2 \tag{B.10}$$

B.3 Townes and Schawlow [69]

Townes and Schawlow (TS) state their final result for RF frequencies as an absorption per unit length (TS 13-22)

$$\gamma = \frac{8\pi^2 N f}{3ckT} \left|\mu_{ij}\right|^2 \nu^2 \frac{\Delta\nu}{(\nu - \nu_0)^2 + (\Delta\nu)^2}, \tag{B.11}$$

where N is the total number density of molecules, f is the fraction of molecules in the bottom state, $\Delta\nu$ is the *HWHM*, and $\frac{\left|\mu_{ij}\right|^2}{3}$ is the average of the sum of the squares of the transition matrix elements (TS 1-76)

$$\left|\mu_{ij}\right|^2 = \sum_{M'} \left|\mu_x(J\,M\,J'\,M')\right|^2 + \left|\mu_y(J\,M\,J'\,M')\right|^2 + \left|\mu_z(J\,M\,J'\,M')\right|^2. \tag{B.12}$$

To compare to the other cross-sections we need to evaluate Eq. (B.11) on resonance, divide by the difference in population density of the two levels, substitute $\left|\langle d \rangle\right|^2$ for $\frac{\left|\mu_{ij}\right|^2}{3}$, and multiply by two to account for the HWHM versus FWHM. The population difference is given by a Boltzmann factor times the population which for the radio frequencies discussed in this book (where $h\nu \ll kT$) is

$$\Delta n = \frac{h\nu_0}{kT} N f. \tag{B.13}$$

Doing all of this gives

$$\sigma_{T\&S} = \frac{8\pi^2}{3hc} \left|\mu_{ij}\right|^2 \frac{\nu}{\Delta\nu} = \frac{8\pi}{\hbar c} \frac{\omega}{\gamma} \left|\langle d \rangle\right|^2. \tag{B.14}$$

Appendix C

Optical alignment hints

This appendix gives a few hints for alignment of the more difficult optical elements. Refer to Fig. 5.39 for a diagram of the optical setup.

C.1 Tapered amplifier

Coupling the beam into the tapered amplifier is similar to coupling into a single mode fiber (SM). Turn on the tapered amplifier and adjust the current to the point where beams on the input and output sides can be seen on an IR card. The incoming beam profile from the DL PRO, which has been shaped by an anamorphic prism pair, should roughly match the shape of the beam coming from the input side of the tapered amp. Make sure the beam coming from the input side of the tapered amplifier is roughly collimated by the input side aspheric lens. Overlap the beams at two points using the two mirrors on the input side. Walk the beam until an amplified beam is seen on the output side. Slowly turn up the power and maximize the output. Adjust the $\lambda/2$ waveplate to rotate the polarization for optimal amplification (the polarization should be roughly vertical). On the output side one axis is collimated by the aspheric lens. The second axis is collimated by the cylindrical lens outside the tapered amp box. The focal length should be such that the collimated beam is circular. Positioning the beam in the center of both lenses is crucial to obtaining a decent output beam shape. A teardrop shape or a series of bands in the laser profile usually indicates the aspheric lens is not centered.

C.2 Polarization maintaining single mode fiber

To achieve maximum coupling it is extremely important to properly shape and collimate the tapered amplifier output beam. Next, connect a single mode (SM) fiber to the fiber collimator with the fiber tester on the other end. Roughly adjust the z-axis of the collimating lens until the output test beam is collimated. Overlap the output beam from the tapered amplifier with the test beam at a point as far as possible from the fiber by adjusting the dielectric mirror mount and collimator mount. Replace the SM fiber with the PM fiber and maximize the coupling by walking the beam with the mirror and collimator mounts. It is often helpful to first loosely attach the fiber to the collimator and then iteratively maximize the coupling and tighten the fiber. Last, iteratively adjust the z-axis of the collimating lens and re-maximize the coupling. The z-axis adjustment screw has some hysteresis so adjustments should be made in a single direction. With some care, over 60% coupling can be achieved.

There are several methods for aligning the input beam polarization to an axis of the PM fiber. We have found the quickest and easiest method is to mount the output end of the PM fiber on a rotation stage and monitor the power after a polarizing beam splitting cube. Iteratively adjust the output rotation stage and the $\lambda/2$ plate before the input end of the fiber until the power is minimized. Next, for a more precise adjustment, rotate the output stage 45 degrees and monitor the power after the PBS while changing the temperature of the fiber (holding it your hand, using a heat gun, or using a dust spray can will all work). Slightly adjust the input $\lambda/2$ plate until the change in power with temperature is minimized. In practice, the second adjustment is usually not needed. Before removing the PBS adjust the output polarization of the PM fiber to vertical if coupling to the PPLN waveguide.

C.3 PPLN

A clean cleave on the bare fiber can be obtained by first stripping the clear cladding off the fiber with a razor blade and then nicking the end with a diamond tip. After gently breaking the fiber at the nick attach the fiber tester to the connectorized end of the fiber. The output beam from the cleaved end should look perfectly circular. The fiber can be multimode at the wavelength of the fiber tester so if two symmetric lobes are seen, adjust the position of the fiber tester. A bad cleave

looks clearly asymmetrical and distorted. Gently using optical fiber polishing paper on the end sometimes helps to remove debris.

Coupling to the PPLN channels can be tricky, particularly with low input powers. A crude microscope made from a short focal length aspheric, a lens tube with an aperture, and a longer focal length lens can help to position the fiber close to the waveguide and align it to one of the channels. With a CCTV camera attached to the microscope, we have found that the channels are visible in higher contrast when the chip is illuminated with an incandescent bulb flashlight, rather than an LED flashlight. Adjusting the aperture on the microscope also helps with contrast. To align the vertical direction monitor the beam on the output side of the chip. As the height of the beam reaches the top edge of the chip a sudden change to a diffraction pattern occurs. The farther the beam height is above the chip the closer the diffraction lines become.

At this point, with high input powers ($> 100\,\mathrm{mW}$) the alignment is fairly easy. The temperature of the PPLN chip should be adjusted to $\approx 62\,^{\circ}\mathrm{C}$. Confirm that the diode laser is running single mode and at the proper frequency ($9120.17\,\mathrm{cm}^{-1}$ for the R0 line). Starting with a distance of about one fiber width between the fiber and chip, scan the fiber across the width of the chip until green light is seen on the output. Maximize the green light by adjusting the horizontal and vertical position of the fiber, move the fiber slightly closer to the chip, and repeat. At low powers the fiber must be positioned as closely as possible to the chip and aligned precisely with the microscope. Once decent coupling is achieved note the positions of the micrometer knobs on the positioning stage. Back the fiber away from the waveguide and gently screw on the top of the oven (which helps with temperature stability). When adjusting the positioning stage in the future be especially careful not to move the axis that controls the spacing between the fiber and chip past the noted point, as contact may scratch the coating on the chip.

C.4 Four pass seeded dye amplifier

To align the four passes first make sure that the seed beam goes through the center of the Faraday rotator and passes through the dye cell between the inner surface of the quartz and the plastic separator in the middle of the dye cell. With a few milliwatts of green power it is easy to see the beam path in the dye cell from above and to the side. Next use the M1 and M2 mirrors to align the first and second passes below PBS2. A small amount of the first pass is deflected by PBS2. Chop

the beam with a piece of paper between M1 and M2 and use M1 to overlap the spots immediately below PBS2. Next overlap the spots near the grating (or remove the grating and look farther away) with M2. Roughly align the grating so that the first order reflects straight back. Look for the spot from the third pass between M1 and M2 while chopping in front of the grating. The fourth pass is automatically aligned at this point although it may not be visible at the output. With the pump laser on there should be a bright spot in the output that disappears when the seed laser is blocked. Direct the output to the monitor étalon. When seeded there will be a clear ring pattern. Adjust M1, M2, and the grating to maximize the contrast of the rings.

Appendix D

Data fitting

D.1 Uncertainty in the beat frequency fit

In this section we will derive the theoretical uncertainty of the quantum beat frequency in a least-squares fit taking into account decohering effects and background signals. For later comparison, we first recall that a naive estimate based on the uncertainty principle and counting statistics gives

$$\delta\omega = \frac{1}{cT\sqrt{N}}. \tag{D.1}$$

We perform a least-squares fit of the fluorescence signal to the functional form,

$$S(t) = \alpha I(t)\left[1 + ce^{-T/T_b}\cos(\omega_b T + \phi)\right] + d. \tag{D.2}$$

I(T) is the "scrambled data" in the absence of quantum beats, normalized such that $I(0) = 1$. We will discuss how I(T) is determined in the next section. For now we use the fact that I(T) is roughly exponential, $I(T) \approx e^{-T/T_1}$, where T_1 is the lifetime of the $a(1)$ state in the vapor cell. The free parameters in the fit are the signal size α, the quantum beat contrast c, the quantum beat frequency ω_b, the quantum beat phase ϕ, the DC background d, and the excess quantum beat decoherence time T_b. The factor T_b accounts for collisions which destroy the coherence of the quantum beats but leave the molecules in the $a(1)$ state which causes the contrast to decrease more quickly than the state lifetime.

To estimate the uncertainty of our fit we follow the analysis outlined in [95], but also consider the case where the background term, d, comparable to the signal size, α. We assume that $I(T) = e^{-T/T_1}$. Analytic and empirical analysis has shown that only the quantum beat phase shows significant correlation with the quantum beat frequency. Thus to determine the uncertainty, $\delta\omega$, in the beat frequency we start with the error matrix,

$$\boldsymbol{E}^{-1} = \begin{pmatrix} (\delta\omega)^2 & \delta\omega\delta\phi \\ \delta\omega\delta\phi & (\delta\phi)^2. \end{pmatrix} \tag{D.3}$$

The error matrix is related to the χ^2 of the fit (see e.g. [132]) by

$$\boldsymbol{E} = \frac{1}{2}\begin{pmatrix} \frac{\partial^2\chi^2}{\partial\omega^2} & \frac{\partial^2\chi^2}{\partial\omega\partial\phi} \\ \frac{\partial^2\chi^2}{\partial\omega\partial\phi} & \frac{\partial^2\chi^2}{\partial\phi^2}. \end{pmatrix} \tag{D.4}$$

Combining these expressions we find

$$\begin{pmatrix} (\delta\omega)^2 & \delta\omega\delta\phi \\ \delta\omega\delta\phi & (\delta\phi)^2 \end{pmatrix} = \frac{2}{\frac{\partial^2\chi^2}{\partial\omega^2}\frac{\partial^2\chi^2}{\partial\omega^2} - \left(\frac{\partial^2\chi^2\omega\phi}{\partial^2 2}\right)} \begin{pmatrix} \frac{\partial^2\chi^2}{\partial\phi^2} & -\frac{\partial^2\chi^2}{\partial\omega\partial\phi} \\ -\frac{\partial^2\chi^2}{\partial\omega\partial\phi} & \frac{\partial^2\chi^2}{\partial\omega^2}. \end{pmatrix}. \tag{D.5}$$

The χ^2 value for a given data set $\{D_i = D(T_i)\}$, with noise $\{\delta S_i = \delta S(T_i)\}$, and fit model values $\{S_i = S(T_i)\}$ is

$$\chi^2 = \sum_{i=1}^{n} \left(\frac{D_i - S_i}{\delta S_i}\right)^2. \tag{D.6}$$

Now consider the second derivate of χ^2 with respect to two of the fit parameters, X and Y,

$$\begin{aligned} \frac{\partial^2\chi^2}{\partial X\partial Y} &= \frac{\partial}{\partial X}\left[2\frac{(D_i - S_i)}{\delta S_i^2}\frac{\partial S_i}{\partial Y}\right] \\ &= -2\frac{1}{\delta S_i^2}\frac{\partial S_i}{\partial X}\frac{\partial S_i}{\partial Y} + 2\frac{(D_i - S_i)}{\delta S_i^2}\frac{\partial^2 S_i}{\partial X\partial Y} \\ &\approx -2\frac{1}{\delta S_i^2}\frac{\partial S_i}{\partial X}\frac{\partial S_i}{\partial Y}. \end{aligned} \tag{D.7}$$

Here we used the fact that D_i and S_i are independent of the fit parameters, and that the residuals,

$D_i - S_i$, average to zero for a good fit. Defining the beat coherence time, $T_2^{-1} = T_b^{-1} + T_1^{-1}$, we find

$$\frac{\partial^2\chi^2}{\partial\phi^2} = 2\sum_i \frac{\alpha^2c^2e^{-2T_i/T_2}\sin^2(\omega_bT_i+\phi)}{\delta S_i^2} \tag{D.8}$$

$$\frac{\partial^2\chi^2}{\partial\phi\partial\omega} = 2\sum_i T_i\frac{\alpha^2c^2e^{-2T_i/T_2}\sin^2(\omega_bT_i+\phi)}{\delta S_i^2} \tag{D.9}$$

$$\frac{\partial^2\chi^2}{\partial\omega^2} = 2\sum_i T_i^2\frac{\alpha^2c^2e^{-2T_i/T_2}\sin^2(\omega_bT_i+\phi)}{\delta S_i^2} \tag{D.10}$$

If our signal is expressed as a counting rate, i.e. in units of photoelectrons per second, the number of photoelectrons detected in each interval is $N_i = S_i\Delta T$. If our detection is shot noise limited then $(\delta S_i\Delta T)^2 = N_i$ which implies $(\delta S_i)^2 = S_i/\Delta T$. In these units $N = \int S(T)\,dT \approx \alpha\int e^{-T/T_1}\,dT = \alpha/T_1$, where N is the total number of photoelectrons detected. Inserting the above expression for $(\delta S_i)^2$ gives

$$\begin{aligned}\frac{\partial^2\chi^2}{\partial\phi^2} &= 2\sum_i \frac{\Delta T\alpha^2c^2e^{-2T_i/T_2}\sin^2(\omega_bT_i+\phi)}{\alpha e^{-T/T_1}\left[1+ce^{-T_i/T_b}\cos(\omega_bT_i+\phi)\right]+d}\\ &\approx \alpha c^2\int_0^\infty \frac{e^{-2T/T_2}}{e^{-T/T_1}+d/\alpha}\,dT \end{aligned}\tag{D.11}$$

$$\frac{\partial^2\chi^2}{\partial\phi\partial\omega} \approx \alpha c^2\int_0^\infty \frac{Te^{-2T/T_2}}{e^{-T/T_1}+d/\alpha}\,dT \tag{D.12}$$

$$\frac{\partial^2\chi^2}{\partial\omega^2} \approx \alpha c^2\int_0^\infty \frac{T^2e^{-2T/T_2}}{e^{-T/T_1}+d/\alpha}\,dT \tag{D.13}$$

In the approximation we have assumed small contrast to eliminate the cosine term in the denominator, replaced the quickly oscillating $\sin^2$ term in the numerator by its average value of $1/2$ (assuming that $\omega_b \gg 1/T_2$), and replaced the sum by an integral. The integral can be expressed in terms of the Lerch transcendental function, but for our purposes we would prefer a simpler approximation. In the limits of either no background or large background these integrals have the common form,

$$\int_0^\infty T^ne^{-T/\tau}\,dT = n!\tau^{n+1}. \tag{D.14}$$

The time constant, τ, in the limit $d/\alpha \ll 1$ is $\tau \approx \frac{T_1T_2}{2T_1-T_2} \equiv \tau_\alpha$ and for $d/\alpha \gg 1$ it is $\tau \approx T_2/2 \equiv \tau_D$. The

exact integrals are well approximated by an interpolation between these values of the form

$$\int_0^\infty \frac{T^n e^{-2T/T_2}}{e^{-T/T1} + d/\alpha}\, dT \approx n!\tau_{(n+1)}^{n+1}$$
$$\frac{1}{\tau_{(n+1)}^{n+1}} = \frac{1}{\tau_\alpha^{n+1}} + \frac{d}{\alpha}\frac{1}{\tau_d^{n+1}}. \tag{D.15}$$

Plugging these values back into Eq. (D.5) we arrive at the result,

$$\begin{pmatrix} (\delta\omega)^2 & \delta\omega\delta\phi \\ \delta\omega\delta\phi & (\delta\phi)^2 \end{pmatrix} = \frac{2}{\alpha c^2}\frac{1}{2\tau_{(3)}^3\tau_{(1)} - \tau_{(2)}^4}\begin{pmatrix} \tau_{(1)} & -\tau_{(2)}^2 \\ -\tau_{(2)}^2 & 2\tau_{(3)}^3 \end{pmatrix}. \tag{D.16}$$

For the frequency uncertainty there is little change in accuracy with the further approximation $\tau_{(n)} = \tau_{(3)}$. This gives

$$\delta\omega = \frac{\sqrt{2}}{c\sqrt{\alpha\tau_{(3)}^3}}. \tag{D.17}$$

With a little algebra one show this is equivalent to

$$\delta\omega = \frac{\sqrt{2}}{c\sqrt{\alpha T_1^3}}\xi\left(\tfrac{T_1}{T_b}, \tfrac{d}{\alpha}\right) = \frac{\sqrt{2}}{cT_1\sqrt{N}}\xi\left(\tfrac{T_1}{T_b}, \tfrac{d}{\alpha}\right), \tag{D.18}$$

where $\xi\left(\frac{T_1}{T_b}, \frac{D}{\alpha}\right) = \sqrt{\left(1 + 2\frac{T_1}{T_b}\right)^3 + 8\left(1 + \frac{T_1}{T_b}\right)^3\frac{d}{\alpha}}$ is a correction factor for our earlier estimate Eq. (D.1). The first term in the square root comes from the correction for T_b, while the second is a factor which takes into account the different contributions to the shot noise from the signal and the constant background.[1] We typically operate in the regime where $T_1 = T_b$, which gives $\xi = \sqrt{27 + 64\frac{d}{\alpha}}$. Thus for a fixed signal size, α, the uncertainty slowly degrades for a background $d > \frac{1}{3}\alpha$.

Using a 100 nm bandpass interference filter and KG4 IR blocking glass, the current value of $d/\alpha \approx 0.5$ gives $\xi \approx 8$. Under this configuration $\alpha = 3.5 \times 10^{11}$photoelectrons/s, $c = 0.08$, and $T_1 \approx T_2 \approx 40 \times 10^{-6}\,\mu$s which gives a single shot uncertainty estimate of $\delta\omega = 2\pi \times 144\,$Hz. The actual uncertainty, determined by the width of a Gaussian fit to a histogram of the fitted frequencies, is 148 Hz, showing that our detection is shot-noise limited. Note these values are at zero electric field without EDM state preparation.

One can show that the $\sqrt{2}$ in the numerator is eliminated if the beat phase, ϕ, is fixed. For a

[1] ξ is similar to F in [29], but defined so that the connection between the frequency uncertainty and T_1 is clear, rather than T_2.

given experimental configuration ϕ should be a constant dependent on the beginning time of the data relative to the laser shot, the position of the PMT detector, and electronic delays in the data acquisition system. In theory we could use a large dataset to determine ϕ, and then fix its value and refit the data. Because the phase is correlated with the beat frequency, we have been hesitant to do so. This caution may have been warranted as the current single shot frequency uncertainty of 150 Hz corresponds to a phase uncertainty of 40 milliradians. For a beat frequency of 300 kHz this corresponds to an uncertainty of 20 ns in the start time of the fit relative to the laser shot. Both the BNC pulse generator used to trigger data acquisition, and the data acquisition board used in the past had 20 MHz internal clocks or 50 ns resolution. The new high speed NI-SCOPE data acquisition board now being used has a time-to-digital converter which records the time between the trigger and first data point conversion to sub-nanosecond accuracy. In future measurements this board will be triggered by a photodiode monitoring the laser system.

D.2 Extracting "scrambled" data

As discussed above, our data fitting model assumes we can fit the quantum beat data to a fluorescence signal with the same time dependence but no quantum beats. Over the years we have developed several methods to acquire this background data.

The first method, before we used magnetic shields, was to simply apply a magnetic field gradient across the cell which caused the quantum beats to quickly decohere or "scramble". This method worked quite well but was inefficient with magnetic shields since it requires degaussing the magnetic shields each time we use it.

When microwaves were introduced to our system we discovered a second method to introduce decoherence. Applying long powerful resonant microwave pulses introduced enough inhomogeneity to wash out the quantum beats. Since the J=2 g-factor is only one-third of the J=1 g-factor, the molecules pick up different phases as they Rabi flop between the two states. Combined with inhomogeneous microwave power in the cell this washes out the J=1 quantum beats. This method has two advantages. First, it only affects the molecules in the quantum state of interest. We have seen some evidence that the slow quantum beats of background molecules in higher J states contribute to the shape of the fluorescence envelope when we use an excitation scheme with the dye laser horizontally polarized. These molecules, and therefore the background, are unaffected by the

microwaves. Second, this method is easy to implement in software. Its only drawback is the time that it takes from EDM data collection.

Before the microwave method was developed we explored the possibility of extracting the scrambled data from the normal quantum beat data. Jiang [52] discusses two methods based on techniques used in the muon g-2 experiment. Here I will discuss in more detail the method of using linear combinations of time-shifted data to cancel the quantum beats.

The basic idea behind this method is to add our quantum beat data to a copy of itself shifted by half a quantum beat cycle. If the envelope has changed little over the half cycle the quantum beats our canceled. To be more concrete we consider a sinusoidal signal on top of some arbitrary background signal $A(t)$,

$$S(t) = A(t)(1 + \cos \omega t). \tag{D.19}$$

Using a Taylor expansion with $\Delta t = \frac{\pi}{\omega}$ we find

$$\begin{aligned} S(t \pm \Delta t) &= A(t \pm \Delta t)[1 + \cos(\omega t \pm \pi)] \\ &= \left[A(t) \pm A'(t)\Delta t + A''(t)\frac{\Delta t^2}{2} \pm A'''(t)\frac{\Delta t^3}{6} + A^{(4)}(t)\frac{\Delta t^4}{24}\right][1 - \cos \omega t]. \end{aligned} \tag{D.20}$$

Now if we take the linear combination

$$\begin{aligned} \tilde{A}_1(t) &= \frac{1}{4}[S(t - \Delta t) + 2S(t) + S(t + \Delta t)] \\ &= \frac{1}{2}A(t)(1 + \cos \omega t) + \frac{1}{2}\left[A(t) + A''(t)\frac{\Delta t^2}{2} + A^{(4)}(t)\frac{\Delta t^4}{24}\right](1 - \cos \omega t) \\ &= A(t) + \left[A''(t)\frac{\Delta t^2}{4} + A^{(4)}(t)\frac{\Delta t^4}{48}\right] \end{aligned} \tag{D.21}$$

We have now recovered the "scrambled" data, $A(t)$, up to some terms involving second or higher order derivatives of $A(t)$. In the actual experiment we have $A(t) \approx e^{-t/\tau}$, with $\tau \approx 50\,\mu s$ and $\Delta t = \frac{1}{2f_{beats}} \approx 2\,\mu s$. This gives

$$A''(t)\frac{\Delta t^2}{4} \approx 4 \times 10^{-4} \times A(t). \tag{D.22}$$

D.2.1 Equivalence to g-2 ratio method

In the g-2 muon experiment the data is not fit to a model function. Instead they first calculate the "ratio" function

$$r(t) = \frac{V(t) - U(t)}{V(t) + U(t)}, \tag{D.23}$$

where $V(t) = 2S(t)$ and $U(t) = S(t - T/2) + S(t + T/2)$. To first order this function is fit to a sinusoid,

$$r(t) \mapsto C \cos \omega t, \tag{D.24}$$

where $\mapsto$ means "is fit to". While not immediately obvious, this ratio method is equivalent to the fitting method described above. Our method can be described by

$$S(t) \mapsto \tilde{A}(t)(1 + C \cos \omega t), \tag{D.25}$$

where $\tilde{A}(t)$ is the estimate of the background function. Our first order estimate is related to $U(t)$ and $V(t)$ by

$$\tilde{A}_{(1)}(t) = \frac{1}{4}[S(t - T/2) + 2S(t) + S(t + T/2)] = \frac{1}{4}(V(t) + U(t)]. \tag{D.26}$$

Manipulating Eq. (D.25) our fitting method is equivalent to

$$\frac{S(t)}{\tilde{A}(t)} - 1 \mapsto C \cos \omega t \tag{D.27}$$

Using $S(t) = \frac{1}{2}V(t)$ we can then show the equivalence between the two methods

$$\frac{S(t)}{\tilde{A}(t)} - 1 = \frac{\frac{1}{2}V(t)}{\frac{1}{4}(V(t) + U(t))} - 1 = \frac{V(t) - U(t)}{V(t) + U(t)} = r(t). \tag{D.28}$$

This equivalence was only recently realized. The g-2 ratio method has the advantage that the fit model is an analytic function which simplifies programming.

Bibliography

[1] E. M. Purcell and N. F. Ramsey, Physical Review Online Archive (Prola), **78**, 807+ (1950).

[2] I. B. Khriplovich, *Parity nonconservation in atomic phenomena* (Gordon and Breach Science Publishers, Philadelphia, 1991).

[3] B. C. Regan, E. D. Commins, C. J. Schmidt, and D. DeMille, Phys. Rev. Lett., **88**, 071805 (2002).

[4] E. E. Salpeter, Phys. Rev., **112**, 1642 (1958).

[5] D. F. Nelson, A. A. Schupp, R. W. Pidd, and H. R. Crane, Physical Review Letters, **2**, 492 (1959).

[6] D. T. Wilkinson and H. R. Crane, Physical Review Online Archive (Prola), **130**, 852 (1963).

[7] J. Goldemberg and Y. Torizuka, Physical Review Online Archive (Prola), **129**, 2580 (1963).

[8] E. S. Ensberg, Bulletin of the American Physical Society, **7**, 534+ (1962).

[9] P. G. H. Sandars and E. Lipworth, Physical Review Letters, **13**, 718 (1964).

[10] E. Lipworth, A. Adler, J. P. Carrico, T. S. Stein, and P. G. H. Sandars, Bulletin of the American Physical Society, **11**, 403+ (1966).

[11] T. S. Stein, J. P. Carrico, E. Lipworth, and M. C. Weisskopf, Physical Review Letters, **19**, 741 (1967).

[12] M. C. Weisskopf, J. P. Carrico, H. Gould, E. Lipworth, and T. S. Stein, Physical Review Letters, **21**, 1645 (1968).

[13] S. A. Murthy, D. Krause, Z. L. Li, and L. R. Hunter, Physical Review Letters, **63**, 965 (1989).

[14] H. Gould, Physical Review Letters, **24**, 1091 (1970).

[15] K. Abdullah, C. Carlberg, E. D. Commins, H. Gould, and S. B. Ross, Physical Review Letters, **65**, 2347 (1990).

[16] E. D. Commins, S. B. Ross, D. DeMille, and B. C. Regan, Physical Review A, **50**, 2960 (1994).

[17] M. A. Player and P. G. H. Sandars, J. Phys. B: At., Mol. Phys., **3**, 1620+ (1970), ISSN 0022-3700.

[18] T. G. Vold, F. J. Raab, B. Heckel, and E. N. Fortson, Physical Review Letters, **52**, 2229 (1984).

[19] E. A. Hinds and P. G. H. Sandars, Physical Review A, **21**, 480 (1980).

[20] D. A. Wilkening, N. F. Ramsey, and D. J. Larson, Physical Review A, **29**, 425 (1984).

[21] D. Schropp, D. Cho, T. Vold, and E. A. Hinds, Physical Review Letters, **59**, 991 (1987).

[22] D. Cho, K. Sangster, and E. A. Hinds, Physical Review Letters, **63**, 2559 (1989).

[23] S. K. Lamoreaux, J. P. Jacobs, B. R. Heckel, F. J. Raab, and N. Fortson, Physical Review Letters, **59**, 2275 (1987).

[24] J. P. Jacobs, W. M. Klipstein, S. K. Lamoreaux, B. R. Heckel, and E. N. Fortson, Physical Review Letters, **71**, 3782 (1993).

[25] J. P. Jacobs, W. M. Klipstein, S. K. Lamoreaux, B. R. Heckel, and E. N. Fortson, Physical Review A, **52**, 3521 (1995).

[26] M. V. Romalis, W. C. Griffith, J. P. Jacobs, and E. N. Fortson, Physical Review Letters, **86**, 2505 (2001).

[27] W. C. Griffith, M. D. Swallows, T. H. Loftus, M. V. Romalis, B. R. Heckel, and E. N. Fortson, Physical Review Letters, **102**, 101601+ (2009).

[28] B. J. Heidenreich, O. T. Elliott, N. D. Charney, K. A. Virgien, A. W. Bridges, M. A. McKeon, S. K. Peck, D. Krause, J. E. Gordon, L. R. Hunter, and S. K. Lamoreaux, Phys. Rev. Lett., **95**, 253004+ (2005).

[29] S. Bickman, P. Hamilton, Y. Jiang, and D. DeMille, Phys. Rev. A, **80**, 023418 (2009).

[30] A. C. Vutha, W. C. Campbell, Y. V. Gurevich, N. R. Hutzler, M. Parsons, D. Patterson, E. Petrik, B. Spaun, J. M. Doyle, G. Gabrielse, and D. DeMille, J. Phys. B: At., Mol. Opt. Phys., **43**, 074007+ (2010), ISSN 0953-4075.

[31] A. O. Sushkov, S. Eckel, and S. K. Lamoreaux, Physical Review A, **81**, 022104+ (2010).

[32] V. Simha and G. Steigman, Journal of Cosmology and Astroparticle Physics, **2008**, 016+ (2008), ISSN 1475-7516.

[33] A. D. Sakharov, Journal of Experimental and Theoretical Physics Letters, **5**, 24+ (1967).

[34] M. B. Gavela, P. Hernández, J. Orloff, and O. Pène, Modern Physics Letters A, **9**, 795 (1994).

[35] P. Huet and E. Sather, Physical Review D, **51**, 379 (1995).

[36] C. A. Baker, D. D. Doyle, P. Geltenbort, K. Green, M. G. D. van der Grinten, P. G. Harris, P. Iaydjiev, S. N. Ivanov, D. J. R. May, J. M. Pendlebury, J. D. Richardson, D. Shiers, and K. F. Smith, Phys. Rev. Lett., **97**, 131801 (2006).

[37] M. Kobayashi and T. Maskawa, Progress of Theoretical Physics, **49**, 652 (1973).

[38] J. H. Christenson, J. W. Cronin, V. L. Fitch, and R. Turlay, Physical Review Letters, **13**, 138 (1964).

[39] K. Abe, K. Abe, R. Abe, I. Adachi, B. S. Ahn, H. Aihara, *et al.*, Physical Review Letters, **87**, 091802+ (2001).

[40] B. Aubert, D. Boutigny, J. M. Gaillard, A. Hicheur, Y. Karyotakis, J. P. Lees, P. Robbe, V. Tisserand, A. Palano, G. P. Chen, *et al.*, Physical Review Letters, **87**, 091801+ (2001).

[41] V. M. Abazov, B. Abbott, M. Abolins, B. S. Acharya, M. Adams, T. Adams, E. Aguilo, G. D. Alexeev, G. Alkhazov, A. Alton, G. Alverson, *et al.*, Physical Review Letters, **105**, 081801+ (2010).

[42] D. DeMille, S. Bickman, P. Hamilton, Y. Jiang, V. Prasad, D. Kawall, and R. Paolino, AIP Conference Proceedings, **842**, 759 (2006).

[43] E. D. Commins, "Electric dipole moments of leptons," in *Advances In Atomic, Molecular, and Optical Physics*, Vol. 40, edited by B. Bederson and H. Walther (Academic Press, 1999) pp. 1–55, ISBN 0-12-003840-4.

[44] N. F. Ramsey, Physical Review Online Archive (Prola), **78**, 695 (1950).

[45] G. Ban, K. Bodek, M. Daum, R. Henneck, S. Heule, M. Kasprzak, N. Khomytov, K. Kirch, A. Knecht, S. Kistryn, P. Knowles, M. Kuzniak, T. Lefort, O. Naviliat-Cuncic, A. Pichlmaier, C. Plonka, G. Quémener, M. Rebetez, D. Rebreyend, G. Rogel, B. Sabirov, M. Tur, A. Weis, and J. Zejma, Hyperfine Interact., **172**, 41 (2006), ISSN 0304-3843.

[46] T. M. Ito and T. Collaboration, J. Phys.: Conference Series, **69**, 012037+ (2007), ISSN 1742-6596.

[47] J. C. Long, P. D. Barnes, J. G. Boissevain, D. J. Clark, M. D. Cooper, J. J. Gomez, S. K. Lamoreaux, R. E. Mischke, and S. I. Penttila, "High voltage test apparatus for a neutron edm experiment and lower limit on the dielectric strength of liquid helium at large volumes," (2006), arXiv:physics/0603231 .

[48] F. J. M. Farley, K. Jungmann, J. P. Miller, W. M. Morse, Y. F. Orlov, B. L. Roberts, Y. K. Semertzidis, A. Silenko, and E. J. Stephenson, Phys. Rev. Lett., **93**, 052001+ (2004).

[49] D. Anastassopoulos, V. Anastassopoulos, D. Babusci, M. Bai, G. Bennett, J. Bengtsson, I. Ben-Zvi, M. Blaskiewicz, K. Brown, G. Cantatore, M. Dabaghyan, V. Dzhordzhadze, P. D. Eversheim, M. E. Emirhan, G. Fanourakis, A. Facco, A. Fedotov, A. Ferrari, T. Geralis, Y. Giomataris, F. Gonnella, F. Gray, R. Gupta, S. Haciomeroglu, G. Hoffstaetter, H. Huang, M. Incagli, K. Jungmann, M. Karuza, D. Kawall, B. Khazin, I. B. Khriplovich, I. A. Koop, Y. Kuno, D. M. Lazarus, R. Larsen, P. L. Sandri, F. Lin, A. Luccio, N. Malitsky, W. W. MacKay, W. Marciano, A. Masaharu, W. Meng, R. Messi, L. Miceli, J. P. Miller, D. Moricciani, W. M. Morse, C. J. G. Onderwater, Y. F. Orlov, C. S. Ozben, T. Papaevangelou, V. Ptitsyn, B. Parker, D. Raparia, S. Redin, S. Rescia, G. Ruoso, T. Russo, A. Sato, Y. K. Semertzidis, Yu, V. Shemelin, A. Sidorin, A. Silenko, da Silva, N. Simos, E. J. Stephenson, G. Venanzoni, A. Vradis, G. Zavattini, A. Zelenski, and K. Zioutas, *AGS Proposal: Search for a permanent electric dipole moment of the deuteron nucleus at the 1029 e cm level.*, Tech. Rep. (Brookhaven National Laboratory, 2008).

[50] A. E. Leanhardt, J. L. Bohn, H. Loh, P. Maletinsky, E. R. Meyer, L. C. Sinclair, R. P. Stutz, and E. A. Cornell, "On measuring the electron electric dipole moment in trapped molecular ions," (2010), arXiv:1008.2997 .

[51] P. G. H. Sandars, in *Atomic physics 4: proceedingd of the Fourth International Conference on Atomic Physics,*, edited by Putlitz (Plenum Press, 1975) pp. 71+, ISBN 0306371944.

[52] Y. Jiang, *Progress toward searching for electron electric dipole moment using Pbo*, Ph.D. thesis, Yale University (2008).

[53] B. E. Sauer, H. T. Ashworth, J. J. Hudson, M. R. Tarbutt, and E. A. Hinds, AIP Conference Proceedings, **869**, 44 (2006).

[54] N. E. Shafer Ray, Phys. Rev. A, **73**, 034102+ (2006).

[55] P. Sivakumar, C. P. McRaven, D. Combs, N. E. S. Ray, and V. Ezhov, Physical Review A, **77**, 062508+ (2008).

[56] J. Lee, E. R. Meyer, R. Paudel, J. L. Bohn, and A. E. Leanhardt, J. Mod. Opt., **56**, 2005 (2009).

[57] J. M. Amini, C. T. Munger, and H. Gould, Phys. Rev. A, **75**, 063416+ (2007).

[58] M. Kittle, T. Burton, L. Feeney, and D. J. Heinzen, in *APS Meeting Abstracts* (2004).

[59] F. Fang and D. S. Weiss, Opt. Lett., **34**, 169 (2009).

[60] M. V. Berry, Proceedings of the Royal Society of London. A. Mathematical and Physical Sciences, **392**, 45 (1984).

[61] E. D. Commins, American Journal of Physics, **59**, 1077 (1991).

[62] J. M. Pendlebury, W. Heil, Yu, P. G. Harris, J. D. Richardson, R. J. Baskin, D. D. Doyle, P. Geltenbort, K. Green, M. G. D. van der Grinten, P. S. Iaydjiev, S. N. Ivanov, D. J. R. May, and K. F. Smith, Physical Review A, **70**, 032102+ (2004).

[63] S. K. Lamoreaux and R. Golub, Physical Review A, **71**, 032104+ (2005).

[64] A. Vutha and D. DeMille, "Geometric phases without geometry," (2009), arXiv:0907.5116 .

[65] E. R. Meyer, A. E. Leanhardt, E. A. Cornell, and J. L. Bohn, Physical Review A, **80**, 062110+ (2009).

[66] A. Vutha, (2008), private communciation.

[67] G. Herzberg, *Spectra of Diatomic Molecules*, 2nd ed., edited by J. W. T. Spinks, Molecular Spectra and Molecular Structure, Vol. I (Van Nostrand Reinhold Company, New York, 1950).

[68] F. Martin, R. Bacis, J. Vergs, J. Bachar, and S. Rosenwaks, Spectrochim. Acta, Part A, **44**, 889 (1988), ISSN 0584-8539.

[69] C. H. Townes and A. L. Schawlow, *Microwave spectroscopy*, International series in pure and applied physics (McGraw-Hill, New York, 1955).

[70] L. Landau and E. Lifshitz, *Quantum mechanics : non-relativistic theory*, 3rd ed., Theoretical Course of Physics, Vol. 3 (Pergamon Press, Cambridge, 1977).

[71] J. M. Brown and A. Carrington, *Rotational spectroscopy of diatomic molecules*, Cambridge molecular science series (Cambridge University Press, Cambridge, 2003).

[72] D. Kawall, F. Bay, S. Bickman, Y. Jiang, and D. DeMille, Phys. Rev. Lett., **92**, 133007 (2004).

[73] J. Brown, J. Hougen, K. Huber, J. Johns, I. Kopp, H. Lefebvrebrion, A. Merer, D. Ramsay, J. Rostas, and R. Zare, J. Mol. Spectrosc., **55**, 500 (1975), ISSN 00222852.

[74] L. R. Hunter, S. E. Maxwell, K. A. Ulmer, N. D. Charney, S. K. Peck, D. Krause, S. Ter-Avetisyan, and D. DeMille, Phys. Rev. A, **65**, 030501 (2002).

[75] M. G. Kozlov and D. DeMille, Phys. Rev. Lett., **89**, 133001 (2002).

[76] I. I. Sobelman, *Atomic spectra and radiative transitions*, 2nd ed., Springer series on atoms + plasmas (Springer-Verlag, Berlin, 1992).

[77] E. A. Dorko, J. W. Glessner, C. M. Ritchey, L. L. Rutger, J. J. Pow, L. D. Brasure, J. P. Duray, and S. R. Snyder, Chem. Phys., **102**, 349 (1986), ISSN 0301-0104.

[78] M. J. Kurylo, W. Braun, S. Abramowitz, and M. Krauss, J. Res. Nat. Bur. Stand. A, **80**, 167+ (1976).

[79] R. C. Oldenborg, C. R. Dickson, and R. N. Zare, J. Mol. Spectrosc., **58**, 283 (1975), ISSN 0022-2852.

[80] L. Veseth, J. Phys. B: At., Mol. Phys., **6**, 1473+ (1973), ISSN 0022-3700.

[81] S. R. Bickman, *Progress towards a measurement of the electric dipole moment of the electron using Pb0**, Ph.D. thesis, Yale University (2007).

[82] L. I. Schiff, Phys. Rev., **132**, 2194 (1963).

[83] P. Ehrenfest, Z. Phys., **45**, 455 (1927).

[84] E. D. Commins, J. D. Jackson, and D. P. DeMille, Am. J. Phys., **75**, 532 (2007).

[85] F. Schwabl, *Advanced Quantum Mechanics*, 4th ed. (Springer, 2008) ISBN 3540850619.

[86] D. Budker, D. F. Kimball, and D. P. DeMille, *Atomic Physics: An Exploration Through Problems and Solutions*, 1st ed. (Oxford University Press, Oxford, 2004).

[87] A. N. Petrov, A. V. Titov, T. A. Isaev, N. S. Mosyagin, and D. DeMille, Phys. Rev. A, **72**, 022505 (2005).

[88] T. A. Isaev, A. N. Petrov, N. S. Mosyagin, A. V. Titov, E. Eliav, and U. Kaldor, Phys. Rev. A, **69**, 030501 (2004).

[89] E. R. Meyer, J. L. Bohn, and M. P. Deskevich, Phys. Rev. A, **73**, 062108 (2006).

[90] J. M. Amini and H. Gould, Phys. Rev. Lett., **91**, 153001+ (2003).

[91] D. DeMille, F. Bay, S. Bickman, D. Kawall, D. Krause, S. E. Maxwell, and L. R. Hunter, Phys. Rev. A, **61**, 052507 (2000).

[92] G. Herzberg, *Atomic Spectra and Atomic Structure*, 2nd ed. (Dover Publications, 1944) ISBN 6000814860.

[93] K. Balasubramanian and K. S. Pitzer, J. Phys. Chem., **87**, 4857 (1983), ISSN 0022-3654.

[94] E. R. Meyer and J. L. Bohn, Phys. Rev. A, **78**, 010502+ (2008).

[95] F. Bay, *Construction of an apparatus and preliminary measurements for a search for the electric dipole moment of the electron using lead monoxide*, Ph.D. thesis, Yale University (2003).

[96] F. G. Will, H. G. DeLorenzi, and K. H. Janora, Journal of the American Ceramic Society, **75**, 295 (1992).

[97] E. Hecht, *Optics (4th Edition)*, 4th ed. (Addison Wesley, 2001) ISBN 0805385665.

[98] M. Born and E. Wolf, *Principles of Optics: Electromagnetic Theory of Propagation, Interference and Diffraction of Light (7th Edition)*, 7th ed. (Cambridge University Press, 1999) ISBN 0521642221.

[99] E. R. Golubyatnikova and M. I. Petelin, Radiophysics and Quantum Electronics, **37**, 335 (1994), ISSN 0033-8443.

[100] J. Krupka, K. Derzakowski, M. Tobar, J. Hartnett, and R. G. Geyer, Measurement Science and Technology, **10**, 387+ (1999), ISSN 0957-0233.

[101] L. Malter and D. B. Langmuir, Physical Review Online Archive (Prola), **55**, 743 (1939).

[102] N. D. Milošević, G. S. Vuković, D. Z. Pavičić, and K. D. Maglić, International Journal of Thermophysics, **20**, 1129 (1999), ISSN 0195928X.

[103] T. M. Yoshida, T. M. Jovin, and B. G. Barisas, Review of Scientific Instruments, **60**, 2924 (1989), ISSN 10897623.

[104] G. M. Hagen, G. Gao, D. A. Roess, and B. G. Barisas, Review of Scientific Instruments, **76**, 083117+ (2005), ISSN 10897623.

[105] C. Christiansen, Annalen der Physik und Chemie, **23**, 298+ (1884).

[106] P. H. Roberts and H. D. Ursell, Philosophical Transactions of the Royal Society of London. Series A, Mathematical and Physical Sciences, **252**, 317 (1960), ISSN 00804614.

[107] H. S. Denmarak and W. M. Cady, J. Opt. Soc. Am., **25**, 330 (1935).

[108] R. H. Clarke, Appl. Opt., **7**, 861 (1968).

[109] R. B. Barnes and L. G. Bonner, Physical Review Online Archive (Prola), **49**, 732 (1936).

[110] T. Weber, E. Riedle, and H. J. Neusser, J. Opt. Soc. Am. B, **7**, 1875 (1990).

[111] T. T. Kajava, H. M. Lauranto, and R. R. E. Salomaa, Appl. Opt., **31**, 6987 (1992).

[112] L. A. Westling, M. G. Raymer, and J. J. Snyder, J. Opt. Soc. Am. B, **1**, 150 (1984).

[113] P. Drell and S. Chu, Optics Communications, **28**, 343 (1979), ISSN 00304018.

[114] T. Volk, M. WÃ¶hlecke, and N. Rubinina, in *Photorefractive Materials and Their Applications 2*, Springer Series in Optical Sciences, Vol. 114, edited by P. GÃnter and J.-P. Huignard (Springer Berlin / Heidelberg, New York, NY, 2007) Chap. 6, pp. 165–203–203, ISBN 978-0-387-33924-5.

[115] Y. Furukawa, K. Kitamura, S. Takekawa, A. Miyamoto, M. Terao, and N. Suda, Applied Physics Letters, **77**, 2494 (2000), ISSN 10773118.

[116] A. Ashkin, G. D. Boyd, J. M. Dziedzic, R. G. Smith, A. A. Ballman, J. J. Levinstein, and K. Nassau, Applied Physics Letters, **9**, 72 (1966), ISSN 10773118.

[117] J. W. Hahn and Y. S. Yoo, Appl. Opt., **37**, 4867 (1998).

[118] A. Schwettmann, C. McGuffey, S. Chauhan, K. R. Overstreet, and J. P. Shaffer, Appl. Opt., **46**, 1310 (2007).

[119] N. H. Tran, R. Kachru, P. Pillet, H. B. van Linden van denHeuvell, T. F. Gallagher, and J. P. Watjen, Appl. Opt., **23**, 1353 (1984).

[120] K. Nemoto, T. Fujii, and Y. Minowa, Japanese Journal of Applied Physics, **34**, L1355 (1995).

[121] W. B. Davenport Jr. and W. L. Root, *An introduction to the theory of random signals and noise* (McGraw-Hill, 1958).

[122] W. Schottky, Ann. Phys., **362**, 541 (1918).

[123] M. Ross, *Laser receivers; devices, techniques, systems.*, Wiley series in pure and applied optics (Wiley, New York, 1966).

[124] D. DeMille, D. Glenn, and J. Petricka, Eur. Phys. J. D, **31**, 375 (2004), ISSN 1434-6060.

[125] D. R. Lide, ed., *CRC Handbook of Chemistry and Physics, 90th Edition*, 90th ed. (CRC Press, 2009) ISBN 1420090844.

[126] F. J. Lovas, E. Tiemann, J. S. Coursey, S. A. Kotochigova, J. Chang, K. Olsen, and R. A. Dragoset, "Nist: Diatomic spectral database," .

[127] T. Törring, Z. Naturforsch, **19a**, 1426+ (1964).

[128] J. Hoeft, F. Lovas, E. Tiemann, R. Tischer, and T. Trrin, Z. Naturforsch, **24a**, 1222 (1969).

[129] A. Popovič, A. Lesar, M. Guček, and L. Bencze, Rapid Commun. Mass Spectrom., **11**, 459 (1997), ISSN 1097-0231.

[130] S. Lopatin, I. Mittova, F. Gerasimov, S. Shugurov, V. Kostryukov, and S. Skorokhodova, Russ. J. Inorg. Chem., **51**, 1646 (2006), ISSN 0036-0236.

[131] J. J. Sakurai, *Modern quantum mechanics*, revised edition ed., edited by S. F. Tuan (Addison-Wesley, Reading, MA, 1994).

[132] W. H. Press, S. A. Teukolsky, W. T. Vetterling, and B. P. Flannery, *Numerical Recipes 3rd Edition: The Art of Scientific Computing*, 3rd ed. (Cambridge University Press, 2007) ISBN 0521880688.